AFRPL-TR-72-72

HOLOGRAPHY AS APPLIED TO JET BREAKUP & AN ANALYTICAL METHOD FOR REDUCING HOLOGRAPHIC DROPLET DATA

D. J. GEORGE
F. W. SPAID

TECHNICAL REPORT AFRPL-TR-72-72

SEPTEMBER 1972

AIR FORCE ROCKET PROPULSION LABORATORY
DIRECTOR OF LABORATORIES
AIR FORCE SYSTEMS COMMAND
UNITED STATES AIR FORCE
EDWARDS, CALIFORNIA

11

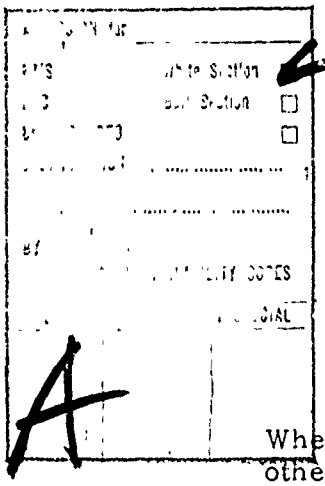

NOTICES

When U.S. Government drawings, specifications, or other data are used for any purpose other than a definitely related Government procurement operation, the Government thereby incurs no responsibility, nor any obligation whatsoever, and the fact that the Government may have formulated, furnished, or in any way supplied the said drawings, specifications, or other data, is not to be regarded by implication or otherwise, or as in any manner licensing the holder or any other person or corporation, or conveying any rights or permission to manufacture, use, or sell any patented invention that may in any way be related thereto.

AFRPL-TR-72-72

HOLOGRAPHY AS APPLIED TO JET BREAKUP AND AN ANALYTICAL METHOD FOR REDUCING HOLOGRAPHIC DROPLET DATA

D. J. George
F. W. Spaid

September 1972

AIR FORCE ROCKET PROPULSION LABORATORY
DIRECTOR OF LABORATORIES
AIR FORCE SYSTEMS COMMAND
UNITED STATES AIR FORCE
EDWARDS, CALIFORNIA

FOREWORD

This research was accomplished under Project 3058, Task 08, during the period from December 1969 to May 1972. It was conducted under the jurisdiction of the Liquid Rocket and Technology Divisions of the Air Force Rocket Propulsion Laboratory. The program was coordinated with the University of California at Los Angeles and, in addition to satisfying Air Force needs, served as the research for the dissertation of Daweel George. Technical direction for the project was provided by Professor Frank W. Spaid.

This technical report has been reviewed and is approved.

Paul J. Daily, Lt Col, USAF
Chief, Technology Division
Air Force Rocket Propulsion Laboratory

UNCLASSIFIED
Security Classification

DOCUMENT CONTROL DATA - R & D

(Security classification of title, body of abstract and indexing annotation must be entered when the overall report is classified)

1 ORIGINATING ACTIVITY (Corporate author)

Air Force Rocket Propulsion Laboratory
Edwards CA 93523

2a. REPORT SECURITY CLASSIFICATION
UNCLASSIFIED

2b GROUP
N/A

3 REPORT TITLE
Holography as Applied to Jet Breakup and An Analytical Method for Reducing Holographic Droplet Data

4 DESCRIPTIVE NOTES (Type of report and inclusive dates)
Final Report, December 1969 to May 1972

5 AUTHOR(S) (First name, middle initial, last name)
Daweel J. George
Frank W. Spaid

6 REPORT DATE	7a. TOTAL NO OF PAGES	7b NO OF REFS
September 1972	275	76

8a. CONTRACT OR GRANT NO	9a ORIGINATOR'S REPORT NUMBER(S)
b PROJECT NO 3058	AFRPL-TR-72-72
c Task No. 08	9b OTHER REPORT NO(S) (Any other numbers that may be assigned this report) N/A
d	

10 DISTRIBUTION STATEMENT
Distribution of this document is unlimited.

This document has been approved for public release and sale; its distribution is unlimited.

11 SUPPLEMENTARY NOTES	12 SPONSORING MILITARY ACTIVITY
Details of illustrations in this document may be better studied on microfiche None	AFRPL, Edwards CA

13 ABSTRACT

The use of holography in studying certain fluid mechanics problems was investigated. This effort specifically examined the application of holography to: (1) high speed (supersonic) flow fields by injecting different liquid jets perpendicularly into a Mach 3 gas stream to observe how jet breakup occurs, and (2) the atomization characteristics (droplet size and spatial distribution) of a liquid jet injected into quiescent, atmospheric air. The holograms were recorded in the off-axis, Fresnel, transmission arrangement.

The variables of interest were wind tunnel total pressure, liquid type, orifice diameter and liquid injection velocity. Twenty-five holograms were taken of flow fields resulting from the different test conditions. Variation in jet amplitude and wavelength as the liquid progressed from the injection point were clearly visible, and these data were quantified. For the test conditions of this investigation, the effect of fluid physical properties (viscosity and surface tension) was negligible. Amplitude and wavelength growth was due to inertial forces.

Radial distribution of the droplet number and mass for a jet injected into still air was found to increase monotonically, then decrease with increase in radial position. Droplet size distribution variation was observed to exist at two different axial regions of the jet. The mode became smaller with increase in axial distance from the injection point.

The analytical method for processing three-dimensional droplet data consisted of a system of computer programs which operated on the droplet size and spatial coordinates to determine size, mass, number and spatial distribution. Two methods for retrieving holographic data were devised.

DD FORM 1 NOV 68 1473

UNCLASSIFIED
Security Classification

14 KEY WORDS	LINK A		LINK B		LINK C	
	ROLE	WT	ROLE	WT	ROLE	WT
Holography						
Jet Breakup						
External Burning						
Jet Interaction						
Droplet Distribution						
Spray Analysis						

ABSTRACT

The use of holography in studying certain fluid mechanics problems was investigated. The holographic technique can record a flow field in three dimensions by one pulse of a laser. This effort specifically examined the application of holography to: (1) high speed (supersonic) flow fields by injecting different liquid jets perpendicularly into a Mach 3 gas stream to observe how jet breakup occurs, and (2) the atomization characteristics (droplet size and spatial distribution) of a liquid jet injected into quiescent, atmospheric air. The holograms were recorded in the off-axis, Fresnel, transmission arrangement. The holographic recording system consisted of a 3 joule, pulsed ruby laser, whose pulse width was 50 nanoseconds, and a holocamera.

Five liquids (water, trichloroethylene, Freon 113, methanol and water/photoflo solution) were injected individually through different size orifices (.042, .050, .062 inches in diameter). The variables of interest were wind tunnel total pressure, liquid type, orifice diameter and liquid injection velocity. Twenty-five holograms were taken of flow fields resulting from the different test conditions. Variation in jet amplitude and wavelength as the liquid progressed from the injection point were clearly visible, and these data were quantified. It was found that an equation of the form

$$\text{Amplitude, Wavelength} = C(\text{injection distance})^{N}(\text{dynamic pressure ratio})^{K}$$

modeled the data well. For the test conditions of this investigation, the effect of fluid physical properties (viscosity and surface tension) was negligible. Amplitude and wavelength growth was due to inertial forces. Droplet data in the supersonic stream was not discernible.

This was attributed to the droplet sizes being less than the resolution capability of the holographic system (approximately 15 microns) and the velocity of the droplets, which moved approximately 10-25 microns within the 50 nanosecond pulse, causing a smear of the droplet image.

Radial distribution of the droplet number and mass for a jet injected into still air was found to increase monotonically, then decrease with increase in radial position. The droplet field spreading increased with increase in distance from the injection point. Droplet size distribution variation was observed to exist at two different axial regions of the jet. The mode became smaller with increase in axial distance from the injection point. Drop size distribution for the data from this investigation was modeled well by either a log-probability or modified general exponential function. Excellent results were obtained with the cumulative volume models, but poor correlation was obtained with the droplet volume derivative. This was attributed to the wide scatter in the data when it was arranged in the volume derivative form.

Two methods for retrieving holographic data were devised: (1) direct -- data is taken directly from the scene volume and input on magnetic tape, and (2) alternate -- photographs are taken at discrete planes within the scene volume, processed through a film reading machine and the data punched on cards. The analytical method for processing three-dimensional droplet data consisted of a system of computer programs which operated on the droplet size and spatial coordinates to determine size, mass, number and spatial distribution. Information is output in tabulated and plotted form. The data can be characterized by selected distribution functions and calculated mean diameters.

TABLE OF CONTENTS

TABLE OF CONTENTS, continued

TABLE OF CONTENTS, continued

NOMENCLATURE

Symbol	Description	Units
a	Sonic velocity, scaling factor (equation 1)	ft/sec
a^*	Rectangular strip half width in expression for $R_{32}=a^*(\rho_g V_g^2 a^*/\sigma)^{n-1}$, page 11.	ft
A	Area, dimensionless amplitude (equation 31)	in^2
b,B	Coefficient	
c	Wave velocity	ft/sec
C_d	Discharge coefficient	
C_D	Drag coefficient	
C_f	Skin friction	
$D^*,\bar{D}$	Constant coefficients (equations 16 and 17)	
D	Diameter	microns, inches
F	Force	lbs.
g,G	Gravitational constant	ft/sec^2
k	Specific heat ratio	
L	Length	in.
m	Mass	lbs.
M	Mach number, V_g/a, momentum	
N	Number	
p	Coefficient	
P	Pressure	lb/in^2
q	Coefficient	
$\bar{q}$	Dynamic pressure ratio, $\rho_1 V_1^2/kPM^2$	

NOMENCLATURE, continued

Symbol	Description	Units
Q	Volume flow rate	ft^3/sec
$\bar{r}$	Mean radius	microns, inches
R	Scaling factor (equation 1), initial drop radius (equation 2)	in.
Re	Reynolds number, $\rho_g V_g D_o/\mu_g$	
S	Dimensionless distance $S'/C_d^{\frac{1}{2}}D_o$ along trajectory	
t	Time	sec.
T	Temperature	
U	Mean lineal velocity	ft/sec
V	Velocity, volume	ft/sec, in^3
W	Weight flow rate	lb/sec
We	Weber number, $\rho_g V_g^2 D_o/\sigma$	
$\bar{x}$	Jet breakup distance from injection point in direction of wave travel	in.
x,y,z	Spatial coordinates	in.
Z	Ohnesorge number, $\mu_l/\sqrt{\sigma\rho_l D}$	
β	Sheltering parameter (equation 1)	
γ	Specific weight	
δ	Boundary layer thickness (equation 1), displacement in radial direction (equation 2), coefficient (equation 16)	in.
ζ_o	Initial dimensionless amplitude, amplitude/wavelength	
θ	Injection angle	
λ	Dimensionless wavelength, $\lambda'/C_d^{\frac{1}{2}}D_o$	

NOMENCLATURE, continued

Symbol	Description	Units
Q	Volume flow rate	ft^3/sec
$\bar{r}$	Mean radius	microns, inches
R	Scaling factor (equation 1), initial drop radius (equation 2)	in.
Re	Reynolds number, $\rho_g V_g D_o/\mu_g$	
S	Dimensionless distance $S'/C_d^{\frac{1}{2}}D_o$ along trajectory	
t	Time	sec.
T	Temperature	
U	Mean lineal velocity	ft/sec
V	Velocity, volume	ft/sec, in^3
W	Weight flow rate	lb/sec
We	Weber number, $\rho_g V_g^2 D_o/\sigma$	
$\bar{x}$	Jet breakup distance from injection point in direction of wave travel	in.
x,y,z	Spatial coordinates	in.
Z	Ohnesorge number, $\mu_l/\sqrt{\sigma\rho_l D}$	
β	Sheltering parameter (equation 1)	
γ	Specific weight	
δ	Boundary layer thickness (equation 1), displacement in radial direction (equation 2), coefficient (equation 16)	in.
ζ_o	Initial dimensionless amplitude, amplitude/wavelength	
θ	Injection angle	
λ	Dimensionless wavelength, $\lambda'/C_d^{\frac{1}{2}}D_o$	

NOMENCLATURE, continued

Symbol	Description	Units
μ	Absolute viscosity	lb/ft.sec.
ν	Kinematic viscosity	ft^2/sec
ρ	Density	lb/ft^3
σ	Surface tension	lb/ft
τ	Shear stress	

Subscripts	Description
aw	Adiabatic wall
g	Gas
l	Liquid
m	Mean
o	Orifice, total
rel	Relative
w	Wall
∞	Free stream

LIST OF FIGURES

LIST OF FIGURES, continued

LIST OF FIGURES, continued

LIST OF TABLES

LIST OF TABLES, continued

ACKNOWLEDGMENTS

I wish to express my sincere appreciation to Dr. Frank Spaid for his direction, assistance and encouragement throughout the course of this research effort. A note of thanks is also given to the other members of my Committee, Drs. Catton, Liu, Pruppacher and Schubert for their willingness to review and comment on the investigation.

I am indebted to the United States Department of Defense for supporting me under its Long-Term Full-Time Study Program which enabled me to pursue my doctoral degree.

Appreciation is extended to the Air Force Rocket Propulsion Laboratory for supporting the dissertation investigation. Gratitude is expressed to the many personnel of the Laboratory for their services and support in the areas of drafting, test system fabrication and operation, data acquisition and reduction.

Special recognition is given to the following individuals: Lt. Milton Marks, Ph.D., Mr. L. Yates and Mrs. C. Gannon, both of Computing and Software Inc., for their assistance in computer programming and data reduction; Lt. T. Veneziano for his assistance in retrieving the holographic data from the holograms; Dr. R. Wuerker and Mr. R. Briones, TRW Systems Group, for their advice on holography; Dr. D. Harvey, McDonnell-Douglas Aircraft, for his advice on liquid injection into a supersonic stream.

A deep debt of gratitude is expressed to my wife, Michelle, who has endured many hours of loneliness and neglect while I pursued my studies. I thank her for her patience, sacrifices, encouragement and support. I also thank her for taking the dictation and doing the typing for this dissertation.

VITA

September 16, 1937--Born, Danbury, Connecticut

1959--B.S., University of Arizona

1960--M.S., Ohio State University

1960-1961--Engineer, AiResearch Manufacturing Co., Phoenix, Arizona

1961-1964--Project Officer, United States Air Force,
Edwards Air Force Base, California

1964-present--Project Engineer, Air Force Rocket Propulsion
Laboratory, Edwards, California

1972--Ph.D., University of California at Los Angeles

PUBLICATIONS

GEORGE, DAWEEL JOSEPH

1960 Master's Thesis: A Theoretical Analysis of the Factors Affecting Radiation Errors in Air Temperature Measurements at Altitudes from 50,000 to 150,000 Feet. Ohio State University.

1965 "Project Scorpio: Liquid-Rocket Propulsion Technology" Air University Review, Vol. XVI No. 6, September-October.

1966 "SCORPIO: Simpler Injectors and Clusters for Large Liquid Rocket Engines." Space/Aeronautics, Vol. 45 No. 5, May.

1968 "Simultaneous Heat, Mass and Momentum Transfer Over a Flat Plate," December, unpublished.

1969 "Application of Galerkin's Method to Hydrodynamic Stability in a Rectangular Duct," March, unpublished.

1972 Doctoral Dissertation: Holography as Applied to Jet Breakup and An Analytical Method for Reducing Holographic Droplet Data. University of California at Los Angeles.

Co-author:

1962 Unique Injector Design and Chamber Cooling Techniques. LPIA, November, LPS 62-1.

1963 Simulated Liquid Air Combustion with Liquid Hydrogen in a Two Dimensional Thrust Chamber. May, RTD-TDR-63-1041.

1965 Investigation of Large Thrust per Element Injectors and A Simplified Clustering Technique for Rocket Engines, ICRPG, October, RPL-TM-65-29.

1965 Investigation of Large Thrust per Element Injectors with Conventional and Two Dimensional Thrust Chambers Utilizing Liquid Oxygen and Liquid Hydrogen Propellants, September, AFRPL-TR-65-149.

1965 Oxygen/Hydrogen Injector Thrust per Element Size Maximization, October, AFRPL-TR-65-199.

1966 A Simplified Clustering Technique for Rocket Engine Modules, February, AFRPL-TR-66-10.

CHAPTER I

INTRODUCTION

1. Background

The interest in liquid jet behavior dates back to Lord Rayleigh[1]*. Since his original paper of 1878, many people have attempted to determine, both analytically and experimentally, the mechanisms and physical processes by which a liquid jet disintegrates into droplets. The atomization process occurs in stages and generally begins with a disturbance of the liquid jet surface, then the formation of ligaments as the perturbed surface becomes more unstable, and finally the ligaments break up further into droplets. Limited success has been achieved in theoretically predicting the form of disturbance that most rapidly leads to jet instability. Jet behavior and structure vary significantly in the different flow regimes; laminar, transition and turbulent. This indicates that the breakup mechanism is different for each regime. Surface tension, capillary, viscous, inertial and combinations of these forces dominate in certain regimes and under certain flow conditions, and influence the jet behavior accordingly. Although it is known that the jet breakup mechanism depends on the flow regime, the ultimate problem of theoretically predicting drop size distribution, given a set of flow conditions, fluid properties and injection geometry, has not been solved. However, empirical relationships have been developed by various investigators studying liquid jet behavior under various flow conditions and geometries. They, Harmon[2], Ingebo and Foster[3], Nukiyama and Tanasawa[4], Volynskiy[5], and Weiss and Worsham[6], to name a few, have correlated various flow parameters with some characteristic mean droplet diameter. Liquid jets were injected into air whose velocity ranged from zero to

*Superscripts in parenthesis indicate the references listed at the end of the report.

supersonic speeds. These and other investigators have established that the most important factors which influence drop size are nozzle geometry, operating conditions and fluid (liquid and gas) properties. The relative velocity between the liquid jet and the gas into which the liquid is injected plays a major role in the resulting drop size over the total range of gas conditions considered. Needless to say, a problem which has defied theoretical analysis for nearly a hundred years is a very complex one.

The interest in liquid jet behavior is as keen today as it has been through the years. This is due to the many practical applications which employ a liquid jet. Some of these uses are: chemical processes, aerosols, atomization of liquid fuels in automobile, jet and rocket engines, agricultural for spraying of crops, meteorological (cloud seeding), aerospace--thrust vector control, supersonic combustion, external burning, hydroquenching of solid rocket motors; fire fighting, pollution control, etc.

Adequate general theory and scaling laws which characterize the resulting spray from breakup of a liquid jet has been and is being sought. Spray information, drop size and mass distribution has, in the past, been primarily obtained by photographic and collection methods, but these have their limitations. More recently, the holographic technique has evolved to a state of development such that it can be applied in the investigation of certain engineering problems. With one pulse of a laser, the holographic technique can record a flow field in three dimensions without disturbing it. Due to the extremely short pulse width of a ruby laser (on the order of tens of nanoseconds), a high-speed flow field can be "frozen" and data about the liquid jet structure and characteristics,

heretofore unattainable, can be acquired.

This investigation applies the holographic technique to liquid jet injection into a supersonic gas stream and into still air, to: (1) examine the usefulness of the technique in certain fluid mechanics problems, and (2) acquire jet structure and droplet data previously unattainable.

2. Purpose

This investigation was a multi-purpose one. The first objective was to investigate liquid jet breakup and droplet formation resulting therefrom using the holographic technique. Of course, the purpose is to gain a better understanding of the mechanism by which the liquid jet breaks up and disintegrates into droplets. The holographic technique can provide, with one pulse of a laser, an instantaneous, full-size, three-dimensional reproduction of a flow field without disturbing it. This effort examined the application of holography in two flow regimes: (1) high speed (supersonic) flow fields by injecting a liquid perpendicularly into a Mach 3 gas stream to observe how jet breakup occurs, and (2) liquid jet injection into quiescent, atmospheric air.

Having taken the holograms, the next objective was to devise an accurate and rapid method for retrieving quantitative holographic data. Of particular interest was the structure of the jet, droplet size distribution and mass spatial distribution.

Once droplet data was retrieved from the hologram, it had to be reduced. Hence, another objective was to develop an analytical method to reduce three-dimensional droplet data, size and spatial coordinates, and operate on it statistically for subsequent correlation with flow

parameters.

Ultimately, the endeavor was to contribute to the formulation of a general theory and scaling laws which govern jet breakup and atomization into droplets, so that, given a set of conditions, the resulting flow field can accurately be characterized.

3. Method of Investigation

A general description of the manner in which the objectives were pursued is herein presented. After defining the problem, the next step was to conduct a review of the literature to determine what is known, how accurately the jet breakup is described and predicted, and what additional information is needed to better understand the atomization mechanism of liquid jets. Since one of the regimes of interest was liquid jet breakup in a supersonic stream, experiments were conducted in a Mach 3, blowdown wind tunnel. Holograms were taken of the flow fields resulting from the interaction of a liquid jet and the supersonic gas stream under various flow conditions. A hologram was also taken of a liquid jet injected into still air. Two methods were devised for retrieving holographic data from the holograms. In order to retrieve data from a hologram, one must first be able to view the hologram. This is accomplished by illuminating the hologram with a light source of the same or similar wavelength to that which was used in recording the hologram. Both methods reconstructed the hologram with a helium-neon laser, but differed in that the first method would retrieve data directly from the holograms and input the information on magnetic tape, while the second method involved taking a series of photographs through the scene volume, and used a film reading machine to retrieve the data which was then punched on

computer cards. These methods were specifically oriented for the retrieval of droplet data; however, they can also be used for retrieval of other types of holographic data. An analytical method to reduce holographic droplet data was developed. A system of computer programs comprised the analytical method. These programs operated on the droplet size and spatial coordinate data to obtain: (1) the drop size distribution, (2) the various mean diameters, and (3) mass spatial distribution. The raw data was also modeled by known distribution functions to determine if these functions could be used to characterize the resulting spray from the jet breakup. The data obtained from liquid jet injection into a supersonic stream and into still air was analyzed and organized for presentation in the most meaningful manner.

Presented in the subsequent chapters is a discussion of the literature survey, a description of the test apparatus and experiments, an explanation of the holographic retrieval methods, an explanation of the holographic data reduction method, a tabulation of the test results, and the analyses.

CHAPTER II

LITERATURE REVIEW

1. General Discussion

A comprehensive search of the literature concerning liquid jet breakup into droplets was conducted. Both analytical and experimental works were reviewed. Jet breakup in a cross-stream, either supersonic or subsonic, parallel gas stream and in still air are discussed below in Section 2. Accompanying jet breakup is droplet breakup. Hence, literature on droplet breakup was also amassed, but will not be discussed in detail here. Those interested in droplet breakup are referred to a report by Luna and Klikoff[7] on the aerodynamic breakup of liquid drops. It comprises a critical survey of droplet breakup literature. The work appears to be quite thorough and contains discussions on practically all of the accepted droplet breakup investigations, including those by Hinze[8], Morrell[9] and Wolfe and Andersen[10]. Luna and Klikoff found that the threshold conditions for breakup were determined by the critical Weber and Ohnesorge numbers. In Section 3 equations which were developed, either analytically or experimentally, to relate turbulent jet breakup under various flow conditions to some mean droplet diameter, are compared and discussed. Various droplet measurement techniques are discussed in Section 4. A qualitative discussion on holography is presented in Section 5, since this was the technique chosen to measure and spatially locate the droplets obtained from this investigation. A discussion as to how droplet data is characterized by various investigators is presented in Section 6.

2. Turbulent Jet Breakup and Droplet Formation

a. In a Supersonic Cross Stream: Dowdy and Newton[11] investigated liquid and gas jet injection into a supersonic stream. Liquid and gaseous nitrogen jets were injected perpendicularly into gas streams whose

Mach numbers ranged from 2.01 to 4.54. A large number of tests was conducted which provided information about the effects of free stream Mach and Reynolds numbers, injection pressure on the shock structure and the pressure distribution induced on the plate by the injection process. In addition to pressure distribution data, schlierens, shadowgraphs and motion pictures were taken of the jet interaction phenomena.

McRae[12] conducted an experimental investigation to study the breakup characteristics of a liquid jet injected perpendicularly into a Mach 4 supersonic gas stream. The variables of interest were gas stream total pressure, injection velocity and flow rate, injector internal configuration, injection angle and injectant physical properties. A total of 269 tests were conducted to provide data to characterize jet penetration and spreading. Shadowgraphs or still photos were presented for each test. Penetration and spreading plots were also presented. McRae found that the jet-gas stream interaction phenomena was unsteady.

Harvey[13] conducted an analytical investigation on longitudinal waves on a liquid jet injected at right angles to a high velocity gas stream. The analysis consisted of a linearized energy balance for surface waves moving along the jet. The motivation for the study was to gain a better understanding of the jet wave behavior, so drop size distribution resulting from jet breakup could be predicted. He found that long waves grow most rapidly under a laminar boundary layer, while short waves grow most rapidly under a turbulent boundary layer. He derived an expression for distance to jet breakup:

$$\bar{x} = \Omega \left(\frac{c}{\rho_g a^2} \right)^{1/3} \left(\frac{\sigma \delta \rho_l}{\zeta_o} \right)^{1/6} \qquad (1)$$

where

$$\Omega = \frac{6R}{\beta\sqrt{2\pi}} \qquad R = .5 \qquad \beta = .5$$

He compared the values for $\bar{x}$ predicted by his theory with measured values obtained from McRae's experimental data and only obtained fair correlation. The lack of good correlation is contributed to the approximations of linearization and deep water theory, and experimental measurement and interpretation difficulties. Graphs showing distance to jet breakup for different injection velocities are presented. There are irregularities in both the predicted and measured values. In general, the predicted values are lower than the measured values. The trends are similar. That is, as injection velocity increases, so does the jet breakup distance. This was also observed in the present investigation. Harvey acknowledges that transverse waves around the jet also occur and a true analysis should take both longitudinal and transverse waves into account. A more recent paper by Harvey[14] concerns itself with lateral capillary waves which occur when a liquid jet injected perpendicularly into a supersonic stream is aerodynamically broken up by the gas stream. It is an analytical investigation and uses an approach similar to that of Mayer[15] and Adelberg[16]. The analysis is conducted in the stand-off region between the normal shock and the windward side of the jet and sonic lines. The analysis differs from those of Mayer and Adelberg, who used Jeffrey's sheltering theory. The basis for the analysis is an equation developed by Chang and Russell for subsonic gas flow. Chang and Russell provided a formulation for Kelvin-Helmholtz instability that includes the effects of compressibility. Harvey's analysis includes Kelvin-Helmholtz and Rayleigh-Taylor instabilities, both of which he

claims are appropriate on the windward side of the liquid jet. He develops an expression for the size distribution of drops produced over the whole windward face of the jet. Some approximations are made to facilitate integration of the distribution expression. He further simplifies by considering only capillary waves. He then relates the number distribution to R_{32} (Sauter mean radius) and finally arrives at the expression $R_{32} = a*We^{n-1}$, which is the Weber number to some power. He compared his results with the experimental data of Bitron[17], Volynskiy[5] and Gooderum[18] and found his theory relates best with Bitron data.

Sherman and Schetz[19] investigated breakup of liquid sheets and jets in a supersonic gas stream. Review of this paper was limited to the sections concerning the jets. Liquid jets were studied with spark shadowgraphs, high speed movies (7,000 frames/second) and photomicrographs (0.4 microsecond spark source). Four different liquids were injected into a Mach 2.1 gas stream. Their high speed movies show that jet breakup is characterized by gross fracture of the jet, initiated at the troughs of waves which span the jet circumference and move axially along the jet. Their droplet data obtained from photomicrographs is not considered good data, since too few drops were measured. Also, droplet size could be in error from approximately 7 to 240 microns, depending on the droplet velocity (injection to free stream) at the time the spark was flashed. They conclude that mean droplet diameter for the same liquid varies inversely to the 1.3 power with liquid injection velocity. $D_m \propto V_j^{-1.3}$. Only 2 of 3 water injection tests substantiate this conclusion.

Yates[20] investigated penetration and spreading of liquid jets transversely injected into supersonic air streams. He cites works of other investigators such as Catton[21] et. al., Forde[22] et. al. and

Horn and Reichenbach[23]. Since jet penetration and spreading were not areas of investigation in the study being presented here, evaluation of Yates' work will not be made. The penetration trajectories for the present investigation were calculated by the method developed by Catton[21]. Close agreement was found between the calculated and actual trajectories.

Two papers by Gooderum and Bushnell[24] [25] were reviewed. The purpose of the first investigation was to define the boundaries of aerodynamic breakup of a liquid jet. They found there is good agreement between theory and experiment for liquid jet breakup in the continuum flow regime, relative to critical Weber number; that is, the number below which no further breakup will occur.

In addition to reviewing data by other investigators in the continuum regime, they conducted "flight" tests in the slip flow regime (Knudsen number 10 -- 10^{-2}). Cool water (40-46°F) was injected perpendicularly into a Mach 5.5 gas stream. Orifice diameters were 0.01, 0.02, 0.04 and 0.08 inches. Injection temperature, pressure and velocity were essentially constant (approximately 43°F, 13 psia, 30fps). Hence, Weber number varied as did orifice diameter, and was found to be 3.9, 8.3, 15.7 and 31.4 for the respective orifices. As expected, all four jets were bent or deflected downstream and the breakup process was found to be a function of jet diameter. By observing photographs of the jet, the critical diameter was seen to be approximately 0.02 inches, and the $We_{crit} \approx 6$. Knudsen numbers for the tests were on the order of 1.0.

Although their data is insufficient to describe with certainty the variation of critical Weber number between continuum and free molecular flow, there appears to be no effect of Knudsen no. or high local static temperature (1620°R) on the critical Weber number for primary atomization

of liquid jets injected into a gaseous crossflow.

The second investigation was conducted to obtain mean drop size in a low gas density environment (3.74×10^{-4}-2.62×10^{-3} lb/ft^3).

Ambient water was injected perpendicularly into the air stream from a circular orifice mounted flush in a flat plate. Orifice diameters were 0.020, 0.052 and 0.120 inches with length/diameter ratios of 12.5, 5 and 2.45 respectively. Measurements were taken at 4.25 inches downstream from the point of injection and at various heights within the spray. Injection velocities ranged from 82 to 200 feet/second into a 3,970 feet/second air stream. The Dobbins[59] light scattering technique was used to determine the mean drop size, D_{32}, (mean diameters are defined by equation 28 on page 122) in the spray.

D_{32} was found to be independent of liquid injection velocity. They observed that for the smaller orifice diameter, the liquid remained a coherent jet for a distance before being atomized, whereas atomization occurred at the nozzle exit for the larger diameter. This is probably due to the difference in L/D_o among the nozzles.

There was too much scatter in the data to determine a definite relationship between D_{32} and orifice diameter and gas density. However, the trends appear to be in the proper direction. That is, D_{32} varies directly with orifice diameter and inversely with gas density.

Williams[26] reviewed papers pertinent to supersonic combustion. The papers concerning atomization and disintegration of liquid jets have all been reviewed in the course of this present investigation. He concludes, as did the author of this investigation, that a good amount of data on jet breakup mechanisms and resulting drop size distributions have been accumulated for liquid jets in subsonic gas streams, but very limited

experimental results are available for mean drop size and droplet distributions in supersonic streams. Theories presented by various investigators for liquid jet breakup in either subsonic or supersonic streams differ greatly in their physical assumptions. Since theories differ widely and experimental data is scarce, estimates of disintegration characteristics of liquid jets in supersonic gas streams are highly uncertain. Williams cited three disintegration mechanisms: (1) steady-shear, (2) capillary-wave, and (3) acceleration-wave breakup. He restricts his attention to the acceleration-wave breakup mechanism, since atomization of a liquid jet in a supersonic ramjet combustor seems to be explained best by this theory, although he acknowledges it is imprecise. He recommends improving the acceleration wave theory by accounting for jet deformation and by calculating droplet size distributions. Catton and Harvey[27] conducted an analysis on deformation of a liquid jet injected across a high velocity gas stream. A recent private communication with these gentlemen revealed they have conducted a more accurate analysis since their report was published.

Morrell[9] [28] [29] investigated liquid jet breakup and the critical conditions for drop and jet shattering. Breakup of a single water jet by a transverse shock wave was studied. He found that breakup time decreased with increase in gas velocity and increased with jet radius. The extent of deformation was a linear function of the ratio of Weber number to the square root of Reynolds number based on initial jet radius. He postulates two theoretical models: (1) atomization by stripping of a liquid boundary layer, and (2) deformation of the liquid mass, and discusses them. He found that for constant gas velocity the critical condition for liquid jet breakup is given by

$$\frac{\delta/R}{\rho_g v_g^2 R/\sigma} = -0.2 \qquad (2)$$

The study "Measurement of Droplet Sizes in Liquid Jets Atomized in Low-Density Supersonic Streams" by Kurzious and Raab[30] provided the first experimental data on droplet sizes and size distributions from the disintegration of liquid jets in low-density (free molecular regime) supersonic gas streams. Stop-motion photographs were taken of water and ethanol jets atomized by perpendicular injection into Mach 3 argon and helium streams. Gas stream static pressures and stagnation temperatures were, respectively, from approximately .015 to .155 psia and from 530 to 1680°R. Weber numbers, based on orifice diameter and free stream flow properties, varied from 8.4 to 130. They attempted to extrapolate, or determine the applicability of, continuum regime atomization correlations into the free molecular regime. The observed mean droplet sizes were all larger than those predicted by the continuum regime correlation, and large metastable droplets persisted for unexpectedly long intervals. Hence, they concluded that a fundamental difference exists between atomization mechanisms and time scales in the low and high density gas environments. Also, aerodynamic breakup of cross injected liquid jets is not expected to occur at low gas stream dynamic pressure.

The relevancy of Kurzious and Raab's work to this effort is the correlation of Ingebo[3], Bitron[17] and Volynskiy's[5] data, which spans the subsonic and supersonic regimes, by one equation:

$$\frac{D_{30}}{D_o} = \frac{48}{\left|We_l\right|^{.375}\left|Re/M\right|^{.25}} \qquad (3)$$

where $We_1 = \frac{\rho_1 V_g^2 D_o}{\sigma}$ $\quad$ $Re = \frac{\rho_g V_g D_o}{\mu_g}$

The equation is a modification of Volynskiy's expression. Also, the form of the equation is similar to that of Ingebo and Foster's, but contains a Mach number term, and the definitions of the Weber and Reynolds numbers are different. Figure 1 shows that Ingebo's subsonic equation over-predicts drop size when used in the supersonic region where Bitron and Volynskiy obtained their data. Figure 2 shows how equation (3) correlates the data. Kurzious and Raab discuss subjectively that the data would lie closer to the correlation line if proper corrections are made to the data to account for data acquisition errors.

Bitron[17] conducted a number of liquid jet atomization tests by transverse injection into a supersonic air stream. Mach numbers ranged from 1.37 to 2. The purpose of his work was to determine the applicability of the classic Nukiyama-Tanasawa equation,

$$10^4 D_{32} = 5.85 \frac{10^4}{V_{rel}} \left(\frac{\sigma}{\rho_1}\right)^{0.5} + 597 \left(\frac{\mu_1}{\sqrt{\sigma \rho_1}}\right)^{0.45} \left(10^3 \frac{Q_1}{Q_g}\right)^{1.5} \qquad (4)$$

which was developed for subsonic gas velocities and parallel liquid-gas flow, in supersonic gas streams. He injected dibutyl phthalate at room temperature in all tests and kept the volume flow rate constant at $Q_1/Q_g = 1.2 \times 10^{-6}$. Hence, the variation of D_{32} in equation (4) then becomes a function of the relative velocity, V_{rel}, only.

The air streams were accelerated through venturi tubes. Throat diameters did not exceed 3mm; the liquid jet tube was .32mm.

Droplet data was collected by impaction on silicon-coated glass slides. Corrections were made for the contact angle between the dibutyl

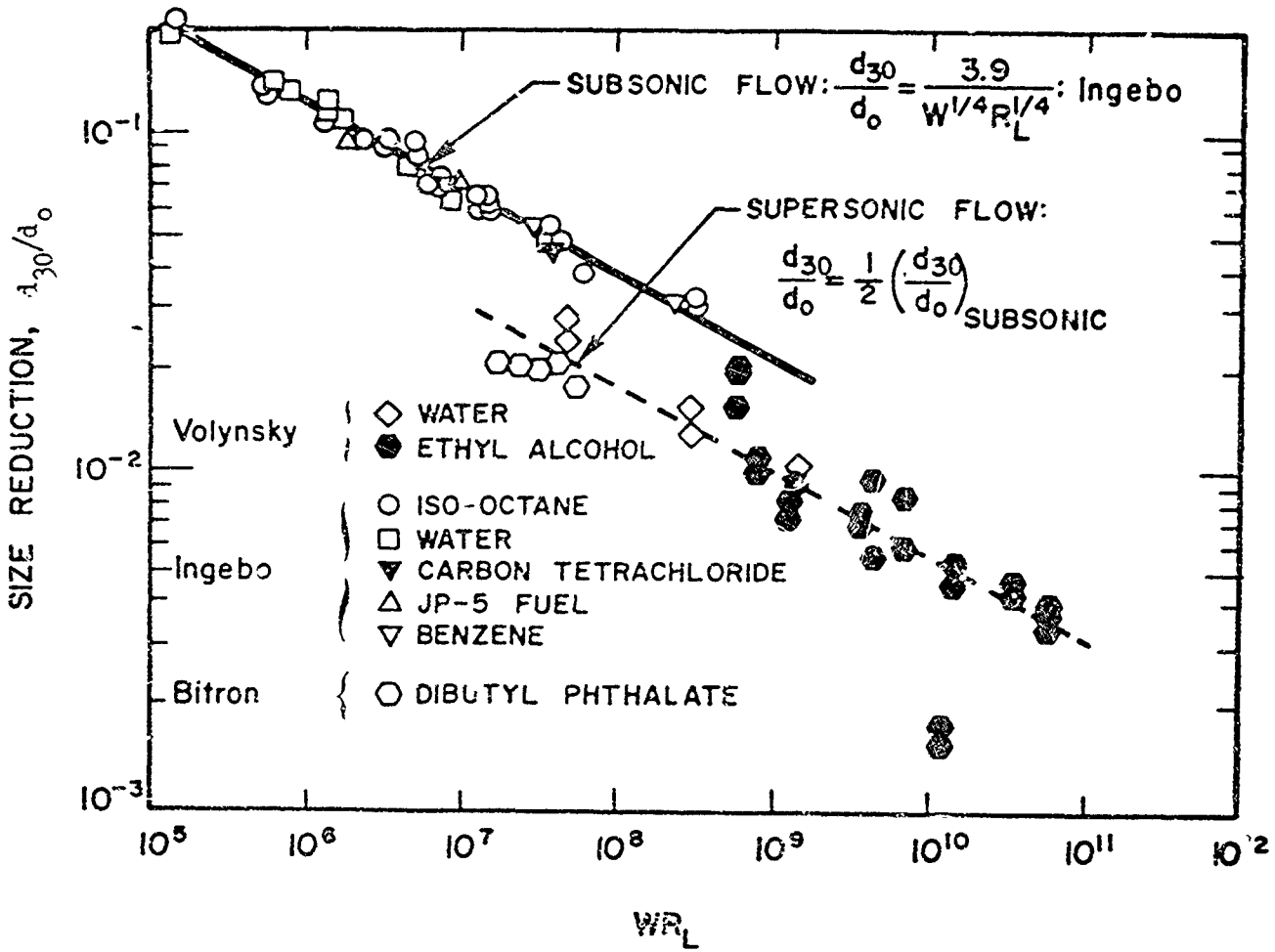

where

$W = \frac{\rho_g V_g^2 D_o}{\sigma}$;

7.6 to 7.2×10^4 ;

$R_L = \frac{\rho_l V_g D_o}{\mu_l}$;

7.0×10^3 to 8.5×10^5

Mach number:

8.7×10^{-2} to 3.1

FIG. 1 INGEBO CORRELATION OF MEAN DROPLET SIZES IN HIGH-VELOCITY SUBSONIC AND SUPERSONIC AIR STREAMS (Ref. 30)

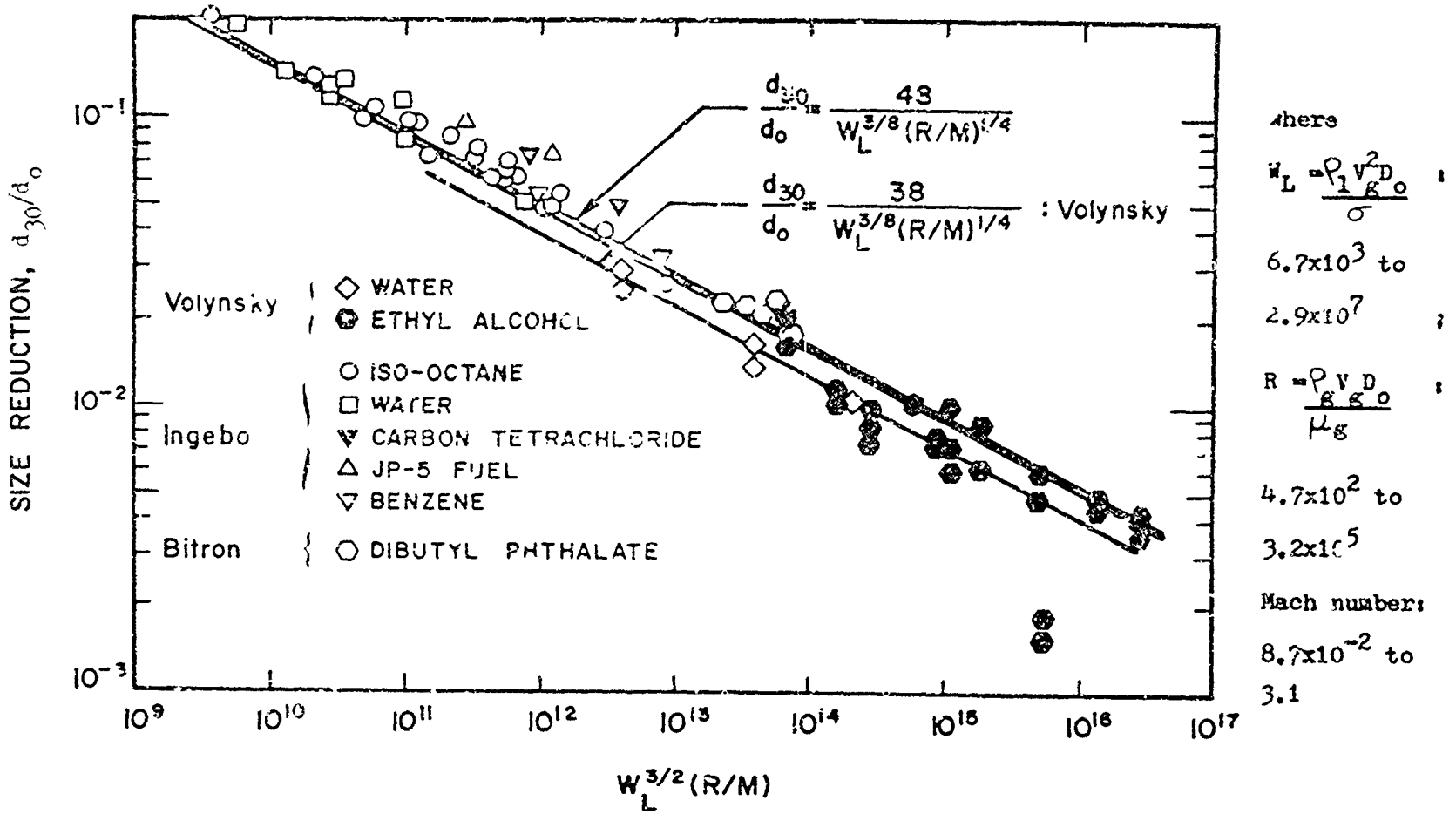

where

$W_L = \frac{\rho_l V_g^2 D_o}{\sigma}$:

6.7×10^3 to

2.9×10^7 ;

$R = \frac{\rho_g V_g D_o}{\mu_g}$:

4.7×10^2 to

3.2×10^5

Mach number:

8.7×10^{-2} to

3.1

FIG. 2 VOLYNSKY CORRELATION OF MEAN DROPLET SIZES IN HIGH-VELOCITY SUBSONIC AND SUPERSONIC AIR STREAMS (Ref. 30)

phthalate and the coated glass. The glass plate was placed at a point in the air stream where the Mach number of the spray jet, as determined by a Pitot tube, was 0.35 (corresponding to a velocity of about 120 meters/second). Sampling time for each test was 0.01 seconds controlled by a shutter placed between the air stream and glass plate. The Mach number choice was a compromise between high impaction efficiency of the small drops, which requires a high velocity at the glass plate, and avoidance of large droplet breakup upon impact, which requires a low velocity at the plate. Samples were collected from within a 1mm diameter circle on the plate whose center was on the axis of the air stream.

Bitron conducted 10 tests at each of 5 gas velocities and collected droplet data for each run. The collective drop size distributions for the different gas velocities are presented in Table III of his paper. Bitron claims that the Nukiyama-Tanasawa equation can be extended into the supersonic region. This conclusion is not warranted by his data, and Figure 3 shows why. Variation of D_{32} is inversely proportional to gas velocity according to the Nukiyama-Tanasawa equation. However, D_{32} calculated from Bitron's raw data shows that the Sauter mean diameter varies as $V_g^{-.39}$.

The flow conditions and fluid properties for Bitron's tests were inserted into Ingebo and Foster's[3] equation

$$\frac{D_{30}}{D_o} = \frac{3.9}{(WeRe)} .25 \qquad \text{where} \quad We = \frac{\rho_g V_g^2 D_o}{\sigma} \quad \text{and} \quad Re = \frac{V_g D_o}{\nu_l} \qquad (5)$$

Ingebo's equation is an empirical relation obtained by injecting various liquids perpendicularly into a subsonic gas stream. This equation, if it could be extended into the supersonic region, would be more apropos than the Nukiyama-Tanasawa equation, which emerged from data obtained from a

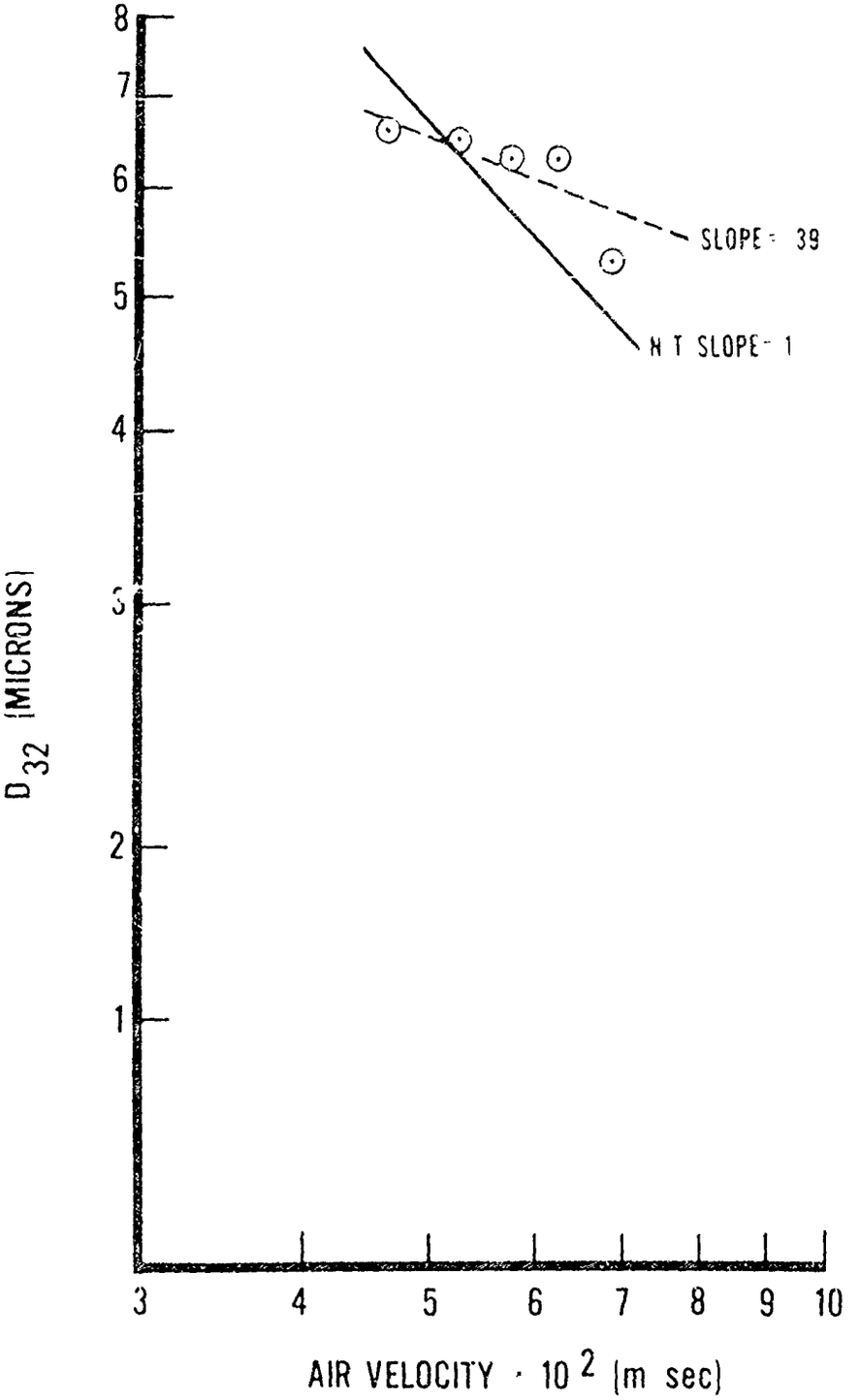

Figure 3. BITRON DATA, D_{32}

parallel liquid jet-gas stream arrangement. Figure 4 shows how the volume mean diameter, D_{30}, varies with gas velocity according to Ingebo's equation. The D_{30} calculated from Bitron's data by the definition

$$D_{30} = \left(\frac{\sum nD^3}{\sum n}\right)^{1/3} \qquad (6)$$

shows that the trend of D_{30} with change in gas velocity is substantially different from that indicated by Ingebo's equation, and that the actual data D_{30} is approximately 5 times smaller than that given by Ingebo's equation. Also shown in Figure 4 is the variation of D_{30} with gas velocity according to a correlation equation by Kurzious and Raab[30] which accounts for change in Mach number.

$$\frac{D_{30}}{D_o} = \frac{48}{\left(We_l\right)^{.375}\left(Re/M\right)^{.25}} \qquad (3)$$

This equation spans the subsonic and supersonic regions. It has a form similar to the Ingebo equation but the Weber and Reynolds numbers are defined differently. The variation of D_{30} with gas velocity is the same in both equations (3) and (5). That is, $D_{30} \propto V_g^{-.75}$. The D_{30} predicted with the Kurzious and Raab equation is closer to that calculated from the data than the D_{30} predicted with the Ingebo and Foster equation.

Bitron made histograms of relative drop volume as a function of nominal drop diameter. On these he superimposed the distribution function of the upper limit equation developed by Mugele and Evans[31]. Comparison of the curves with the histograms showed that the upper limit equation gave the proper trend in all cases. However, a Chi-square goodness of fit test applied to the data and upper limit distribution curves gave

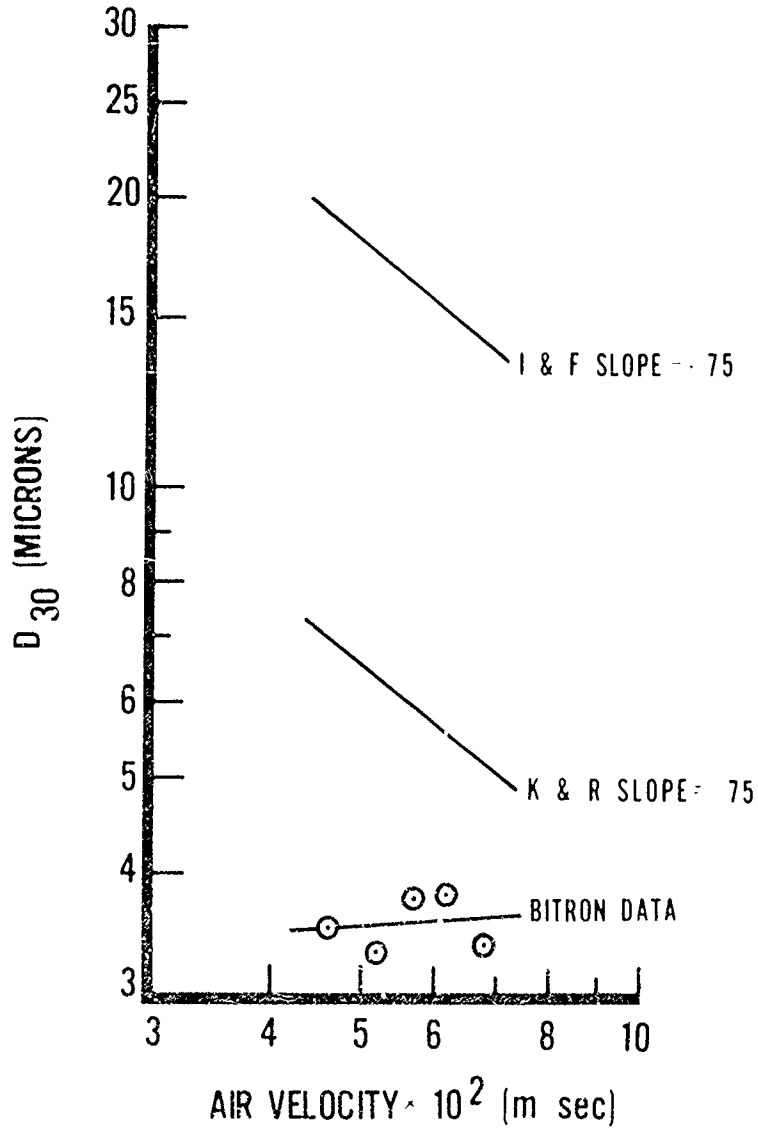

Figure 4. BITRON DATA

poor results.

Bitron also showed that droplet evaporation during injection could be neglected even for the highest stagnation temperature (473°F) in his experiments.

The work conducted by Volynskiy[5] is similar, in many respects, to that conducted in the present investigation. The main differences are in the geometric configurations, stream conditions and liquid injection pressure. Based on his experiments, Volynskiy correlated flow conditions and fluid physical properties to obtain expressions for the maximum and median droplet diameters.

$$\frac{D_{max}}{D_o} = \frac{78}{(We)^{3/8}\left|Re/M\right|^{1/4}\left(\frac{\rho_l}{\rho_g}\right)^{3/8}\left[1+\left(\frac{V_l}{V_g}\right)^2\right]^{-3/8}} \qquad (7)$$

$$\frac{D_{med}}{D_o} = \frac{45}{(We)^{2/5}\left|Re/M\right|^{1/4}\left(\frac{\rho_l}{\rho_g}\right)^{3/8}\left[1+\left(\frac{V_l}{V_g}\right)^2\right]^{-3/8}} \qquad (8)$$

As can be seen in the equations, the gas stream velocity and orifice diameter exert the greatest influence on the size of the drops and the effect of Mach number is weak. Volynskiy did not attempt to derive a drop size distribution expression or determine characteristic diameters, such as D_{30} and D_{32}. His data is presented in Table I. The various geometric arrangements referred to in the table are shown in Figure 5. In all cases, injection of the liquid was from a cylindrical aperture at an angle of 90° to the gas stream. By closely scrutinizing the data in Table I, one can make the following observations and conclusions:

TABLE I: VOLYNSKIY DATA, LIQUID INJECTION INTO A SUPERSONIC STREAM

Group	$\bar{A}_m$, median drop dia. (microns)	A_{max}, max. drop dia. (microns)	n, no. of drops counted	M Mach no.	T_{og}, (^oK)	P_{og}, atmos	d, orif. dia. (mm)	$\triangle P$; liq. press. drop (atmos)	liquid type	liq-gas arrange.
I	6.5	12	1017	1.8	275	5.4	0.4	5	Alcohol	a
	7.5	13.5	1616	↓	↓	↓	↓	15	↓	↓
	8	16	1695					40		
	7	16	2325				1	15		
	7.5	17	1931					40		
	9	17	2175				2	5		
	11	18	1790					15		
II	5.7	14	1165	1.8	275	5.4	1.1	5	Alcohol	b
	7.7	13.5	1026	↓	↓	↓	↓	15	↓	↓
	10.5	18	1923					40		
III	10	20	991	1.8	275	5.4	1	5	H_2O	b
	10	21	1168	↓	↓	↓	↓	15	↓	↓
	10	24	809					40		
IV	13	26	2200	1.8	275	5.4	3	5	Alcohol	c
	14	31	1700					15		
	13.5	31	1540				4	5		
	16	36	1500	↓	↓	↓	↓	10	↓	↓
	15	35	1352					12		
V	6	15	450	1	271	1.9	↓	0.315	Alcohol	
	7	16	470					40		
	10	18	864	↓	↓	↓	1	5	↓	↓
	11	23	1364					15		

TABLE I: VOLYNSKIY DATA, LIQUID INJECTION INTO A SUPERSONIC STREAM, continued

Group	A_m, median drop dia. (microns)	A_{max} max. drop dia. (microns)	n, no. of drops counted	M Mach no.	T, (°K)	P_{og}, atmos	d, orif. dia. (mm)	ΔP; liq. press. drop (atmos)	liquid type	liq-gas arrange.
	13	26	1897	1	271	1.9	1	5	H_2O	d
	16	30	1199	↓	↓	↓	↓	15	↓	↓
VI	10	19	1443				0.4	5		
	11.5	23	1317					15		
	16	30	880	1	271	1.9	1	5	H_2O	e
VII	13	29	773	↓	↓	↓	↓	15	↓	↓
	8	17	1373	1.2	272	1.9	1.1	5	Alcohol	f
VIII	9	14	1046	↓	↓	↓	↓	15	↓	↓
	10.5	22	1888					40		
	6	11	275	2.4	277	13	1	15	Alcohol	g
IX	8.5	16	587	↓	↓	↓	↓	40	↓	↓

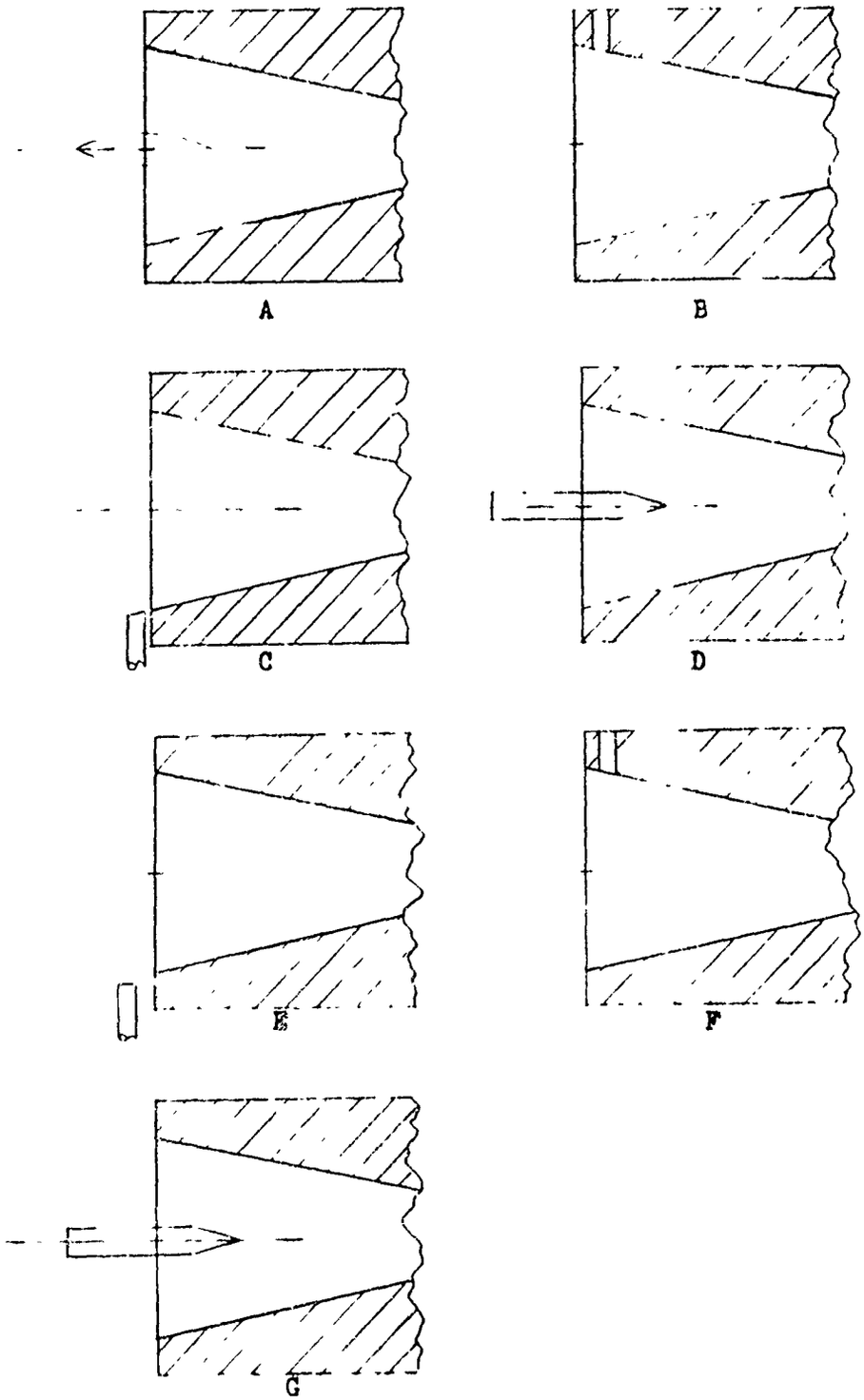

Figure 5. Volynskiy Orifice-Gas Stream Geometric Arrangement

Group I (Alcohol)

For a given liquid injection velocity (pressure drop), droplet median and maximum diameters vary directly with orifice diameter with one exception.

Group II (Alcohol)

For constant orifice diameter, droplet diameter increases with increase in injection pressure drop. This is also observed in Group I.

Group III (Water)

For constant orifice diameter, droplet median diameter remained constant with increase in injection pressure drop. This was not the case in Groups I and II.

Group IV (Alcohol)

No conclusion about droplet diameter variation with orifice diameter and pressure drop could be drawn with any degree of certainty. There appears to be a trend but scatter in the data negates it.

Group V (Alcohol)

a) Same conclusion as in Group II

b) Comparing the results with those of Group IV for the same orifice diameter, droplet diameters decreased with decrease in Mach number and gas stream total pressure, which is contrary to what one might expect.

Group VI (Water)

Same observations as those for Groups I and II.

Group VII (Water)

Results contradict observations for Groups II and VI.

Group VIII (Alcohol)

Results substantiate conclusion for Group II.

Group IX (Alcohol)

Results substantiate conclusion for Group II.

Comparing Groups II and VIII, no conclusion can be made with confidence about the variation in droplet diameter with flow condition changes, although there appears to be a slight increase in droplet diameter at the lower Mach number and total pressure.

Comparing Groups II and IV, droplet diameter increases with increase in orifice diameter, all other conditions the same.

Comparing Groups I, V and IX at the same orifice diameter and injection pressure, the droplet diameter decreases with increase in Mach number and total pressure.

Comparing Groups II and III, the H_2O droplets are larger than those of alcohol at the same conditions. A similar conclusion can be made for Groups VII and VIII.

It appears that the method of injecting the liquid into the gas stream has no effect on droplet diameter, at least among the seven schemes used by Volynskiy. This may not necessarily be true. Volynskiy collected his droplet data at some distance downstream of the injection point, where the gas velocity was 200 to 260fps. By the time the droplets reached that location, it is quite possible that the method of injection could not be discerned from the droplet data.

The droplets were collected on a layer of carbon covered by the vapors of burnt magnesium (MgO), at a distance from the point of injection where the speed of the gas flow was 60 to 80 m/sec. The layer was applied to the flat of a special rod (closed cylindrical case with a slot) placed along the cross-sectional diameter of the gas flow. Volynskiy claims that since the carbon layer thickness was 0.5 to 0.6mm, the difference between imprints of the drops and their actual size could be ignored. That is, he did not apply a correction factor (impression coefficient = imprint diameter/droplet diameter) to his measurements. The imprint diameters were measured with a microscope. The average error of measurements was $\pm$ 2 to $\pm$ 4 microns.

Volynskiy criticizes Bitron for attempting to use the Nukiyama-Tanasawa equation to describe drop size in the supersonic regime.

Also in his paper, Volynskiy investigates jet penetration analytically and experimentally using the photographic spark method to make his observations.

b. Liquid Jet in Subsonic Gas Stream: Hrubecky[32] conducted experiments in liquid atomization by air streams. Water was injected both parallel and normal to subsonic air streams, although 4 tests were conducted at Mach 1. He found that the Sauter mean diameter, D_{32}, decreased with increase in air velocity, and that parallel liquid injection gave a better degree of atomization than did perpendicular injection. Good agreement was found for D_{32} between his experiments and the Nukiyama-Tanasawa correlation for $V_g > 107$ meters/second and $1{,}000 < Q_g/Q_l < 5{,}000$. For $V_g > 140$ meters/second and $Q_g/Q_l > 10{,}000$ his experiments produced consistently lower values of D_{32} than those predicted by Nukiyama-Tanasawa.

Clark[33] studied the breakup of a water jet injected at right

angles to a subsonic gas stream. He produced an expression for relative cross-sectional area remaining at any point in the jet:

$$A/A_o = \left[0.00392(7.68\epsilon - 1)\ (\epsilon - 1)^{2.34} + 1\right]^{-1} \qquad (9)$$

where $\epsilon = \frac{\rho_g}{\rho_l}\left(\frac{V_{rel}L}{V_l D_o}\right)^2 = \frac{\rho_g}{\rho_l}\left(\frac{V_{rel}t}{D_o}\right)^2$

He found liquid jet breakup to increase with (1) increase in gas velocity, gas density and action distance and with (2) decrease in liquid jet diameter and velocity. Also, he found that liquid jet spreading takes place transversely to the gas flow. A look at the spreading parameter, ϵ, reveals that spreading of the jet is an inertial effect.

Limper[34] injected two different liquids, water and oil, parallel in a gas stream (235 to 900fps). A tube through which the liquid was injected was placed in the throat of a venturi tube. He compared the observed D_{32} with those predicted by the Nukiyama-Tanasawa equation. In all cases the observed D_{32} was substantially larger than predicted, even though the Nukiyama-Tanasawa equation was developed from a parallel, subsonic gas flow arrangement.

Weiss and Worsham[6] conducted an experimental study to determine the drop sizes obtained when a liquid (molten synthetic wax) was injected contra or costream to high velocity airstreams. They developed the correlation equation

$$\left(\frac{X\rho_g V^2}{\sigma}\right) = 0.61\left(\frac{V\mu_l}{\sigma}\right)^{2/3}\left(1 + 10^3\frac{\rho_g}{\rho_l}\right)\left(W\rho_l\sigma\frac{\mu_g}{\mu_l^4}\right)^{1/12} \qquad (10)$$

where $X = D_{\text{mass median}}$ and $V = V_{rel}$

One can see that the terms on the left side of the equation form a Weber number. They found that (1) relative velocity between the liquid and airstreams is of primary importance; (2) physical properties of the fluids

affect spray fineness but their influence is not dominating; and (3) the way in which the liquid is introduced is least important. The drop diameters observed in their study were 35 to 100% larger than those predicted by the Nukiyama-Tanasawa equation.

Mayer[15] [35] conducted a theoretical analysis to determine drop size distribution obtained by atomization of a liquid jet in a high-velocity gas stream. The analysis was based on the sheltering theory of Jeffreys. He postulates that drop size distribution is a function of wavelength. Ultimately, he derives an expression for mean droplet diameter

$$\bar{D} = 9\pi \sqrt[3]{16}\, B \left(\frac{\mu_l \sqrt{\sigma/\rho_l}}{\rho_g v_g^2} \right)^{2/3} \qquad (11)$$

He claims the theoretical result for $\bar{D}$ is in satisfactory agreement with the data of Weiss and Worsham[6].

Adelberg[16] [36] conducted an analytical study to determine drop size resulting from liquid jet breakup in a high velocity gas stream. His approach was similar to that of Mayer[15] but oriented for a liquid jet rather than an infinite liquid surface. He divides the flow field into two regimes according to relative dynamic pressure: (1) capillary wave and (2) acceleration wave regimes. Adelberg's analysis in the acceleration regime has been shown by Harvey[14] to be incorrect. An equation for mean drop size is derived for each regime:

Capillary Wave Regime

$$2\bar{r} = 2.4 D_o^{1/2} \left[\frac{\mu_l \left| \frac{\sigma}{\rho_l} \right|^{1/2}}{\beta \rho_g V_g^2} \right]^{1/3} \left[\frac{1 - K_1 \beta (\pi/2)^{1/2} e^{3/2}}{5 j_\sigma} \right] \quad (12)$$

Acceleration Wave Regime

$$2\bar{r} = 65.3 \left[\frac{\mu_l \left| \sigma/\rho_l \right|^{1/2}}{\beta \rho_g V_g^2} \right]^{2/3} \quad (13)$$

He suggests $\beta = 1$, $e = .06$, $K_1 = 1$

j_σ = sheltering parameter for capillary regime

Critical Wavelength

$$l_{cr} = \left[\pi^3 \sigma D / C_{D_o} (\sin^2\theta) 1/2 \, \bar{\rho}_g \bar{V}_g^2 \right]^{1/2} \quad (14)$$

If $l < l_{cr}$, capillary waves dominate

If $l > l_{cr}$, acceleration waves dominate

The report by Ingebo and Foster[3] is one of the most referenced works relative to drop-size distribution resulting from transverse injection of a liquid jet into a high velocity gas stream. Various liquids (iso-octane, JP-5 fuel, water, benzene, carbon tetrachloride) were injected through simple orifices (.010, .020, .030 and .040 inches in diameter) at right angles to a subsonic gas stream. Air velocities ranged from 100 to 700 feet/second while the air temperature range was from 80 to 900°F. Maximum Mach number was less than 0.4. Liquid injection velocities were varied from 35.5 to 204 feet/second. The length-to-diameter ratios for the orifices were short, being 1.00 and 4.65. Ingebo

and Foster concluded that liquid jet velocity and length-diameter ratio had little effect on mean droplet diameter. Thirteen of 43 tests were conducted at elevated temperatures (temperatures above 90°F). No consideration was given to droplet evaporation at the elevated temperatures.

By means of dimensional analysis, the investigators were able to correlate the volume mean diameter, D_{30}, and orifice diameter, Do, with the Weber and Reynolds numbers in the following manner:

$$D_{30}/_{Dc} = 3.9/(WeRe)^{0.25} \qquad (5)$$

where $We = \rho_g Vg^2 Do/\sigma$ and $Re = DoVg/\nu_1$

A similar expression was obtained for the maximum drop diameter, Dmax:

$$Dmax/Do = 22.3/(WeRe)^{0.29} \qquad (15)$$

The ranges for Dmax, D_{30}, We and Re were respectively 60 to 375 microns, 34 to 103 microns, 7×10^{-3}--13 and 11,100 to 366,000.

Three distribution functions: log-probability, Rosin-Rammler and Nukiyama-Tanasawa, were used to determine the volume mean diameter, D_{30}, for the experimental data. These expressions are respectively:

$$1-R = \frac{\delta}{\sqrt{\pi}} \int_{\infty}^{\delta} v_e^{-\delta^2 y^2} dy \qquad (16)$$

where R = volume fraction of drops having diameters greater than D

and $y = \ln(D/_{D^*})$

$$R = e^{-(D/\bar{D})^q} \quad \text{(Rosin-Rammler)} \qquad (17)$$

and

$$\frac{dR}{dD} = \frac{b^6 D^5 e^{-bD}}{120} \qquad (18)$$

Best results were obtained with expression (18). Using the empirical

relations (5) and (15) and $D_{30} = 3.915/b$, equation (18) becomes

$$\frac{dR}{dD} = 10^6 \frac{D^5}{D_{max}} (WeRe)^{+0.24} e^{-22.3(WeRe)^{+0.04} D/D_{max}} \quad (19)$$

This is the drop size distribution expression which best fits the data.

Droplet data was obtained by using a high speed camera, capable of taking photomicrographs, in conjunction with a sampling probe from which liquid concentration data was obtained. Photographs and sampling data were obtained by making vertical transverses along the spray centerline normal to the airstream and at a distance of 1 inch downstream from the injector. They discovered that vertical transverses made at distances of 1 inch on either side of the spray centerline showed no measurable effect of horizontal displacement on drop size distribution. They also noted that the larger drops tended to move farther out into the airstream than did the smaller drops because of the greater momentum of the larger drops. Further, they observed that D_{30} decreased as airstream velocity increased. D_{30} is affected very little when both liquid and air temperature are increased. The effect of air viscosity was found to be negligible, hence liquid-film resistance, surface tension, appeared to control the breakup process.

c. Liquid Jet in Still Air: The purpose of Popov's paper[37] was to determine the similarity laws for the atomization of liquids with constant properties and verify them by comparison with model experiments. He wrote the mass and momentum conservation equations for the liquid stream and gas into which the liquid was injected. He also wrote the Laplace equation for the pressure difference between the liquid and gas due to surface tension. These five equations were then nondimensionalized and various dimensionless parameters were identified. Those which

were significant for a liquid jet injected into still air were Reynolds number, Ohnesorge number, $\mu_1/\sqrt{\sigma\rho_1 D}$, density and viscosity ratios. He found that gas viscosity effect on atomization was negligible. Hence, the gas-liquid viscosity ratio need not be considered in the modeling experiments. The liquids he modeled, and to which he applied the scaling laws, were water and carbon tetrachloride. He obtained very close results between the "full scale" and model liquid data. Correlation was excellent. Drop size distribution and variation of mean diameter as a function of the dimensionless parameters are presented.

Eisenklam and Hooper[38] studied the flow characteristics of laminar and turbulent liquid jets injected into still air, but no drop size measurements were taken.

Harmon[2] presents a review of many of the early works on the breakup mechanism, disintegration and atomization of liquid jets in his dissertation. The works of Schweitzer, Haenlein, Merrington and Richardson, Baron, Balje and Larson, Castleman and Lee and Spencer are discussed. The regimes in which these investigations were conducted are outside that of interest in this investigation. A comprehensive review of the early (up to 1954) theories and investigations on liquid jets is also presented by Pilcher and Miesse in the first chapter of the report by Putnam[39] et. al. It would be superfluous to reiterate a discussion on these works here, since they are so adequately discussed by Harmon and Pilcher. Harmon developed an equation for the prediction of the Sauter mean (volume to surface) drop diameter resulting from injecting a liquid jet into still air. The derivation of the equation was initiated by an energy balance on the jet-spray system. The equation was nondimensionalized and correlated with available data to obtain

$$\frac{D_o}{D_{32}We} = 3.00(10^{-4}) \frac{\left(\frac{\mu_g^2}{g\sigma D_o \gamma_1}\right)^{0.3} \left(\frac{\mu_1}{\mu_g}\right)^{1.38}}{\left(\frac{U\mu_1}{\sigma}\right)^{1.45} \left(\frac{\gamma_1}{\gamma_g}\right)^{0.052}} \qquad (20)$$

In a latter publication[40], Harmon revised the form of the equation to

$$\frac{D_{32}}{D_o} = \frac{3.33(10^3) \left(\frac{\mu_g^2}{\sigma D_o \rho_1}\right)^{.15}}{\left(\frac{\rho_1 V_1 D_o}{\mu_g}\right)^{.5} \left(\frac{V_1 \rho_g D_o}{\mu_1}\right)^{.05}} \qquad (21)$$

The term in the numerator can be identified as a mixed Ohnesorge number while those in the denominator are mixed Reynolds numbers. Harmon concludes that drag on the jet is the most important drop forming mechanism in a high speed spray issuing from a short nozzle.

Chen and Davis[41] studied the disintegration of a turbulent water jet injected into still air. They investigated the characteristics of the jet surface disturbance, length of the continuous jet and the initial drop size. These were formulated by dimensional analysis and expressed in terms of the Weber and Reynolds numbers. Pipe diameters were 1/4, 3/8, 1/2 and 3/4 inches. Length/diameter ratio was 100. The ranges for injection velocity, We and Re were respectively 16 to 60fps, 50 to 250, $20x10^3$-$500x10^3$. They found that turbulence and surface tension forces were the predominant factors affecting disintegration. Amplitude and wavelength increased along the axis of the jet. Breakup distance and initial drop size increased with We. Unfortunately, no mean drop size data or drop size distribution information was presented.

Two Russian reports which investigate the atomization of liquids and jets are those by Borodin[42] et. al. and Sitkei[43]. The report (book) by Borodin mainly discusses atomizers, while Sitkei is interested in fuel atomization for diesel engines.

d. Closure: The papers discussed above comprise virtually all the pertinent investigations which attempted to correlate mean droplet diameter resulting from a turbulent liquid jet with flow conditions and fluid properties. Only one paper was found that attempted to correlate droplet data for a jet injected into still air, that of Harmon[2]. Much of the early work on liquid jets dealt with laminar flow because it was more amenable to analysis. Practically all papers in recent years were motivated more by application than by primary interest in liquid jet breakup. Many reports were found regarding atomization devices; however, since the spray resulting from these devices is not that of a true liquid jet, discussion of these reports was not included.

3. Comparison of Droplet Equations

Table II presents the exponent values for the variables which appear in the various droplet correlation equations. The slash mark shown for some variables indicates that two values for those variables resulted from the particular equations. The correlation equations span the supersonic, subsonic and quiescent gas environments. The manner in which the liquid was injected was either transverse or parallel to the gas streams. Although the method of injection and the range of gas conditions were quite different, some similarities exist among the equations. By scrutinizing Table II one can make the following observations:

TABLE II: FUNDAMENTAL VARIABLE EXPONENTS FOR CORRELATION EQUATIONS

DIA (RAD)	INVESTIGATOR	GAS/LIQ ARRANGE.	D_o	ρ_g	V_g	μ_g	V_{rel}	V_{sonic}	ρ_l	V_l	μ_l	σ
(R_{32})	HARVEY	SUPERSONIC, TRANSVERSE	.8	-.2	-.4							.2
D_{32}	BITRON (NUKIYAMA-TANASAWA)	SUPERSONIC, TRANSVERSE	3		-1.5		-1		-.5/-.23	1.5	.45	.5/-.23
D_{30}	KURZIONS & RAAB	SUPER & SUBSONIC, TRANSVERSE	.375	-.25	-.75	.25		-.25	-.375			.375
D_{Med}	VOLYNSKIY	SUPERSONIC, TRANSVERSE	.35	-.275	-.8/-.75	.25		-.25	-.375	.75		.4
$\overline{D}$	ADELBERG (CAPILL.)	SUBSONIC, PARALLEL	.5	-.33	-.67				-.17		.33	.17
$\overline{D}$	ADELBERG (ACCEL.)	SUBSONIC, PARALLEL		-.67	-1.33				-.33		.67	.33
D_{30}	INGEBO & FOSTER	SUBSONIC, TRANSVERSE	.5	-.25	-.75				-.25		.25	.25
$\overline{D}$	MAYER	SUBSONIC, PARALLEL		-.67	-1.33				-.33		.67	.33
$D_{Mass\ Median}$	WEISS & WORSHAM	SUBSONIC, PARALLEL	.17	-1/0		.08	-1.33		.17/-.83	.08	.33	.42
D_{32}	HARMON	STILL AIR	.3	-.05		.8			-.65	-.55	.05	-.15

1) The most prevalent variables, regardless of gas environment, are jet orifice diameter, gas and liquid densities, gas velocity and surface tension;

2) The effect different variables have on droplet diameter (directly or inversely proportional) is consistent, regardless of gas environment. Two exceptions to this are liquid velocity and surface tension in the Harmon equation, which was the only correlation equation found for a jet injecting into still air; and

3) The significance of a given variable, i.e., strong or weak influence on droplet diameter, varies within and among the flow regimes. Bitron attempted to extend the Nukiyama-Tanasawa equation, which was developed for subsonic parallel flow, to supersonic transverse flow. Although he concluded this could be done, his data does not substantiate his conclusion. This was discussed in Section 2. The Kurzious and Raab equation resulted from the correlation of Bitron, Ingebo and Foster and Volynskiy data. There is an incongruity in the Kurzious and Raab correlation in that Bitron, Ingebo and Foster and Volynskiy each correlated to a different mean droplet diameter, these being D_{32}, D_{30} and D_{median}, respectively. It would be extremely fortuitous if all these coincided. A look at the Mayer and Adelberg acceleration wave equations will reveal that these have the same form and the same exponent value for each variable. However, Mayer's equation was developed for the capillary wave regime. A review of all the equations in Section 2 will also reveal that Reynolds and Weber numbers are prevalent, but mixed in that the variables in some of the dimensionless groups belong in part to the liquid and in part to the gas; that is, the dimensionless groups are not defined in their

conventional manner.

4. Droplet Measurement Techniques

The analysis of a spray in terms of drop size distribution is probably the most important single problem in the study of atomization of liquids. Research on the mechanism of atomization would be greatly enhanced by a simple, accurate and rapid method for determining the drop size distribution of the spray. The fact that such a method is lacking is the main obstacle in atomization studies. Lewis[44] established a list of criteria for the ideal droplet measurement and recording system. The system should:

1) not disturb the spray pattern or atomization mechanism;
2) be able to sample at various times and at various points in a given spray;
3) not be restrictive as to the choice of liquids employed;
4) not be restricted to ambient test conditions;
5) apply to all ranges of flow, velocity and dispersion;
6) provide a permanent record, and
7) be inexpensive to purchase and operate.

Two investigators, Matthews[45] et.al. and Putnam[39] et.al., have conducted extensive surveys on the various droplet measurement techniques and categorized them as shown below:

TABLE III: DROPLET MEASUREMENT TECHNIQUES

	Matthews, et.al.	Putnam, et.al.
1.	Electrical and Electronic	Electronic and Radioautographic
2.	Deposition and Collection	Slide or Cell Collection
3.	Light Scattering	Light Scattering or absorption
4.	Fluorescent Photography	Direct Photographic
5.	Streak Photography	Cascade-Impactor
6.	Spark Photography	Freezing and Sieving (Wax)
7.	Pulsed Laser Holography	

Each method has its advantages and disadvantages, but none is entirely satisfactory. All of the techniques may be criticized for one or more reasons; questionable accuracy and assumptions, undesirable physical disturbance of the spray, complicated equipment, etc. The most common objection to any method is that it is too tedious and time-consuming.

All of the drop size investigators used one or more of the techniques listed in the Table. Nukiyama and Tanasawa[4] used the glass slide method from which photomicrographs were made to size the droplets. Bitron[17] used the same technique as did Volynskiy[5]. Ingebo and Foster[3] used a high speed camera to obtain photomicrographs. Weiss and Worsham[6] in their investigation used the frozen wax method. The data produced by these investigators is considered good and is generally accepted.

A brief description, along with advantages and disadvantages, of some of the droplet measurement techniques listed in Table III is given below:

TABLE IV: DESCRIPTION OF DROPLET MEASUREMENT TECHNIQUES

Method	Advantages	Disadvantages
Slide Collection. Drops are collected on greased slides. The drops are subsequently microscopically examined.	1. The method is simple.	1. Small droplets (less than 20 microns) are discriminated against, since these smaller drops follow the gas stream around the slide. 2. Droplets splatter and flatten upon impact with the slide. 3. The slide disturbs the spray and gas flow.
Frozen Drop or Wax. Hot wax of a low melting temperature metal alloy is injected into a medium, after which the injectant quickly solidifies upon droplet formation. The droplets are collected in a sieve to determine drop size distribution.	1. Data reduction is simple. 2. Method can distinguish between an oxidizer and a fuel.	1. Lack of availability of very fine sieves (below 37 microns). 2. Coalescence of the droplet becomes a problem at higher flux levels.
Photographic. A camera (still or movie) is set up in a certain orientation such that observation of the flow field can be made.	1. No object is placed in the path of the spray; thus, the flow field is not disturbed. 2. An instantaneous highly resolved picture of a small volume can be obtained.	1. The method is not adequate for relatively dense sprays. 2. Small drops hide behind large drops. 3. In order to record small droplets, large magnifications are required. In order to obtain large magnifications, the depth of field becomes small, thus requiring a large number of photographs to be taken in order to obtain a representative drop count. This increases dark room and data reduction time.

TABLE IV: DESCRIPTION OF DROPLET MEASUREMENT TECHNIQUES, continued

Method	Advantages	Disadvantages
		4. Still photographs provide an instantaneous record rather than a temporal record of the spray.
Optical. Optical methods depend on the transmission or scattering of a light beam by the dispersed droplets. See Dobbins[59].	1. The spray is not disturbed.	1. The method only provides information about the average drop size or the predominant drop size. 2. Drop size distribution cannot be obtained.
Pulsed Laser Holography.	1. The total spray in 3 dimensions can be recorded on one holographic plate in one exposure. 2. The flow field is not disturbed. 3. There is no depth of field problem. 4. Both size and spatial distributions of the droplets can be obtained. Thus characterization of the whole flow field or regions of it can be made. 5. Small droplets (on the order of 10 microns) can be resolved. 6. The system is not biased to any particular drop size.	1. Only an instantaneous rather than a time average record of the phenomena is recorded on a single plate. 2. Although the laser pulse is extremely fast, image smear problems still occur in high speed flow fields.

The techniques listed in the Table above are the type investigators might consider in selecting a means for measuring droplet size in a high speed flow field. The Table is by no means complete, since a number of techniques such as electrical and electronics systems, fluorescent photography (which uses fluorescent light emitted by the drops in an exciting radiation sheet, Rice[46]) and the Cascade-impactor have not been discussed.

The holographic technique was chosen for this work because of its many advantages. While not devoid of disadvantages, it satisfies many of the criteria as set forth by Lewis. Assuming the recording and reconstruction systems are operational, acquisition and reduction of the droplet data is quite simple and, relatively speaking, more rapid than any of the other techniques. The characterization of the spray is more comprehensive in that a three-dimensional record is obtained in one exposure, but temporal variations are not recorded. This shortcoming can be eliminated by taking a number of holograms at the same test conditions to obtain a time average of the size and spatial distribution of the droplets. Although holography does alleviate some of the tediousness of acquiring a large amount of data, the ultimate goal of automatically retrieving the droplet data from the holograms has not yet been achieved.

5. Holography

The intent of this section is to familiarize the reader with holography. A qualitative discussion follows which describes holography, how to make and view a hologram, and the particulars one must consider and tasks he must perform in order to produce and properly view a

high-quality hologram. A discussion on the pulsed ruby laser is also included.

"Holography* is the technique of recording an image of an object using the entire content of the light reflected or transmitted by that object"[47]. The entire content of light includes its intensity, wavelength and phase. Only the first two are used in conventional photography. In holography, the phase content of the light is also used. For a light wave to have phase content, the light source must emit waves with a well-defined phase relationship. A laser provides the light source which satisfies the phase content requirement. Holography is a two-step process by which images can be formed. In the first step, a complex interference pattern is recorded and becomes a hologram. In the second step, the hologram is illuminated in such a way that part of the transmitted light is an exact replica of the original object wave. This is called reconstruction of the wave front. The concept of the two-step method of optical imagery was first conceived in 1947 by Dennis Gabor, a British research scientist. Holography as is known today had to wait until the advent of the laser (1962) which provides a light source with the necessary temporal and spatial coherence required to produce good holograms.

The holographic method differs significantly from the conventional photographic process in several basic respects, and has distinct advantages in many areas. The basic difference between conventional photo-

*"Holo" is derived from the Greek word "holos" which means complete, entire or total; "gram" means writing, drawing or recording; when the two are combined, they produce the word "hologram" which means the complete or total record of a scene.

graphy and holography is that in holography the object wave itself is recorded rather than an image of the object. This wave is recorded in such a way that a subsequent illumination of this record serves to reconstruct the original wave object even in the absence of the original object. The most obvious advantage of holography is the ability to store enough information about the object in the hologram to produce a direct three-dimensional image complete with parallax and large depth of focus. The quality of the holographic image is less sensitive to the characteristics of the recording medium than is the quality of a photograph. In addition to the three-dimensional capability, holograms possess other properties:

a) the hologram has a field of view that is limited in general only by the resolution of the recording medium;

b) the depth of field recorded in a hologram is limited only by source bandwith;

c) every small part of the photographic material on which a hologram is recorded contains all elements of the image. The hologram may be cut into small pieces and it still will be possible to reconstruct the entire image from each piece;

d) if the light source used for wave front reconstruction is monochromatic, the image is also monochromatic; and

e) the image is reconstructed only as a result of the diffraction of the light and not because of the actual intensity.

There are many types of holograms, some of which are: Fresnel (near-field), Fraunhofer (far-field), in-line, off-axis, transmission, [illegible], and [illegible] transform, to name a few. The paper by Leith and [illegible] describes the various types of holograms. The

original Gabor type hologram was in-line. With this type of hologram, the source beam is not split into two components. The beam is directed toward the object. Some of the light is scattered by the object and some impinges on the photographic plate without first encountering the object. This type of holography has some disadvantages which can be eliminated with an off-axis arrangement which splits the source beam into two components, the scene and reference beams. The idea of off-axis holography is credited to E. Leith and J. Upatnieks of the University of Michigan[49]. The component beam that is directed toward the object is scattered or diffracted by the object. The beam that proceeds directly to the recording media is the reference beam. Since the scene and reference beams are mutually coherent, both having originated from the same monochromatic light source, they will form a suitable interference pattern when they meet at the holographic plate. Some advantages of the off-axis (sideband) reference beam method are:

a) elimination of critical film processing;

b) elimination of the effects of self-interference between different points of the object;

c) it makes reconstruction possible for objects that do not transmit a large portion of the incident wave. Any transmitting or reflecting object can be photographed;

d) the real and virtual images are separated; and

e) the image quality is relatively insensitive to recording nonlinearities.

The disadvantages are: high requirements on coherence and stability of the system and necessity for high resolution films.

In 1964 with the advent of the gas laser, Leith and Upatnieks intro-

duced the concept of diffuse illumination holography[50]. By placing a diffuser such as an opal glass behind the object, a hologram is formed of both the diffuser and the object. In this way, it is possible to view the image formed from the hologram by merely looking through the hologram as through a window, which was not the case prior to this time. This type of hologram has other advantages:

a) the information about any single object point is recorded over the whole photographic plate instead of a 1:1 correspondence between a portion of the hologram and a region of the object. Therefore, only a small part of the hologram is required to form an image of the whole object; and

b) another advantage is that dirt or scratches on mirrors, beam splitters and/or lenses used in making the holograms no longer represent the problem they did in the earlier types. Most of these imperfections are, to a great extent, smeared out over the whole plate and thus have a negligbly small effect on the reconstruction.

Perhaps the single most important aspect of this technique is the ability to record holograms of diffusely reflecting three-dimensional objects. The type of hologram which was produced in this investigation was an off-axis, Fresnel, diffuse illumination hologram, which explains why the detailed discussion of this type of hologram was presented above. In the following paragraphs, the recording, reconstruction and considerations involved with the off-axis type hologram will be presented.

A holographic system consists of three major components:

1) a laser illuminator (a coherent light source);

2) a hologram camera (a system of mirrors, lenses and beam splitters), and

3) a reconstructor (a means of duplicating the reference beam to reconstruct the wave front).

By far the most common and important light source for holography is the laser-gas or solid state (pulsed ruby laser). Of primary interests are the temporal and spatial properties of the light. All light waves emitted by a laser start together and therefore are in phase. This is called coherent light. Coherence can only be obtained with monochromatic light that is consisting of a single or a few wavelengths. The wavelength is characteristic of the type of laser, such as helium-neon, ruby, etc. The pulsed ruby laser is the most often used solid state laser for holographic application, emitting light at a wavelength of 6,943 angstroms. This wavelength is approximately at the limit of the long wavelength cut-off for red sensitized photographic emulsions, but is nevertheless still quite usable. The ruby laser has a much smaller coherence length (a few centimeters) than the gas laser, so that one must be careful that the path length differences between the scene and reference beams do not exceed this length. Because a ruby laser is pulsed, it has some very definite advantages over a continuous source such as a gas laser for some holographic applications. Because of this short pulse duration, some object movement can be tolerated during a exposure. Pulsed laser holography has an advantage of circumventing the depth of focus problem associated with small objects in motion. Short pulse duration is accomplished by Q-switching the laser oscillator. It is the technique of isolating one of the end mirrors of the laser cavity. Q-switching is accomplished with a Kerr cell which contains nitrobenzene or a dye cell which contains a dye such as chlorophyl D or cryptocyanine. A detailed description of Q-switching and cells which accomplish it can

be found in Wuerker[51].

The major drawback in making a hologram with a pulsed laser is the limited coherence length. Another drawback to the use of a pulsed ruby laser as a source for holography is that the wave front of the output is not simply defined. However, holograms can be successfully produced using a pulsed ruby laser without mode control by careful choice of the optical arrangement to minimize the effects of the relatively low temporal and spatial coherence of the ruby laser light. This is accomplished by arranging the holographic system for zero path difference between object and reference beams and also by matching as closely as possible the relative operational positions of the two wave fronts. When these two conditions are met, the two waves will be coherent with each other and a good hologram will be recorded. If there is a path mis-match, the reconstructed hologram appears dim and hazy instead of bright and clear with good contrast and high resolution. Spatial coherence is the consistency of phase across the output of the laser as a function of time. The desired situation is where phase is constant across the full output of the beam independent of time. In recording the hologram, both reference object beams must have well-defined wave fronts which are constant in time. Temporal coherence (coherence length) is the distance two beams from the same source can be mis-matched and still interfere. Temporal coherence limits the size of the object that can be photographed holographically. In this investigation, a pulsed ruby laser was used because of its high energy and ability to make holograms of moving objects. In the paper Wuerker and Heflinger[52] describe how coherence length of a ruby laser can be improved.

To obtain a hologram, one must have a light source with sufficient

temporal and spatial coherence. The optical system must be stable and one must have high resolution film to record the fine interference pattern. The following components are required for constructing holograms of three-dimensional objects:

1) a gas or pulsed laser;

2) a stable platform for maintaining all components except the laser (not necessary for pulsed lasers);

3) front surface mirrors 1/4 wavelength flat;

4) beam splitters 1/4 wavelength flat;

5) lenses for diverging and collimating laser beams;

6) photographic plate or film holder; and

7) high resolution photographic plates.

Figure 6 shows the arrangement for recording an off-axis Fresnel hologram. One starts with a single monochromatic beam of light which has originated from a very small source. This single beam of light is diverged and collimated and then split into two components, one of which is directed toward the object or the scene; the other is directed to a suitable recording medium, usually a photographic emulsion. The component beam that is directed toward the object is scattered or diffracted by the object. This scattered wave constitutes the object wave which is now allowed to fall on the recording medium. The wave that proceeds directly to the recording medium is termed the "reference" wave or beam. Of fundamental importance in making holograms is the relative strength or intensity ratio of the object and reference beams. An object reference beam ratio of unity at the hologram is recommended for reconstruction with maximum contrast. All investigators are not in agreement with this. The intensity ratio of the beams, for best results,

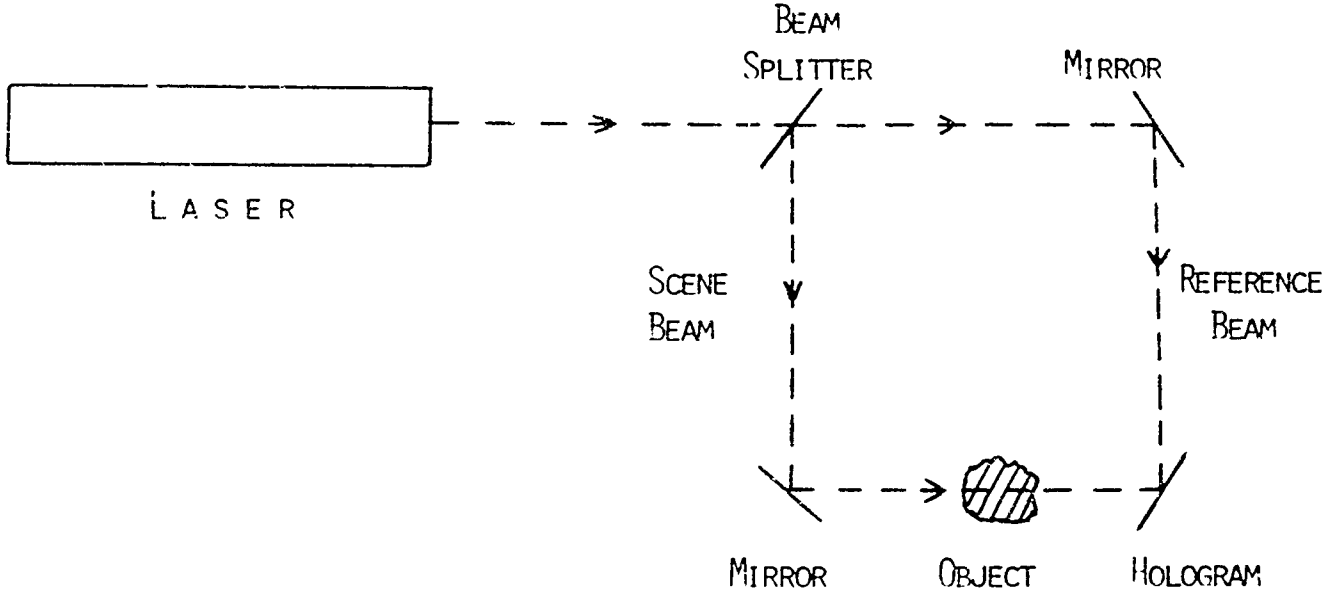

Figure 6. Arrangement for Off-Axis Fresnel Transmission Holography

varies with the application and the object of which a hologram is being made. Since the object and reference waves are mutually coherent, they will form a suitable interference pattern when they meet at the recording medium. This interference pattern is a complex system of fringes in spatial variations of irradiance which are recorded in detail on the photographic emulsion. The emulsion will be exposed only in areas where the beams reinforce and not where they cancel. The microscopic details of the interference pattern are unique to the object wave. Different object waves will produce different interference patterns. Holograms may be recorded with diverging, collimated or converging reference beams. If care is taken to maintain the recording geometry during reconstruction, it is possible to form holograms with an arbitrary reference beam. The only requirement is that it be coherent with the object beam.

As mentioned earlier in this Section, holography is a two-step process, recording and reconstruction. After recording the scene on the hologram, the holographic plate is then developed in a manner similar to a photograph. See Chapter III, Section 2.c. The hologram can now be reconstructed; that is, the true scene image is made visible by suitable illumination even though the object is not present during the reconstruction process. Reconstruction of the hologram wavefront is required so the data can be retrieved from the hologram. Reconstruction is accomplished by illuminating the hologram with a light source whose wavelength is the same as or similar to that of the reference beam used in recording. In other words, one reconstructs the hologram by simulating the recording reference beam. The holographic plate is oriented to the reconstruction light source similar to the way it was oriented to the recording light source. That is, the emulsion side of the plate faces

the illuminator and the angle the plate makes with the reconstruction beam is approximately the same as it was during recording. If the recording reference beam was collimated, the reconstruction beam should be collimated, otherwise some aberrations are introduced and the image will be distorted. Coherence requirements are much lower for viewing than for constructing a hologram. In the reconstruction process, two images can be recovered; a virtual image which forms behind the hologram plate, and a conjugate or real image which forms in front of the hologram. The virtual or real image of the scene can be viewed depending on how the plate is oriented to the light source. If one of the images is being viewed, the other can be viewed by rotating the plate 180° keeping the emulsion side of the plate facing the illuminator. The virtual image is usually viewed for qualitative information, since it can be readily seen with the naked eye, while the real image is used in the retrieval of quantitative data. The real image is difficult to view without the aid of a lens or backdrop.

There are several factors that can limit the resolution of holographic image:

1) the size and bandwith of the source providing the reference and reconstruction beams;

2) the resolution capability of the recording medium; and

3) the geometric aberrations that can arise.

High quality holographic images require a narrow band light source both for recording and reconstructing the hologram. Every recording medium will have an upper limit on the spatial frequencies it is capable of recording. The five Seidel aberrations, spherical, coma, astigmatism, field curvature and distortion, are all present in a general holographic

system. All of these primary aberrations will disappear simultaneously by using plane wave (collimated) reference and reconstruction beams of equal but opposite off-set angles and by scaling the hologram in the ratio of the wavelengths. Champagne and Massey[53] have found that the limiting factor in the resolution of images was the angular alignment of the reconstruction wavefront. In their paper, they also present the equations for spherical aberration, coma, astigmatism and the correction needed to compensate for change in wavelength by the recording reference and reconstruction beams. Latta[54] [55] has analyzed hologram imagery and aberrations peculiar to the type of hologram and those introduced by a wavelength shift. He developed a technique for aberration balancing to reduce aberrations in off-axis holograms. Meier[56] concludes that all aberrations can be made to disappear simultaneously from an image by using parallel reference and illuminating beams, by giving the latter an off-axis position proportional to that of the reference beam and by scaling up the hologram according to the wavelength ratio. A change in wavelength between the recording and reconstruction reference beams causes a shift in the position of the object by a ratio of the wavelengths of the two beams. If the reconstruction light source has a wavelength different from the recording light source, the angle at which the hologram is placed relative to the reconstruction light source has to be different from that used in recording in order to properly illuminate the hologram. Smith[57] shows the sensitivity of a hologram to orientation and wavelength. His book and that of DeVelis and Reynolds[58] are excellent treaties on the principles and theory of holography.

6. Droplet Statistics and Distribution Functions

It has already been stated that accurate knowledge of the droplet size distribution as a function of system parameters, flow conditions and physical properties of the spray, is fundamental to determining the mechanism by which the jet is atomized. This is why an accurate method for measuring drop size is needed. Once the droplet data is obtained, then a means of handling and reducing it into a form which can be used to describe the spray is necessary for mathematical analysis and correlation purposes. This is where the concept of the various mean droplet diameters and size distribution functions come into play. They provide a mathematical means for characterizing the spray in order to make analysis more tractable, so a better understanding of the atomization mechanism can be obtained. In this Section, a discussion of the mean diameter concept and some of the distribution functions used in droplet and particle size investigations will be presented.

a. Mean Diameter Concept: A spray may be characterized by an appropriate mean diameter. In some cases, it is desirable to work with an average diameter rather than the complete drop size distribution. However, a given mean diameter only describes a single point of a distribution and there are many possible distributions which have the same mean diameter. Hence, in order to use the mean diameters properly and effectively, they must be used in conjunction with a given distribution function. The number mean or linear average diameter is obtained using the equation

$$\bar{D}_{10} = \frac{\sum D_i N_i}{\sum N_i} \qquad (22)$$

where D_i = mid-diameter of a given size class

N_i = number of droplets in a given size class

For a smooth distribution, the equation can be expressed in integral form:

$$\bar{D}_{10} = \frac{\int_{D_{min}}^{D_{max}} D \frac{dN}{dD} dD}{\int_{D_{min}}^{D_{max}} \frac{dN}{dD} dD} \tag{23}$$

where dN/dD represents a number distribution function; rate of change of number of droplets with change in diameter. If droplet surface area is of interest, one would choose the surface mean diameter

$$\bar{D}_{20}^{2} = \frac{\int_{D_{min}}^{D_{max}} D^2 \frac{dN}{dD} dD}{\int_{D_{min}}^{D_{max}} \frac{dN}{dD} dD} \tag{24}$$

The general equation for mean diameters in terms of number distribution is

$$\bar{D}_{qp}^{q-p} = \frac{\int_{D_{min}}^{D_{max}} D^q \frac{dN}{dD} dD}{\int_{D_{min}}^{D_{max}} D^p \frac{dN}{dD} dD} \tag{25}$$

In terms of volume distribution the equation becomes

$$\bar{D}_{q-p}^{q-p} = \frac{\int_{D_{min}}^{D_{max}} D^{q-3} \frac{dV}{dD} dD}{\int_{Dmin}^{D_{max}} D^{p-3} \frac{dV}{dD} dD} \tag{26}$$

since the number and volume distributions are related by

$$\frac{dN}{dD} = \frac{6}{\pi D^3} \frac{dV}{dD} \qquad (27)$$

Equations (25) and (26) relate the various mean diameters to a given distribution function.

Mugele and Evans[31] presented the following table of mean diameters and their fields of application:

TABLE V: MEAN DIAMETERS

p	q	p + q (Order)	NAME OF MEAN DIAMETER	FIELD OF APPLICATION
0	1	1	Linear	Comparisons, evaporation
0	2	2	Surface	Surface controlling - e.g., absorption
0	3	3	Volume	Volume controlling - e.g., hydrology
1	2	3	Surface diameter	Adsorption
1	3	4	Volume diameter	Evaporation, molecular diffusion
2	3	5	Sauter (Volume-surface)	Efficiency studies, mass transfer, reaction
3	4	7	DeBrouckere	Combustion equilibrium

Another mean diameter which is often of interest but not listed in the Table is the number (volume, mass, etc.) median diameter. It is the size above and below which the total number (volume, mass, etc.) is the same, irrespective of their size. It is the 50% point. One can see that a spray has four characteristics: the number of droplets, their diameters, surface area and volume.

The mean diameters are not all independent from each other and

certain relationships exist among them. By using equation (25) one can show that

$$\bar{D}_{qp} = \bar{D}_{pq}.$$

In general

$$\bar{D}_{qp}^{q-p} = \bar{D}_{qc}^{q-c} \Big/ \bar{D}_{pc}^{p-c}$$

where c is an uncommon index. For a relationship to exist between two diameters, one of the indices, either the p or q, of one diameter must be common (the same as) with one of the indices of the second diameter. For example, D_{43} and D_{30} or D_{32} and D_{31} can be related, but not D_{20} and D_{31}. Two different distributions of drop sizes may have the same value for one of the mean diameters and yet entirely different values for the other mean diameters. This is illustrated in Table II of Mugele and Evans[31].

b. Distribution Functions: The real task of droplet data processing is to replace the actual droplet point distribution with a representative curve distribution. Distribution expressions are used to mathematically describe the drop-size distribution in a spray. According to Miesse and Putnam[39] a suitable expression would:

1) fit the data adequately;

2) allow for extrapolation;

3) permit easy calculation of mean sizes and other parameters of interest;

4) furnish a means of consolidating large amounts of data; and

5) give an insight into the fundamental mechanism of droplet production.

Size distributions can be expressed in terms of any of the following four quantities:

1) the incremental number ΔN, of droplets within a size range $(D - \frac{\Delta D}{2}) < D < (D + \frac{\Delta D}{2})$;

2) the incremental volume (mass), ΔV, of droplets in the size range ΔD;

3) the cumulative number of droplets, N, less than a given size, D; and

4) the cumulative volume of droplets, V, less than a given size, D.

The type of curves obtained from items 1) or 2) when $\frac{dN}{dD}$ and $\frac{dV}{dD}$ are plotted versus diameter, D, is a skewed "bell" shape, in general. When $\frac{dN}{dD}$ and $\frac{dV}{dD}$ are integrated and plotted versus D, the cumulative distribution of items 3) and 4) are obtained, and the curve shapes are usually stretched out "S's". The number and volume distributions are related by equation (27). A convenient way of using these distribution functions is to normalize the number and volume with the total number and volume, such that N and V are the number and volume fractions of droplets having a diameter less (or greater) than a given incremental diameter, D. Data representing volume fraction instead of number fraction will yield a curve skewed toward the larger diameters on a dV/dD versus D plot because each class size is now weighted in proportion to D^3. One large drop could overshadow the effect of many small drops.

Ideally, the correlation coefficients or parameters of a distribution function can be related to the fundamental mechanisms of the spray [illegible] to distribution functions to characterize the droplet [illegible] fractions obtained from the raw data with [illegible] to evaluate how

well a given curve represents the actual spray. Certain statistical tests such as Chi-square goodness of fit, F-ratio and T-distribution, are applied to determine how well a given distribution function models the data and at what confidence level. The manner in which the droplet data is grouped into intervals or class sizes plays an important part in confidence level. The more diameter class sizes there are, the more droplet counts need to be made in order to maintain a given confidence level. The monograph by Herdan[60] gives a comprehensive treatment to small particle (droplet) statistics.

Four unimodal distribution functions were selected to model the droplet data resulting from this investigation. They were Log-Probability, Upper-Limit, General Exponential and Nukiyama-Tanasawa. The equations for these four distribution functions and their corresponding mean diameters will be discussed in detail in Chapter V. The Upper-Limit function is a modification of the Log-Probability function and was developed by Mugele and Evans[31]. The Nukiyama-Tanasawa[4] function is a modification of the General Exponential function. Other distribution functions are discussed in Hiroyasu[61] (Chi-square distribution) and Brown and Leonard[62] (Weibull). Multimodal distribution functions were not considered in this investigation. Other reports of interest in the area of droplet statistics and distribution functions are Sauter[63] and Gary, [illegible] and Harrje[64].

CHAPTER III

SYSTEM AID EXPERIMENT DESCRIPTIONS AND PROCEDURES

1. Test System Description and Operating Procedure

The test system was located on Test Stand 1-46A at the Air Force Rocket Propulsion Laboratory. A schematic of this system is shown in Figure 7. The major subsystems which comprise the total test system are: high pressure gas supply, supersonic wind tunnel, liquid supply, instrumentation, electrical and laser-holocamera. The wind tunnel was located on T.S. 1-46A so connection to existing fluid supply systems could be made, thus reducing the cost and time required to render the test system operational. Since the test stand was designed for testing rocket thrust chamber assemblies, all systems could be operated remotely from a blockhouse. Although remote operation of the wind tunnel was not required, it was expedient to make use of this capability to facilitate test system buildup. Each of the subsystems will now be discussed in detail.

a. High Pressure Gas System: The high pressure, gaseous nitrogen system consisted of two, 270 cubic foot, 5,000 psig rated vessels and four, 310 cubic foot, 2,400 psig rated vessels. These more than adequately provided sufficient gas to flow the wind tunnel, pressurize the liquid system and control pneumatically operated remote valves. All the vessels were connected to one main gas supply line to the test stand. The two 5,000 psig vessels were mainly used. The lower pressure vessels were isolated from the higher pressure vessels by check valves to avoid over-pressurization. Also, relief valves were installed on the lower pressure vessels in the event the check valves failed. The 2,400 psig vessels would automatically come on line in the event gas pressure went below 2,400 psig. This never occurred during the course of the test program, although as many as four, 10 second tests were conducted on test day.

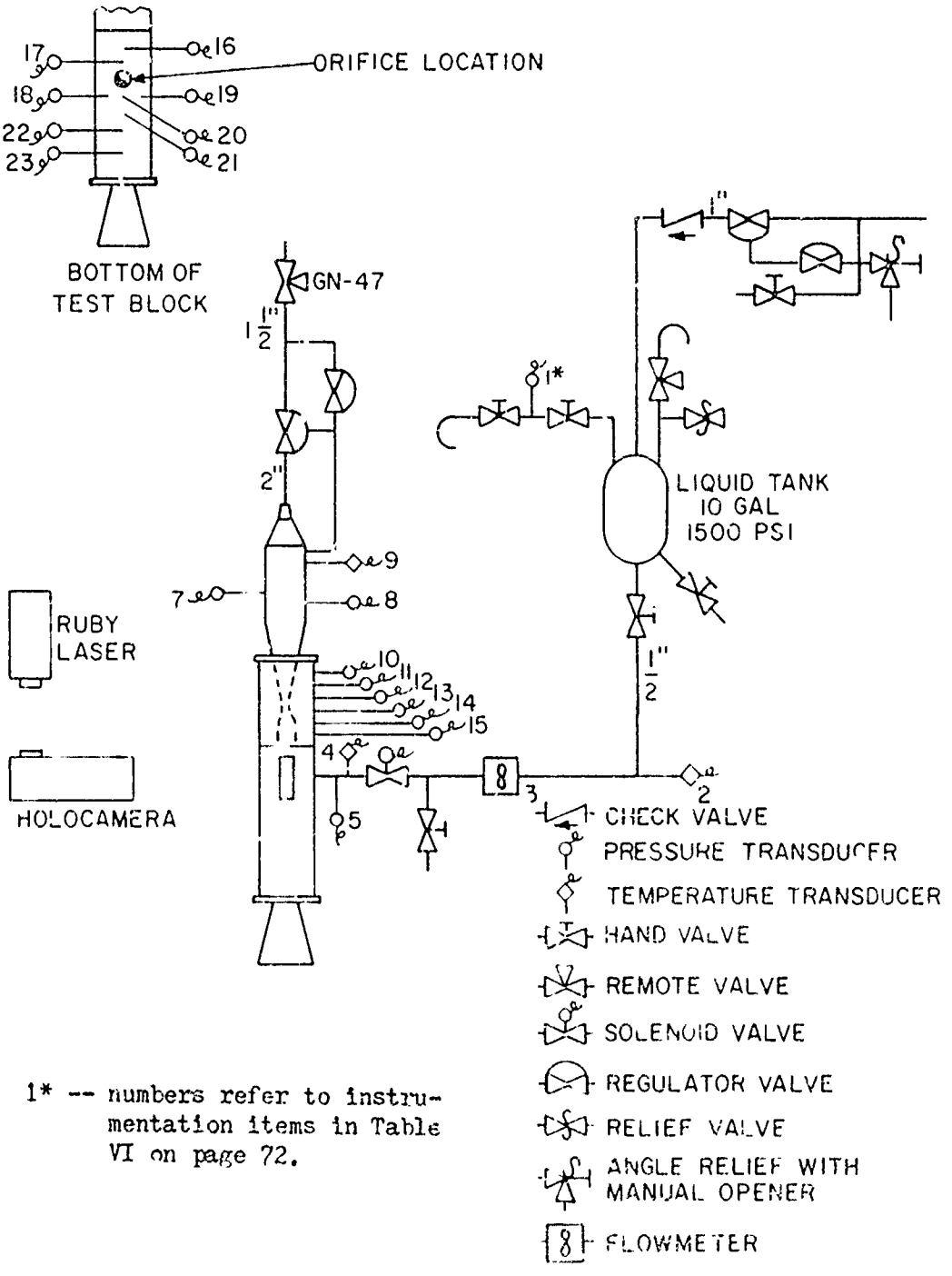

1* -- numbers refer to instrumentation items in Table VI on page 72.

Fig 7 Test System Schematic

The gas could be regulated in the main line to an operating pressure which was selected as 3,000 psig. The gas was then branched and regulated again for use in the various systems: wind tunnel plenum pressure, liquid tank pressurization and remote, pneumatic valve operation.

The feed line to the wind tunnel upstream of the remote isolation valve (GN - 47 on the schematic of Figure 7) was made of 300 series stainless steel tubing 3000 psig rated. Located downstream of the isolation valve, was the high pressure Grove regulator which was used to set the gas pressure in the plenum chamber of the wind tunnel at the desired test conditions. The dome pressure for the regulator was set by a remote operated, variable dome loader. The exit line from the regulator to the plenum chamber was made larger (2") than the inlet line to accommodate the gas flow rate without excessive pressure drop, since the gas was expanded to a pressure range of 100-300 psig downstream of the regulator.

The liquid tank pressurization system consisted of a 1½" Grove regulator which was remotely set by a variable dome loader. The regulator was set to maintain a given liquid tank pressure to provide a steady liquid flow rate at the desired test condition.

b. Supersonic Wind Tunnel: The experimental apparatus was an intermittant, blowdown, supersonic wind tunnel. A photograph of the wind tunnel is shown in Figure 8 (sidewalls removed on one side, plenum chamber not shown). The wind tunnel consists of four main parts: the plenum (stilling) chamber, nozzle blocks, test section and diffuser. Design of the wind tunnel was accomplished with the aid of Pope and Goin[65] and Liepmann and Roshko[66]. The wind tunnel has the following operating characteristics:

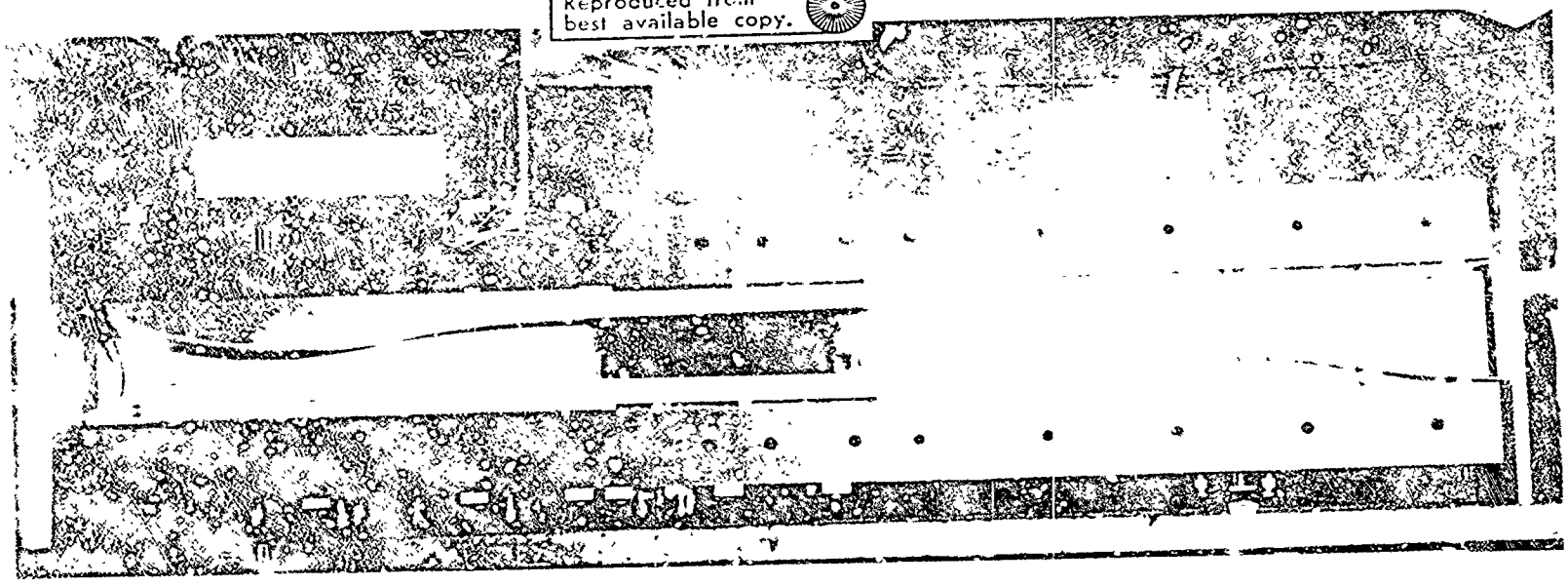

Figure 8. Wind Tunnel Side View, one sidewall removed.

a. Mach No. 3

b. Plenum Chamber Total Pressure Range 100-400 psia

c. Plenum Chamber Temperature ambient

The operating gas was nitrogen, although other gases could be used. The test section nominal dimensions were 3" x 3" cross section and 12" long. The centerline of the wind tunnel is 40 inches above the floor. It's external dimensions are 10 feet long, 14 inches in diameter at the plenum chamber and 4½ inches wide in the nozzle block and test section regions. Silicon rubber O-ring seals were used throughout the system. The tunnel support stand was an I-beam arrangement.

The plenum chamber provides a large-area, low-velocity section immediately upstream of the nozzle. Such a chamber, sometimes called a stilling chamber, greatly improves the uniformity of flow in the wind tunnel. The plenum is usually cylindrical and one or more diameters long. Screens are installed in the plenum to promote uniformity of gas flow and to reduce turbulence in the gas stream before the gas is expanded through the supersonic nozzles. The plenum chamber was fabricated from schedule 40, 12 inch, 300 series stainless steel pipe. Bell type reducers were used at the gas entrance section for smooth transition of the gas into the plenum chamber. A plate was also installed at the gas entrance section so the gas would diffuse around it and not tunnel its way through the plenum chamber, thus producing an undesirable velocity gradient. Placed inside the pipe section of the plenum chamber are two sets of fine mesh (340) stainless steel screen and grid backing network. The velocity in the chamber varied from approximately 5 to 12 feet per second for the low and high flow rates, respectively. The instrumentation

for the plenum chamber and rest of the wind tunnel will be discussed in the instrumentation section. The exit section of the plenum chamber consists of a reducer which goes from circular to rectangular in cross-section at the entrance of the supersonic nozzle blocks, since the wind tunnel proper is two-dimensional.

The nozzle, test section and diffuser regions are two-dimensional and are installed within a carbon steel frame referred to as the test bed. The opening between the top and bottom rails of the test bed is sufficiently large to allow installation of the nozzle blocks at the proper throat height. The opening is actually larger than necessary to allow adjustment of the throat by using shims. The side walls are flat, parallel carbon steel plates which are bolted to the test bed and press against O-ring seals placed in grooves along the sides of the nozzle and test section blocks. There is a forward and aft plate for each side with a window in each forward plate for viewing the test section.

The two-dimensional nozzle blocks, through which the gas accelerates from the plenum chamber velocity to Mach 3 at the test section entrance, are made from tool and jig aluminum. Design of the nozzle blocks was patterned after those used in the UCLA supersonic wind tunnel. Since the blowdown system operates at higher total pressure conditions than does the UCLA indraft, continuous system, boundary layer corrections had to be made to the nozzle block design. Appendix I explains how the correction was made. The nozzle block contours were machined by means of a computer-controlled milling machine. The method is explained in Spaid[67]. If a different Mach number is desired, the present blocks can easily be removed and a different set installed.

The test section blocks are made of 6061T aluminum and are mated flush with the nozzle blocks to insure smooth, uniform flow into the test section. The blocks have a slight outward taper in the flow direction to account for the increase in boundary layer thickness through the test section. Length of the test section blocks is approximately 12 inches. The bottom test section block is tapped such that different liquid injection orifices (see Figure 9) could be screwed flush into it. Flow of the gas stream through the test section must be as undisturbed as possible when not obstructed by a model or liquid jet, as is the case in this study, so test results will not have an external bias which could cause one to make erroneous conclusions. Mach number variations through the test section and across it were less than 0.7% and 0.5%, respectively. The test section has two windows, one in each side plate. Each window was 3/4 inches thick, optical quality, tempered glass, through which a 12-inch length and complete cross-section of the test section could be seen.

The exit section or supersonic diffuser was about 30 inches long and had two flexible walls (top and bottom) which could be adjusted as desired to provide a second throat.

c. Liquid Supply System: The liquid supply system was used to provide the desired liquid flow rate and injection velocity through the orifice mounted in the test section block. This system can be seen in Figure 7. Liquid injection into the test section was supplied from a 10 gallon, 1,500 psig operating pressure rated, stainless tank.

Tank pressurization was provided by the regulator system described above. Installed downstream of the tank are isolation, bleed and injection valves. A $\frac{1}{4}$-inch stainless steel line connects the valves with the

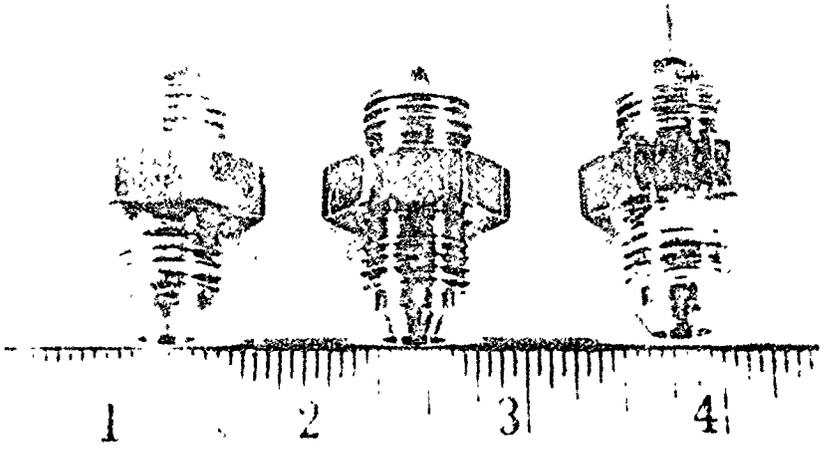

Figure 9. Liquid Injection Orifices.

tank and orifice. Prior to a test, liquid is bled through the bleed valve to insure that the line is full of liquid up to the injection valve. This is done to expel any gas which might be trapped in the line, that could overspin the flowmeter and damage it when the injection valve opened after the system has been pressurized. The liquid injection valve is a $\frac{1}{2}$ inch, remote, solenoid valve which is opened on demand after tank pressure has been set.

d. Instrumentation: Twenty-one channels of instrumentation were used to record pressures, temperatures and liquid flowrate. The various parameters were recorded on three different types of recorders; strip charts, oscillographs and magnetic tape. The manufacturer and model for each of these recording systems is respectively as follows: Leeds Northrup Model "G", Consolidated Electrodynamics Corp. Model 5-123, and System Engineering Laboratory Model 600 Digital Data Acquisition System. These provided the necessary frequency response ranges to adequately monitor the flow conditions during a test. The instrumentation specification sheet, Table VI , presents the particulars for each instrumentation item. The test system schematic, Figure 7 , shows the physical location of each instrument in the system.

A pressure transducer was placed at the top of the liquid tank and was used to set the pressure required to provide the desired flowrate and injection velocity. A temperature probe was placed in the liquid line near the flowmeter and was used along with the tank pressure to determine the liquid density. The flowmeter measures the volumetric flowrate of the liquid. This is converted to mass flowrate by multiplying the calibration constant and the cycles per second. Just upstream of the liquid injection orifice, temperature and pressure are recorded.

TABLE VI: INSTRUMENTATION SPECIFICATION SHEET

ITEM NO	PARAMETER	LOCATION	TYPE	RANGE	FREQUENCY RESPONSE	RECORDING SYSTEM
1	PRESSURE	LIQ TANK	DATA SENSORS	0-2000 PSIG	1Hz	SEL/OSC/L&N
2	TEMPERATURE	LIQ LINE	CHROMEL-ALUMEL THERMOCOUPLE	-37/+699°F	1Hz	SEL/L&N
3	FLOWMETER	LIQ LINE	POTTER	.5-5GPM	30Hz	SEL/OSC
4	TEMPERATURE	LIQ MANIFOLD	CHROMEL-ALUMEL THERMOCOUPLE	-37/+699°F	1Hz	SEL
5	PRESSURE	LIQ MANIFOLD	TABER	0-2000 PSIG	"	SEL/OSC/L&N
7	PRESSURE	PLENUM CH	DATA SENSORS	0-750 PSIG	"	SEL/L&N
8	PRESSURE	PLENUM CH	DATA SENSORS	0-750 PSIG	"	SEL/OSC/L&N
9	TEMPERATURE	PLENUM CH	CHROMEL-ALUMEL THERMOCOUPLE	-37/+699°F	"	SEL/L&N
10	PRESSURE	NOZZLE	TABER	0-500 PSIG	30Hz	SEL/OSC
11	"	"	TRANSDUCERS, INC.	0-300 PSIG	"	SEL
12	"	"	TABER	0-100 PSIG	"	SEL/OSC
13	"	"	TABER	0-50 PSIG	"	SEL
14	ABS. PRESS.	"	ALINCO	0-15 PSIA	"	SEL
15	" "	"	TABER	"	"	SEL/OSC
16	" "	TEST SECTION	ALINCO	"	30Hz	"
17	" "	" "	ALINCO	"	"	"
18	" "	" "	ALINCO	"	"	"
19	" "	" "	ALINCO	"	"	"
20	" "	" "	TABER	"	"	"
21	" "	" "	TABER	"	"	"
22	" "	" "	TABER	"	"	"
25	EVENT	HOLOCAMERA		0-28vdc	-	SEL
26	EVENT	INJ. VALVE	MARRATTA	0-28vdc	-	SEL

These indicate the liquid condition just prior to injection.

In the gas system, two pressure transducers and one temperature probe were located in the plenum chamber to determine the total pressure and temperature there. These were placed downstream of the screens. The pressure taps were placed opposite each other in order to detect any pressure variation from one side of the chamber to the other. These pressure transducers were used to set plenum chamber pressure as well as record pressure during a test. The temperature probe was an open-end thermocouple which protruded through the chamber wall close to the centerline of the plenum to insure a good temperature reading. Six pressure taps were spaced along the lower nozzle block length on the centerline. These were used mainly during checkout tests to determine if the proper pressure profile was being obtained through the nozzle blocks. Seven pressure taps were placed in the lower test section block; two upstream and three downstream of the orifice on the longitudinal centerline and two off-axis. See Figure 7.

All instruments were calibrated at the AFRPL Precision Measurement Equipment Laboratory prior to installation into the test system. The absolute pressure transducers were also calibrated in place by drawing a vacuum on them at increments over the operating range, recording the results and comparing them with secondary standards. Each parameter was sense-stepped prior to and after each test to insure each was functioning properly and that a zero shift had not occurred.

e. Electrical System: An electrical system was required to signal operation of the remote valves and gas regulator dome loaders. These components were operated from a console in the blockhouse. See Figure 10. Along with the switches for the mechanical system, ...

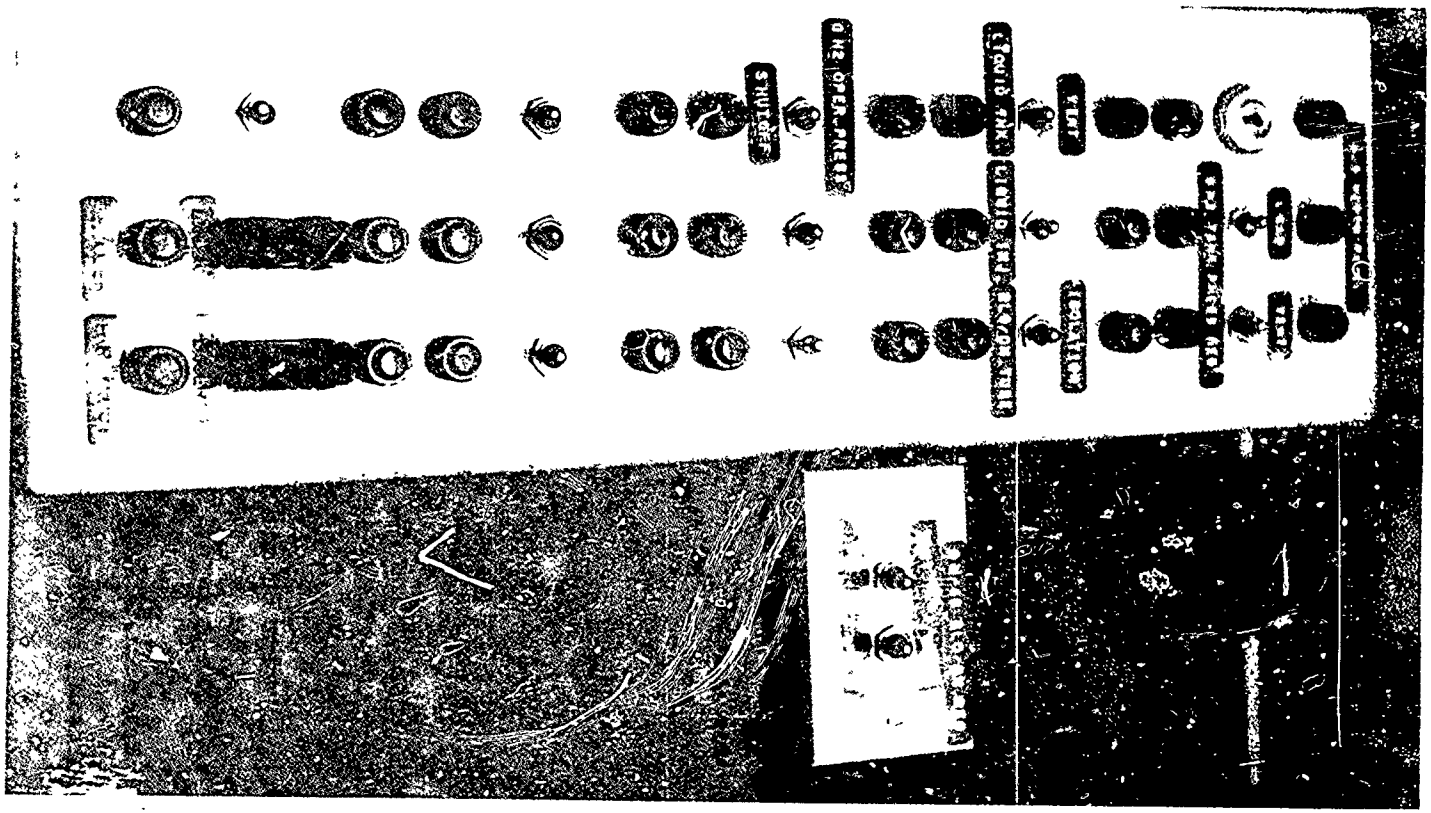

Figure 10. Control Console.

tion are two switches for the laser and holocamera operation. The use of these two switches will be discussed in the section describing the laser and holocamera. Switch SW-7 operates a solenoid valve which is an emergency shutoff for the operating gas pressure. Some spare switches are also on the console.

f. Injector Orifices: The orifices were designed with a large enough length/diameter ratio to feel confident that fully developed turbulent flow had been established prior to liquid injection into the supersonic stream. Figure 11 shows a cross-section of the orifices, while Figure 9 shows the actual orifices. A 3/8" stainless steel AN union was modified by truncating one end slightly and inserting a steel rod part way into the union. The rod was then welded to the union. The union threads were chased after welding to eliminate any warping which may have occurred. The desired orifice diameter was then drilled and reamed through the rod insuring that the drill-through and union centerlines were true with each other. The injector was then screwed into the test section block to determine the exact length the rod should be to fit flush in the block. Then the excess metal was removed. Table VII presents some pertinent information about the three orifices used.

TABLE VII: LIQUID INJECTOR ORIFICE INFORMATION

Actual Dia. (in.)	Length/Dia.	Discharge Coeff.
.042	24.95	.685
.050	23.68	.785
.062	19.02	.719

Liquid flow in all three orifices was turbulent in all tests; Re $O(10^4)$.

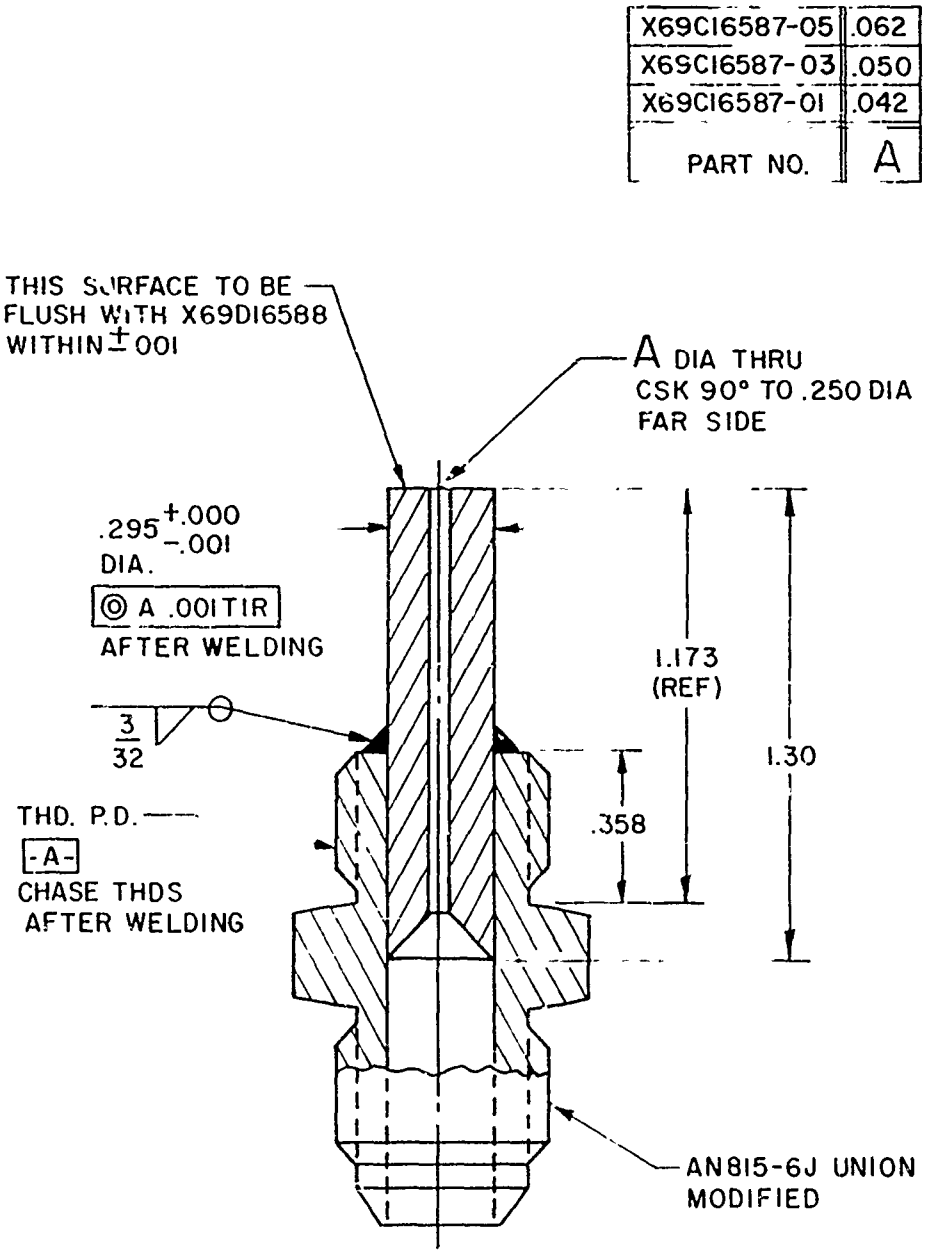

Fig. 11 Liquid Injection Orifice Cross-Section

g. Test System Operating Procedure: After insuring that all the valves were in their normal positions, the electrical console in the blockhouse was activated. Operating pressure for the pneumatic remote valves was set. The valves were then functionally checked for proper operation.

Instrumentation items such as pressure transducers and thermocouples were physically checked to insure that they were properly installed and electrically connected. These items were pre-sensed before each test and post-sensed after a day's testing to insure that no zero shift occurred. The data recorders were prepared for test.

The liquid tank was filled with fluid. The fluid was then bled through the system to insure liquid was at the injection valve. The liquid tank was pressurized to approximately 30 psig, and the liquid was allowed to flow through the bleed valve which was positioned very close to the injection valve. Flowmeter spin was then monitored on an oscillograph to insure it was functioning properly. The liquid system was flow-calibrated to determine flow rate vs. pressure drop through the system, so that tank pressure could be set for the desired injection velocity of the liquid into the wind tunnel.

After the system set-up was completed, final test preparations were made. The liquid tank was pressurized to the proper pressure. The gas flow through the wind tunnel was started and plenum chamber pressure was set for the desired test condition. The liquid injection valve was then opened and a hologram of the resulting flow field; that is, liquid jet breakup in a supersonic stream, was taken. The liquid injection valve was then closed and the gas flow to the wind tunnel was turned off. This completed the test procedure, and the systems were then secured. A

description and operating procedure for the holographic system follows in the next portion of this chapter.

2. Hologram Recording System and Operating Procedure

a. Pulsed Ruby Laser: A schematic of the pulsed ruby laser which was designed and built by TRW for use with the holocamera is shown in Figure 12 . The system consists of a Kerr cell Q-switched oscillator and a power amplifier. When operated in the Q-switched mode, the complete system emits a single pulse of 1 to 3 joules power, 50 nanoseconds duration, at a wavelength of .6943 microns. The output from the oscillator is intensified by the amplifier, whose capacitor bank discharges .25 milliseconds after that of the oscillator. The beam is then diverged and collimated to a 5-inch diameter before it is output into the input port of the holocamera. The design is such that the coherence, spacial and temporal, allows recording of high quality transmission holograms in the holocamera. A detailed description of this laser system can be found in Wuerker[51] . A condensed description is given below.

The ruby oscillator consists of a $\frac{1}{2}$-inch diameter by 3 3/4-inch long ruby rod, a plane 99 percent dielectric end reflector, a nitrobenzene Kerr cell, a calcite Glan polarizing prism, and a sapphire resonant reflector. An inner-cavity aperture has been included to select the most homogeneous part of the rod for good spacial coherence.

The laser rod is mounted in a watertight housing which also contains the helical zenon flash lamp and a surrounding cylindrical silver reflector. The lamp is connected via an ignitron to an external high voltage (5,000 volts maximum) 375μF capacitor bank.

The Kerr cell is an electro-optical device which is used for

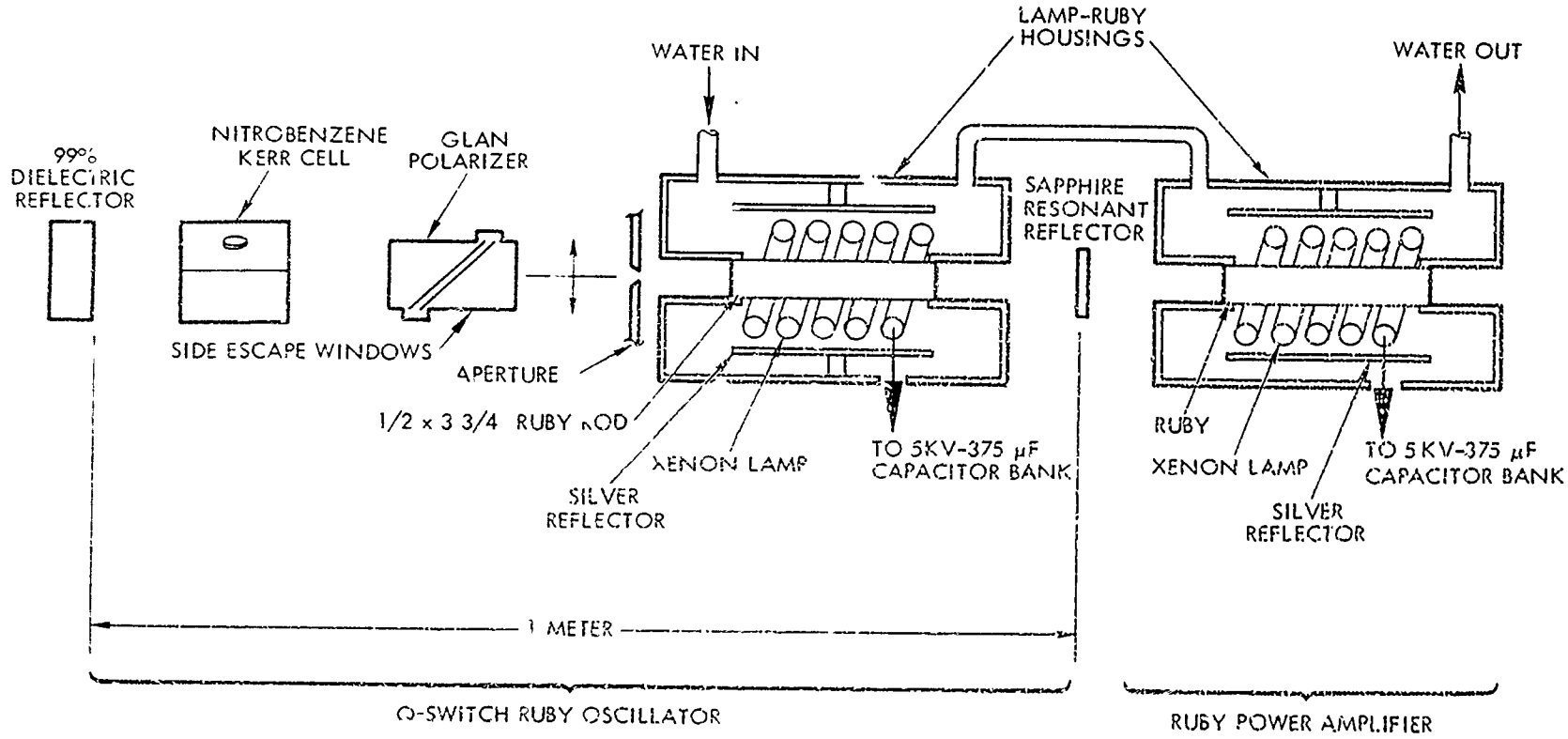

Figure 12. Pulsed Ruby Laser Schematic

Q-switching the oscillator. It isolates the 99 percent dielectric end reflector from the rest of the system, then opens for an extremely short duration to permit a single extremely short pulse (50 nanoseconds) to be emitted from the solid state ruby laser. The Kerr cell is biased by an independent high voltage supply. A hydrogen thyratron is used to discharge the Kerr cell, removing the quarter wave bias. Timing circuits are used to time the discharge of the Kerr cell relative to the initiation of current through the oscillator flash lamp. Delay is typically 0.85 milliseconds after initiation of lamp current.

A sapphire resonant reflector functions as the output mirror of the oscillator and is 1 meter away from the dielectric reflector.

The amplifier consists of a rod identical in size to the one in the oscillator, but of slightly greater chromium concentration. The oscillator rod has a concentration of 0.03 percent chromium dioxide. The amplifier rod has a concentration of 0.05 percent. The initial intensity gain of this rod is ~ 3. The amplifier rod is mounted within a housing identical to that of the oscillator. The rod and flash lamp are also water-immersed. The lamp is also connected via an ignitron to a second identical 5,000 volt maximum, 375μF capacitor bank.

The actual layout of the components for the ruby laser system is shown schematically in Figure 13 . The figure is a top view looking down into the laser. The laser system is folded. Two prisms jog the beam from the Q-switched oscillator and turn it through 180 degrees. The beam then passes through the amplifier and on into the beam expanding lens. Figure 14 is a photograph of the actual system. Folding the laser about the output of the oscillator section acts to make the system more compact. A dark field autocollimator and a 1 millivolt helium-neon gas

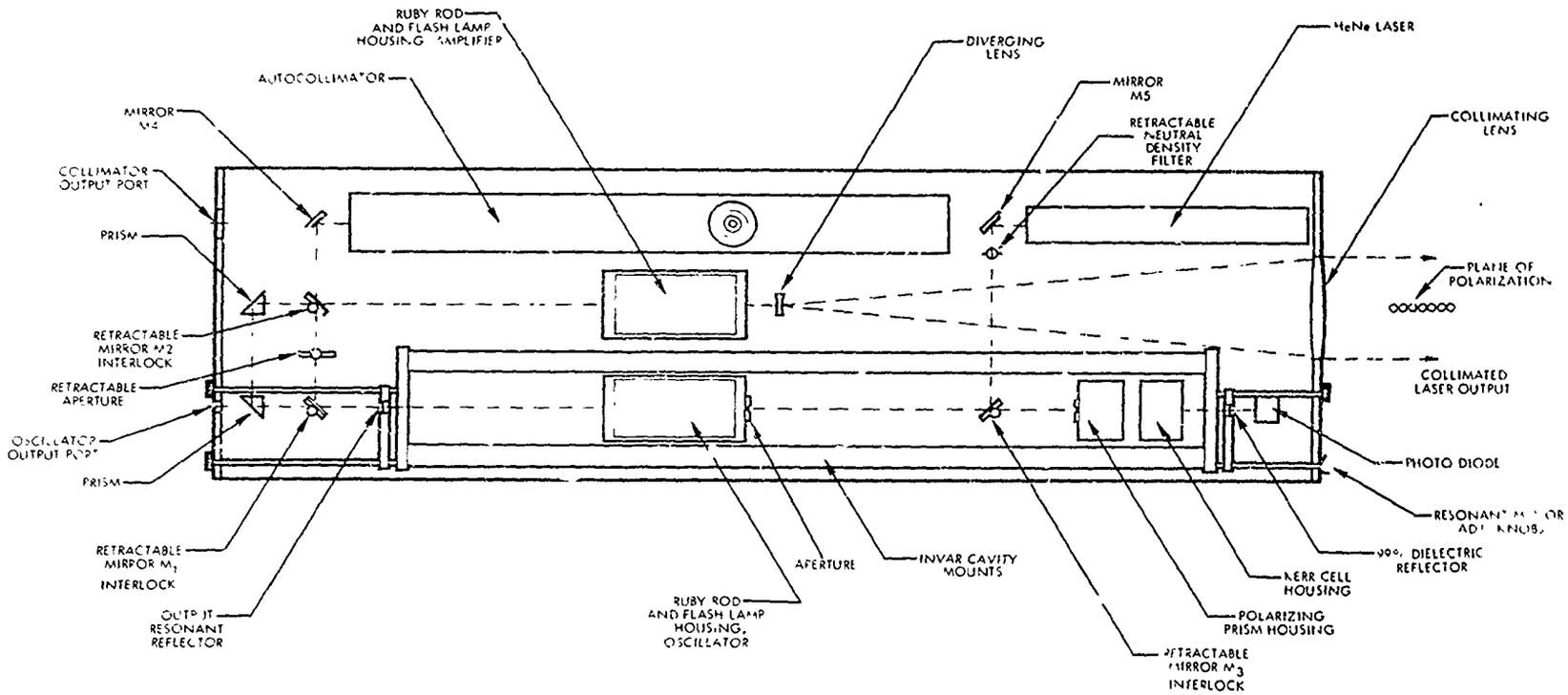

Figure 13. Top View Ruby Laser Components

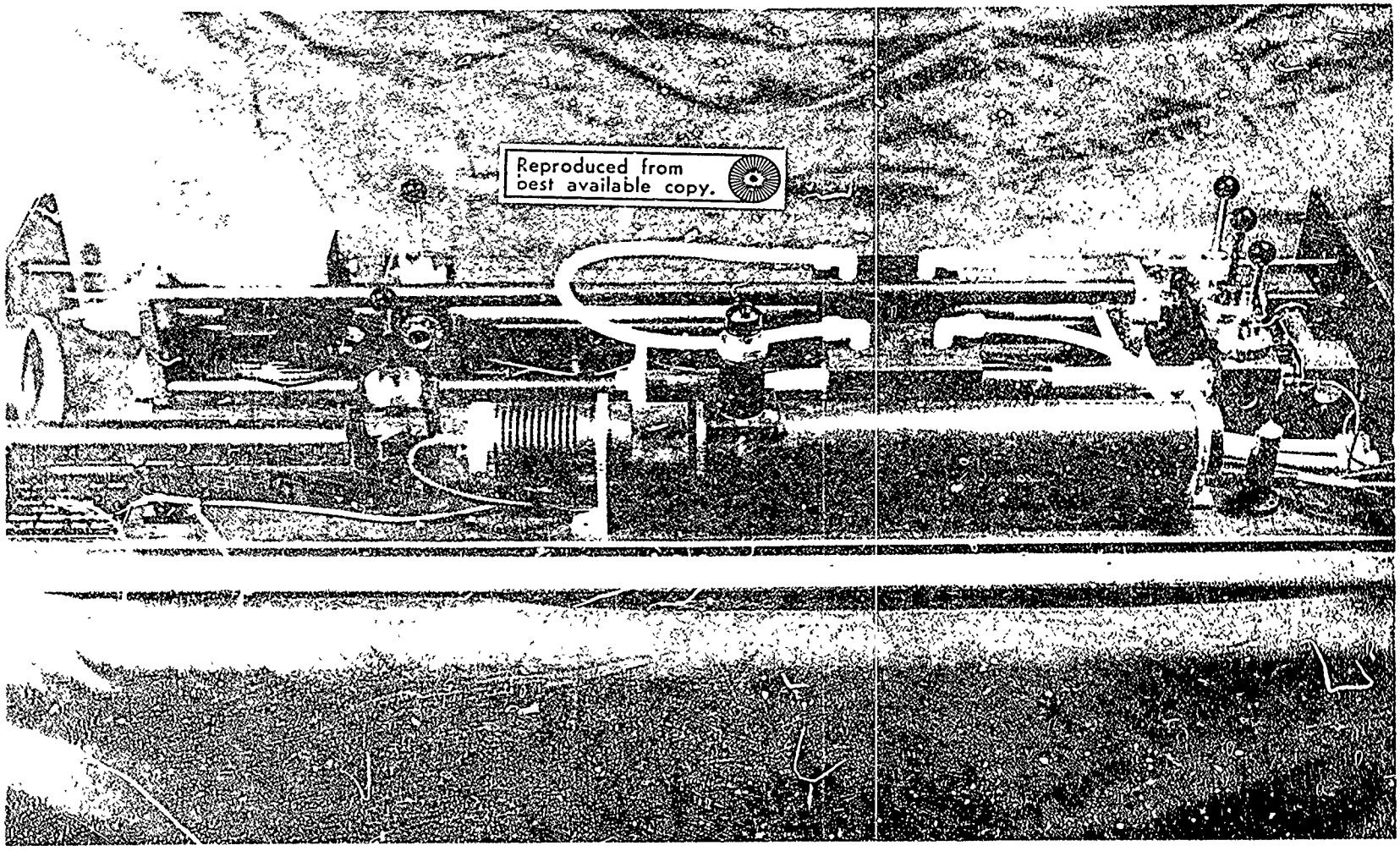

Figure 14. Pulsed Ruby Laser Component Arrangment.

laser, whose beam is used to align the optics for ruby beam, are mounted on the same base as the ruby laser optics. All components are mounted on a 0.4-inch thick by 15-inch wide aluminum channel, which functions as the main mounting base for the entire laser. The sapphire resonant reflector and 99 percent end mirror are mounted on an independent carriage made from 3/4-inch diameter invar spacers, to decrease thermal misalignment of the end mirrors caused by climatic temperature changes.

The channel and all the laser components are mounted within aluminum covers, the inside of which are covered with polypropylene olefin fiber insulation. The external covers are indirectly mounted to the channel by phenolic insulators. These are used to minimize the flow of heat to the internal components. The external covers serve also to shield the optics from dust, solar heating and protect the operator from accidental explosion of either the lamp or the two high voltage lamp insulators.

The autocollimator inside the laser illuminator housing is for the purpose of aligning the 99 percent dielectric end mirror and the resonant reflector parallel to one another. It is also used to measure and check the quarter wave retardation voltage of the Kerr cell. It can also be used as a sight by depressing mirror M_2. The autocollimator is basically a high power telescope with a point light source at the focal plane of the collimating lens. An internal beam splitter and the eye piece are arranged to enable one to observe light reflected by external surfaces. This autocollimator is classified as a dark field autocollimator, to distinguish it from the more common bright field versions used in metrology and machine shops. The dark field variety is particularly valuable for aligning and distinguishing the various surfaces within the solid-state

ruby laser described here. No means of absolute measurement is needed once alignment is achieved by superposition.

The most favorable transition in ruby is the one in which the electric vector of the emitted light vibrates perpendicular to the optic axis. For this reason, the beam from the ruby laser is plane polarized. In addition, the sapphire host is birefringent. The ruby thus must be properly oriented with respect to the Kerr cell, calcite Glan polarizer, and the sapphire resonant reflector. The latter, since it is also birefringent, must be properly oriented with respect to the ruby. The proper orientation of the laser components is explained in detail in Wuerker(51).

The system is intended to operate with the electric vector of the emitted light polarized vertically. However, by rotation of the ruby and Glan polarizer, it can also be arranged to emit a horizontally polarized output beam. If the plane of polarization of the oscillator is changed, the amplifier must also be changed, or else its gain will be greatly degraded.

The two flash lamps and the Kerr cell are electrically excited. Passage of a high current pulse of ~1500 amps through each lamp, produces the extreme thermal fluxes which populate the two flourescent levels in ruby rod. Atom population inversion is via the absorption by the rubies of the green and blue components of the white thermal (~5000°K) light from the flash lamps. The lamp current surge is via the electrical energy stored in high voltage capacitors. An electronic timing circuit is used to open the Kerr cell at the optimum time. A second timing circuit is used to retard the pumping of the amplifier relative to the initiation of pumping in the oscillator. Tests have shown that maximum amplification

in the second rod is not achieved when both lamps are started simultaneously.

A block diagram of the electronic equipment for the operation of the laser is shown in Figure 15.

The amplifier lamp and oscillator are connected individually to their separate 375μF ignitron fired capacitor banks. The two capacitor banks are charged from a single high voltage power supply (220 VAC, 1-phase). The charging of the banks is controlled by an API controller.

The Kerr cell is biased by a 0 to 30,000 volt supply which is connected across a high voltage hydrogen thyratron (type KU-27). The pulse from the thyratron is coupled to the Kerr cell by a coupling network inside the laser chest.

A firing circuit fires the ignitron in the oscillator bank. The signal is fed to the two delay circuits which, after appropriate delays, fire the amplifier's ignitron through its firing circuit, and the thyratron which fires the Kerr cell.

The electronics are contained in two floor-standing consoles, shown in Figure 16. The unit seen on the left contains the charging power supply, the oscillator capacitor bank, the amplifier capacitor bank, the safety crowbars, and some of the control relays. The console on the right contains the charging logic, the oscillator and amplifier firing circuits, the delay circuits, the Kerr cell high voltage bias supply, and the Kerr cell pulser. The charging logic panel can be removed from the console so that the function of charging and discharging the laser can be done remotely.

in the second rod is not achieved when both lamps are started simultaneously.

A block diagram of the electronic equipment for the operation of the laser is shown in Figure 15.

The amplifier lamp and oscillator are connected individually to their separate 375μF ignitron fired capacitor banks. The two capacitor banks are charged from a single high voltage power supply (220 VAC, 1-phase). The charging of the banks is controlled by an API controller.

The Kerr cell is biased by a 0 to 30,000 volt supply which is connected across a high voltage hydrogen thyratron (type KU-27). The pulse from the thyratron is coupled to the Kerr cell by a coupling network inside the laser chest.

A firing circuit fires the ignitron in the oscillator bank. The signal is fed to the two delay circuits which, after appropriate delays, fire the amplifier's ignitron through its firing circuit, and the thyratron which fires the Kerr cell.

The electronics are contained in two floor-standing consoles, shown in Figure 16. The unit seen on the left contains the charging power supply, the oscillator capacitor bank, the amplifier capacitor bank, the safety crowbars, and some of the control relays. The console on the right contains the charging logic, the oscillator and amplifier firing circuits, the delay circuits, the Kerr cell high voltage bias supply, and the Kerr cell pulser. The charging logic panel can be removed from the console so that the function of charging and discharging the laser can be done remotely.

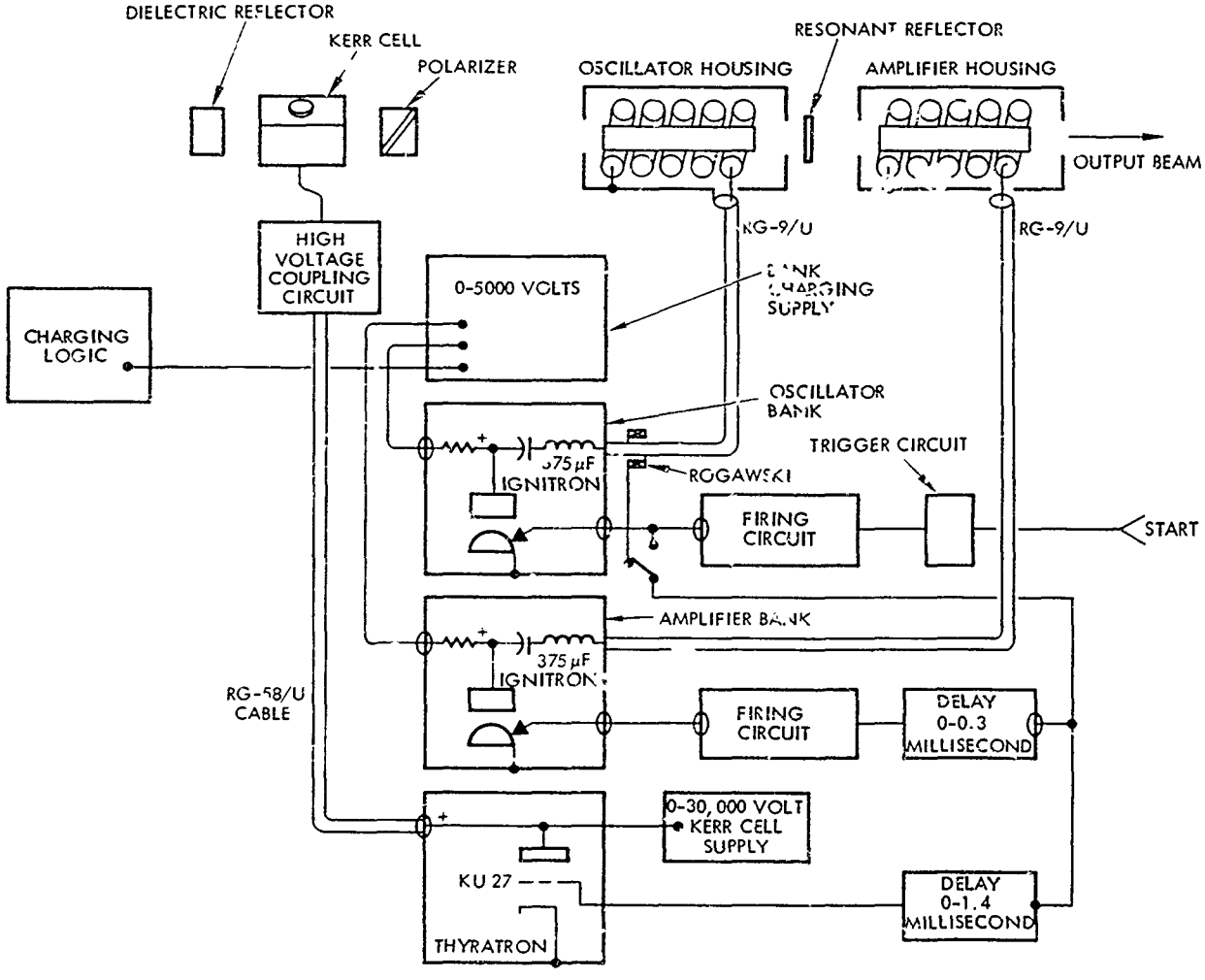

Figure 15. Laser Electronic Block Diagram

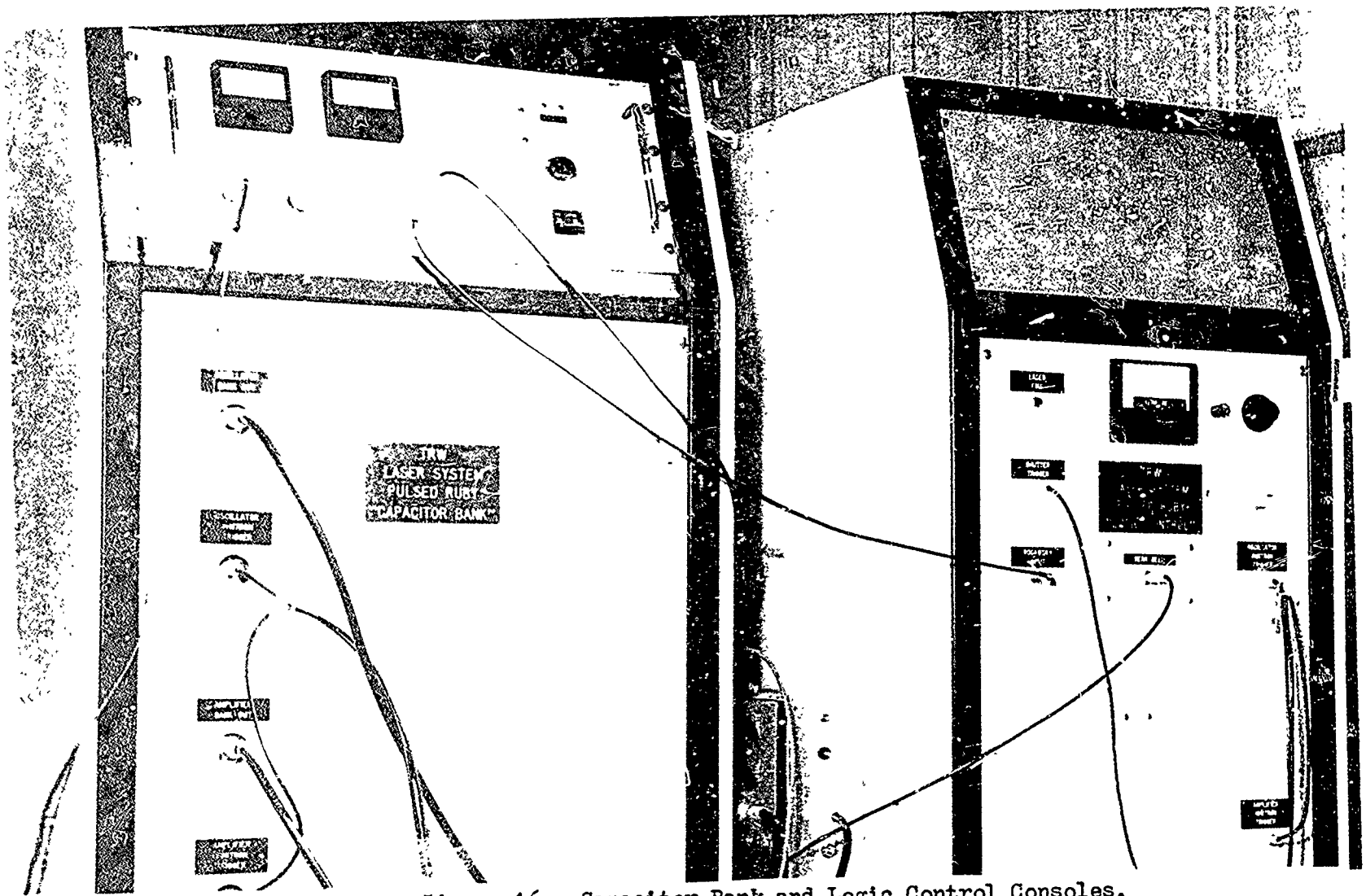

Figure 16. Capacitor Bank and Logic Control Consoles.

b. Holocamera: The RPL 75° transmission holocamera was developed by TRW Systems under contract to the United States Air Force. See Wuerker[68]. The 75 degrees refers to the angle between the scene and reference beams. This angle was selected for the following reasons: 1) to give a very wide viewing angle to the reconstructed hologram; 2) to have a reference beam which did not interfere with the scene, and 3) to permit more efficient use of the Agfa 8E75 high resolution film emulsion. The major components in the holocamera are the quadruple lens set, beam splitter, prism plate, ground glass diffuser and mirrors.

A schematic of the holocamera is shown in Figure 17. Figure 18 is a side elevation of the holocamera, and Figure 19 is an actual photograph of the device along with the laser. Referring to Figure 17, the collimated, laser input beam enters the holocamera through the large diameter port in the side of the holocamera. The beam then impinges on a 50% beam splitter, which divides the beam into a scene and reference beam. The scene beam passes through the splitter and is reflected by mirrors numbers 1 and 2 arranged as a roof prism. Mirror number 3 directs the scene beam onto the prism plate by bending the beam 105°. The beam is then scattered isotropically by a ground glass diffuser (not shown) attached to the far side of the prism plate. Light scattered by the diffuser is focused by the quadruple lens set onto the hologram. The quadruple lens set provides a very large aperture, short working distance system, which minimizes spherical aberration. The hologram and prism plate are at 1:1 conjugate image locations, and their separation is determined by the focal distance (16 inches) of the quadruple lens set. The portion of the incident laser beam which is reflected by the beam splitter comprises the reference beam, which is further reflected by

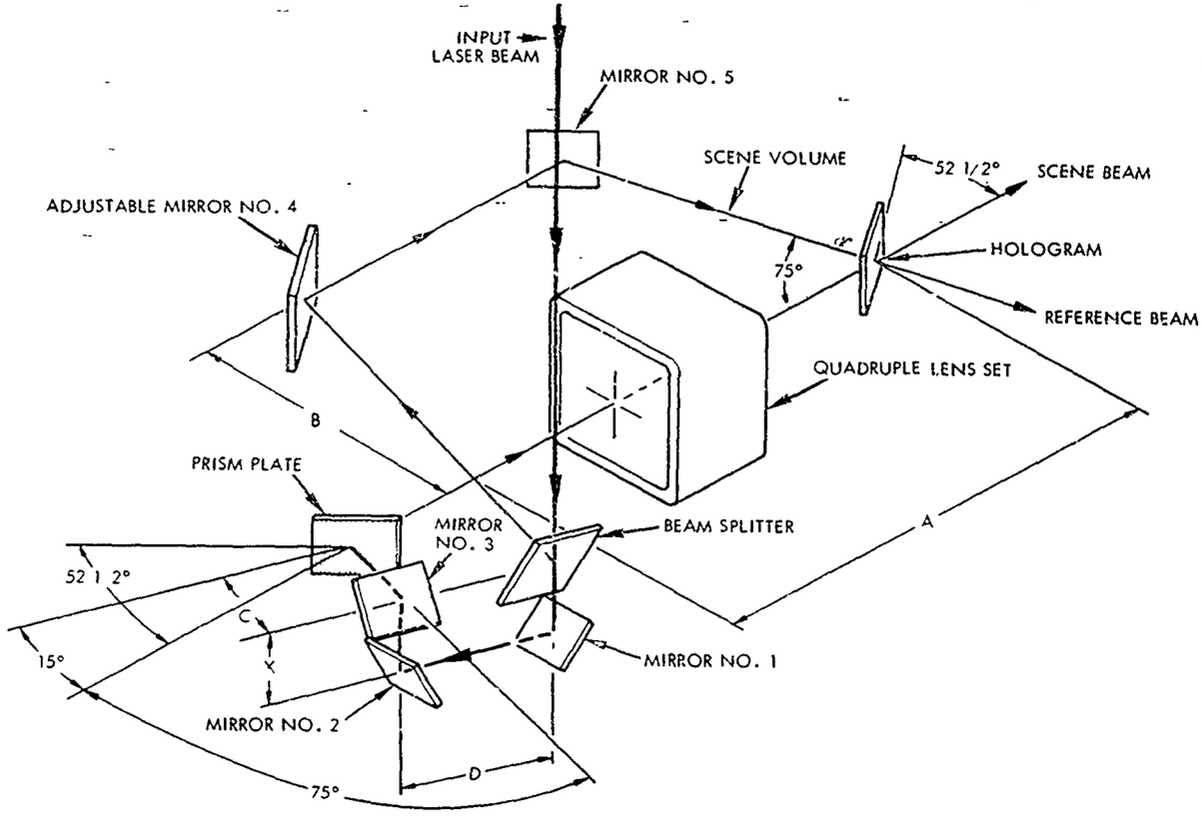

Figure 17. Holocamera Components Schematic

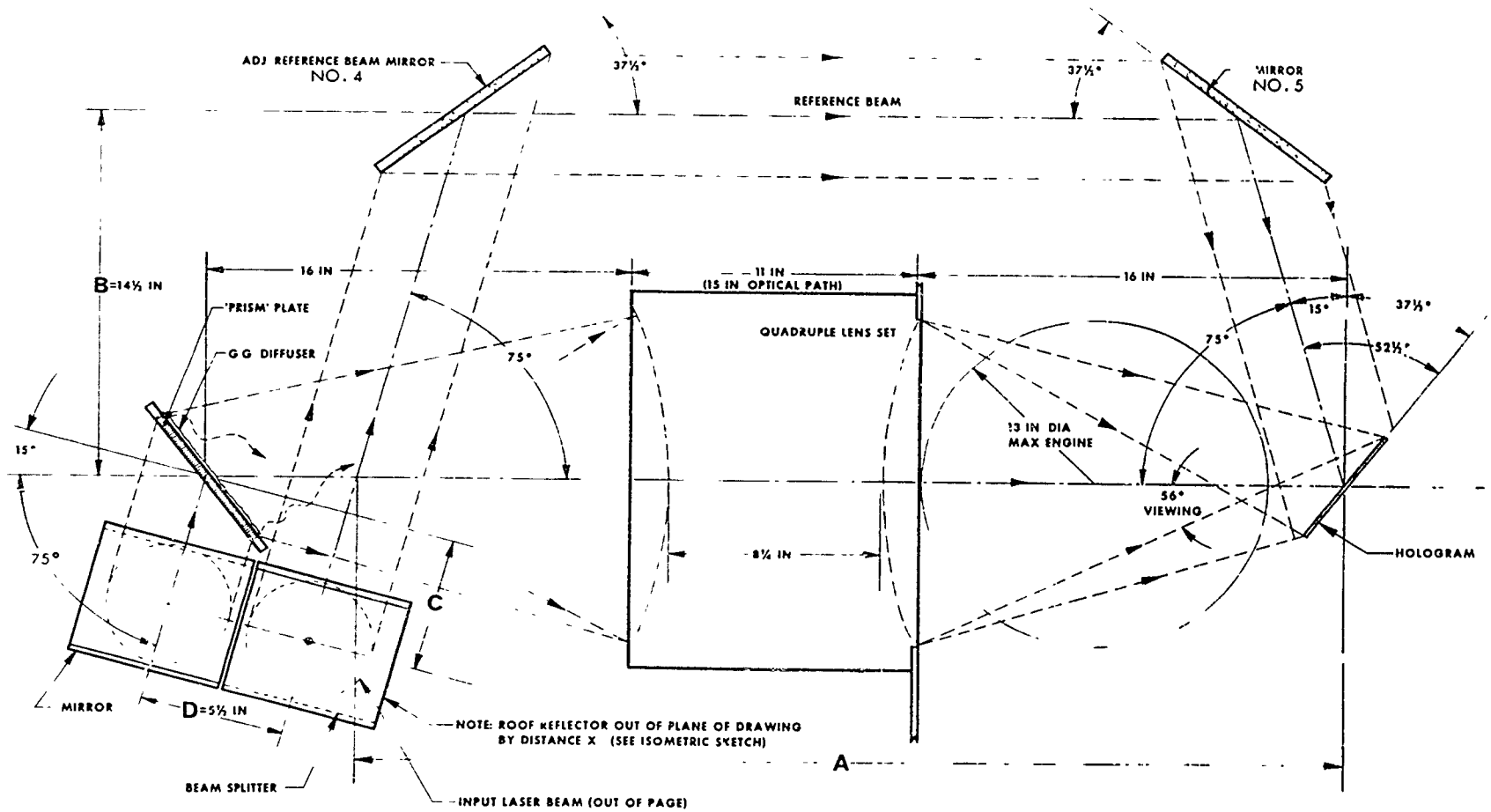

Figure 18. Holocamera Side Elevation View

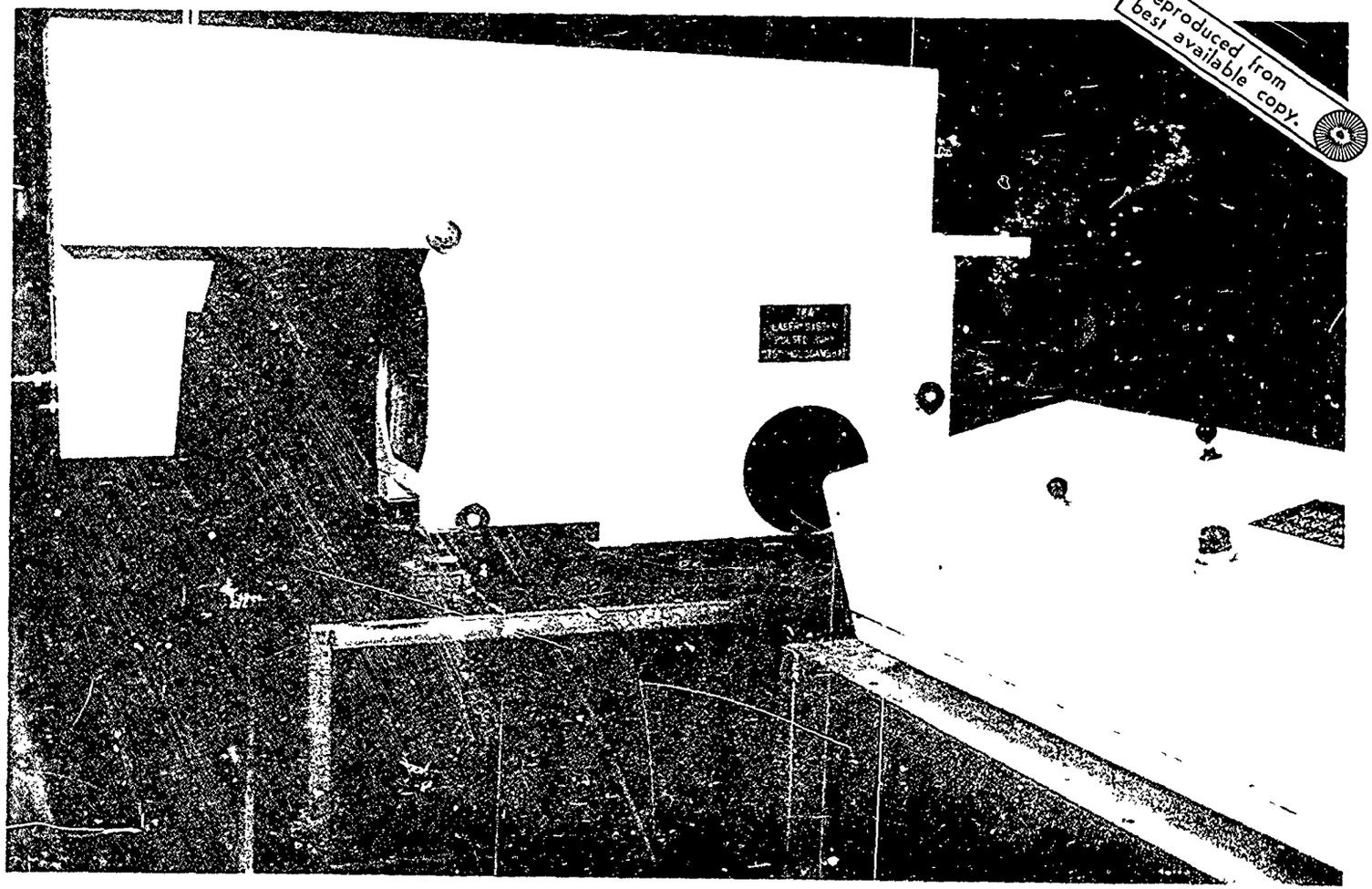

Figure 19. Holocamera with Pulsed Ruby Laser.

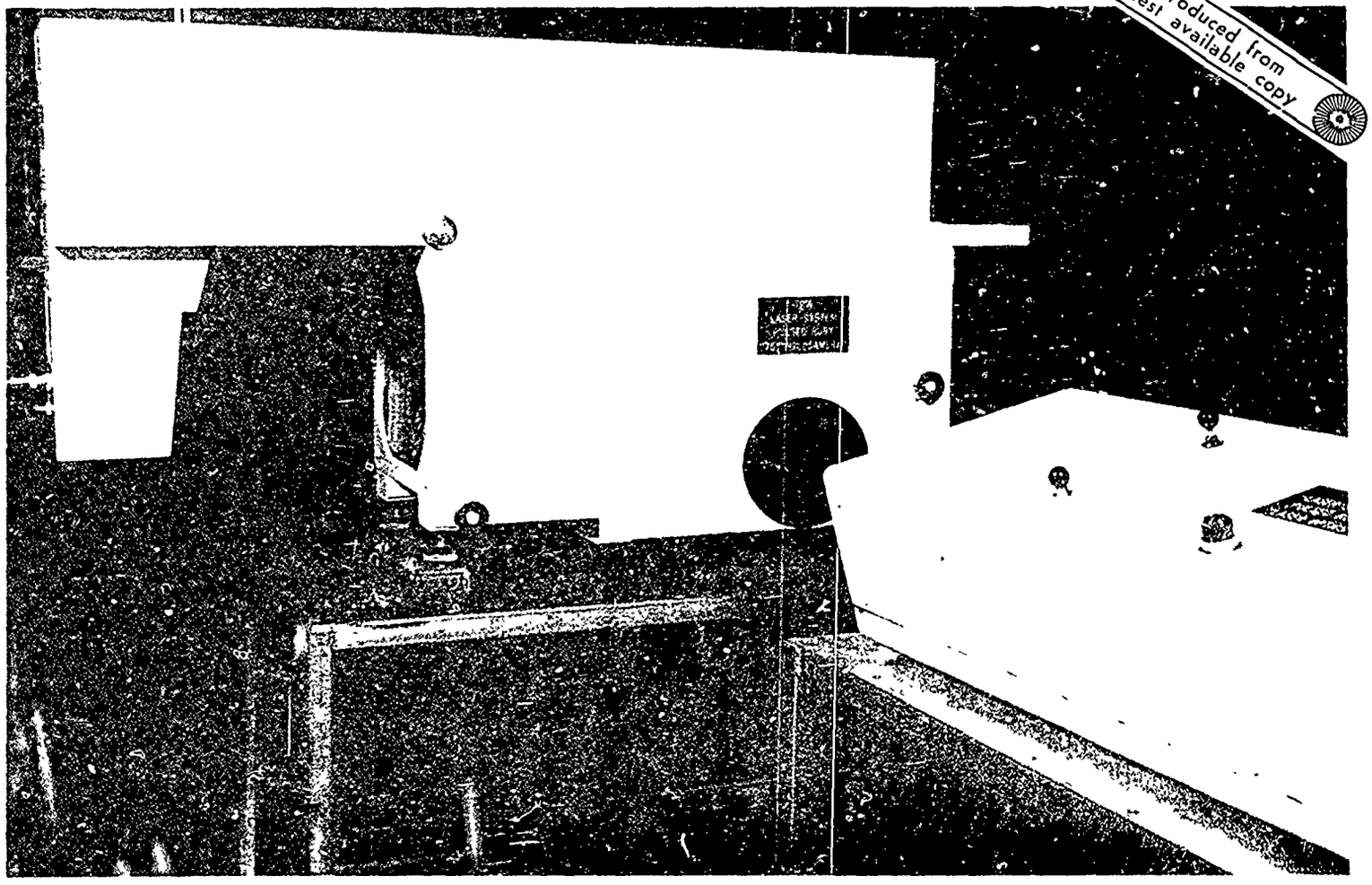

Figure 19. Holocamera with Pulsed Ruby Laser.

mirrors 4 and 5, before reaching the hologram. These mirrors are located so the scene-reference beam angle is at the desired value of 75 degrees.

The two beams recombine at the plane of the hologram after each component has traveled the same optical path. Path equality is determined by accurate placing of the mirrors, beam splitter and prism plate in the holocamera. All the components in the holocamera are oriented and positioned to maintain a temporal and spatial match of the scene and reference beams. The scene beam must be incident on the back side of the ground glass diffuser at the same angle that the reference beam is incident on the hologram. This insures that all scene-reference ray components travel approximately the same optical path length from the beam splitter to the hologram. The condition for equal scene and reference beam path match is explained in Wuerker[68] . Mirrors 1 and 2, the roof prism, are mounted on an adjustable base plate which has a screw drive. The screw is connected to a ten-turn potentiometer dial on the side of the holocamera. This arrangement makes it possible to control the scene beam path length, thereby compensating for increases in the scene beam path, perhaps due to the addition of thick windows. It also makes possible the experimental discovery and verification of the path match condition.

The film plane is located so that its normal bisects the scene-reference beam included angle. The 4 x 5 inch film plate is oriented such that it projects a nearly square format in the direction of the axis of the quadruple lens set. The plane of the hologram plate is $52\frac{1}{2}$ degrees with respect to the direction of propagation of the reference beam.

The scene volume, the region between the lens set and the structure enclosing the film holder, will accommodate an object approximately

13 inches in diameter. Total viewing angle of the reconstruction is 56 degrees.

The holocamera is properly operated with scene and reference beams polarized horizontally at the plane of the photographic plate when the holocamera is standing as shown in Figure 19 on the bottom feet. Thus, the vibrating electric vector of the two beams at the plate are horizontal. This gives the best interference of the combining rays at the plane of the hologram. For horizontal scene and reference beams at the photographic plate, the input laser beam must be polarized so that the plane of vibration of the electric vector is canted at 15 degrees with respect to the vertical. This correct orientation is shown in Figure 19 . This seemingly strange cant of the polarization is a result of the choice of the 75 degree scene-reference beam angle. The beam splitter is canted at 15 degrees along with mirrors 1, 2 and 3.

The holocamera is fitted with a mechanical focal plane shutter. Speed is approximately 60 milliseconds. The combination of shutter and red filters protects the plate from overexposure. The mechanical shutter is wound by hand and can be released either manually or remotely by an electric solenoid. Releasing the shutter trips a microswitch which fires the laser when the shutter is in the open position. Firing the laser by the shutter is accomplished by interconnecting a coaxial cable between the connectors on the holocamera and laser control console.

The holocamera normally accommodates horizontal scenes. However, it can be placed on its side, in which case vertical scenes can be holographed.

c. Holographic Plates: The holograms were recorded on Agfa Gevaert Scientia 8E75 glass plates. The plates are 4" x 5" and possess red-sensitized, high resolution (capable of resolving 3000 lines/mm) emulsion on one side. The reason for selecting the 8E75 plates was explained in the previous section.

After taking the hologram, insuring that the emulsion side of the plate was facing the scene at the time of recording, the plate had to be developed so the image on it could be reconstructed and viewed. A darkroom having a green safelight was used, since the plates were red-sensitized.

The development procedure was as follows:

a) the holographic plate was placed in a tray containing a solution of 1 part Kodak HRP developer and 4 parts water, ideally at 68°F, for approximately 40 seconds, or until the plate was 50% transparent as determined by looking at the safelight through the developing plate. The solution may be agitated by tipping the plate forward and back to aid the development process. The development process was then stopped;

b) stopping was accomplished by putting the plate in a photographic acetic acid stop bath for one minute;

c) the plate was then placed in the hypo (Kodak Rapid Fix) for two minutes;

d) next, the plate was rinsed in cool running water for at least five minutes; and

e) finally, the plate was dipped in Photoflo solution, placed in a rack and hung up to dry.

After the plate was dry, it was ready for image reconstruction and viewing.

1. Hologram Recording System Operating Procedure: The holocamera is first oriented relative to the scene of which a hologram is to be taken. The ruby laser is then oriented properly to the holocamera such that the output collimating lens of the laser faces the input port of the holocamera. The protective covers from the various lenses are then removed. Electrical connections are made to all the components: laser, holocamera, capacitor banks, logic control, autocollimator, alignment laser, cooling unit and oscilloscope. After the electrical connections were made, power was turned on to each component. The ruby laser and holocamera were then aligned with each other. This was accomplished with a Helium-Neon (He-Ne) alignment laser. The holocamera and ruby laser are aligned when the alignment laser beam, which is split into scene and reference beams in the holocamera, are superimposed at the center of the holographic film plate. The ruby laser internal alignment was accomplished next. This is done when the red dot reflection from the 99% dielectric reflector is superimposed on the white dot reflection from the sapphire resonator when the two dots are viewed in the eyepiece of the autocollimator. These dots are also superimposed on the He-Ne alignment laser reflection in the autocollimator eyepiece, which forces the ruby laser beam to follow the alignment laser beam; hence, alignment of the ruby laser with the holocamera. The potentiometer dial on the holocamera is then set for the proper optical path match. Filters are installed in the scene or reference beam for the proper intensity ratios between the beams. The Kerr cell voltage is then set, the film plate holder is loaded and placed in the holocamera, the holocamera

shutter is cocked and the slide is pulled from the film holder. The capacitor banks are then charged. A signal is obtained when both banks, oscillator and amplifier, are fully charged. A switch on the main console in the blockhouse activates the solenoid which releases the holocamera shutter. When the shutter is full open, a micro-switch is tripped which fires the laser. The film holder slide is then returned to its closed position and the film holder retrieved so the film plate can be developed.

The holographic system and test system operations were coordinated when tests were conducted. After the day's testing was completed, electrical power to the components was turned off and the lenses covers reinstalled. The electrical lines were not disconnected unless the laser and holocamera were to be moved elsewhere.

3. Description of Experiments.

The high-speed flow field experiments consisted of injecting various liquids (water, methyl alcohol, trichloroethylene, Freon 113 and a water-photoflo solution) normally into a Mach 3, gaseous nitrogen stream through different sized orifices (.042, .050, .062 inches in diameter), which could be flush-mounted into one of the test section blocks of the wind tunnel. Liquid injection velocities were varied from 190 to 450 feet/second. The wind tunnel was operated over a total pressure range from 100 to 300 psia. The parameters of interest were liquid type, injection velocity, orifice diameter, and wind tunnel total pressure. The penetration trajectories of the liquid into the gas stream were calculated according to a method developed by Catton, Hill and McRae[21]. The dynamic pressures of the liquid and the supersonic gas stream had to

be balanced to insure that the liquid would penetrate the gas stream, yet not impinge on the opposite side of the wind tunnel from the injection point. Holograms were taken during each test. Figure 20 shows the actual orientation of the laser and holocamera relative to each other and the wind tunnel. Typically, the flow field resulting from injection of the liquid into the supersonic gas stream is shown in Figure 21. The liquid jet disturbs the gas stream and a bow shock wave results. As the liquid jet penetrates the gas stream, it is aerodynamically broken up and spreads laterally. The envelope of the spray resembles a section of an ellipsoid. A combustion region is also shown in the Figure. This would be applicable if combustible liquids were burned in an air stream; however, this was not the case with the experiments conducted in this investigation.

The experiment of the liquid jet injecting into still air was conducted by Dr. R. Wuerker, TRW Systems Group. Its corresponding hologram was given to the Air Force Rocket Propulsion Laboratory for reconstruction and analysis.

Actual test conditions, results and analyses of the experiments are presented and discussed in Chapters VI and VII.

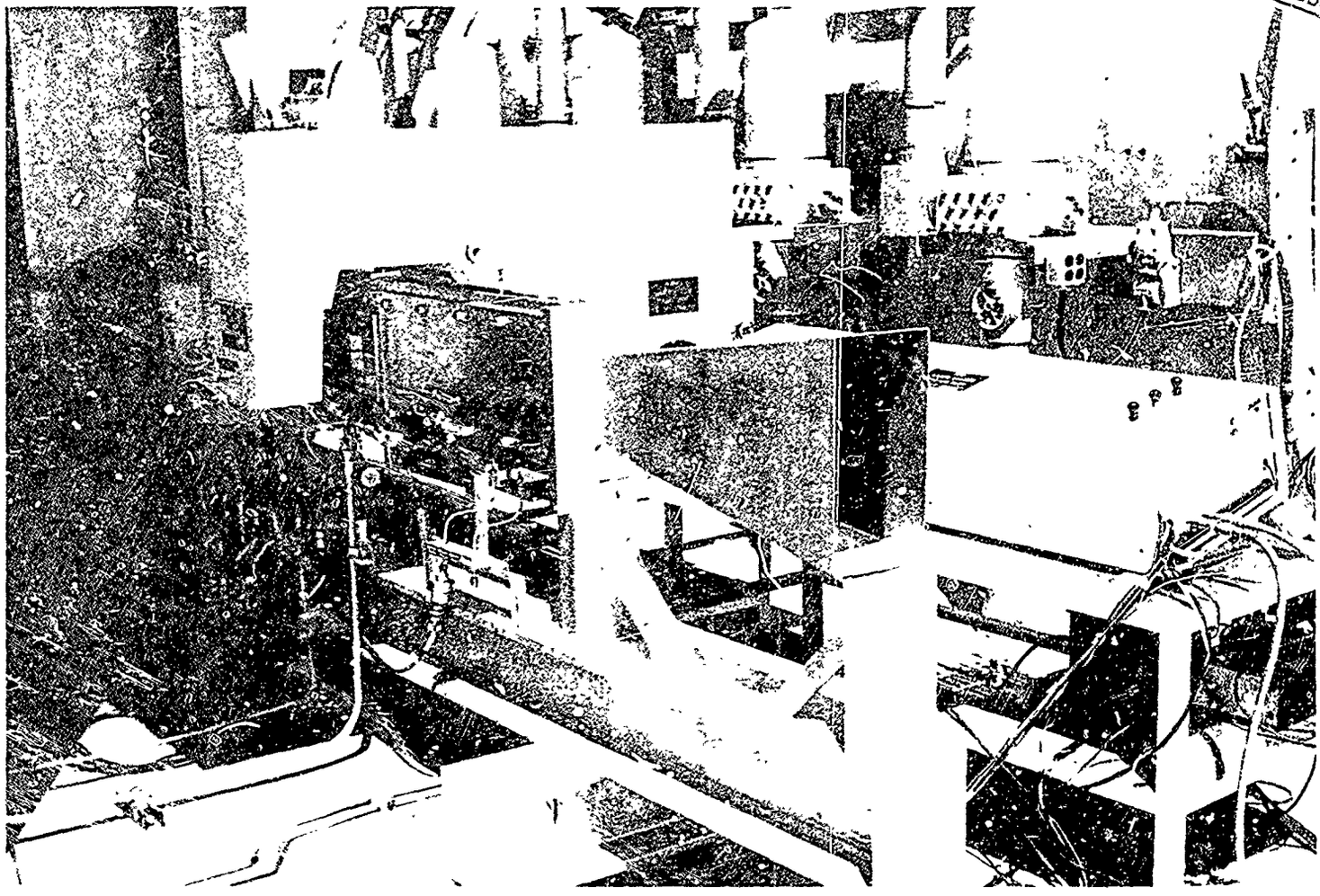

Figure 20. Wind Tunnel, Ruby Laser and Holocamera in test setup orientation.

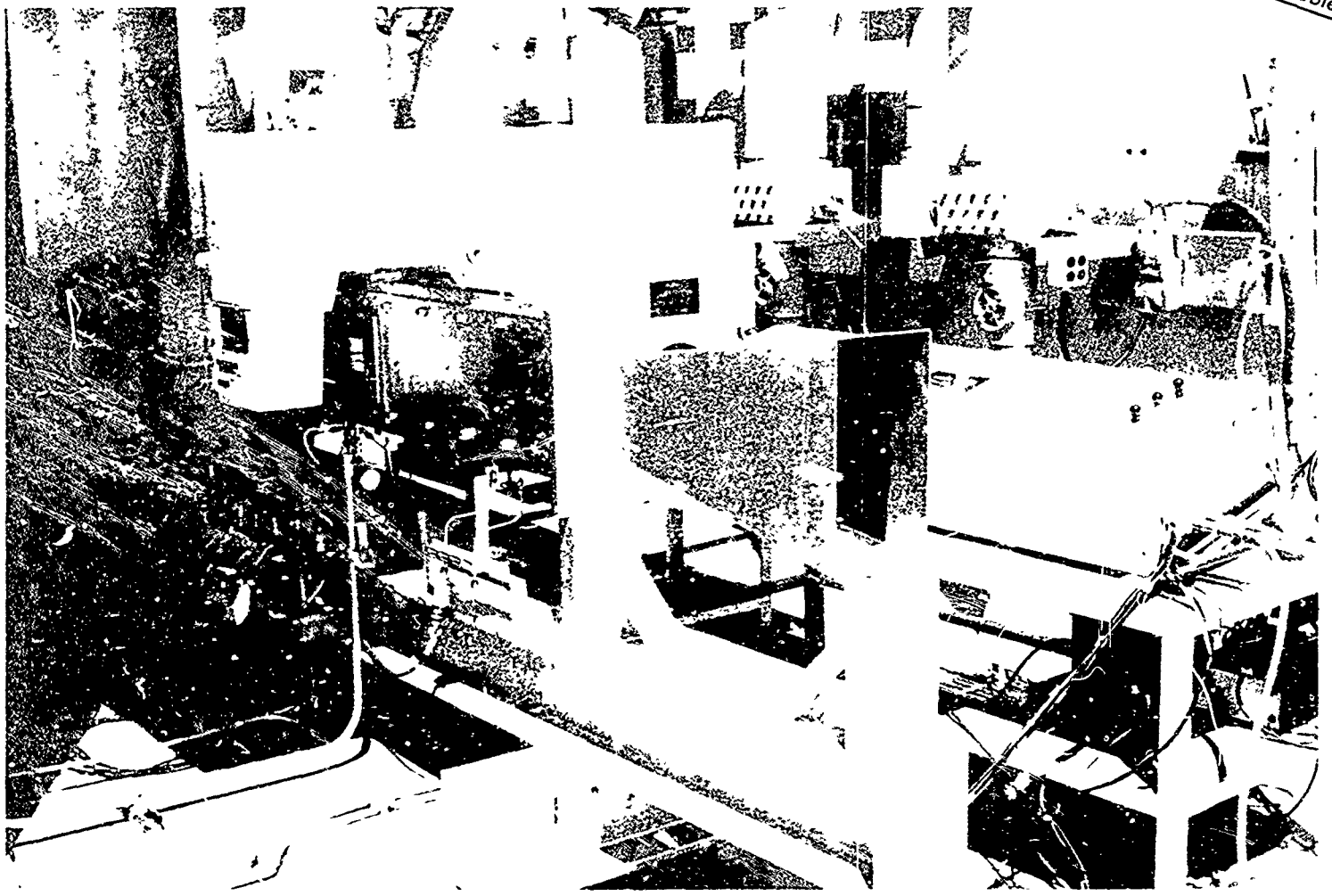

Figure 20. Wind Tunnel, Ruby Laser and Holocamera in test setup orientation.

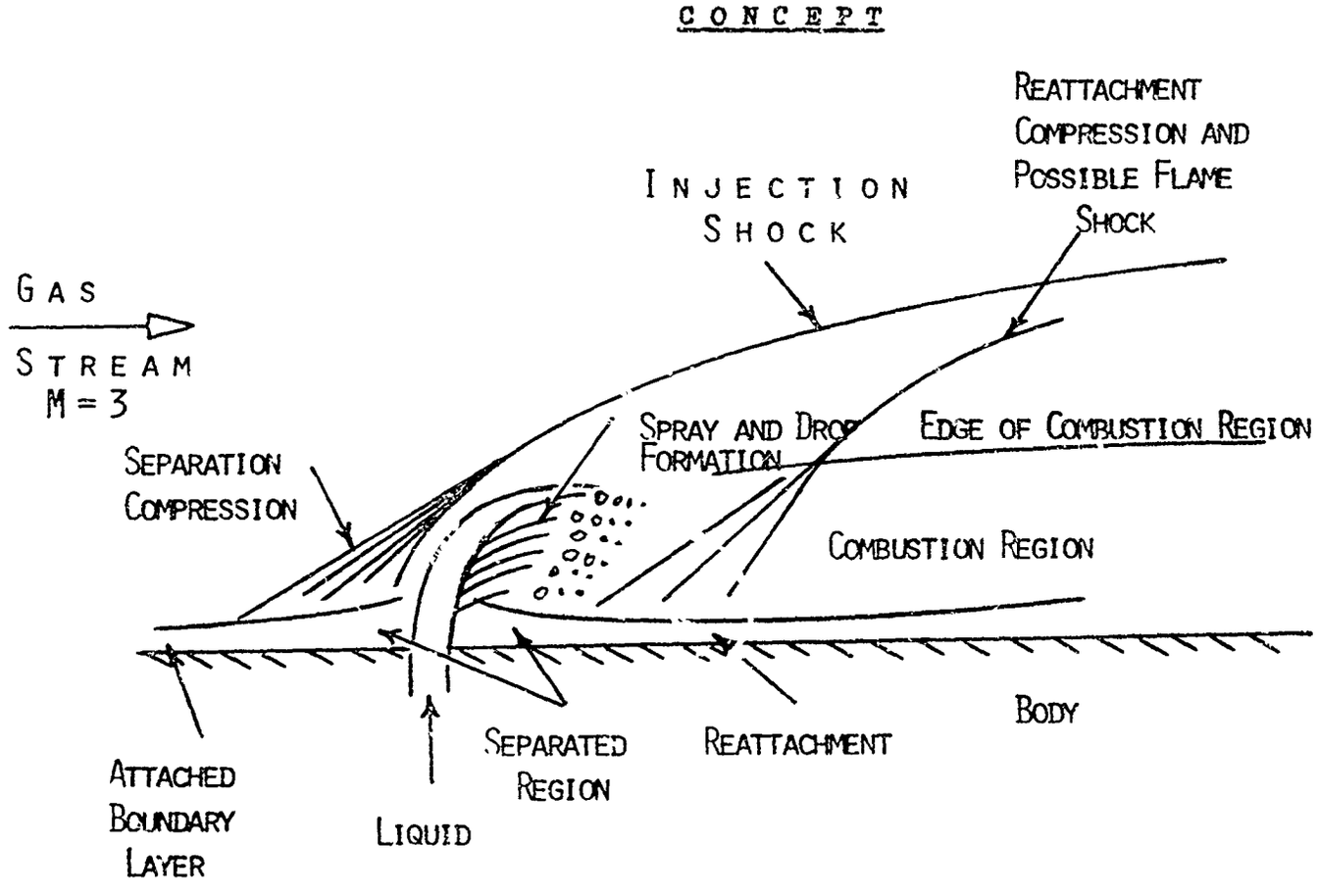

Figure 21. Supersonic Jet Interaction Flow Field

CHAPTER IV

RETRIEVAL OF HOLOGRAPHIC DATA

1. Hologram Information Processor (Primary Holographic Data Retrieval Method)

a. System Description: Hologram reconstruction and data retrieval is accomplished by a system called the Hologram Information Processor. A schematic of the system is shown in Figure 22 . The actual system is shown in Figures 23 and 24 . The system consists of a laser, spatial filter and diverging lens arrangement, collimator, hologram support stage, reticle wheel, magnification lens system, TV camera and set, coordinate position carriage, magnetic tape deck and a control console. The laser is used to simulate the recording reference beam and to illuminate the hologram, thereby making the real image of the scene visible on a 1:1 basis so the data can be retrieved. The TV camera and lenses mounted on the scanning carriage allow the observer to view the magnified scene on a TV monitor as the carriage is moved through the scene volume. A detailed description of the system operating procedure will be presented in a subsequent section.

The original laser for the system was a Siemens pulsed ruby laser (SLR 1P1). It was a quasicontinuous wave laser, since it pulsed at 60 Hz and had a maximum rated mean power output of 1 watt. Operational difficulties with this laser made it imperative to obtain another laser so data from the holograms could be retrieved. The system was then fitted with a Spectra Physics 125A, continuous wave, Helium-Neon gas laser, 80mw mean power output. This laser facilitated the data retrieval. The laser has its own spatial filter, 6 microns, diverging and collimating lenses. The output beam can be collimated to a 50mm diameter. The collimating lens renders the diverging beam rays parallel. The collimated beam illuminates the hologram which is mounted on its support stage. The hologram

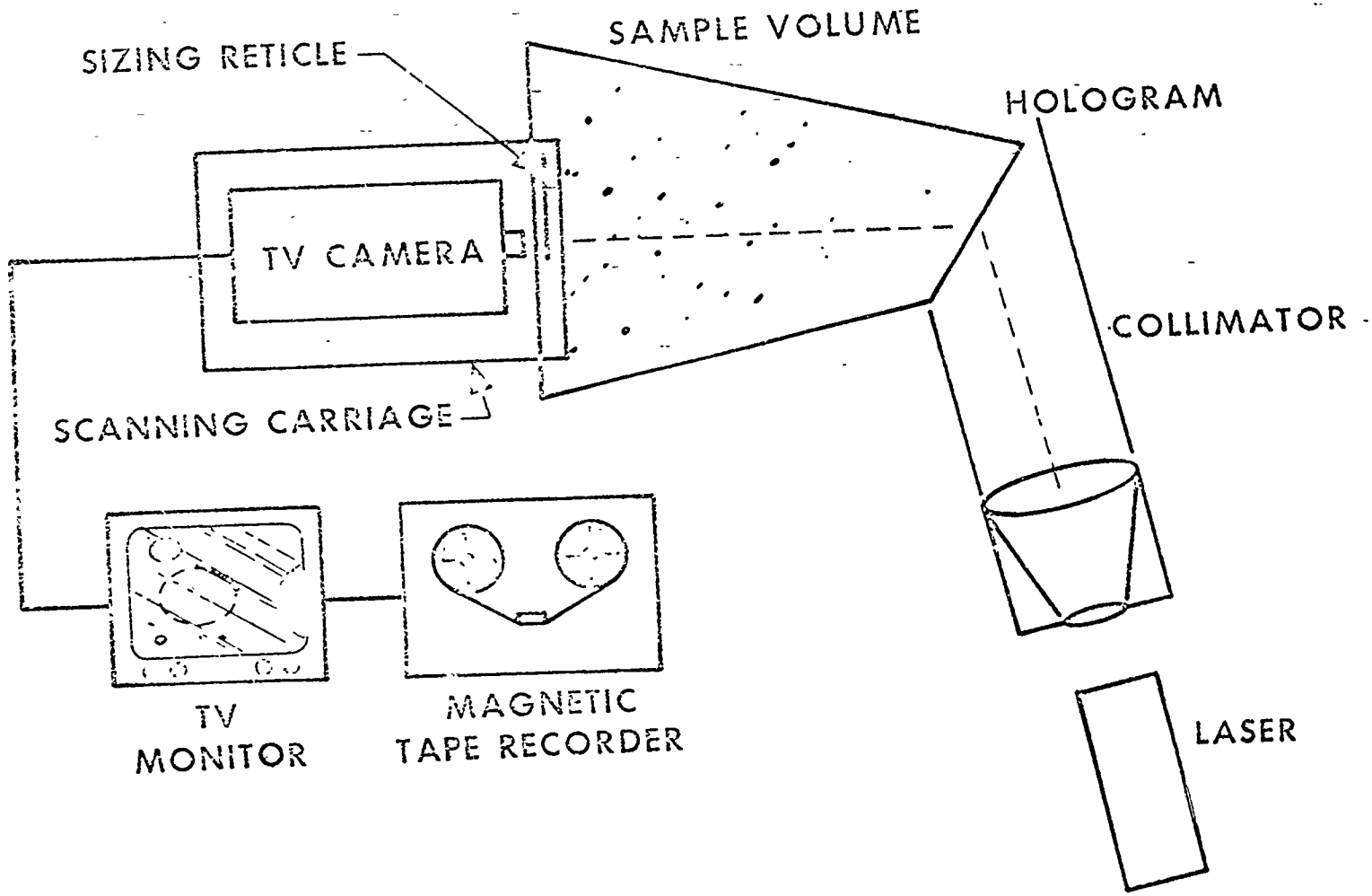

Figure 22. Hologram Information Processor Schematic

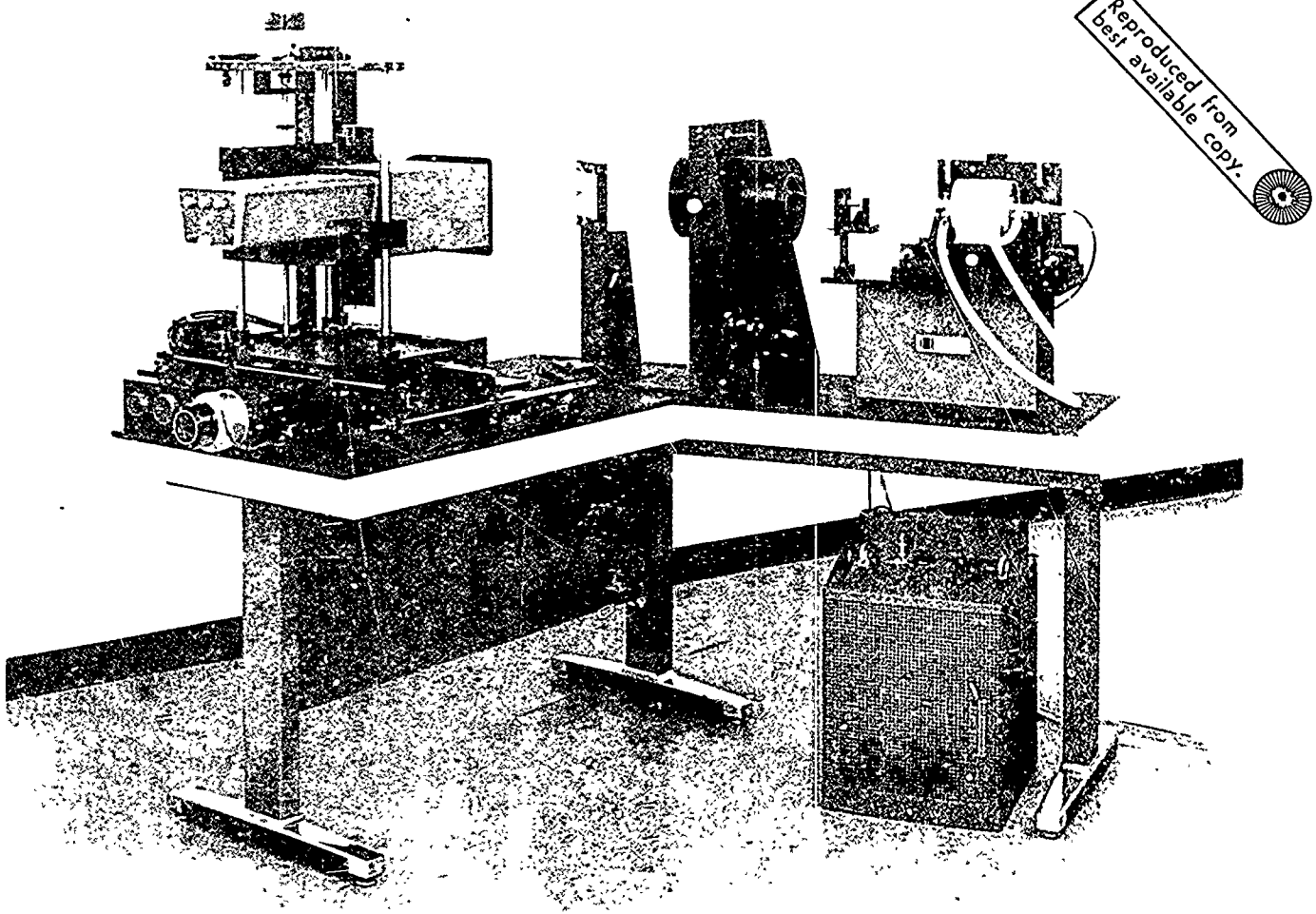

Figure 23. Hologram Information Processor Components - laser, collimating lens, hologram stage, T.V. camera and moveable carriage.

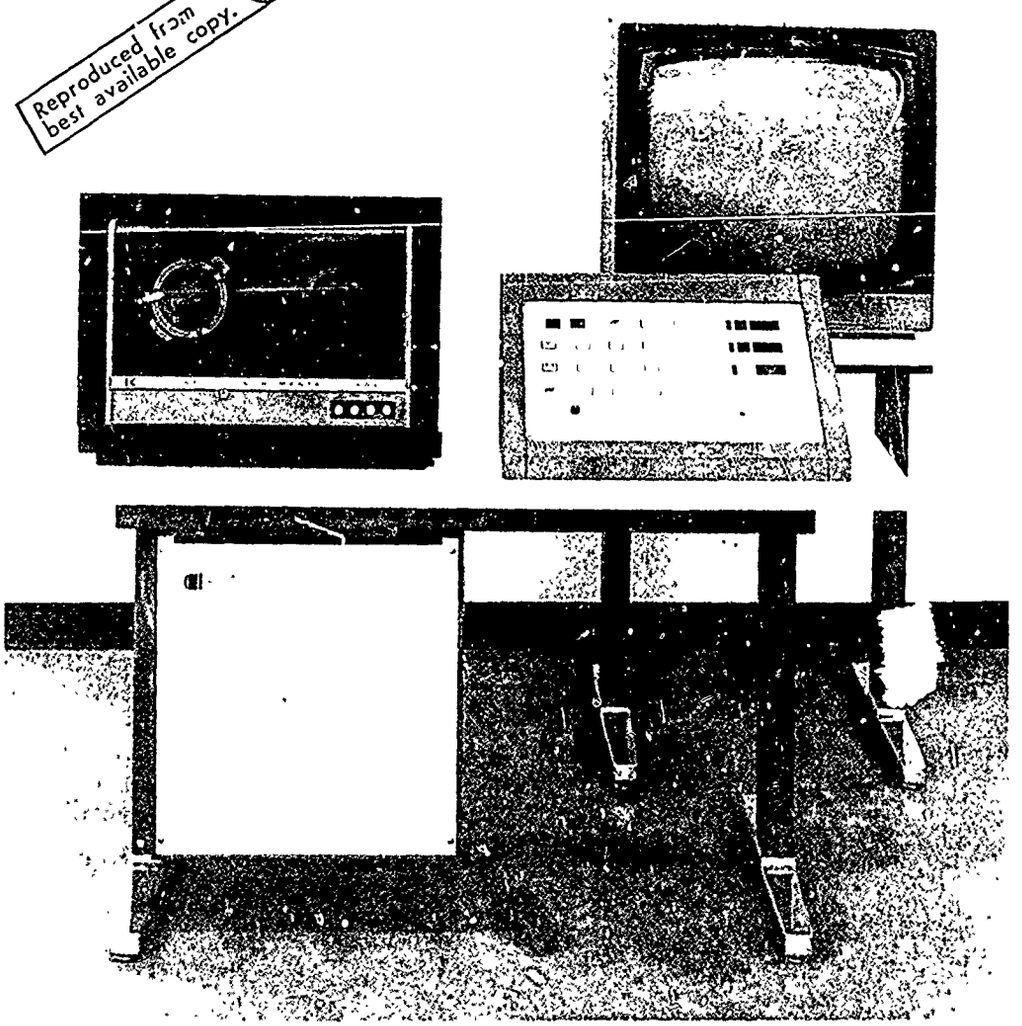

Figure 24. Hologram Information Processor Components - T.V. monitor, control console and magnetic tape unit.

support stage is a Jodon Model PH-45A. The stage has 6 degrees of freedom which allows proper hologram orientation relative to the laser, for maximum brightness and resolution, and minimum distortion and aberration of the image. Once the hologram and laser are properly oriented to each other, they must be arranged such that their optical axis passes through the center of the imaging lenses and TV camera mounted on the scanning carriage.

Mounted on the spatial coordinate (scanning) carriage are the TV camera, imaging lenses and reticle wheel. This arrangement is used to scan the scene volume to determine the droplet size and position coordinates. The glass reticle wheel has 50 circles photoetched on it, on a 6-inch diameter bolt circle. These represent 50 sizing intervals ranging from 20 microns to 1,000 in 20 micron increments. The imaging lens arrangement consists of two Nikon lenses (50mm, f/1.4) mounted in a manner to give magnifications of 4:1, 1:1, and 1:4. The resolution range and field of view for each magnification are respectively 10-1,000 microns, 2.5 x 3.3mm; 20-1,000 microns, 10 x 13.2mm; 100-1,000 microns, 3.8 x 5.1cm. The lenses are placed between the TV camera and reticle wheel such that they focus on the reticle wheel. The TV camera is a Telemation TMC-2100. The carriage can move $\pm$ 6.000 inches in each direction (x,y,z) or a total of 12 inches in any one direction depending on where the origin is placed. The carriage is moved by drive motors whose switches are mounted on the control console. Encoders placed along side the carriage provide position accuracy of 0.0005 inches.

The TV camera and monitor (23-inch, Conrac RVB) comprise a closed circuit video system which is used to display the reconstructed scene volume. . The system has the standard 525 scan line raster with resolution

along the scan direction of 200 TV lines at the center of the field.

The droplet data which consists of size and position coordinates is recorded on a Kennedy incremental magnetic tape recorder, Model 1600.

The control console contains the switches which reset the system and operate the scanning carriage and reticle wheel. A foot switch is provided to input the droplet size and spatial coordinate data on the magnetic tape. The console displays the position coordinates and number count in each drop size interval on Nixie tubes. The memory system which provides the number count storage is a United Telecontrol Electric Model 5030. The reset switch clears the memory core and establishes the zero reference for the spatial coordinates by moving the carriage to the desired point prior to depressing the reset button. A lock-on feature was provided which restricts the scanning area in the transverse and vertical directions. With this, the operator can subsection the hologram for scanning in a systematic manner.

Although the system is oriented to retrieve holographic droplet data, it can also be used to retrieve other holographic data.

b. Operating Procedure: After all the electrical connections to the various components were made, the master switch on the control console was turned on. This turned on the TV set and camera and magnetic tape recorder and rendered the scanning carriage and sizing reticle wheel operable. The laser was then turned on and its beam diverged and collimated according to the procedures in its operating manual. The hologram was mounted in its support stage and oriented relative to the laser and imaging lenses as described above. The lenses and TV camera were aligned such that they focused on the reticle wheel. The operator set the desired imaging lens magnification and moved the carriage to the desired

reference point by operating the switches on the console. The reset button was then depressed and the system was ready to retrieve data.

The carriage was moved in the x,y,z positions until a droplet in the scene volume came into focus at the center of the TV screen. The droplet was sized by rotating the reticle wheel, via a console switch, until one of the 50 circles on the wheel best circumscribed the droplet. A foot pedal switch was then depressed and the spatial coordinates and size interval which appear on the console Nixie tubes were recorded on the magnetic tape. The operator proceeded in this manner until all or a statistically sufficient number of droplets in the scene volume were recorded.

After the droplet data was recorded on the magnetic tape, the tape was then processed through a system of computer programs to obtain the various mean droplet diameters, spatial mass distribution and other information of interest.

2. Alternative Holographic Data Retrieval Method

a. System Description: The Hologram Information Processor was a new system and operational difficulties were encountered with it. After the laser problem was resolved, electronic problems developed. At one time or another all the components functioned properly, but all did not work at the same time. In order to retrieve the holographic data, an alternative method was devised.

At the time the alternative method was devised, all parts of the Processor system were functioning properly with the exception of the sizing reticle wheel. The alternative method uses part of the Processor

system as shown in the upper part of the schematic in Figure 25 . In place of the TV camera, a lens (58mm, f/1.5) and 35mm camera were installed on the scanning carriage. The lens was used in conjunction with the 1:1 lens arrangement for the Processor. The new lens was placed between the imaging lenses and 35mm camera and magnified the scene 1.6X at the film plane. The lens system was still focused on the reticle wheel and gave a very narrow depth of field, 300 microns. This allowed photographs to be taken at discrete planes in the scene volume as the carriage was moved. Each frame represented one of the spatial coordinates, while the other two coordinates were on a given frame.

In addition to using the Processor and 35mm camera to produce photographs through the scene volume, the alternative method used a film reading system, schematically shown in the lower part of Figure 25. Negatives of the frames obtained from developing the film roll were mounted on a Telereadex film reading machine, Model 29A. The machine can magnify the negatives 5X, 10X, 20X and 50X. The film can be indexed forward or backward, frame by frame, and at variable speeds. The film is imaged on a board with moveable crosshairs. The moveable crosshairs allow a two-coordinate "fix" on a droplet in a given frame. Hence, the spatial coordinates of a droplet can be obtained from a given reference point. The reference point is established by setting the crosshairs where desired and then depressing a reset button. As the crosshairs are moved, counts are observed on the Nixie tubes of the Telecordex Analog-digital converter. This is similar to the Processor positional coordinate system, but different in that the Processor reads out actual coordinates, to the nearest .001 inch, rather than counts. The counts need to be converted to actual coordinates. Additional information, such as droplet

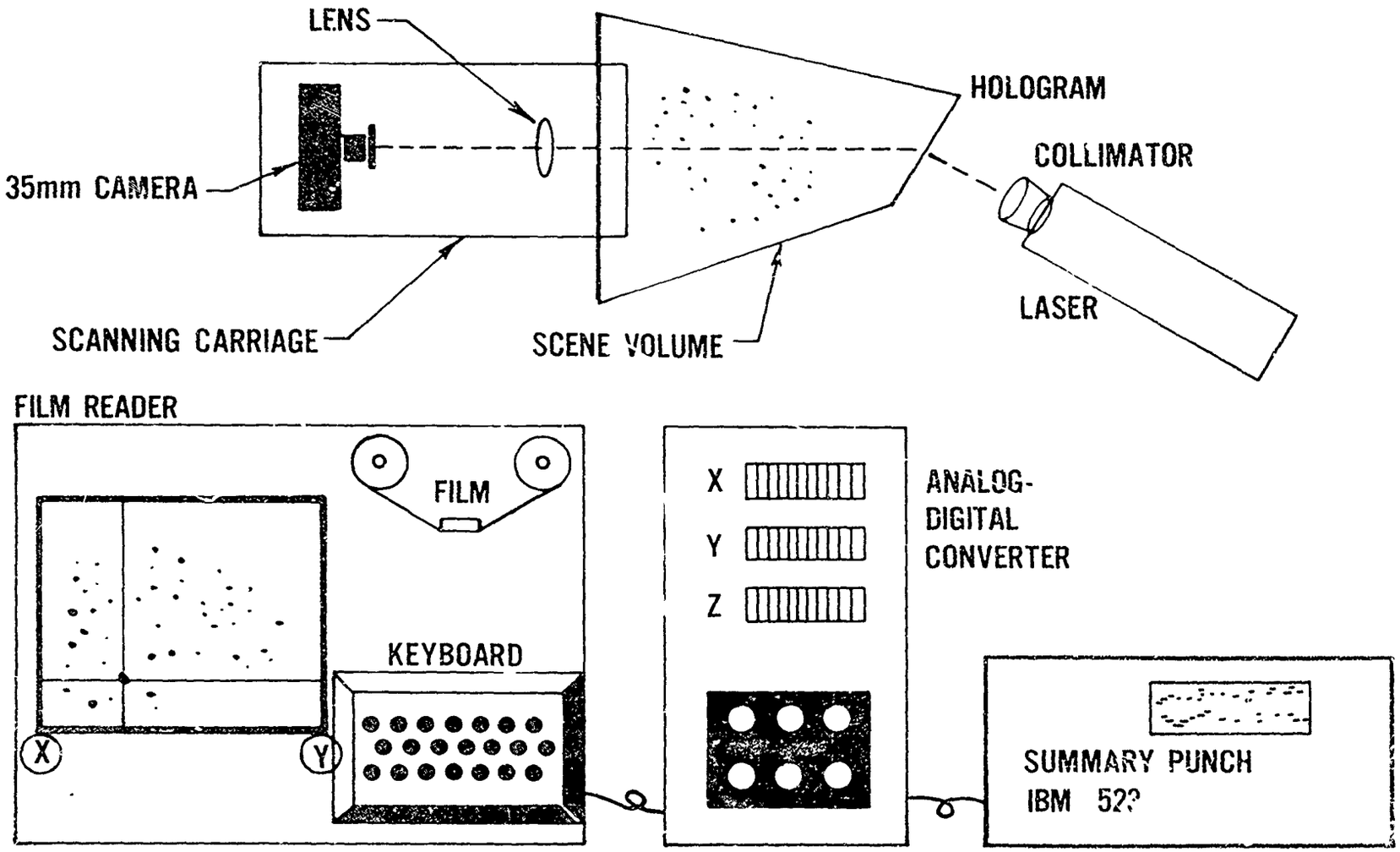

Figure 25. ALTERNATE HOLOGRAPHIC DATA RETRIEVAL METHOD

size, can be punched on the 12-digit keyboard (Type 56B) of the film reader. When a foot pedal is depressed, information on the keyboard and on the A-D converter Nixie tubes is punched on computer cards loaded in an IBM 523 Summary Punch. Figure 26 shows the actual film reading system.

b. Operating Procedure: The operating procedure for the Processor was the same as was described above with the exception of statements relating to the TV camera and reticle wheel. After lens system and camera (35mm) alignment were accomplished, the camera was loaded with GAF black and white, 125ASA film. The scanning carriage was moved through the scene volume and photographs were taken at depth increments of .050 inches through the liquid jet. Exposure time for each photograph was one second. Care was taken to collate the film frame with the depth positional coordinate for data reduction purposes. The film roll was then developed using microdol X developer and Kodak fixer to obtain the negatives. The film roll was then mounted on the film reading machine. The 20X magnification lens (105mm, f/3.7) was used, since this gave the best image on the viewing board. Actual magnification was 32X. A calibration scale was used to determine the number of counts per inch as the crosshairs were moved. The reference point was selected at the base of the image for one coordinate and at the center of the jet for the second coordinate. The third spatial coordinate was represented by the frame, and this information was input directly to the A-D converter. As the frame was changed, so was the corresponding information. After establishing the reference point for a given frame, data then could be retrieved. Droplet sizing was accomplished by taking the difference between the counts given by one of the crosshairs as it was placed on each

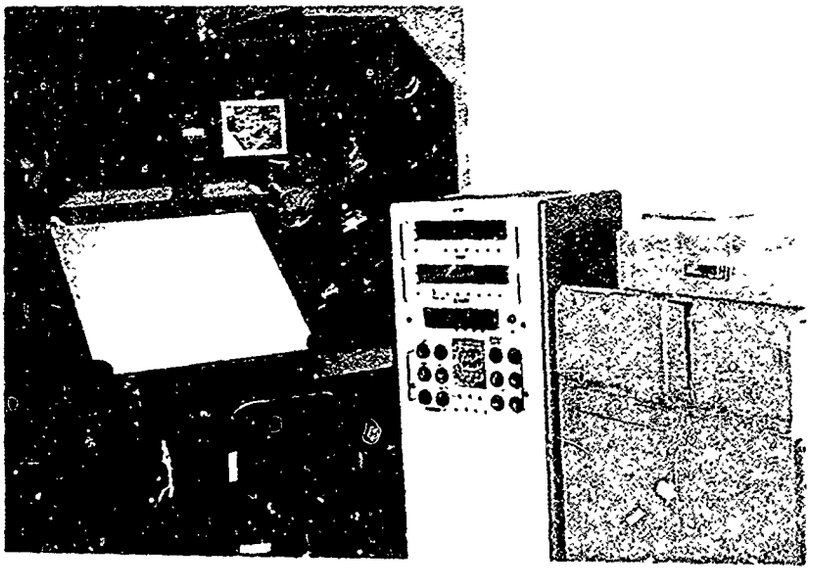

Figure 26a. Film Reading System - film reader, analog-digital converter and summary punch.

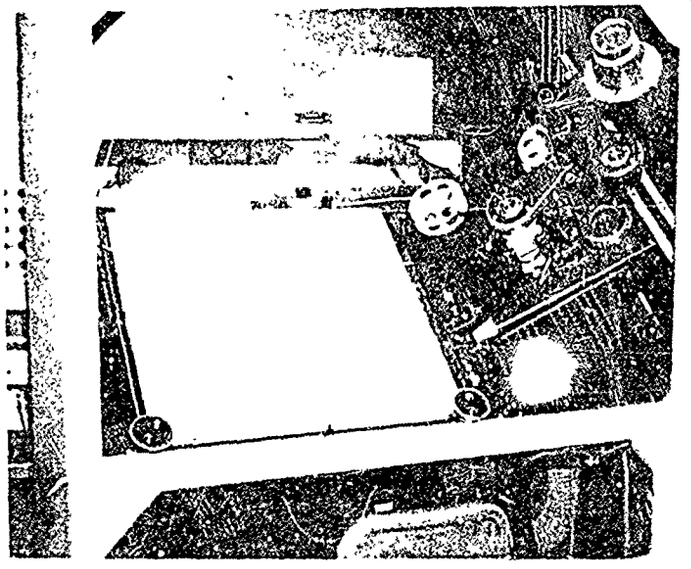

Figure 26b. Film Reader Close-up.

side of the droplet. This number was then punched on the film reader keyboard, the crosshairs were then centered on the particular droplet and when the foot pedal switch was depressed, drop size and spatial coordinates were punched on a computer card. The procedure was continued drop by drop and frame by frame until all the data was retrieved. The cards were then input to the system of computer programs, to be described in the next chapter, for data reduction.

CHAPTER V

ANALYTICAL METHOD FOR REDUCING HOLOGRAPHIC DROPLET DATA

1. Description of System of Computer Programs

After retrieving the droplet data from the holograms, by either the primary or alternative retrieval method, the data has to be reduced, analyzed and presented in a meaningful manner. A method for reducing the droplet data, drop size and corresponding spatial coordinates, was developed as part of this investigation. The manner in which the droplet data was operated on is described below. A system of computer programs was used to handle the droplet data. A schematic diagram of how these programs were combined to reduce and analyze the droplet data is shown in Figure 27. The programs were written for use on the IBM 7040 computer, since this was the type of computer available at the Air Force Rocket Propulsion Laboratory, where the investigation was conducted. A description of each program is presented below.

a. PR-470 Holograph Tape Unpack Program: This program performs the preliminary processing on the digital information, droplet size and positional coordinates (x,y,z) on the magnetic tape. The objective of this program was to provide a FORTRAN compatible magnetic tape for subsequent processing of the data. The program provides the opportunity to view the raw data, if desired, before it is processed. The program consists of a FORTRAN main with one FORTRAN subroutine and three MAP subroutines. Also, the program has the facility to process a variable number of input tapes. This program is used only when the primary holographic data retrieval method is used. The output from the alternative retrieval method is on punched cards; hence, the PR-470 program is by-passed.

b. PR-471, $IBSRT Edit-Sort Program: The PR-471 program, along with the standard IBM $IBSRT program, begin the operation on the raw data.

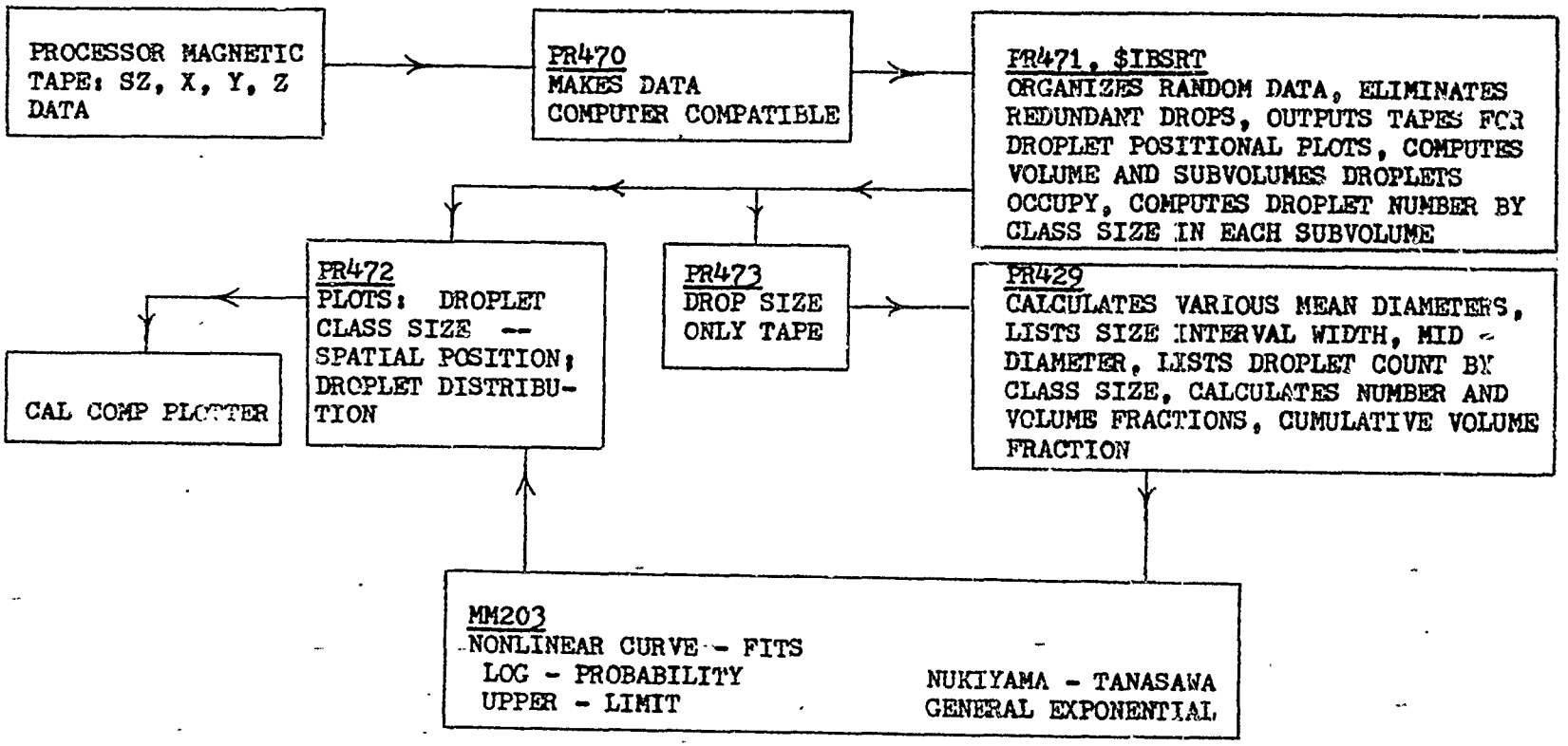

Figure 27. System of Computer Programs for Droplet Data Analysis

These programs perform a multitude of functions:

1) Organize and sort the random droplet data;
2) Eliminate redundant droplets;
3) Determine the minimum and maximum positional coordinates for the volume occupied by the unique droplets;
4) Determine the number of droplets in each class size;
5) Set up the graph slice for the drop size-positional coordinate plots;
6) Sub-volume the total volume occupied by the unique droplets; and
7) Determine the number and class size of the droplets in each sub-volume.

Basically, the data reduction process deals with two problems: 1) that concerned with droplet position coordinates, and 2) that concerned with the droplet sizes and their frequency of occurrence.

The first step in the operation was to order the random data. This was accomplished by the system library program, $IBSRT. Ordering was done on one of the position coordinates, preferably the one on which the graph slice was to be taken. The coordinate on which the ordering was performed was printed out monotonically increasing, while its corresponding other two coordinates and droplet size were printed out in an unpatterned manner. Ordering can be done on any one of the coordinates or on droplet size. The ordering sets up the editing process by which the droplets are scrutinized to determine if they are unique or redundant.

Editing of a droplet to determine if it is unique; that is, a given droplet has not been counted more than once, was accomplished by applying a tolerance band to each of its position coordinates. The

tolerance bands on the coordinates are input items and can be varied as desired. The theory behind determining uniqueness by interrogating the positional coordinates is based on the fact that no more than one droplet can occupy the same position at a given time. The tolerance band applied to the spatial coordinates is an indication of how closely a reader of the hologram volume can focus on a droplet at its true position. Each droplet may undergo two editing cycles to determine if it is unique. The first edit interrogates the droplet data on the ordered coordinate. Those droplets which have the same ordered coordinate are subjected to a second interrogation on the other two coordinates. The editing process for determining uniqueness is biased by the first droplet of the set which has the same ordered coordinate. The two-edit method speeds up the scrutinizing process, since those droplets which passed the uniqueness test on the first edit are not interrogated during the second edit. The unique and redundant droplets are separated into two groups, the total of which must agree with the total droplet population. Subsequent droplet processing then is confined to the unique droplets.

The FR-471 program next determines the minimum and maximum drop size classes and positional coordinates for the volume occupied by the unique droplets. Each minimum and maximum positional coordinate does not necessarily belong to the same droplet.

The number of droplets in each class size is the next block of information output. This is frequency distribution information. Each class size number represents a droplet size interval. For example:

Class No.	Droplet Size (Microns)	
	Min.	Max.
1	0	20
2	20	40
•	•	•
•	•	•
•	•	•

The size interval used in this investigation was nominally 20 microns, since this was the expected resolution capability of the holographic recording system, and the circles on the Processor reticle wheel were sized accordingly.

Next, the program prepared the data to be used in the positional coordinate-droplet size plots. This is referred to as graph slice and can be performed on any one of the three positional coordinates. A spatial band width was applied to one of the positional coordinates, preferably to the ordered coordinate, since this facilitates operating on the data. The droplet data contained within the graph slice band, which is now assumed to be infinitely thin, is treated as two-dimensional data. Graphs plotting the other two coordinates as dependent and independent variables with drop size as the parameter can now be made using the PR-472 program. Coordinate slicing and the resulting plot are pictorially illustrated in Figure 28.

In order to organize the unique droplets so that one may analyze droplet distribution, areas of droplet concentration and trends of drop size and position, a method of subvolume griding was devised. The total volume occupied by the unique droplets, as determined by the minimum and maximum positional coordinates previously identified, is subsectioned

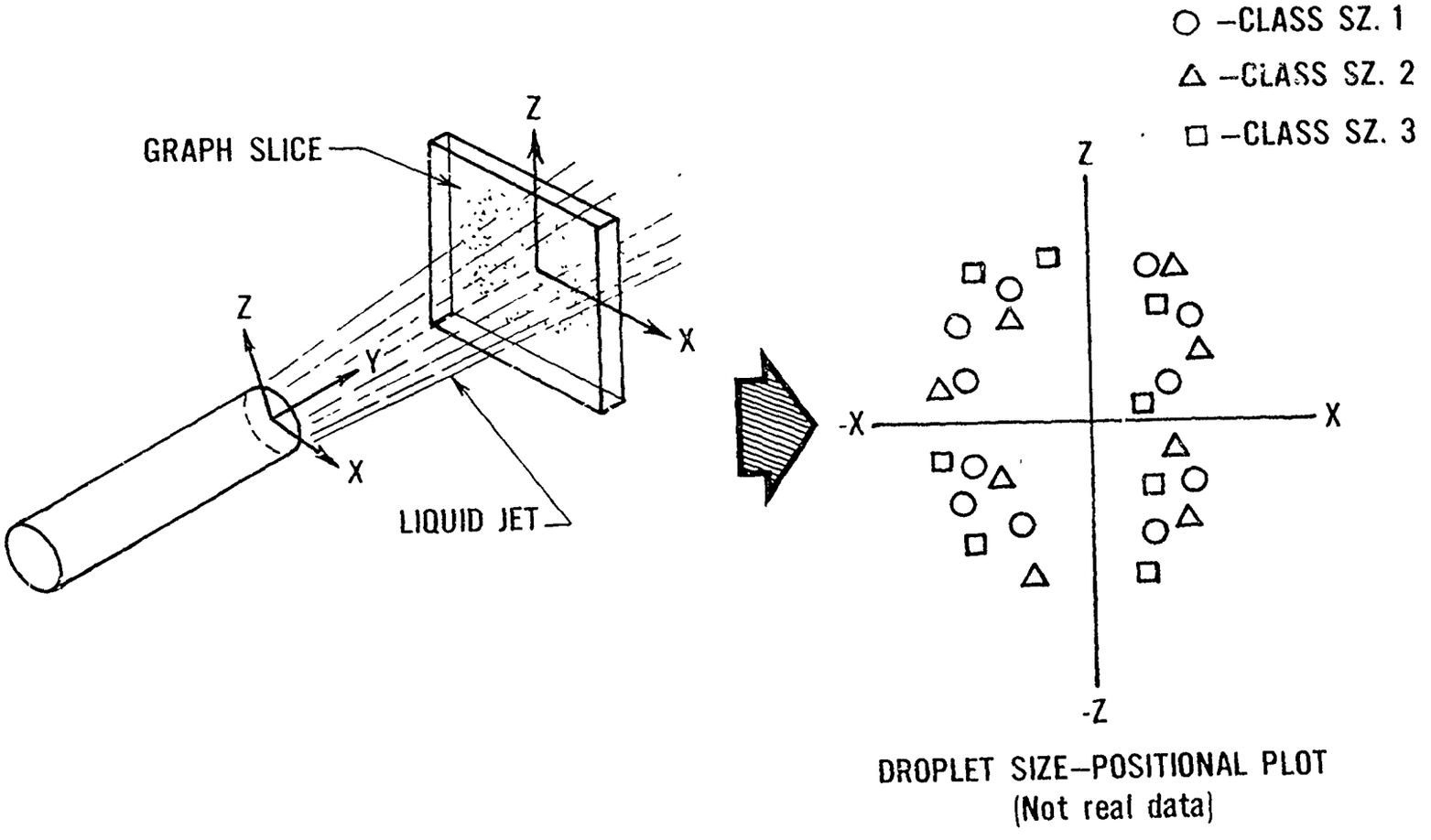

Figure 28. DROPLET CLASS SIZE-POSITIONAL PLOT

into a number of smaller volumes. If the number of grids in each coordinate is not specified, the program uses a default of 2 on the ordered coordinate (sometimes referred to as the pure variable), 5 and 4 on the independent and dependent variables, respectively. This gives 40 subvolumes. The number of grids along each axis is limited by the input format to 99 or a maximum number of subvolumes of 970,299. The program determines the number of droplets of each class size in each subvolume so that mass distribution can be calculated. The frequency distribution in each subvolume is output.

PR-471 has a number of options. One can elect whether or not to edit the data, prepare for a graph slice plot or subvolume the data. Another feature is that the total volume occupied by the unique droplets can be reduced, by so specifying the coordinates, and then perform the other operations on the reduced volume as if it were the total volume.

c. PR-472 Plot Program: This program is used to plot droplet positional data or droplet diameter distributions. That is, the program can supply two types of plots to obtain a visual representation of the droplet positional data and the distribution function data for the droplet diameters. The plots are made with a CalComp Plotter. The positional data to be plotted is obtained from PR-471, while the distribution function data is provided by the MM-203 program, which will be discussed below.

The positional data is plotted using two coordinates for a given drop size as shown in Figure 28. Up to 5 droplet class sizes can be plotted on each graph, with any number of droplets in each class size. As many graphs as desired can be made for a given set of data. The positional plots enable one to observe if the droplets are segregating

spatially according to size, such that contour lines can be drawn.

The data obtained from the MM-203 program is frequency information involving only the droplet diameters. The ordinate for the distribution plots can be any of these four: cumulative volume fraction, volume fraction derivative, droplet number (for frequency distribution) or number fraction derivative. The abscissa is droplet diameter. The raw droplet data along with the four distribution functions (Log-Probability, Upper-Limit, Nukiyama-Tanasawa and General Exponential) used to model the data are plotted on a given graph. That is, one curve will be the observed distribution of the droplet data versus diameter and the other four curves will be the predicted distributions from the various models versus diameter.

The program is designed to process data sorted in ascending order. The values must be sorted as follows: Each in ascending order, independent variable first, dependent variable second and class size or distribution function number third. Symbol or line plots can be made. Along with the main program are 15 subroutines, 9 of which are needed in the submittal deck, since the others are part of the computer system.

d. PR-473 Drop Size Tape Program: This program provides the input data, in the form of number of droplets in each class size, for the PR-429 program. The sorted (ordered) unique droplet data, size and positional coordinates, is accepted from the $IBSRT and PR-471 programs. The positional coordinate data is eliminated and number count for each class size, up to 48 classes, is retained. Any number of droplets can be read into any of the 48 classes. This frequency distribution data is output on a magnetic tape which is then available for future use.

e. PR-429 Spray Analysis Program: This program calculates the various mean droplet diameters used in characterizing sprays and in correlating with the physical and fluid parameters. These diameters are average diameter (D_{10}), surface mean (D_{20}), volume mean (D_{30}), Sauter mean (D_{32}), mass mean (D_{43}) and mass median (the diameter above or below which 50% of the spray mass lies). The general equation used in calculating the diameters, with the exception of the mass median diameter, is

$$D_{pq}^{p-q} = \frac{\sum n_i D_i^{\,p}}{\sum n_i D_i^{\,q}} \qquad (28)$$

where n_i = number count in each class size interval

D_i = mid-diameter in each size interval

The class size number (1 through 48 in ascending order), the corresponding minimum, mid and maximum droplet diameters for each class size and the number of droplets in each class size are output. Other distribution data, droplet number fraction below a given class size, volume fraction and cumulative volume fraction are also output.

Two distribution functions, Log-Probability and Upper-Limit, are calculated using a linear regression analysis. The linear regression analysis approach to modeling the data was found to be inadequate. However, the correlation coefficients which the program calculates for the two distribution functions are used as initial estimates for the non-linear regression analysis approach, which was adopted and will be discussed below. In addition to the correlation coefficients, the program also outputs D_{30}, D_{32} and the observed and predicted volume fraction derivative and cumulative volume fraction for each distribution function. This information, though, is no longer used.

The total program consists of a main and six FORTRAN subroutines. The program can accept either tape from PR-473, or punched card input. Two tapes are output by this program: one which contains the droplet count, mid-diameter and interval width for each class size to be used as input to the MM-203 Nonlinear Regression Analysis Program, and one which contains mid-diameter, volume fraction derivative for each class size and the distribution function number (for identification) to be used as input to the PR-472 Plot Program.

f. MM-203 Nonlinear Regression Analysis Program: This program is used to model the data obtained from PR-429 with various, selected distribution functions. The modeling is accomplished by estimating the correlation coefficients of the models. A nonlinear regression analysis method developed by Marquardt[69] is used to iteratively obtain the least squares estimates for the coefficients. Initial estimates are required for the coefficients.

Any number of models may be used, and operations on them can be performed sequentially. Four distribution functions were selected to model the data from this investigation: Log-Probability, Upper-Limit, Nukiyama-Tanasawa and General Exponential. Two types of models, 1) volume derivative, and 2) cumulative volume were used for each distribution function. Hence, each data set could be compared with as many as 8 models. The equations for all the models are presented in Appendix II according to their distribution functions. Included in each set are the equations for volume derivative, cumulative volume (which is the integral of the previous equation), D_{30} and D_{32} as obtained for each distribution function and the partial derivative for each model with respect to its coefficients.

The MM-203 program not only models the data and provides statistical information concerning the curve fits as printed output, but also produces output tapes for use in the PR-472 plot program. These tapes contain droplet size interval mid-diameter and observed and predicted volume fraction derivatives, and interval maximum diameter and observed and predicted cumulative volume fractions for each distribution.

The total program consists of a FORTRAN main program with thirteen FORTRAN subroutines and one MAP subroutine. The user must supply nine of the subroutines for each model; volume derivative and cumulative volume. The other subroutines are system-supplied. The logic for each model is the same. This program is a very strong tool for analyzing the droplet data. It has the capability of modeling the data with any number of expressions and provides the user with statistical information (F-ratio, per cent variation explained, calculated t-statistics, residuals and percentage of points exceeding 1, 2 or 3 sigma) so he can assess the relative merits of each model.

CHAPTER VI

EXPERIMENTAL RESULTS

1. Liquid Injection into a Supersonic Stream

As mentioned earlier, various liquids were injected perpendicularly through different orifices into a Mach 3 gaseous nitrogen stream. Liquid jet breakup data was sought: droplet size and distribution, jet wavelength and amplitude change. Droplet data was not retrievable in the high Mach number gas stream with the holographic recording equipment used. The reasons for this will be explained in the next chapter. The gas stream conditions, liquid type, liquid injection conditions and certain calculated parameters of interest are tabulated in Table VIII. The equations used to calculate the various parameters are presented in Appendix III. The physical properties of the injectants are presented in Table IX. These properties were obtained from Strobridge[70], International Critical Tables[71] and du Pont Technical Bulletins[72].

Jet amplitude and wavelength data were obtained from the holograms. This was accomplished by taking photographs of the flow fields which were observed when the holograms were reconstructed. These photographs are presented in Figures 29 to 41. One inch measured = 0.77 inches actual for all photographs. The photographs were enlarged to 8 x 10 inches to facilitate retrieval of the amplitude and wavelength information. Accuracy of measurement was also improved with photo enlargement. The manner in which the measurements were taken is shown in Figure 42. The Figure shows the jet as a straight line for explanation purposes. Actually the measurements were made along the natural curvature of the jet trajectory. The measurement procedure was as follows:

1) a line was drawn from the injection point outward along the jet trajectory such that the wave troughs were connected by this line;

2) a line was drawn through the crest of each wave and

TABLE VIIIa: LIQUID INJECTION INTO A SUPERSONIC STREAM

LIQUID PARAMETERS

TEST NO.	LIQUID TYPE	ORIF. SIZE (IN.)	DIS-CHARGE COEFF. C_d	$C_d^{\frac{1}{2}} D_o$	INJ. PRESS. (PSIG)	INJ. VEL. (FPS)	LIQ. FLOW (LB/SEC)	Re, $\frac{\rho_l V_l D_o}{\mu_l}$
DR-2	H_2O	.050	.785	.044	980	300	.275	137,830
DR-3	H_2O	.050	.785	.044	980	300	.274	177,739
DR-4	H_2O	.050	.785	.044	967	300	.275	155,240
DR-5	H_2O	.050	.785	.044	489	215	.198	114,521
DR-8	H_2O	.050	.785	.044	1450	365	.333	210,955
DR-10	H_2O	.042	.685	.035	1510	319	.191	121,466
DR-11	H_2O	.042	.685	.035	1472	318	.190	121,598
DR-12	H_2O	.042	.685	.035	1426	313	.188	118,198
DR-13	H_2O	.062	.719	.053	1166	299	.396	190,024
DR-14	H_2O	.062	.719	.053	1135	298	.393	220,051
DR-15	H_2O	.062	.719	.053	1212	307	.406	226,183
DR-17	H_2O	.062	.719	.053	567	209	.277	130,811
DR-19	H_2O	.042	.685	.035	1482	330	.197	146,250
DR-20	H_2O	.042	.685	.035	735	233	.139	102,369
DR-22	H_2O	.042	.685	.035	747	237	.142	105,896
DR-23	TRICH	.050	.845	.046	506	194	.238	2,117
DR-24	TRICH	.050	.845	.046	739	232	.284	2,507
DR-25	TRICH	.050	.845	.046	1476	326	.398	3,600
DR-26	TRICH	.050	.845	.046	735	232	.284	2,552
DR-27	FREON 113	.050	.83	.046	1473	310	.415	311,774
DR-28	FREON 113	.050	.83	.046	978	254	.337	250,093
DR-29	METHANOL	.050	.85	.046	1433	445	.297	272,429
DR-30	METHANOL	.050	.85	.046	967	364	.242	227,440
DR-31	H_2O/PHOTOFLO *	.050	.84	.046	959	324	.276	149,050
DR-32	H_2O/PHOTOFLO	.050	.84	.046	1447	398	.339	182,819

*H_2O/Photoflo ratio 20:1 by volume.

TABLE VIIIb: LIQUID INJECTION INTO A SUPERSONIC STREAM

GAS PARAMETERS

TEST NO.	TOTAL PRESS. (PSIA)	STAT. PRESS. (PSIA)	TOTAL TEMP. (^{o}R)	STAT. TEMP. (^{o}R)	k	MACH NO.	GAS VEL. (FPS)	GAS FLOW (LB/SEC)	We, $\frac{\rho_g v_g^2 D_o}{\sigma}$
DR-2	216	5.95	504	171	1.431	3.01	1982	10.77	9,587
DR-3	126	3.47	515	179	1.417	3.00	2012	6.18	5,645
DR-4	305	8.36	509	169	1.443	3.02	1982	15.1	13,973
DR-5	108	3.00	511	179	1.417	2.99	2006	5.3	4,835
DR-8	128	3.53	520	181	1.416	3.00	2022	6.23	5,740
DR-10	121	3.33	505	176	1.417	3.00	1992	5.97	4,371
DR-11	230	6.32	508	171	1.433	3.01	1986	11.4	8,451
DR-12	254	6.97	518	174	1.435	3.01	2005	12.5	9,347
DR-13	119	3.28	519	181	1.416	3.00	2021	5.8	6,425
DR-14	212	5.84	513	174	1.430	3.01	1998	10.5	11,578
DR-15	309	8.48	523	174	1.442	3.02	2010	15.1	17,072
DR-17	120	3.31	516	180	1.416	3.00	2015	5.9	6,436
DR-19	111	3.08	526	184	1.414	3.00	2035	5.4	4,018
DR-20	126	3.49	502	174	1.418	3.00	1985	6.25	4,576
DR-22	312	8.57	515	170	1.443	3.02	1993	15.4	11,588
DR-23	119	3.31	508	177	1.417	3.00	1998	5.9	13,295
DR-24	123	3.43	485	168	1.420	3.00	1947	6.2	13,671
DR-25	111	3.10	527	185	1.414	2.99	2035	5.4	12,384
DR-26	118	3.30	526	184	1.415	2.99	2033	5.7	13,164
DR-27	128	3.52	521	181	1.417	3.00	2025	6.3	22,391
DR-28	120	3.33	515	179	1.416	3.00	2012	5.9	20,911
DR-29	125	3.44	520	181	1.416	3.00	2022	6.1	17,819
DR-30	110	3.07	520	182	1.414	2.99	2023	5.4	15,950
DR-31	113	3.11	512	179	1.415	3.00	2008	5.5	11,350
DR-32	114	3.15	499	174	1.417	3.00	1980	5.7	11,471

TABLE VIIIc: LIQUID INJECTION INTO A SUPERSONIC STREAM

LIQUID-GAS PARAMETERS

TEST NO.	VEL. RATIO V_g/V_l	MOM. RATIO $W_g V_g/W_l V_l$	$\bar{q}$ $\rho_l V_l^2/RPM^2(144g)$
DR-2	6.6	258	15.7
DR-3	6.72	151	27.2
DR-4	6.6	364	11.0
DR-5	9.3	250	16.4
DR-8	5.5	103	39.6
DR-10	6.25	195	32.0
DR-11	6.24	373	16.6
DR-12	6.4	425	14.5
DR-13	6.8	100	28.6
DR-14	6.7	179	15.7
DR-15	6.5	243	11.4
DR-17	9.6	203	14.0
DR-19	6.2	168	37.3
DR-20	8.5	384	16.4
DR-22	8.4	914	6.7
DR-23	10.3	255	17.4
DR-24	8.4	184	23.9
DR-25	6.3	84	52.5
DR-26	8.7	175	25.0
DR-27	6.5	98	45.5
DR-28	7.9	139	32.0
DR-29	4.5	93	47.7
DR-30	5.6	124	35.9
DR-31	6.2	124	35.8
DR-32	5.0	83	53.2

TABLE IX: INJECTANT PHYSICAL PROPERTIES

INJECTANT	DENSITY (LB/FT^3)	ABSOLUTE VISCOSITY (LB/FT-SEC)	KINEMATIC VISCOSITY (FT^2/SEC)	SURFACE TENSION (LB/FT)
H_2O	62.2	$5x10^{-4}$	$8.1x10^{-6}$	.0049
TRICH	89.6	$7.1x10^{-3}$	$8x10^{-5}$	.0019
FREON 113	97.6	$4x10^{-4}$	$4.1x10^{-6}$	.0012
METHANOL	48.9	$3.3x10^{-4}$	$6.7x10^{-5}$	.0015
H_2O/PHOTOFLO	62.4	$5.7x10^{-4}$	$9.1x10^{-6}$	.0021

TEST NO.	DR-2
INJECTANT	H_2O
ORIFICE DIA.	.050"
INJ. VEL.	300fps
$\bar{q}$	15.7

TEST NO.	DR-3
INJECTANT	H_2O
ORIFICE DIA.	.050"
INJ. VEL.	300fps
$\bar{q}$	27.2

Figure 29. Liquid Injection into Supersonic Stream, Tests DR-2 and DR-3.

TEST NO.	DR-4
INJECTANT	H_2O
ORIFICE DIA.	.050"
INJ. VEL.	300fps
$\bar{q}$	11.0

TEST NO.	DR-5
INJECTANT	H_2O
ORIFICE DIA.	.050"
INJ. VEL.	215fps
$\bar{q}$	16.4

Figure 30. Liquid Injection into Supersonic Stream, Tests DR-4 and DR-5.

TEST NO.	DR-8
INJECTANT	H_2O
ORIFICE DIA.	.050"
INJ. VEL.	365fps
$\bar{q}$	39.6

TEST NO.	DR-10
INJECTANT	H_2O
ORIFICE DIA.	.042"
INJ. VEL.	319fps
$\bar{q}$	32.0

Figure 31. Liquid Injection into Supersonic Stream, Tests DR-8 and DR-10.

TEST NO.	DR-11
INJECTANT	H_2O
ORIFICE DIA.	.042"
INJ. VEL.	318fps
$\bar{q}$	16.6

TEST NO.	DR-12
INJECTANT	H_2O
ORIFICE DIA.	.042"
INJ. VEL.	313fps
$\bar{q}$	14.5

Figure 32. Liquid Injection into Supersonic Stream, Tests DR-11 and DR-12.

TEST NO.	DR-13
INJECTANT	H_2O
ORIFICE DIA.	.062"
INJ. VEL.	299fps
$\bar{q}$	28.6

TEST NO.	DR-14
INJECTANT	H_2O
ORIFICE DIA.	.062"
INJ. VEL.	298fps
$\bar{q}$	15.7

Figure 33. Liquid Injection into Supersonic Stream, Tests DR-13 and DR-14.

TEST NO.	DR-15
INJECTANT	H_2O
ORIFICE DIA.	.062"
INJ. VEL.	307fps
$\bar{q}$	11.4

TEST NO.	DR-17
INJECTANT	H_2O
ORIFICE DIA.	.062"
INJ. VEL.	209fps
$\bar{q}$	14.0

Figure 34. Liquid Injection into Supersonic Stream, Tests DR-15 and DR-17.

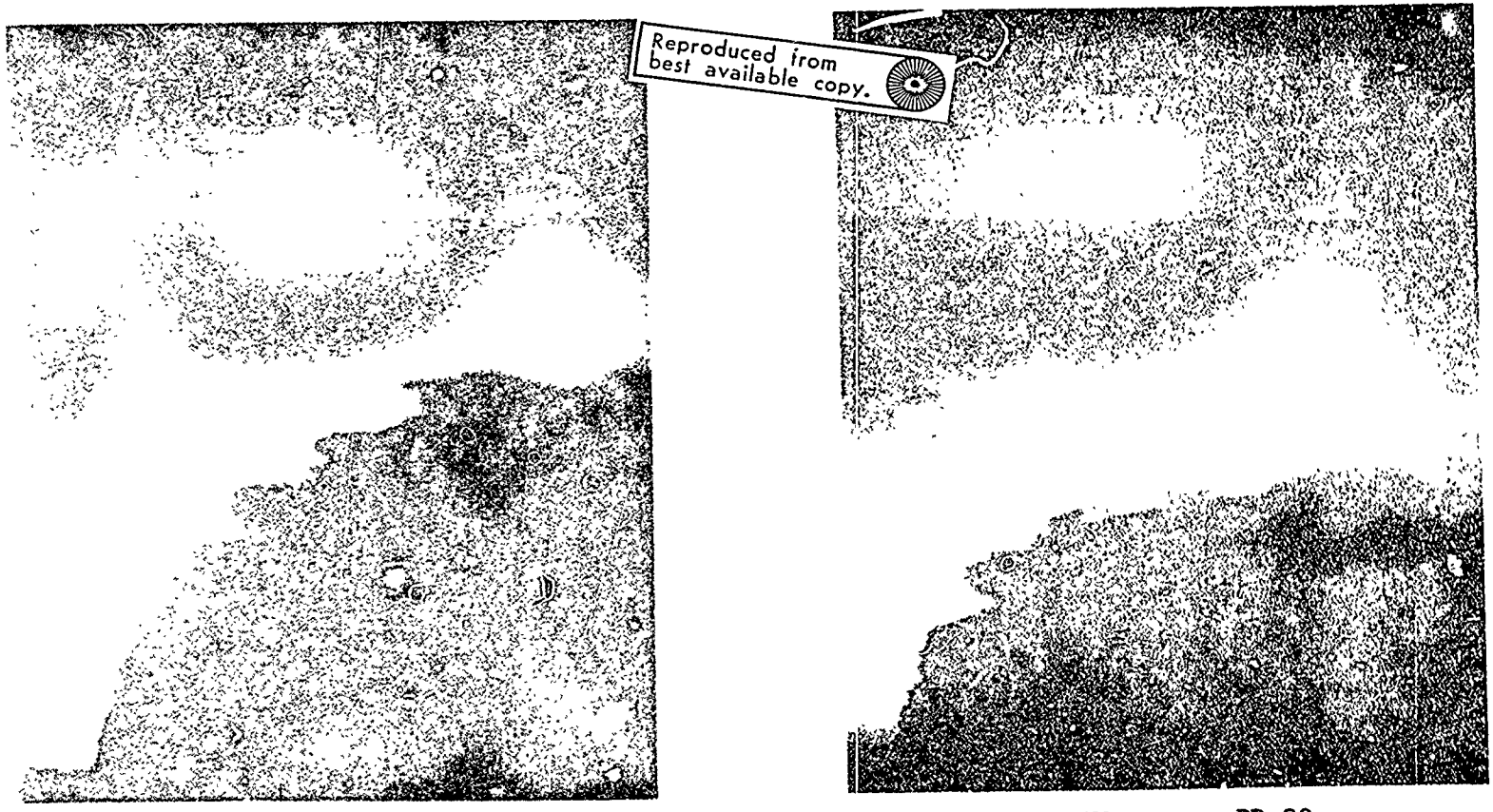

TEST NO.	DR-19
INJECTANT	H_2O
ORIFICE DIA.	.042"
INJ. VEL.	330fps
$\bar{q}$	37.3

TEST NO.	DR-20
INJECTANT	H_2O
ORIFICE DIA.	.042"
INJ. VEL.	233fps
$\bar{q}$	16.4

Figure 35. Liquid Injection into Supersonic Stream, Tests DR-19 and DR-20.

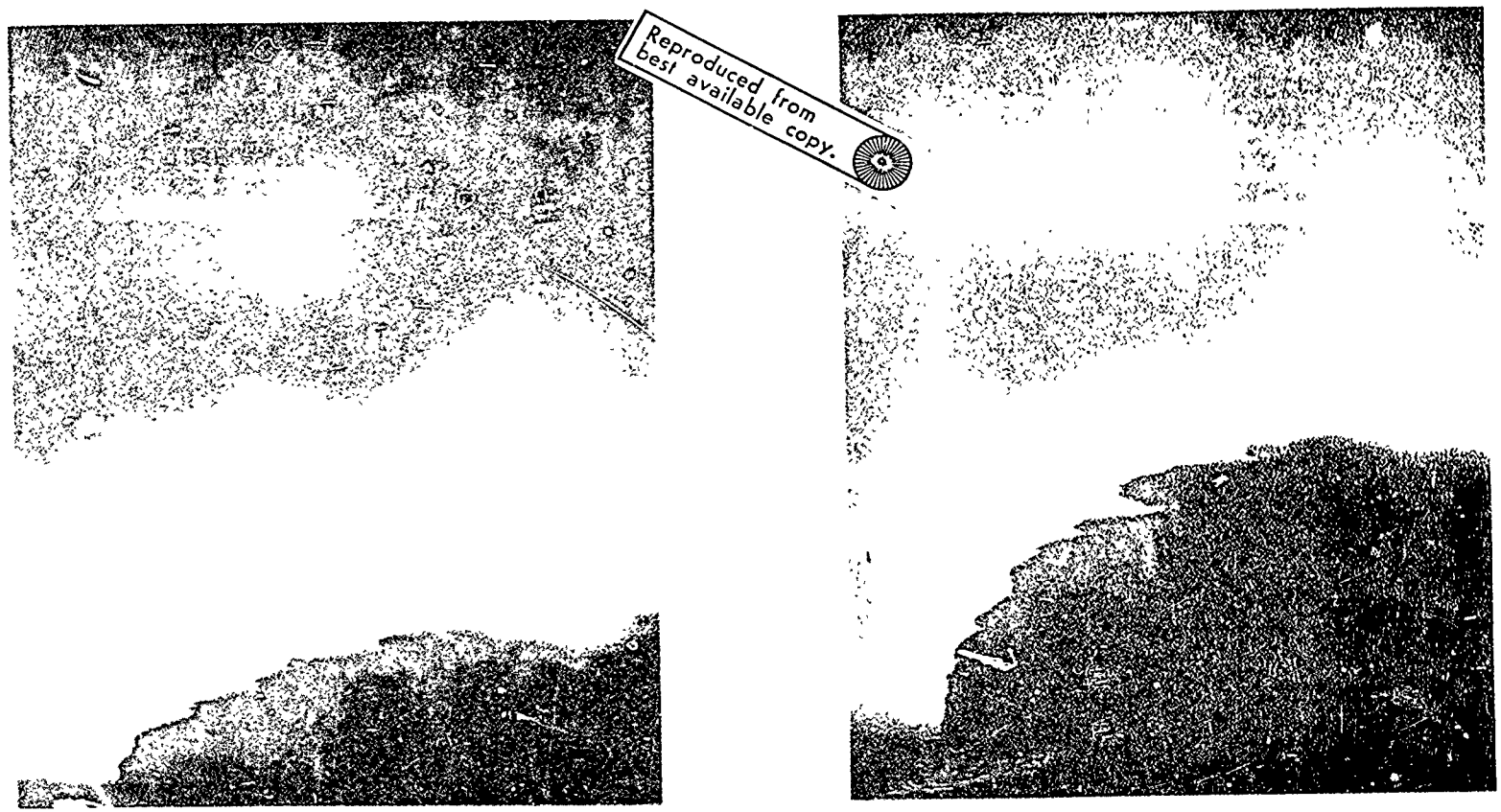

TEST NO.	DR-22
INJECTANT	H_2O
ORIFICE DIA.	.042"
INJ. VEL.	237fps
$\bar{q}$	6.7

TEST NO.	DR-23
INJECTANT	TRICH
ORIFICE DIA.	.050"
INJ. VEL.	194fps
$\bar{q}$	17.4

Figure 36. Liquid Injection into Supersonic Stream, Tests DR-22 and DR-23.

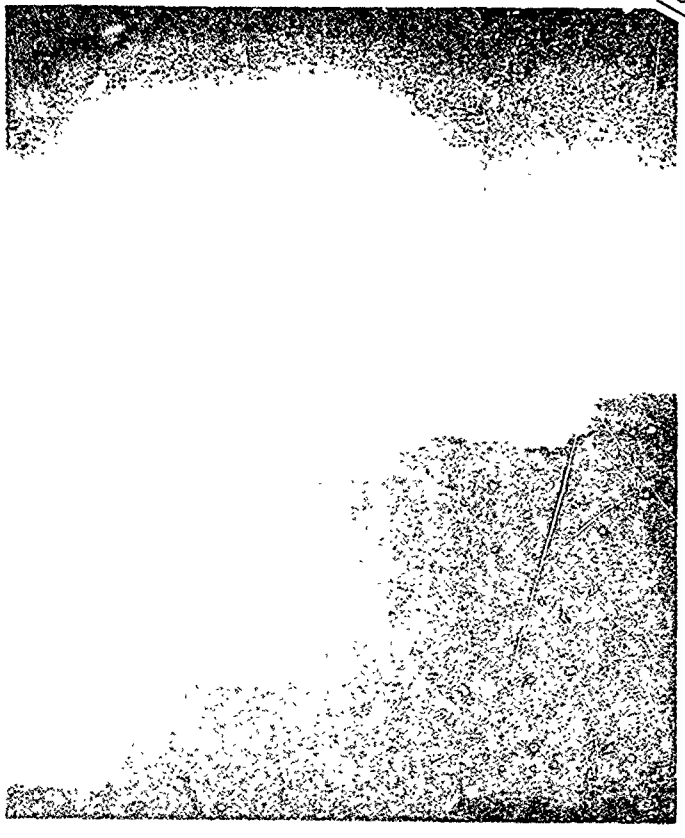

TEST NO.	DR-24
INJECTANT	TRICH
ORIFICE DIA.	.050"
INJ. VEL.	232fps
$\bar{q}$	23.9

TEST NO.	DR-25
INJECTANT	TRICH
ORIFICE DIA.	.050"
INJ. VEL.	326fps
$\bar{q}$	52.5

Figure 37. Liquid Injection into Supersonic Stream, Tests DR-24 and DR-25.

TEST NO.	DR-26
INJECTANT	TRICH
ORIFICE DIA.	.050"
INJ. VEL.	232fps
$\bar{q}$	25.0

TEST NO.	DR-27
INJECTANT	FREON 113
ORIFICE DIA.	.050"
INJ. VEL.	310fps
$\bar{q}$	45.5

Figure 38. Liquid Injection into Supersonic Stream, Tests DR-26 and DR-27.

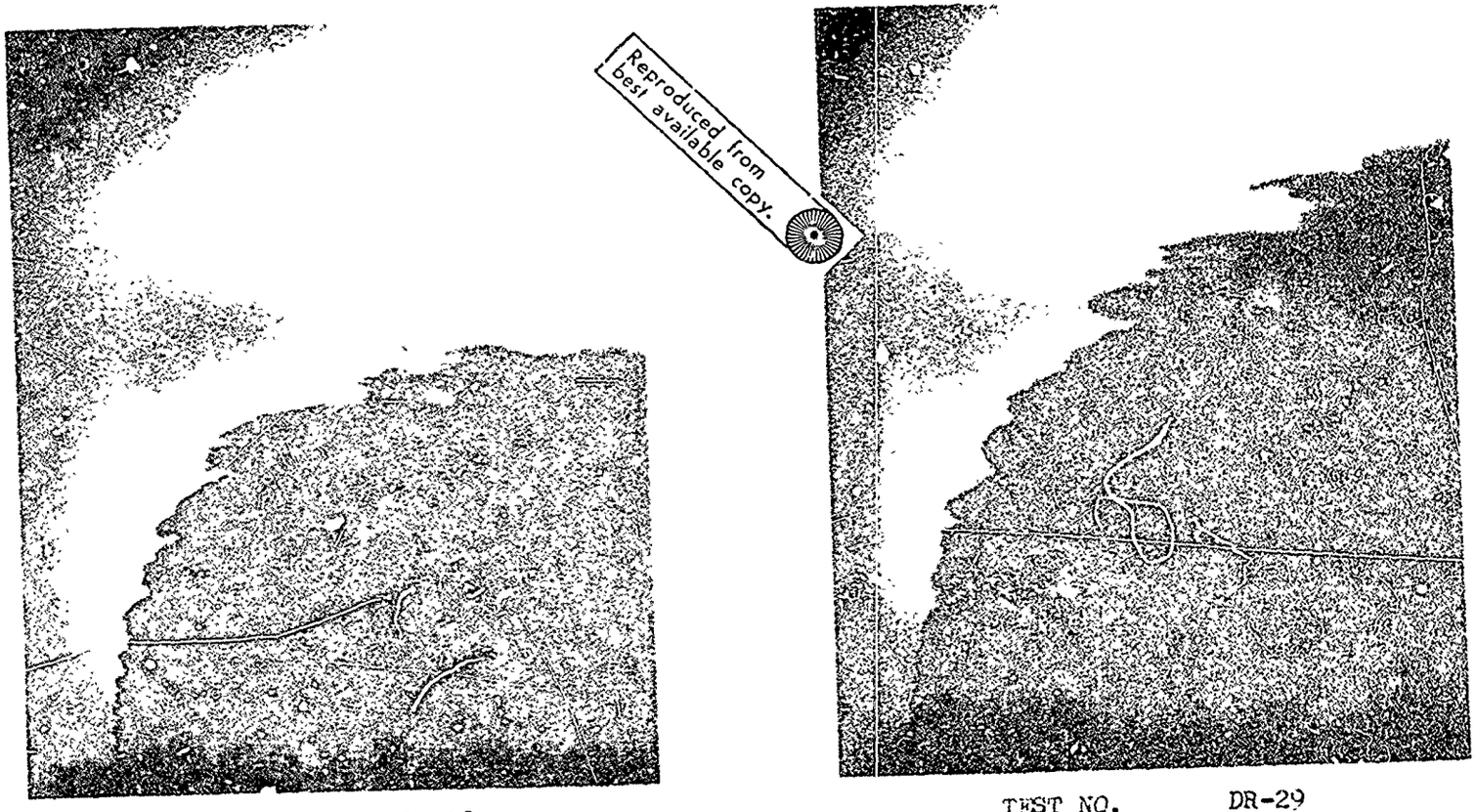

TEST NC.	DR-28
INJECTANT	FREON 113
ORIFICE DIA.	.050"
INJ. VEL.	254fps
$\bar{q}$	32.0

TEST NO.	DR-29
INJECTANT	METHANOL
ORIFICE DIA.	.050"
INJ. VEL.	445fps
$\bar{q}$	47.9

Figure 39. Liquid Injection into Supersonic Stream, Tests DR-28 and DR-29.

TEST NO.	DR-30
INJECTANT	METHANOL
ORIFICE DIA.	.050"
INJ. VEL.	364fps
$\bar{q}$	35.9

TEST NO.	DR-31
INJECTANT	H_2O/PHOTOFLO
ORIFICE DIA.	.050"
INJ. VEL.	324fps
$\bar{q}$	35.8

Figure 40. Liquid Injection into Supersonic Stream, Tests DR-30 and DR-31.

TEST NO.	DR-32
INJECTANT	H_2O/PHOTOFLO
ORIFICE DIA.	.050"
INJ. VEL.	398fps
$\bar{q}$	53.2

Figure 41. Liquid Injection into Supersonic Stream, Test DR-32.

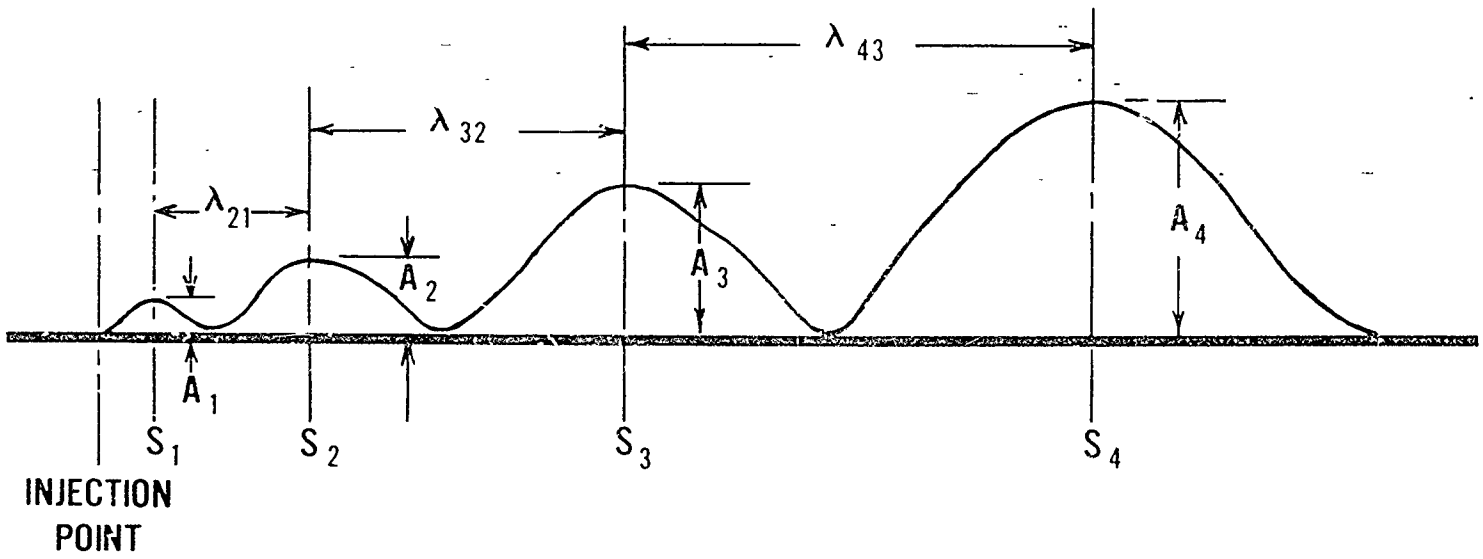

Figure 42. JET AM.. ITUDE & WAVELENGTH DATA RETRIEVAL METHOD

oriented to perpendicularly intersect the wave trough connecting line;

3) distance from the injection point to the intersection of each crest and trough connecting lines were measured with a map tracing instrument accurate to 0.01 inches. These distances were designated $S_1, S_2, \cdots S_n$. The corresponding amplitudes $A_1, A_2, \cdots A_n$ were obtained by measuring the line drawn from the crest of each wave to the intersection point with the trough line;

4) the true measurements were determined by dividing the S's and A's by the magnification factor (2.6). The resulting values were then nondimensionalized by the appropriate $C_d^{1/2}D_o$ for a given test; and

5) the wavelengths were obtained by taking the difference between two adjacent S's

$$\lambda_{n,\,n-1} = S_n - S_{n-1} \qquad (29)$$

The distance from the injection point at which the wavelength was assumed to "occur" was the mid-distance between the corresponding S's.

$$S_{n,n-1} = S_{n-1} + \frac{\lambda_{n,\,n-1}}{2} \qquad (30)$$

The nondimensionalized amplitude and wavelength data are presented in Tables X and XI, respectively. Their corresponding dimensionless distance from the injection point, dynamic pressure ratio, test number and injectant type are also presented.

2. Liquid Injection into Still Air

Droplet data, size and spatial coordinates, was obtained from a liquid (water) jet injected into quiescent, atmospheric air. The data was taken at two axial regions in the spray. These regions were nominally 3.0 - 3.5 and 3.5 - 4.0 inches from the injection plane. The

TABLE X: LIQUID JET AMPLITUDE DATA

DATA POINT	TEST NO.	LIQUID TYPE	AMPLITUDE $A/C_d^{1/2}D_o$	DISTANCE $S/C_d^{1/2}D_o$	DYN. PRESS. RATIO, q
1	DR-2	H_2O	1.32	3.93	15.7
2	"		1.93	10.50	15.7
3	"		3.23	21.07	15.7
4	DR-3		.43	6.11	27.2
5	"		.80	10.32	27.2
6	"		1.05	13.98	27.2
7	"		1.57	19.23	27.2
8	"		2.98	26.23	27.2
9	"		6.02	54.11	27.2
10	DR-4		.71	4.21	11.0
11	"		.89	8.05	11.0
12	"		2.27	15.05	11.0
13	"		2.36	26.75	11.0
14	DR-5		1.23	8.75	16.4
15	"		1.84	21.16	16.4
16	DR-8		.27	2.46	39.6
17	"		.34	5.25	39.6
18	"		.34	7.52	39.6
19	"		.43	12.16	39.6
20	"		.61	17.66	39.6
21	"		.89	22.64	39.6
22	"		1.84	30.07	39.6
23	"		3.32	44.66	39.6
24	DR-10		.89	3.51	32.0
25	"		.89	10.11	32.0
26	"		2.09	16.26	32.0
27	"		3.74	39.57	32.0
28	"		7.49	72.31	32.0
29	DR-11		.43	2.20	16.6
30	"		.43	8.26	16.6
31	"		1.77	16.26	16.6
32	"		3.09	25.49	16.6
33	DR-12		.77	5.29	14.5
34	"		1.11	12.09	14.5
35	"		5.71	25.17	14.5
36	DR-13		.43	3.85	28.6
37	"		.51	9.43	28.6
38	"		1.02	13.79	28.6
39	"		1.45	19.23	28.6
40	"		2.11	25.62	28.6
41	"		2.32	34.83	28.6

TABLE X: LIQUID JET AMPLITUDE DATA, continued

DATA POINT	TEST NO.	LIQUID TYPE	AMPLITUDE $A/C_d^{1/2}D_o$	DISTANCE $S/C_d^{1/2}D_o$	DYN. PRESS. RATIO, q
42	DR-14	H_2O	.51	1.81	15.7
43	"		.59	4.51	15.7
44	"		1.53	12.34	15.7
45	"		8.34	58.92	15.7
46	DR-15		.79	2.32	11.4
47	"		1.02	6.83	11.4
48	"		5.23	32.00	11.4
49	DR-17		.51	3.49	14.0
50	"		.66	10.17	14.0
51	"		1.23	19.45	14.0
52	"		3.06	31.21	14.0
53	DR-19		.54	4.63	37.3
54	"		1.00	14.51	37.3
55	"		2.31	26.37	37.3
56	"		4.40	43.40	37.3
57	DR-20		.77	2.51	16.4
58	"		.66	5.83	16.4
59	"		2.63	12.63	16.4
60	DR-22		.77	1.31	6.7
61	"		1.66	5.83	6.7
62	"		4.06	28.14	6.7
63	DR-23	TRICH	.33	4.35	17.4
64	"		.76	6.61	17.4
65	"		1.17	9.61	17.4
66	"		1.50	13.46	17.4
67	"		2.26	19.57	17.4
68	"		4.85	31.94	17.4
69	DR-24		.33	1.50	23.9
70	"		.59	6.70	23.9
71	"		1.09	12.04	23.9
72	"		1.00	16.57	23.9
73	DR-25		.33	8.37	52.5
74	"		.50	12.87	52.5
75	"		.85	18.30	52.5
76	"		1.35	24.91	52.5
77	"		3.26	33.61	52.5
78	"		4.35	48.33	52.5
79	DR-26		.85	4.02	25.0
80	"		.85	9.87	25.0
81	"		1.85	13.72	25.0
82	"		2.50	20.83	25.0
83	"		3.67	30.70	25.0

TABLE X: LIQUID JET AMPLITUDE DATA, continued

DATA POINT	TEST NO.	LIQUID TYPE	AMPLITUDE $A/C_d^{1/2}D_o$	DISTANCE $S/C_d^{1/2}D_o$	DYN. PRESS. RATIO, $\bar{q}$
84	DR-27	FREON 113	.17	4.35	45.5
85	"		.33	7.37	45.5
86	"		.76	12.04	45.5
87	"		.67	18.07	45.5
88	"		.91	23.74	45.5
89	"		1.85	31.11	45.5
90	"		3.85	41.80	45.5
91	DR-28		.59	4.11	32.0
92	"		.91	8.37	32.0
93	"		1.26	13.54	32.0
94	"		1.85	17.39	32.0
95	"		2.00	23.74	32.0
96	"		2.94	28.43	32.0
97	"		3.67	39.98	32.0
98	DR-29	METHANOL	.33	2.94	47.9
99	"		.67	9.61	47.9
100	"		2.67	24.50	47.9
101	"		2.94	35.11	47.9
102	"		6.28	63.54	47.9
103	DR-30		.26	6.61	35.9
104	"		.50	18.98	35.9
105	"		1.76	32.28	35.9
106	"		5.70	60.87	35.9
107	DR-31	PHOTOFLO/H_2O	.41	4.02	35.8
108	"		1.35	10.87	35.8
109	"		1.59	15.13	35.8
110	"		2.00	20.07	35.8
111	"		2.26	25.00	35.8
112	DR-32		.50	3.85	53.2
113	"		.59	10.28	53.2
114	"		.33	14.63	53.2
115	"		.85	20.33	53.2
116	"		2.17	30.44	53.2
117	"		3.17	44.98	53.2

TABLE XI: LIQUID JET WAVELENGTH DATA

DATA POINT	TEST NO.	LIQUID TYPE	WAVELENGTH $\lambda/C_d^{1/2}D_o$	DISTANCE $s/C_d^{1/2}D_o$	DYN. PRESS. RATIO, $\bar{q}$
1	DR-2	H_2O	6.57	7.22	15.7
2	"		10.57	15.79	15.7
3	DR-3		4.21	8.22	27.2
4	"		3.66	12.15	27.2
5	"		5.25	16.61	27.2
6	"		7.00	22.73	27.2
7	"		27.88	40.17	27.2
8	DR-4		3.84	6.13	11.0
9	"		7.00	11.55	11.0
10	"		11.70	20.90	11.0
11	DR-5		12.41	14.96	16.4
12	DR-8		2.79	3.86	39.6
13	"		2.27	6.39	39.6
14	"		4.64	9.84	39.6
15	"		5.50	14.91	39.6
16	"		4.98	20.15	39.6
17	"		7.43	26.36	39.6
18	"		14.59	37.37	39.6
19	DR-10		6.60	6.81	32.0
20	"		6.15	13.19	32.0
21	"		23.31	27.92	32.0
22	"		32.74	55.94	32.0
23	DR-11		6.06	5.23	16.6
24	"		8.00	12.26	16.6
25	"		9.23	20.88	16.6
26	DR-12		6.80	8.69	14.5
27	"		13.08	18.63	14.5
28	DR-13		5.58	6.64	28.6
29	"		4.36	11.61	28.6
30	"		5.44	16.51	28.6
31	"		6.39	22.43	28.6
32	"		9.21	30.23	28.6
33	DR-14		2.70	3.16	15.7
34	"		7.83	8.43	15.7
35	"		46.58	35.63	15.7
36	DR-15		4.51	4.58	11.4
37	"		25.17	19.42	11.4
38	DR-17		6.68	6.83	14.0
39	"		9.28	14.81	14.0
40	"		11.76	25.33	14.0
41	DR-19		9.88	9.57	37.3
42	"		11.86	20.44	37.3
43	"		17.03	34.89	37.3
44	DR-20		3.32	4.17	16.4
45	"		6.80	9.23	16.4
46	DR-22		4.52	3.57	6.7
47	"		22.31	16.99	6.7

TABLE XI: LIQUID JET WAVELENGTH DATA, continued

DATA POINT	TEST NO.	LIQUID TYPE	WAVELENGTH $\lambda/C_d^{1/2}D_o$	DISTANCE $s/C_d^{1/2}D_o$	DYN. PRESS. RATIO, q
48	DR-23	TRICH	2.26	5.48	17.4
49	"		3.00	8.11	17.4
50	"		3.85	11.54	17.4
51	"		6.11	16.52	17.4
52	"		12.37	25.76	17.4
53	DR-24		5.20	4.10	23.9
54	"		5.34	9.37	23.9
55	"		4.53	14.31	23.9
56	DR-25		5.02	5.86	52.5
57	"		4.50	10.62	52.5
58	"		5.43	15.59	52.5
59	"		6.61	21.61	52.5
60	"		8.70	29.26	52.5
61	"		14.72	40.97	52.5
62	DR-26		5.85	6.95	25.0
63	"		3.85	11.80	25.0
64	"		7.11	17.28	25.0
65	"		9.87	25.77	25.0
66	DR-27	FREON 113	3.02	5.86	45.5
67	"		4.67	9.71	45.5
68	"		6.03	15.06	45.5
69	"		5.67	20.91	45.5
70	"		7.37	27.43	45.5
71	"		10.69	36.46	45.5
72	DR-28		4.26	6.24	32.0
73	"		5.17	10.96	32.0
74	"		3.85	15.47	32.0
75	"		6.35	20.57	32.0
76	"		4.69	26.09	32.0
77	"		11.55	34.21	32.0
78	DR-29	METHANOL	6.67	6.28	47.9
79	"		14.89	17.06	47.9
80	"		10.61	29.81	47.9
81	"		28.43	49.33	47.9
82	DR-30		12.37	12.80	35.9
83	"		13.30	25.63	35.9
84	"		28.59	46.58	35.9
85	DR-31	PHOTOFLO/H_2O	6.85	7.45	35.8
86	"		4.26	13.00	35.8
87	"		4.94	17.60	35.8
88	"		4.93	22.54	35.8
89	DR-32		6.43	7.07	53.2
90	"		4.35	12.46	53.2
91	"		5.70	17.48	53.2
92	"		10.11	25.39	53.2
93	"		14.54	37.71	53.2

injection conditions and data slice locations are shown in Figure 43. A photograph of the actual spray is shown in Figure 44. The size and spatial coordinates for each droplet in the two axial regions are presented in Tables XII and XIII. The true longitudinal positions of the droplets in the 3.0 - 3.5 inch slice are obtained by adding 3 inches to the y-coordinate, since this was not done in the computer program. The numbers in the size columns identify the size intervals in which the droplets belong. For example, 3 indicates the nominal class size 40-60 microns, 4 indicates class size 60-80 microns, etc. The corresponding physical sizes for all the class numbers are given in Table XIV along with the interval mid-diameters and droplet count in each interval (class size) for both axial slices. The droplet number fraction, cumulative volume fraction (below a given class size) and volume fraction for the two axial regions are presented in Tables XV and XVI. The various mean diameters and total droplet count for both axial regions are given in Table XVII. These data were operated on to characterize the spray in terms of droplet spatial and size distribution. How this characterization was accomplished and a discussion of the results are presented in the next Chapter.

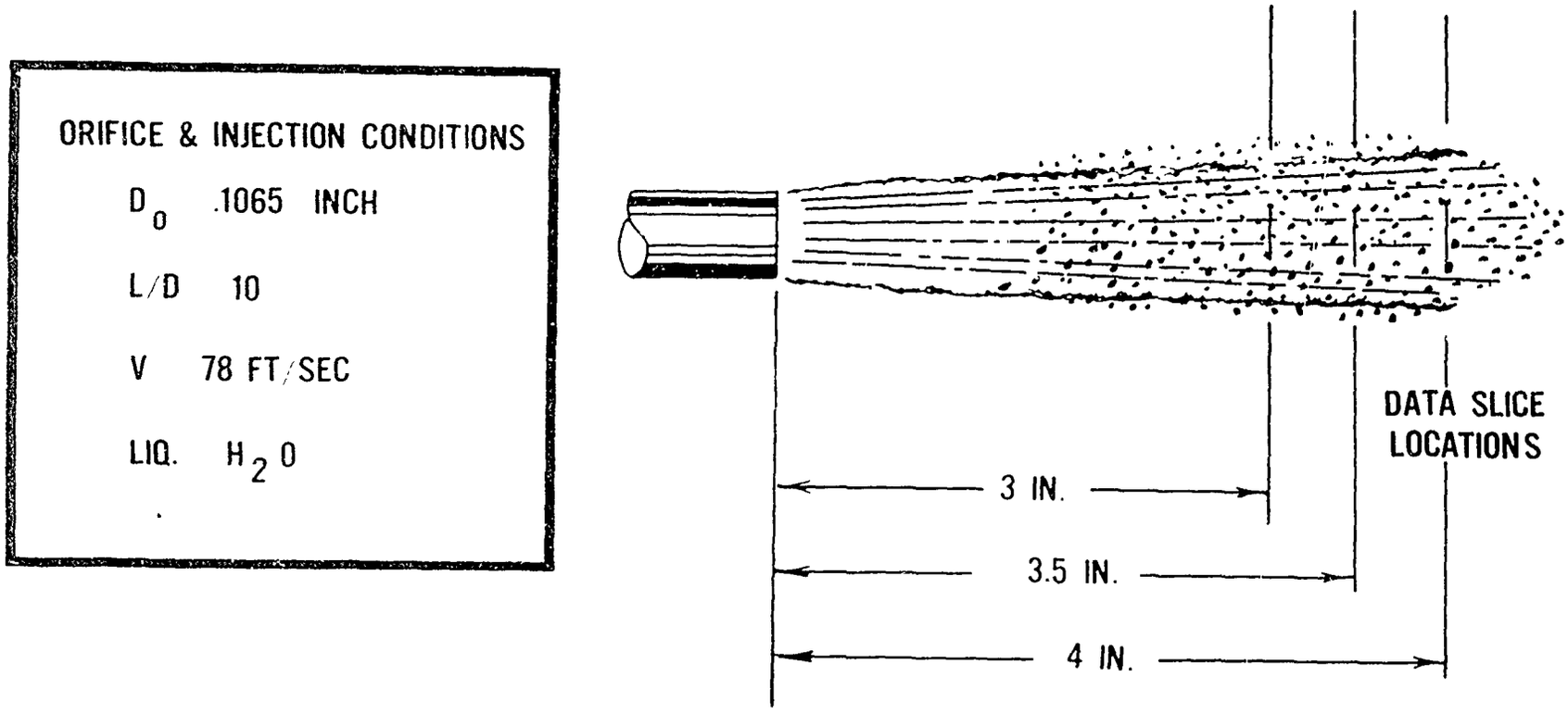

Figure 43. LIQUID JET INJECTION INTO STILL, ATMOSPHERIC AIR

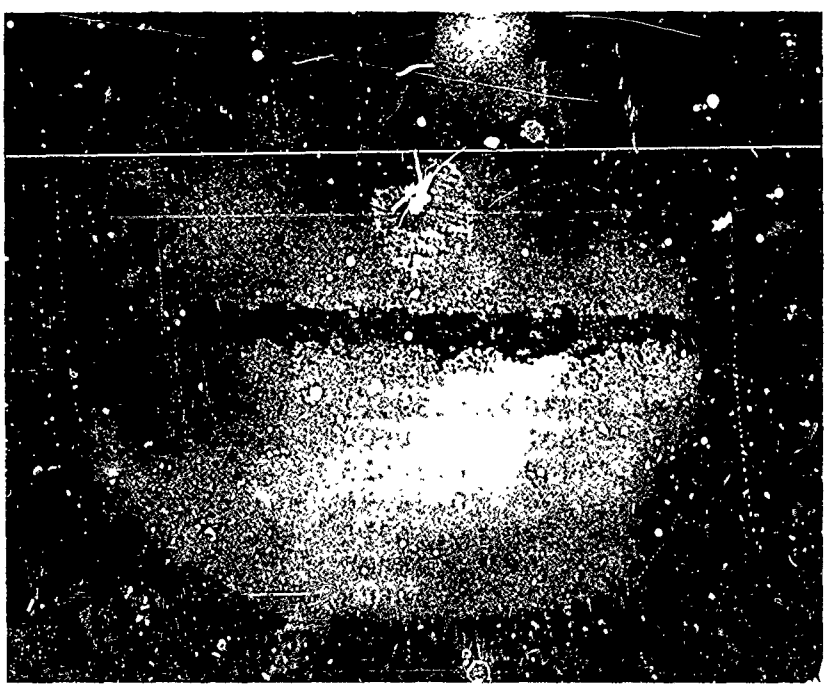

Figure 44. Liquid Jet Injected into Quiescent, Atmospheric Air.

TABLE XII: DROPLET SIZE AND SPATIAL COORDINATES, SLICE 1

AXIAL SLICE 3.0-3.5 INCHES

X	Y	Z	SIZE
-0.21222	0.04926	-0.17901	3.
-0.33420	0.14278	-0.17134	4.
-0.30187	0.25647	-0.23056	4.
-0.20912	0.37610	0.44009	4.
-0.29696	0.13146	-0.16545	5.
-0.26800	0.48412	0.27107	5.
-0.26058	0.17260	-0.18687	5.
-0.21990	-0.00549	-0.15050	5.
-0.15163	0.27669	-0.01557	5.
0.16964	0.17634	-0.18883	5.
-0.32980	0.27452	-0.23996	6.
-0.31549	0.15564	-0.06528	6.
-0.25627	0.19593	-0.14264	6.
0.21533	0.12307	-0.49937	6.
0.27179	0.32592	-0.09759	6.
0.33575	-0.02804	-0.13875	6.
-0.35109	0.37062	0.16104	7.
-0.29765	0.54132	0.29766	7.
-0.26981	0.31790	0.41402	7.
-0.26739	0.17534	-0.24469	7.
-0.23274	0.08880	-0.14323	7.
-0.18352	0.24428	0.00132	7.
-0.12413	0.56107	0.00546	7.
0.41824	0.51885	0.36574	7.
-0.35385	0.22836	-0.04678	8.
-0.32730	0.39911	0.42811	8.
-0.32601	0.60500	0.20811	8.
-0.30748	0.24823	-0.11351	8.
-0.30334	0.28096	-0.13055	8.
-0.28480	0.46318	0.33836	8.
-0.25765	0.25880	0.44481	8.
-0.22533	0.06508	-0.18726	8.
-0.21757	0.18295	0.03326	8.
0.12490	0.20983	-0.20627	8.
0.19938	0.29276	0.03245	8.
0.20223	0.08994	-0.14382	8.
-0.36756	0.41354	0.30783	9.
-0.34256	0.21238	-0.03845	9.
-0.32385	0.40484	-0.08231	9.
-0.30756	0.33304	-0.04492	9.
-0.30420	0.39459	-0.07698	9.
-0.29437	0.30482	-0.08660	9.
-0.27972	0.42028	0.36070	9.
-0.17938	0.23189	0.00777	9.

TABLE XII: DROPLET SIZE AND SPATIAL COORDINATES, SLICE 1, continued

AXIAL SLICE 3:0-3.5 INCHES

X	Y	Z	SIZE
0.16352	0.32915	-0.04289	9.
0.29567	0.40032	0.31472	9.
0.31472	0.12867	0.06153	9.
0.41462	0.53467	0.35750	9.
-0.35523	0.39158	0.20650	10.
-0.33394	0.45953	0.00197	10.
-0.33066	0.32393	-0.15293	10.
-0.31032	0.44294	0.01061	10.
-0.30213	0.65622	0.12505	10.
-0.26679	0.41335	0.02602	10.
-0.25869	0.43712	.01363	10.
-0.24610	0.64834	0.12915	10.
-0.21791	0.62259	0.25532	10.
-0.20128	0.41067	0.02741	10.
-0.18343	0.50570	0.37259	10.
-0.17481	0.62680	0.25313	10.
-0.17093	0.28373	-0.01923	10.
0.16068	0.13188	0.05986	10.
0.21257	0.06062	0.09698	10.
0.22472	0.06303	-0.12981	10.
0.26558	0.27590	-0.18430	10.
0.30739	0.49033	0.38060	10.
0.32997	-0.07159	-0.39798	10.
0.41876	0.00991	-0.44043	10.
-0.32101	0.58779	0.16069	11.
-0.31179	0.29688	-0.02608	11.
-0.30541	0.43773	-0.04306	11.
-0.30101	0.44760	0.00818	11.
-0.28980	0.21761	0.12797	11.
-0.28291	0.40951	0.42269	11.
-0.28058	0.32127	0.41227	11.
-0.27324	0.34238	0.45766	11.
-0.26351	0.23723	0.39966	11.
-0.26205	0.00072	-0.09735	11.
-0.25429	0.23880	0.17332	11.
-0.21334	0.16719	-0.07129	11.
-0.21205	0.16047	-0.01141	11.
-0.20748	0.14601	-0.06026	11.
-0.20128	0.31594	0.07676	11.
-0.19817	0.15793	-0.06647	11.
-0.14102	0.61438	0.03408	11.
-0.13913	0.58761	-0.00836	11.
0.13258	0.16555	-0.23959	11.
0.13844	0.19163	-0.19079	11.
0.14982	-0.06226	-0.34646	11.

TABLE XII: DROPLET SIZE AND SPATIAL COORDINATES, SLICE 1, continued

AXIAL SLICE 3.0-3.5 INCHES

X	Y	Z	SIZE
0.17240	0.20097	-0.14527	11.
0.17593	-0.09620	-0.27240	11.
0.18128	0.34132	0.06353	11.
0.19111	0.27048	0.32596	11.
0.22309	0.31317	0.02181	11.
0.23903	0.14329	0.16668	11.
0.32213	0.56602	0.34117	11.
0.34006	0.51127	-0.13775	11.
0.39876	0.19384	-0.25432	11.
-0.38135	0.25153	-0.05884	12.
-0.33971	0.18699	-0.08161	12.
-0.33540	0.37479	-0.06666	12.
-0.31247	0.42785	-0.09430	12.
-0.29998	0.51768	0.25358	12.
-0.29799	0.32945	-0.04305	12.
-0.29161	0.25908	0.27552	12.
-0.26291	0.60522	0.16111	12.
-0.26067	0.26222	0.33026	12.
-0.25851	0.66868	0.11855	12.
-0.25377	0.43115	-0.03964	12.
-0.25343	0.33532	0.29219	12.
-0.25343	0.61690	0.03276	12.
-0.24610	0.25015	0.39293	12.
-0.22214	0.37280	0.38543	12.
-0.16869	0.32885	0.01365	12.
-0.13576	0.70105	0.27084	12.
0.25282	0.44017	0.40672	12.
0.27679	0.37338	0.15960	12.
0.31239	0.48867	0.04317	12.
0.32842	0.52935	0.07836	12.
0.39626	0.41871	0.07961	12.
0.40221	0.35474	0.28207	12.
-0.32937	0.30602	0.25106	13.
-0.30765	0.25763	0.27627	13.
-0.28093	0.14295	-0.05867	13.
0.21429	0.10361	0.18735	13.
0.45781	0.31969	-0.31987	13.
-0.33497	0.48431	0.04544	14.
-0.31713	0.47956	-0.00847	14.
-0.31170	0.47275	-0.06130	14.
-0.30765	0.56214	-0.05148	14.
-0.30239	0.21326	0.18662	14.
-0.29351	0.44484	-0.04676	14.
-0.17688	0.4184.	0.13615	14.
-0.17671	0.65036	0.29724	14.

TABLE XII: DROPLET SIZE AND SPATIAL COORDINATES, SLICE 1, continued

AXIAL SLICE 3.0-3.5 INCHES

X	Y	Z	SIZE
-0.15542	0.17619	-0.18875	14.
0.18223	0.37168	0.04772	14.
0.21007	0.40717	0.14200	14.
0.22196	0.19973	0.19367	14.
0.25213	0.34734	-0.05237	14.
0.25265	0.34390	-0.05057	14.
0.29808	0.28818	0.09121	14.
0.31204	0.03720	-0.00359	14.
0.33247	0.03790	-0.45501	14.
0.34695	0.34780	-0.05260	14.
0.34997	0.35423	0.45148	14.
-0.35376	0.26827	0.38349	15.
-0.33894	0.37968	0.38184	15.
-0.32006	0.33098	-0.04384	15.
-0.31592	0.28149	-0.13083	15.
-0.31515	0.27721	0.32246	15.
-0.23696	0.22629	-0.10208	15.
0.26119	0.52416	0.13745	15.
0.37100	0.50730	-0.13568	15.
0.40161	0.11595	-0.10099	15.
-0.26808	0.61883	0.14452	16.
-0.25843	0.35911	0.33618	16.
-0.25532	0.24004	0.28543	16.
-0.22636	0.35039	0.34072	16.
-0.22136	0.44973	0.40174	16.
-0.20826	0.21738	0.12809	16.
-0.17843	0.45661	0.39816	16.
-0.16809	0.44590	0.34736	16.
-0.16680	0.39914	0.14618	16.
0.19369	0.31783	0.41406	16.
0.19878	0.31150	0.07907	16.
0.20938	0.32536	0.18461	16.
0.24774	0.32157	-0.09532	16.
0.25446	0.25817	0.33237	16.
0.25869	0.36940	0.16167	16.
0.29420	0.36691	-0.11894	16.
0.36437	0.53488	0.18825	16.
-0.30601	0.23016	0.17782	17.
-0.30411	0.13849	-0.22549	17.
-0.28480	0.54513	0.23929	17.
-0.22446	0.39407	0.43073	17.
0.22196	0.33408	-0.27098	17.
0.25782	0.09143	0.08093	17.
0.41117	0.51792	0.30984	17.
-0.36273	0.23271	-0.10542	18.

TABLE XII. DROPLET SIZE AND SPATIAL COORDINATES, SLICE 1, continued

AXIAL SLICE 3.0-3.5 INCHES

X	Y	Z	SIZE
-0.35911	0.20770	-0.14878	18.
-0.32678	0.45088	-0.04991	18.
-0.31722	0.29808	0.31158	18.
-0.30765	0.52712	-0.03324	18.
-0.30049	0.44964	-0.16203	18.
-0.25007	0.10530	-0.20821	18.
-0.24972	0.46645	0.28027	18.
-0.24265	0.41506	0.19428	18.
-0.23050	0.24372	0.33990	18.
-0.18197	0.60545	0.15149	18.
0.15188	0.08729	-0.02968	18.
0.15861	0.22618	0.17989	18.
0.19136	0.27557	0.15416	18.
0.24377	0.29686	-0.13884	18.
0.26731	0.25677	0.16396	18.
0.30549	0.45421	0.23026	18.
0.32066	0.04921	-0.00984	18.
0.32696	0.43741	0.35178	18.
0.34825	0.39345	0.43105	18.
0.42428	0.55700	0.34587	18.
-0.30049	0.47330	0.05117	19.
-0.23558	0.20548	0.30343	19.
-0.14102	0.54986	0.18044	19.
0.20395	0.28057	0.32070	19.
0.23576	0.38109	0.09920	19.
0.25748	0.09678	0.02176	19.
0.32066	0.49535	-0.24222	19.
0.42798	0.35502	-0.33827	19.
-0.36859	0.39604	0.31695	20.
-0.22593	0.22238	0.29463	20.
-0.17464	0.64742	0.07325	20.
-0.14283	0.42287	0.30297	20.
0.18395	0.22437	0.29360	20.
0.21153	0.34953	0.22840	20.
0.24222	0.43264	0.18512	20.
0.25619	0.38647	-0.18551	20.
0.26756	0.43870	0.29472	20.
0.28549	0.43441	0.24058	20.
0.29834	0.17466	-0.18795	20.
0.29972	0.19807	-0.14376	20.
0.37566	0.46815	0.33577	20.
-0.26438	0.59030	0.10300	21.
-0.19507	0.53431	0.01940	21.
-0.19326	0.54953	0.01147	21.
0.20128	0.40534	0.14296	21.

TABLE XII: DROPLET SIZE AND SPATIAL COORDINATES, SLICE 1, continued

AXIAL SLICE 3.0-3.5 INCHES

X	Y	Z	SIZE
0.20619	0.62230	0.31186	21.
0.24627	0.52226	0.19482	21.
0.34575	0.04867	-0.00957	21.
0.35351	0.07055	0.03542	21.
-0.23696	0.43964	-0.04406	22.
-0.20947	0.12961	0.23019	22.
0.18654	0.29244	0.42728	22.
0.22593	0.19672	0.02609	22.
0.29403	0.36429	-0.23034	22.
0.32213	-0.13627	-0.30791	22.
0.33678	0.12818	-0.10736	22.
-0.32023	0.37610	-0.01096	23.
0.25808	0.41614	0.25009	23.
0.26722	0.56975	0.22646	23.
0.32230	0.08019	0.08678	23.
-0.14025	0.52248	0.13832	24.
0.16688	0.43772	0.35162	24.
0.18481	-0.05705	-0.29279	24.
0.19490	-0.07991	-0.26088	24.
0.23912	0.24623	-0.22523	24.
0.25800	0.15966	0.21453	24.
0.26541	0.42262	0.19033	24.
0.34290	0.15251	-0.06365	24.
-0.35101	0.29008	0.03384	25.
0.21153	0.32907	0.40821	25.
0.22843	0.32085	-0.26409	25.
0.31325	0.52726	0.36136	25.
0.21541	0.55629	0.17710	26.
-0.24257	0.48990	0.09891	27.
-0.23653	0.22358	0.18124	27.
-0.18516	0.63349	0.02412	27.
-0.17395	0.21767	0.01518	27.
-0.15257	0.38913	0.15140	27.
0.16602	0.53956	0.29857	27.
0.20972	0.40056	-0.08008	27.
0.22576	0.36690	0.27574	27.
0.29213	0.35564	0.16884	27.
0.32989	0.54621	-0.15595	27.
-0.36825	0.25847	-0.17522	28.
-0.30360	0.22307	-0.15678	28.
-0.20033	0.58078	0.33348	28.
-0.19878	0.50651	0.20302	28.
0.21102	0.57082	0.22591	28.
0.29929	0.41309	-0.14299	33.
0.30067	0.41687	0.08057	37.

TABLE XII: DROPLET SIZE AND SPATIAL COORDINATES, SLICE 1, continued

AXIAL SLICE 3.0-3.5 INCHES

X	Y	Z	SIZE
0.27136	0.42988	0.13017	39.
0.23567	0.39718	-0.13471	42.
0.18981	0.35024	-0.11026	46.

TABLE XIII: DROPLET SIZE AND SPATIAL COORDINATES, SLICE 2

AXIAL SLICE 3.5-4.0 INCHES

X	Y	Z	SIZE
-0.36265	4.11906	0.03835	3.
-0.18752	4.19544	0.22409	3.
-0.12321	3.97063	-0.10986	3.
0.25611	4.03476	-0.19965	3.
0.29668	4.00264	-0.18292	3.
-0.30515	4.43663	-0.01429	4.
-0.28560	3.91855	-0.30827	4.
-0.23796	4.3[illegible]98	-0.04481	4.
-0.19773	4.41084	0.22467	4.
-0.13229	4.29465	-0.10[illegible]49	4.
-0.08482	4.30626	-0.11553	4.
0.40951	3.96541	-0.16353	4.
-0.38482	4.24684	0.19733	5.
-0.36030	4.09739	0.04964	5.
-0.34101	3.97884	-0.22690	5.
-0.34005	4.19931	0.22208	5.
-0.30375	4.41190	-0.05780	5.
-0.30244	4.38548	0.40702	5.
-0.29389	3.92435	-0.19852	5.
-0.27042	4.49088	-0.04255	5.
-0.26981	4.12129	-0.24472	5.
-0.23647	4.44663	0.26241	5.
-0.20558	4.36754	0.07807	5.
-0.20070	4.43649	0.26769	5.
-0.18979	4.09285	-0.28629	5.
-0.18412	4.17099	-0.49614	5.
-0.16387	4.06861	-0.16090	5.
-0.13499	4.41978	0.16363	5.
-0.11684	4.38402	0.18225	5.
-0.07897	4.09611	-0.40075	5.
0.23822	4.18032	-0.44461	5.
0.25436	4.26154	0.18967	5.
0.26675	4.46821	-0.03074	5.
0.27880	4.10957	-0.29500	5.
0.27923	4.06692	-0.27278	5.
0.27976	4.18894	-0.39272	5.
0.31126	4.04829	0.01883	5.
0.31658	4.10462	-0.40518	5.
0.32871	4.07513	-0.38982	5.
0.34415	4.22098	0.21079	5.
0.36152	4.10779	-0.29407	5.
0.36702	4.10496	0.27122	5.
0.38255	4.06061	-0.21311	5.
0.38709	3.95880	-0.32923	5.

TABLE XIII: DROPLET SIZE AND SPATIAL COORDINATES, SLICE 2, continued

AXIAL SLICE 3.5-4.0 INCHES

X	Y	Z	SIZE
0.43010	4.40372	0.11561	5.
0.45052	4.10572	-0.12385	5.
0.46579	3.98321	-0.17280	5.
0.46806	4.15332	-0.03587	5.
0.48569	4.09207	-0.28588	5.
-0.38674	4.21816	0.15588	6.
-0.37199	3.95961	-0.27327	6.
-0.35297	4.35104	0.31219	6.
-0.34485	4.05022	0.01782	6.
-0.30506	4.38633	-0.10086	6.
-0.30279	3.89596	-0.40926	6.
-0.29677	4.20741	-0.45872	6.
-0.28106	4.16574	0.01404	6.
-0.26466	4.14040	-0.14191	6.
-0.23901	4.55166	0.20770	6.
-0.21946	4.05454	-0.37910	6.
-0.20716	4.23384	0.09133	6.
-0.17469	3.91031	-0.36036	6.
-0.17269	4.51619	-0.05574	6.
-0.14145	4.36673	0.13488	6.
-0.13935	4.39730	0.11895	6.
-0.13517	4.00363	0.04209	6.
-0.13037	4.31891	-0.06574	6.
-0.12496	4.31761	0.21684	6.
-0.07845	4.21355	-0.29277	6.
0.24546	4.23850	0.48358	6.
0.24660	4.16155	-0.49122	6.
0.26632	4.15714	0.01851	6.
0.28525	4.40957	0.05618	6.
0.31361	4.36529	0.19201	6.
0.32426	4.20867	-0.17747	6.
0.35846	4.01583	-0.13341	6.
0.36178	4.15964	-0.20831	6.
0.37155	4.2746.	0.46475	6.
0.38665	3.88984	-0.29331	6.
-0.34398	4.06461	-0.38434	7.
-0.32836	4.22651	0.26429	7.
-0.31719	4.36682	0.41674	7.
-0.31108	4.15551	0.13213	7.
-0.29529	4.53722	0.27160	7.
-0.28805	4.04630	-0.43119	7.
-0.27714	4.22778	-0.18742	7.
-0.27522	4.30835	-0.11662	7.
-0.23927	4.35970	-0.08699	7.
-0.20550	4.32193	-0.06731	7.

TABLE XIII: DROPLET SIZE AND SPATIAL COORDINATES, SLICE 2, continued

AXIAL SLICE 3.5-4.0 INCHES

X	Y	Z	SIZE
-0.20122	4.41955	0.16375	7.
-0.15672	4.34798	-0.13726	7.
-0.14913	4.46672	0.19556	7.
-0.14729	4.22717	-0.29987	7.
-0.14442	4.52617	0.05183	7.
-0.09223	4.05238	-0.49074	7.
0.24860	4.06010	-0.15647	7.
0.27373	4.23592	-0.30442	7.
0.29267	4.42296	0.04921	7.
0.30205	3.98163	-0.22836	7.
0.35175	4.29040	0.28740	7.
0.35401	3.98909	-0.17586	7.
0.35602	4.23546	0.20325	7.
0.38455	3.87721	-0.17397	7.
0.38613	4.36973	0.35937	7.
0.45384	4.03471	-0.03048	7.
0.48045	4.11572	-0.24182	7.
-0.34921	4.09382	-0.34317	8.
-0.34494	4.15280	0.13354	8.
-0.32845	4.08064	0.00198	8.
-0.32635	4.10211	0.04718	8.
-0.30916	3.87000	-0.45212	8.
-0.29551	3.77193	-0.40104	8.
-0.28063	4.17555	-0.27298	8.
-0.27958	4.19749	-0.22802	8.
-0.27818	4.07033	-0.38732	8.
-0.25384	4.30919	-0.00430	8.
-0.22661	3.97291	-0.16744	8.
-0.20489	4.34797	-0.02450	8.
-0.17452	4.19394	-0.45170	8.
-0.14232	4.47318	0.24858	8.
-0.07740	4.14889	-0.42824	8.
-0.04825	4.18832	-0.27963	8.
0.24145	4.12877	0.08967	8.
0.24729	4.28875	0.11911	8.
0.25070	4.30805	-0.34200	8.
0.25183	4.13760	-0.53512	8.
0.27941	4.16817	-0.43828	8.
0.28447	4.46953	-0.14419	8.
0.31562	4.33941	0.14911	8.
0.33281	4.07075	-0.21839	8.
0.33822	4.04904	-0.26347	8.
0.33839	4.09663	-0.17550	8.
0.35227	4.26444	0.24454	8.
0.35750	4.13290	-0.25077	8.

TABLE XIII: DROPLET SIZE AND SPATIAL COORDINATES, SLICE 2, continued

AXIAL SLICE 3.5-4.0 INCHES

X	Y	Z	SIZE
0.36702	4.44936	-0.07731	8.
0.37138	4.42626	-0.12166	8.
0.37260	4.28425	0.34698	8.
0.46448	4.05506	-0.04108	8.
0.51126	4.14296	-0.25601	8.
-0.34572	4.27068	0.07214	9.
-0.31370	3.81481	-0.42338	9.
-0.29250	3.81140	-0.42160	9.
-0.27818	4.27975	-0.15811	9.
-0.23045	4.02920	-0.42228	9.
-0.21710	4.25153	0.02574	9.
-0.19965	4.44847	-0.02046	9.
-0.19668	4.21682	-0.01257	9.
-0.18202	4.23560	-0.19150	9.
-0.17382	4.12619	-0.07813	9.
-0.17024	4.17711	0.00811	9.
-0.16466	4.44461	-0.13121	9.
-0.15183	4.36980	-0.14863	9.
-0.13185	4.12533	-0.47235	9.
-0.12487	4.22476	-0.07308	9.
-0.12373	4.10864	-0.01261	9.
0.25532	4.33123	-0.29769	9.
0.28298	4.43329	0.10021	9.
0.31326	4.39280	0.23406	9.
0.35262	4.25466	-0.42695	9.
0.37155	4.24907	0.42169	9.
0.37478	4.38153	-0.21112	9.
0.40009	4.27455	-0.43731	9.
0.47173	4.12828	-0.07922	9.
0.51562	4.16923	-0.21331	9.
-0.37443	4.15079	-0.37285	10.
-0.36606	4.17474	-0.32894	10.
-0.33028	3.90210	-0.24332	10.
-0.31763	4.19831	0.10983	10.
-0.26876	4.19808	-0.39748	10.
-0.26379	4.03880	-0.42728	10.
-0.25899	4.22226	-0.35369	10.
-0.25864	4.24451	-0.30890	10.
-0.22243	4.25316	-0.08788	10.
-0.21675	4.13023	-0.30576	10.
-0.21588	4.15318	-0.26133	10.
-0.19023	4.40044	0.06094	10.
-0.16876	4.39895	-0.22019	10.
-0.16640	4.42375	-0.17673	10.
-0.15340	4.49253	0.23850	10.

TABLE XIII: DROPLET SIZE AND SPATIAL COORDINATES, SLICE 2, continued

AXIAL SLICE 3.5-4.0 INCHES

X	Y	Z	SIZE
-0.12565	4.19601	-0.11449	10.
-0.12487	4.33379	0.20842	10.
-0.11850	4.23784	-0.07990	10.
-0.10532	4.19454	-0.22649	10.
-0.10401	4.16793	-0.32539	10.
-0.05611	4.31546	-0.00756	10.
0.18857	4.13499	-0.25185	10.
0.25349	4.28573	-0.38675	10.
0.27696	4.21166	-0.34817	10.
0.46684	4.08448	-0.16917	10.
-0.29389	4.05634	0.01464	11.
-0.29127	4.07959	0.05891	11.
-0.28054	4.25758	-0.20294	11.
-0.27557	4.36173	0.19386	11.
-0.25375	4.35663	0.08376	11.
-0.20681	4.22225	-0.24092	11.
-0.17190	4.15386	-0.03616	11.
-0.17147	4.35337	-0.30922	11.
-0.15646	4.49862	-0.04658	11.
-0.15035	4.30961	0.05186	11.
-0.14895	4.51470	0.28333	11.
-0.14651	4.25058	-0.25568	11.
-0.13272	4.49702	0.23616	11.
-0.12531	4.54585	0.32349	11.
-0.11527	4.20098	0.16483	11.
0.20384	4.48285	0.35631	11.
0.21073	4.08012	-0.33604	11.
0.26527	4.33729	-0.01893	11.
0.26911	4.28590	-0.10493	11.
0.28386	4.31158	0.10722	11.
0.28735	4.38423	0.01300	11.
0.29005	4.47117	0.13686	11.
0.31161	4.33513	-0.13057	11.
0.34852	4.27985	-0.38369	11.
0.37653	4.23255	0.26115	11.
0.38080	4.00872	-0.24247	11.
0.44485	4.55321	0.20689	11.
0.46291	4.05805	-0.21178	11.
0.47339	4.33944	0.20547	11.
0.47600	4.31441	0.16213	11.
0.47862	4.04606	-0.31830	11.
0.47880	4.29146	0.11770	11.
-0.33752	4.30525	-0.11501	12.
-0.31658	4.14337	0.02569	12.
-0.29511	4.45473	0.08904	12.

TABLE XIII: DROPLET SIZE AND SPATIAL COORDINATES, SLICE 2, continued

AXIAL SLICE 3.5-4.0 INCHES

X	Y	Z	SIZE
-0.28586	4.26069	0.19011	12.
-0.27312	3.95817	-0.10337	12.
-0.23438	4.26820	0.18620	12.
-0.1[illegible]	4.09209	-0.00399	12.
-0.11134	4.14119	-0.36785	12.
0.19267	4.11181	-0.29616	12.
0.19564	4.08763	-0.33995	12.
0.20366	4.45890	0.31240	12.
0.21553	4.51960	-0.05751	12.
0.26867	4.31318	-0.06276	12.
0.32644	4.04994	-0.43308	12.
0.32792	4.03188	0.02738	12.
0.35401	4.23341	-0.47227	12.
0.37513	4.26006	0.30320	12.
0.40270	4.25122	-0.48154	12.
0.40995	4.26197	-0.37437	12.
-0.29782	4.03140	-0.36705	13.
-0.29302	4.33459	-0.13029	13.
-0.22731	3.97208	-0.39253	13.
-0.22461	4.02308	-0.30633	13.
-0.22347	4.22550	-0.12985	13.
-0.21126	4.29420	0.17265	13.
-0.19904	4.42498	-0.06461	13.
-0.16082	4.04521	-0.20509	13.
0.24869	4.05641	-0.49283	13.
0.26222	4.44453	-0.13117	13.
0.26396	4.39879	-0.22011	13.
0.34311	3.87447	-0.22892	13.
0.38508	3.98414	-0.28605	13.
0.41571	4.24366	0.19898	13.
0.43918	4.59639	0.29717	13.
0.45864	4.38919	-0.10235	13.
-0.37487	4.05777	-0.54992	14.
-0.36859	4.06861	-0.04813	14.
-0.34782	4.37461	0.35630	14.
-0.31710	3.97759	-0.11349	14.
-0.28909	4.21209	0.10266	14.
-0.28717	4.23302	0.14814	14.
-0.26850	4.21949	-0.07034	14.
-0.25646	4.33562	0.03832	14.
-0.24520	4.28929	-0.38860	14.
-0.22714	3.77371	-0.40197	14.
-0.21178	4.55553	0.20568	14.
-0.19127	3.85527	-0.21893	14.
-0.12827	4.12050	-0.01878	14.

TABLE XIII: DROPLET SIZE AND SPATIAL COORDINATES, SLICE 2, continued

AXIAL SLICE 3.5-4.0 INCHES

X	Y	Z	SIZE
-0.12007	4.27512	0.23897	14.
-0.11335	4.34504	0.37170	14.
0.41274	4.38546	0.12512	14.
-0.34520	4.40119	0.39884	15.
-0.33455	4.32626	-0.06957	15.
-0.29852	4.09739	0.04964	15.
-0.28211	4.28903	0.06259	15.
-0.27845	4.33794	0.14988	15.
-0.25986	4.09096	-0.34168	15.
-0.25166	4.26634	-0.43304	15.
-0.21195	4.26723	0.13032	15.
-0.18848	4.47967	-0.14947	15.
-0.16466	3.85380	-0.21816	15.
-0.14721	4.12063	-0.18799	15.
-0.11771	4.15501	0.07601	15.
0.21361	4.23994	-0.19375	15.
0.36161	4.29329	-0.05240	15.
0.37129	4.21382	-0.23653	15.
-0.39171	4.32462	0.15681	16.
-0.37103	4.04450	-0.09196	16.
-0.29773	4.43055	0.04526	16.
-0.28054	4.31127	0.10738	16.
-0.22391	4.43877	-0.18455	16.
-0.22382	4.50753	-0.05122	16.
-0.20244	4.37956	-0.15371	16.
-0.16213	4.11348	0.15402	16.
-0.15576	4.33219	-0.12904	16.
-0.15445	4.04444	-0.31745	16.
-0.11789	4.18113	0.11878	16.
-0.11675	4.30031	0.28224	16.
0.20628	4.02262	-0.41885	16.
0.21806	4.47975	-0.14951	16.
0.24188	4.19450	0.45011	16.
0.25183	4.17578	-0.27310	16.
0.25611	4.15136	-0.31676	16.
0.41422	4.23964	-0.41913	16.
0.41597	3.93747	-0.26174	16.
0.41780	3.91649	-0.13805	16.
-0.33290	4.37703	0.01675	17.
-0.30035	4.14994	0.13503	17.
-0.25304	4.01392	0.03673	17.
-0.24494	4.35925	0.19515	17.
-0.21824	4.48623	0.07263	17.
-0.18970	4.46067	-0.19596	17.
-0.15201	4.41403	-0.00252	17.

TABLE XIII: DROPLET SIZE AND SPATIAL COORDINATES, SLICE 2, continued

AXIAL SLICE 3.5-4.0 INCHES

X	Y	Z	SIZE
-0.11928	4.32573	0.32538	17.
0.23970	4.22031	0.49305	17.
0.25969	4.12648	-0.36019	17.
0.31056	4.46192	0.19806	17.
0.36073	4.26818	-0.09570	17.
0.41475	3.91128	-0.30448	17.
0.41789	4.22157	0.15410	17.
0.49031	4.37253	0.24462	17.
-0.29538	4.08372	-0.28153	18.
-0.25951	4.05198	-0.26500	18.
-0.25637	3.91270	-0.24884	18.
-0.22443	4.36033	-0.20008	18.
-0.16126	4.08659	0.11164	18.
-0.14869	4.23079	-0.07623	18.
-0.14825	4.28071	0.01054	18.
-0.14747	4.25289	-0.03135	18.
-0.14180	4.38428	-0.15617	18.
0.21449	4.50192	-0.10468	18.
0.37251	4.40767	0.11355	18.
0.41449	4.36396	0.07993	18.
0.41518	4.21592	-0.46315	18.
-0.39599	4.29765	0.11448	19.
-0.32086	3.91001	-0.47296	19.
-0.26719	4.02493	-0.30730	19.
-0.21981	4.43172	-0.06812	19.
0.30750	4.64128	0.27378	19.
0.37373	4.38449	0.06924	19.
0.38595	4.50445	0.23229	19.
-0.34625	4.18299	0.11782	20.
-0.34581	4.15602	0.07548	20.
-0.26187	3.99858	-0.34995	20.
-0.23691	4.22053	0.09826	20.
-0.23490	4.24208	0.14342	20.
-0.23473	4.16558	0.01412	20.
-0.22277	4.48241	-0.09452	20.
-0.19049	4.52380	0.22221	20.
-0.17347	4.05931	0.06947	20.
-0.15262	4.04259	0.07818	20.
-0.14075	4.45776	-0.02530	20.
0.38970	4.48027	0.18851	20.
-0.30358	4.05914	-0.32511	21.
-0.29852	4.12320	0.09258	21.
-0.20829	4.17915	-0.33124	21.
-0.17574	4.03668	0.02488	21.
-0.15934	4.00550	-0.18441	21.

TABLE XIII: DROPLET SIZE AND SPATIAL COORDINATES, SLICE 2, continued

AXIAL SLICE 3.5-4.0 INCHES

X	Y	Z	SIZE
-0.15646	4.03228	-0.19836	21.
-0.11920	4.39963	0.00498	21.
-0.11291	4.36884	0.41569	21.
0.03019	4.43607	0.21152	21.
0.23752	4.50288	-0.04880	21.
-0.39930	4.27834	0.06815	22.
-0.35017	4.55847	0.31692	22.
-0.21990	4.54792	0.04050	22.
-0.21527	4.15450	-0.37478	22.
-0.15881	4.00373	-0.29625	22.
-0.15489	4.01887	0.03415	22.
0.24049	4.46396	-0.14129	22.
0.31187	4.43611	0.15512	22.
0.31257	4.41077	0.11194	22.
0.31649	4.36201	0.02457	22.
0.33613	4.29684	0.17128	22.
-0.24756	4.33538	0.15121	23.
-0.18490	4.32164	0.21475	23.
-0.15742	4.08014	-0.05414	23.
0.02679	4.46087	0.25499	23.
-0.24817	4.26028	0.02118	24.
-0.18656	4.54504	0.26753	24.
-0.18255	4.57139	0.31019	24.
-0.18019	4.39767	0.34429	24.
0.25375	4.27366	0.12697	24.
0.26894	4.36507	0.07936	24.
-0.24834	4.30818	0.10899	26.
-0.18133	4.34969	0.25652	27.
-0.12583	4.60956	0.17754	28.
0.30079	4.56327	0.31442	28.
-0.18482	4.37519	0.28962	29.
-0.12007	4.27375	-0.09860	29.
-0.23281	4.20411	-0.40062	31.
-0.22513	4.22876	-0.35708	32.
-0.17051	4.38050	0.24047	32.
-0.14668	4.52968	0.21915	32.
-0.14686	4.46027	0.13214	34.
0.38421	4.41320	0.16705	34.
0.33630	4.19070	-0.05535	36.
0.32120	4.45864	0.03062	40.
-0.17661	4.30997	-0.11747	43.

TABLE XIV: CLASS SIZE INTERVAL WIDTH and DROPLET NUMBER COUNT

CLASS NO.	CLASS DIA. (MICRONS) MINIMUM	/ MAXIMUM	MID-DIA. (MICRONS)	DROPLET COUNT (AX. SLICE 1)	DROPLET COUNT (AX. SLICE 2)
1.	0.0	20.3	10.1	0.	0.
2.	20.3	40.6	30.4	0.	0.
3.	40.6	63.5	52.0	1.	5.
4.	63.5	83.8	73.6	3.	7.
5.	83.8	106.7	95.2	6.	37.
6.	106.7	127.0	116.8	6.	30.
7.	127.0	144.8	135.9	8.	27.
8.	144.8	165.1	154.9	12.	33.
9.	165.1	182.9	174.0	12.	25.
10.	182.9	203.2	193.0	20.	25.
11.	203.2	228.6	215.9	20.	32.
12.	228.6	246.4	237.5	13.	19.
13.	246.4	261.6	254.0	5.	16.
14.	261.6	284.5	273.0	19.	16.
15.	284.5	304.8	294.6	9.	15.
16.	304.8	325.1	314.9	17.	20.
17.	325.1	342.9	334.0	7.	15.
18.	342.9	365.8	354.3	21.	13.
19.	365.8	381.0	373.4	8.	7.
20.	381.0	406.4	393.7	13.	12.
21.	406.4	426.7	416.5	8.	10.
22.	426.7	447.0	436.8	7.	11.
23.	447.0	464.8	455.9	4.	4.
24.	464.8	490.2	477.5	8.	6.
25.	490.2	508.0	499.1	4.	0.
26.	508.0	523.2	515.6	1.	1.
27.	523.2	548.6	535.9	10.	1.
28.	548.6	563.4	556.0	5.	2.
29.	563.4	584.2	573.8	0.	2.
30.	584.2	607.1	595.6	0.	0.
31.	607.1	624.8	615.9	0.	1.
32.	624.8	642.6	633.7	0.	3.
33.	642.6	662.9	652.7	1.	0.
34.	662.9	685.8	674.3	0.	2.
35.	685.8	703.6	694.7	0.	0.
36.	703.6	726.4	715.0	0.	1.
37.	726.4	744.2	735.3	1.	0.
38.	744.2	762.0	753.1	0.	0.
39.	762.0	784.9	773.4	1.	0.
40.	784.9	807.7	796.3	0.	1.
41.	807.7	823.0	815.3	0.	0.
42.	823.0	845.8	834.4	1.	0.
43.	845.8	866.1	855.9	0.	1.
44.	866.1	883.9	875.0	0.	0.
45.	883.9	904.2	894.0	0.	0.
46.	904.2	922.0	913.1	1.	0.
47.	922.0	947.4	934.7	0.	0.
48.	947.4	967.7	957.5	0.	0.

TABLE XV: DROPLET DISTRIBUTION DATA, SLICE 1

CLASS NO.	DROPLET NO. FRACTION	CUM. VOL. FRACTION	VOLUME FRACTION
1.	...	...	...
2.	...	...	...
3.	0.00368	0.00001	0.00001
4.	0.01103	0.00011	0.00010
5.	0.02206	0.00052	0.00042
6.	0.02206	0.00129	0.00077
7.	0.02941	0.00290	0.00161
8.	0.04412	0.00649	0.00358
9.	0.04412	0.01156	0.00507
10.	0.07353	0.02311	0.01155
11.	0.11029	0.04735	0.02423
12.	0.08456	0.07208	0.02473
13.	0.01838	0.07865	0.00658
14.	0.06985	0.10970	0.03105
15.	0.03309	0.12818	0.01848
16.	0.06250	0.17081	0.04263
17.	0.02574	0.19175	0.02094
18.	0.07721	0.26675	0.07500
19.	0.02941	0.30018	0.03343
20.	0.04779	0.36386	0.06368
21.	0.02941	0.41027	0.04641
22.	0.02574	0.45711	0.04684
23.	0.01471	0.48753	0.03042
24.	0.02941	0.55745	0.06991
25.	0.01471	0.59737	0.03992
26.	0.00368	0.60837	0.01100
27.	0.03676	0.73190	0.12354
28.	0.01838	0.80089	0.06898
29.	...	...	...
30.	...	...	...
31.	...	...	...
32.	...	...	...
33.	0.00368	0.82321	0.02232
34.	...	...	...
35.	...	...	...
36.	...	...	...
37.	0.00368	0.85512	0.03191
38.	...	...	...
39.	0.00368	0.89226	0.03714
40.	...	...	...
41.	...	...	...
42.	0.00368	0.93889	0.04663
43.	...	...	...
44.	...	...	...
45.	...	...	...
46.	0.00368	1.00000	0.06111
47.	...	...	...
48.	...	...	...

TABLE XVI: DROPLET DISTRIBUTION DATA, SLICE 2

CLASS NO.	DROPLET NO. FRACTION	CUM. VOL. FRACTION	VOLUME FRACTION
1.	...	...	...
2.	...	...	...
3.	0.01250	0.00006	0.00006
4.	0.01750	0.00030	0.00024
5.	0.09250	0.00301	0.00271
6.	0.07500	0.00707	0.00406
7.	0.06750	0.01282	0.00575
8.	0.08250	0.02324	0.01042
9.	0.06250	0.03441	0.01118
10.	0.06250	0.04968	0.01526
11.	0.08000	0.07700	0.02733
12.	0.04750	0.09860	0.02160
13.	0.04000	0.12085	0.02225
14.	0.04000	0.14849	0.02764
15.	0.03750	0.18105	0.03256
16.	0.05000	0.23406	0.05301
17.	0.03750	0.28149	0.04742
18.	0.03250	0.33057	0.04908
19.	0.01750	0.36149	0.03092
20.	0.03000	0.42363	0.06214
21.	0.02500	0.48495	0.06132
22.	0.02750	0.56277	0.07781
23.	0.01000	0.59493	0.03216
24.	0.01500	0.65036	0.05543
25.	...	...	...
26.	0.00250	0.66199	0.01163
27.	0.00250	0.67505	0.01306
28.	0.00500	0.70422	0.02917
29.	0.00500	0.73628	0.03206
30.	...	...	...
31.	0.00250	0.75611	0.01983
32.	0.00750	0.82089	0.06478
33.	...	...	...
34.	0.00500	0.87293	0.05204
35.	...	...	...
36.	0.00250	0.90394	0.03102
37.	...	...	...
38.	...	...	...
39.	...	...	...
40.	0.00250	0.94679	0.04284
41.	...	...	...
42.	...	...	...
43.	0.00250	1.00000	0.05321
44.	...	...	...
45.	...	...	...
46.	...	...	...
47.	...	...	...
48.	...	...	...

TABLE XVII: MEAN DIAMETERS--TOTAL DROPLET COUNT

CALCULATED MEAN DIAMETERS	SLICE 1	SLICE 2
Average Diameter, D_{10}	299	241
Surface Mean Diameter, D_{20}	328	275
Volume Mean Diameter, D_{30}	358	309
Sauter Mean Diameter, D_{32}	425	390
Mass Median Diameter, D_{MM}	460	420
Mass Mean Diameter, D_{43}	494	466
Total Droplet Count	272	400

CHAPTER VII ANALYSIS AND DISCUSSION OF RESULTS

1. General Discussion

Application of the holographic technique permits one to size droplets and obtain the spatial coordinates of the droplets without disturbing the flow field. Although holography adds a new dimension to the acquisition of data, there are limits as to the resolution of the data and the speed an object can have and still be resolvable. The holographic equipment, the manner in which the hologram is taken and the scene (static or dynamic) all have a bearing on the achievable resolution.

Prior to this investigation, no other investigation was known to have applied holography to the breakup of a liquid jet in a supersonic gas stream. The attempt in the present effort was to obtain droplet data in the near-field, breakup region of the jet, in contrast to the droplet data of Bitron[17] and Volynskiy[5], which was obtained in the far-field after jet breakup was completed and the gas velocity became subsonic again. However, supersonic droplet data was not retrievable in this investigation for the following reasons: (1) the apparent fineness of the spray or droplet sizes was less than the resolution capability of the holographic recording system, approximately 15 microns; and (2) the droplets moved on the order of 10 to 25 microns within the 50 nanosecond pulse, resulting in image smear. Matthews[73], in a recent investigation on JP-4 fuel injected perpendicularly into gas streams, whose velocities ranged from 200 to 800fps, encountered a similar situation and drew the same conclusions why droplets were not discernible. He was able to obtain drop size information in gas streams whose velocities were below 400fps, but he did not characterize the sprays.

In the subsequent sections of this chapter, jet amplitude and wavelength data obtained in the supersonic flow fields and droplet data obtained from a jet injected into still air are analyzed and discussed.

2. Liquid Jet Injection into a Supersonic Stream

a. Liquid Jet Amplitude: The jet amplitude data presented in Chapter VI was reviewed for correlation purposes. The investigation conducted by Catton[21] et.al. on jet penetration revealed that penetration was dominated by inertial forces. Considering this, a model was assumed for amplitude variation based on distance from the injection point and dynamic pressure ratio:

$$A = \frac{A'}{C_d^{1/2} D_o} = C \left(\frac{S}{C_d^{1/2} D_o} \right)^N \left(\bar{q} \right)^M \qquad (31)$$

where C, N and M are correlation coefficients.

A nonlinear regression analysis was conducted to determine the values for the coefficients. The resulting equation which characterized jet amplitude behavior is:

$$A = 0.246 \left(\bar{S} \right)^{1.146} \left(\bar{q} \right)^{-0.428} \qquad (32)$$

The observed amplitudes from all five test liquids are plotted against the amplitude predicted by equation (32) in Figure 45. One can see from the data scatter about the line in the Figure that liquid physical property effects on amplitude behavior cannot be discerned. This would lead one to conclude that amplitude behavior under the flow conditions

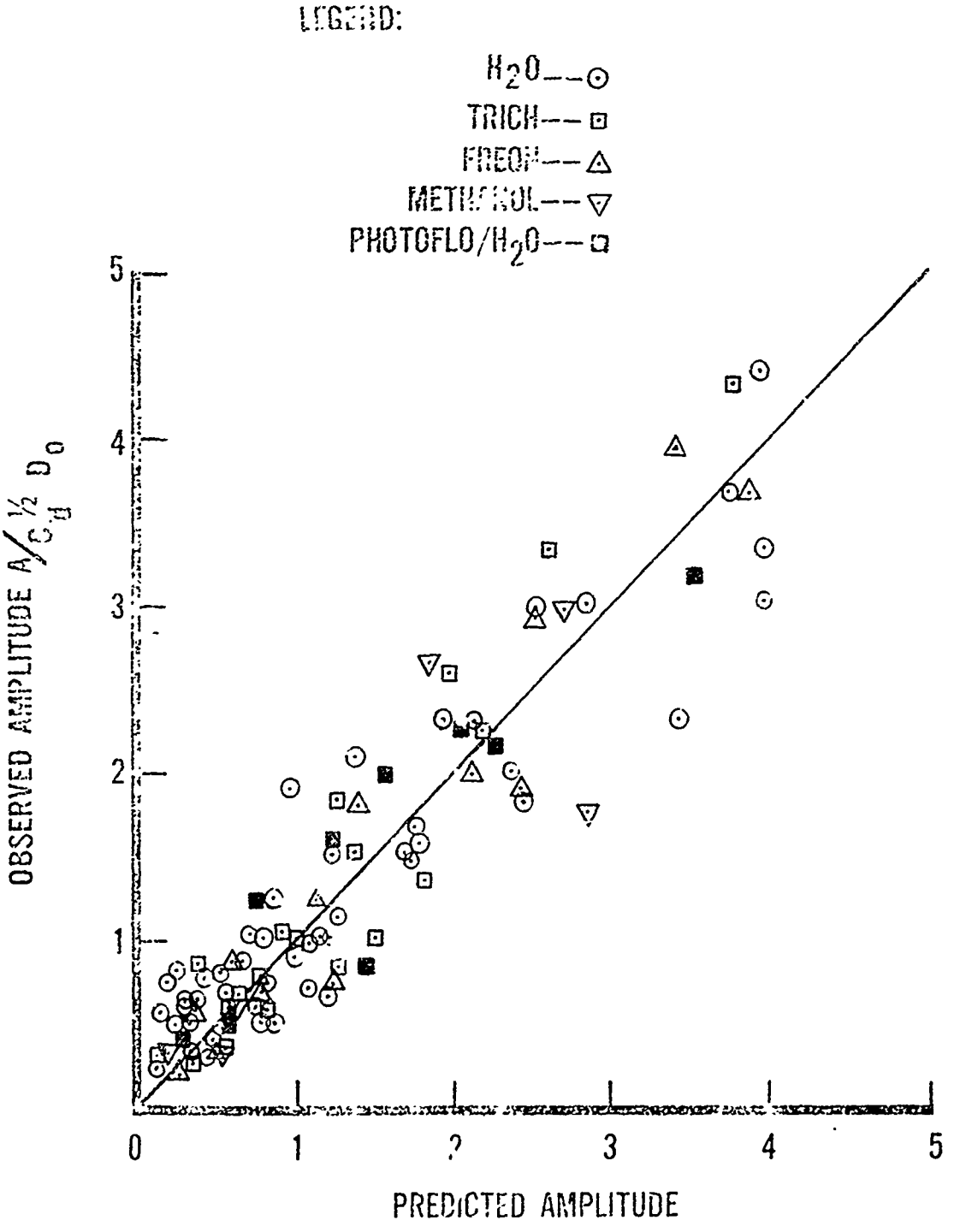

Figure 45. OBSERVED VS PREDICTED AMPLITUDE

of the tests performed is predominately, if not solely, due to inertial forces. The fact that the Weber numbers for all tests were $O(10^4)$ substantiates the dominating role of inertial forces over surface tension forces.

As mentioned in Chapter VI, the amplitude data was retrieved from photographs of holograms taken of the flow fields. The holograms provide an instantaneous (50 nanosecond pulse) record of the flow fields. High speed movies (5000 frame/second) taken of the flow fields of this investigation and by McRae[12] reveal that the jet is fluctuating quite rapidly during the breakup process. When an instantaneous record is taken of the interaction flow field, the jet may be at maximum or minimum penetration or somewhere in between. This could account for some of the scatter in the data. The mean penetration trajectory which passes through the wave troughs of the jet is shown in Figure 46a. The equation for this similarity or universal curve is:

$$\bar{y} = 2.64(\bar{q})^{0.50} \ln(1 + 0.44\bar{x}) \qquad (32a)$$

where $\bar{x} = \dfrac{x}{C_d^{1/2} D_o}$ and $\bar{y} = \dfrac{y}{C_d^{1/2} D_o}$.

This penetration equation was postulated to be

$$\bar{y} = C\bar{q}^{n} \ln(1 + B\bar{x}) \qquad (32b)$$

The values for C, n and B were obtained by conducting a nonlinear regression analysis on penetration data obtained from the photographs of the holograms of the flow fields. The penetration, $\bar{y}$, was measured at three axial positions, $\bar{x} = 5$, 15 and 30, downstream from the injection

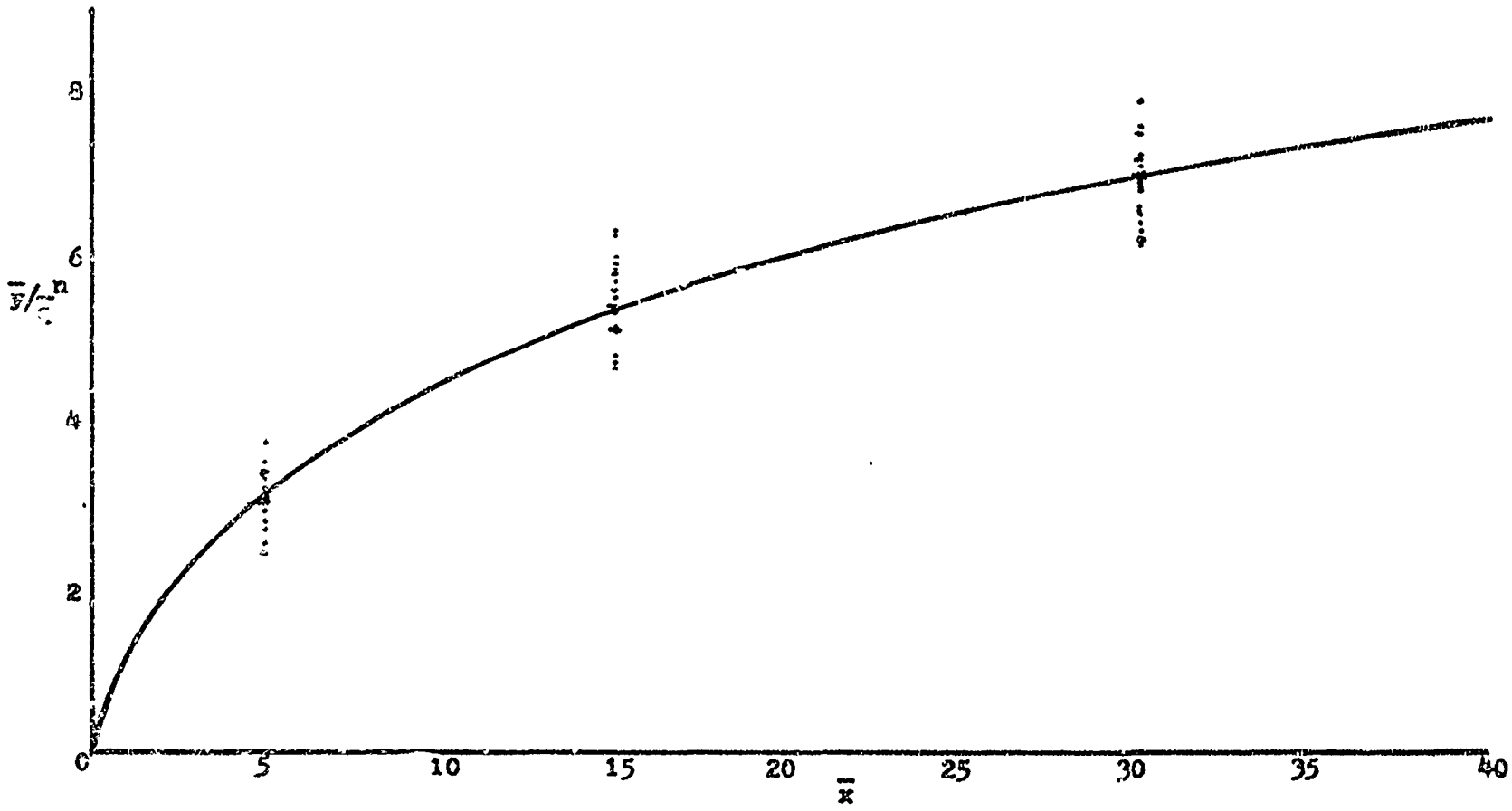

Figure 46a. Mean Penetration Trajectory for Wave Trough Line

point for each of the 25 tests. By normalizing the penetration, $\bar{y}$, values with the corresponding dynamic pressure ratio to the 1/2 power for each test, the universal trajectory of Figure 46a was obtained. The data points at the three axial locations are shown in the Figure. Here again the data is not distinguishable by liquid type. This is consistent with Catton's findings in his penetration studies. The data scatter is most likely due to the fluctuating nature of the jet breakup and the fact that the holograms provide only an instantaneous record of a time varying phenomena.

The amplitude data, and also the wavelength data which will be discussed in the next section, are presented in terms of distance along the jet trajectory, $\bar{S}$, and dynamic pressure ratio, $\bar{q}$. Jet penetration data is normally presented in terms of nondimensionalized Cartesian coordinates $\bar{x}$ and $\bar{y}$ and dynamic pressure ratio. In order to relate amplitude, wavelength and penetration data their coordinate systems need to be related. This is accomplished by performing a line integration with the penetration equation to determine the length of the jet trajectory for a given downstream distance, $\bar{x}$, or penetration, $\bar{y}$, for known $\bar{q}$. The line integral equation is obtained as follows:

Start with the penetration equation

$$\bar{y} = C\bar{q}^{n} \ln(1 + B\bar{x}) \tag{32b}$$

The nondimensionalized line integral can be written in the form

$$\bar{S} = \int_{0}^{\bar{x}} \left[1 + \left(\frac{d\bar{y}}{d\bar{x}}\right)^2\right]^{1/2} d\bar{x} \tag{32c}$$

Differentiate equation (32b) and substitute into equation (32c) to obtain

$$\bar{S} = \int_0^{\bar{X}} \left[1 + \left(\frac{C\bar{q}^{n} B}{1+B\bar{x}} \right)^2 \right]^{1/2} d\bar{x} \qquad (32d)$$

The values for C, n and B were substituted into equation (32d) from (32a) and a numerical integration was performed to obtain Figure 46b. A similarity curve for $\bar{S}$ cannot be obtained by normalizing equation (32d) with $\bar{q}^{n}$ since $\bar{q}^{n}$ remains implicit in the integral expression for $\bar{S}$. Figures 46a and 46b can be used to relate data given in Cartesian coordinates to distance along the jet trajectory for known dynamic pressure ratio. Having $\bar{S}$ and $\bar{q}$, amplitude variation can then be predicted from equation (32).

The details of the jet characteristics on the windward side of the jet were vividly visible in the 8 x 10 photographs. An example of these details is shown in Figure 47. The clearness of the jet characteristics is attributed to the extremely short pulse of the laser (50 nanoseconds) and the fact that the hologram was taken on a 1:1 correspondence (full size). Due to the clarity of the jet characteristics, retrieval of the data from the photographs was readily and accurately obtained. The shadowgraphs taken by McRae[12] and Dowdy and Newton[11] in their investigations did not produce the details of the jet characteristics that were obtained in this investigation. Another item of interest found in this investigation, which was not apparent from the shadowgraphs of the other investigations, is that practically all the jets had a bimodal amplitude. That is, every other crest instead of each crest can be related. A close look at Figure 47 will reveal this

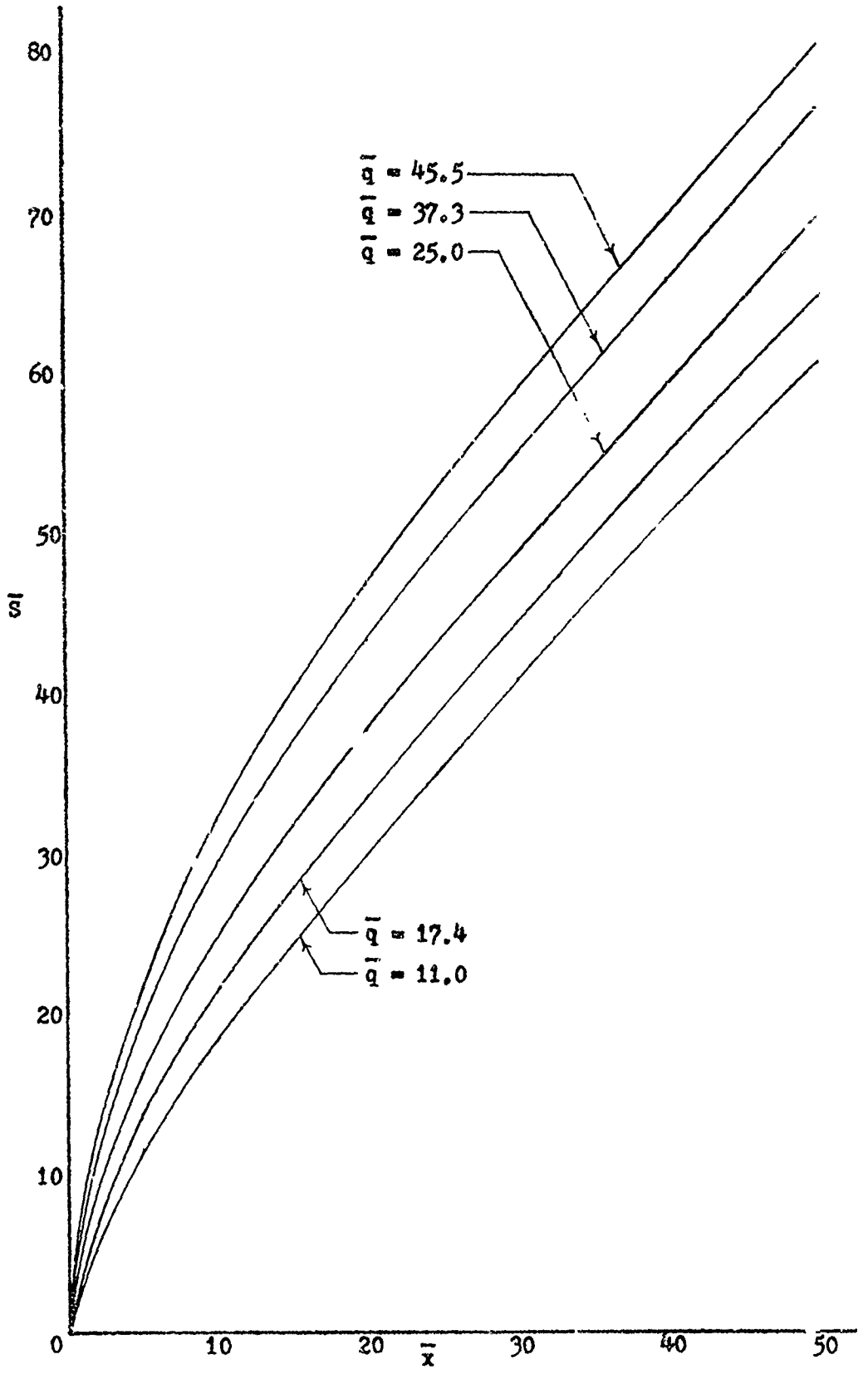

Figure 46b. Distance along Jet Trajectory vs. Downstream Distance

Figure 47. Enlarged View of Jet Characteristics in Supersonic Stream, Test No. DR-3.

binodal amplitude behavior. For the sake of simplicity only the first mode amplitude data was analyzed.

b. Liquid Jet Wavelength: An approach similar to the one taken in the analysis of the amplitude data was taken in the analysis of the wavelength data. The modeling equation assumed had the same form as the amplitude equation:

$$\lambda = \frac{\lambda'}{C_d^{1/2} D_o} = C\left(\frac{S}{C_d^{1/2} D_o}\right)^N \left(\bar{q}\right)^M \qquad (33)$$

The values for C, N and M were obtained from a nonlinear regression analysis performed on the data. The resulting equation which characterized wavelength behavior is:

$$\lambda = 1.748(\bar{S})^{1.361} (\bar{q})^{-0.720} \qquad (34)$$

The observed wavelength data for all the liquids is plotted against the wavelength predicted by equation (34) in Figure 48. Similar to the amplitude data, one cannot isolate wavelength behavior by liquid type. The data scatter for wavelength is greater than that for amplitude. Perhaps wavelength variations are more sensitive to jet penetration fluctuations than are amplitude variations.

The jet wavelengths and amplitudes behave similarly. That is, both increase with increase in distance from the injection point and decrease with increase in dynamic pressure ratio, $\bar{q}$. A relationship between wavelength and amplitude can be drawn:

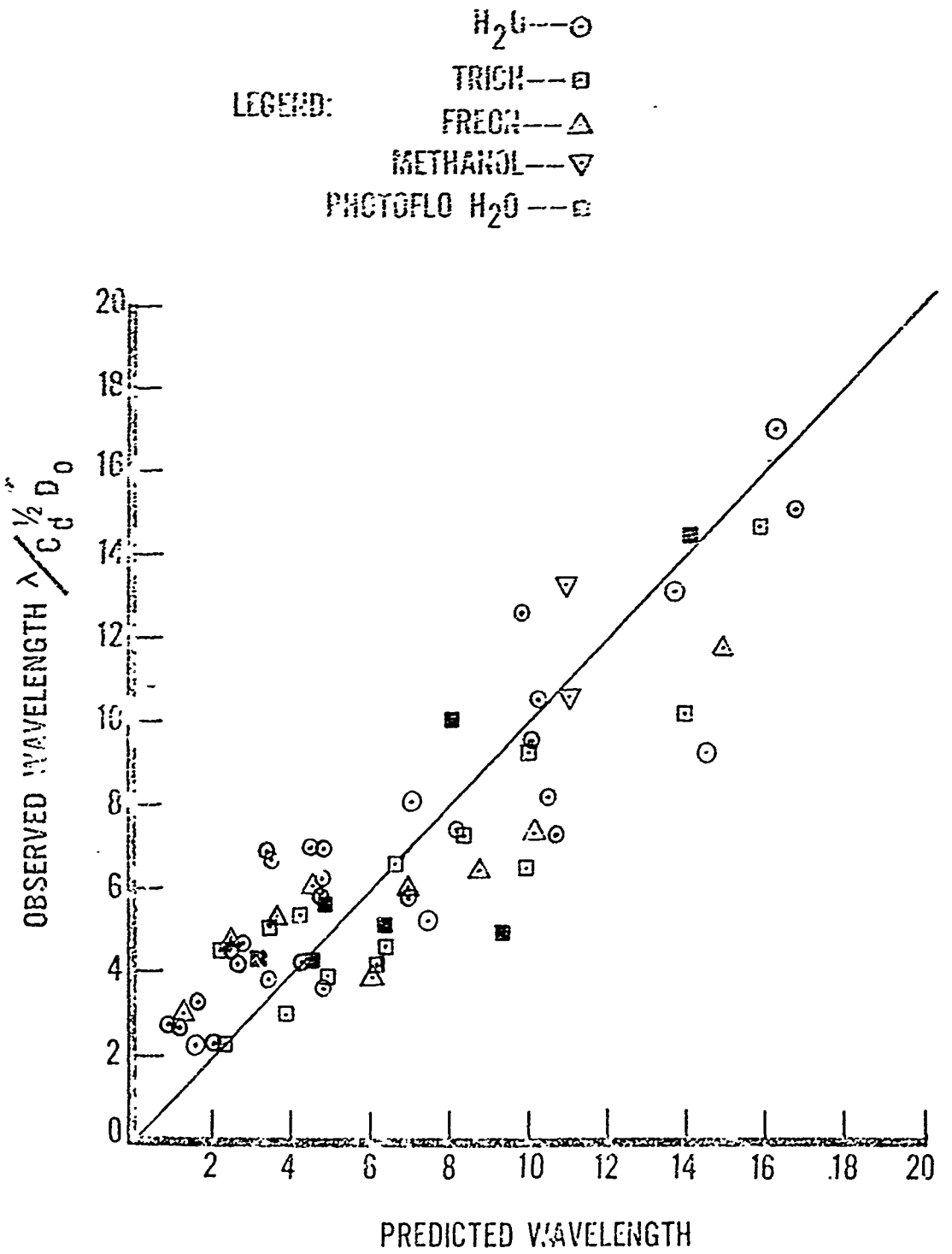

Figure 48. OBSERVED VS PREDICTED WAVELENGTH

$$\frac{A}{\lambda} = 0.141 \left(\frac{S}{C_d^{1/2} D_o}\right)^{-0.215} \left(\bar{q}\right)^{0.292} \qquad (35)$$

There are some analyses, Harvey[14], Mayer[15] and Adelberg[16], which postulate that droplets formed as a result of jet breakup are a function of wavelength only. Perhaps wave amplitude plays a part in drop size distribution. In light of the jet characteristics showing more than one amplitude mode, the drop size distribution may be related to these modes. Unfortunately, droplet data was not retrievable from the holograms of the supersonic flow field, and to pursue these thoughts analytically is beyond the scope of this investigation.

In this section, and in the previous one on amplitude, an attempt to characterize the jet behavior by model equations was made. Figures 45 and 48 presented the observed vs. predicted amplitude and wavelength, respectively. Supplemental figures and discussion regarding the behavior of these two items with respect to trajectory distance, $\bar{S}$, and dynamic pressure ratio, $\bar{q}$, are presented in Appendix V.

3. Liquid Jet Injection into Still Air

a. Droplet Spatial Distribution: The spray resulting from a cylindrical jet can be characterized in the axial and radial directions from the injection point. The axial position characterization will be discussed in the next subsection. Drop size and mass distribution in the radial direction for each of the two axial regions denoted in Chapter VI will be discussed in this subsection.

The initial endeavor at characterizing the spray in the radial direction attempted to produce droplet class size-positional coordinate plots. These plots were output from the PR-472 computer program described in Chapter V. Each of the two axial regions of the spray was treated as an infinitely thin slice; hence, the resulting positional information for each region became two-dimensional. Each plot represented a plane perpendicular to the jet longitudinal axis; the abscissa and ordinate represented the coordinates of the plane. Each class size was identified by different symbols (up to 5 classes per plot) and the droplets in each class were plotted according to their positional coordinates. These plots were reviewed to determine if contour lines joining the droplet class size symbols could be drawn, or if the droplets congregated in regions according to their size. Two observations were made when the plots were reviewed:

1) The droplets appeared randomly dispersed. That is, segregation according to drop size was not detectable, droplets of a given size did not congregate in isolated regions and spatial stratification of the droplets by size was not evident. Hence, meaningful contour

lines could not be drawn.

2) The solid core of the horizontal jet blocked those droplets in front and behind the jet in a profile view. Only those droplets above and below the core were visible in the hologram. The explanation for this is that transmission holography is a back lighting technique which silhouettes the objects. The core of the jet overshadowed the small droplets which are closely dispersed about the core, rendering these droplets undetectable, although they scattered some of the laser light. This problem was not encountered where the solid core of the jet was nonexistent.

The radial characterization of the droplet data was then accomplished as follows:

1) The orifice radius (.053 inches) was used as the reference dimension for determining the spreading of the spray;

2) The transverse coordinates for each droplet in a given axial slice (again assumed infinitely thin) were used to calculate the magnitude of the position vector

$$R = \sqrt{X^2 + Z^2}$$

3) The droplets were then placed in the proper annuli according to the magnitude of their position vectors. The spacing between the annular rings was in terms of the orifice radius:

Position Radius, $R_1 = .053$ (orifice radius)

" " $R_2 = .107$ ($R_2 = 2R_1$)

" " $R_3 = .160$ ($R_3 = 3R_1$)

. .

. .

. .

" " $R_N = NR_1$

4) The droplet class size-number count, volume fraction and cumulative volume fraction were then determined for each annulus.

The arrangement of the data as determined by the procedure explained above is presented in Table XX. These data are also plotted in Figures 49, 50 and 51. The droplet number count and volume fraction in each annulus are plotted against the mid-position radius while the cumulative volume fraction is plotted against the maximum position radius. It is more meaningful to present the data in this manner.

One can observe the following from the Table and Figures:

1) The data is well-behaved and monotonic in nature. The number of droplets and volume fraction increase to a peak and then decrease with increase in radial distance.

2) The radial spreading of the droplets is greater at the longer axial slice, 2.

The droplet number and mass distribution in the radial direction for both axial regions are statistically significant. A Chi-square goodness-of-fit test was applied to the data to make this determination. In axial slice 1 there were 272 droplets. These droplets occurred in 10 annuli or intervals. Applying the Chi-square criteria to these conditions, only 12 droplets would be needed for 95% confidence (17 droplets for 99% confidence) that the radial distribution of the data is meaningful. In axial slice 2 there were 400 droplets. These droplets occurred in 12 annuli or intervals. Again, applying the Chi-square criteria to these conditions, approximately 20 droplets would be needed for 95% confidence (30 droplets for 99% confidence) that the radial distribution of the data is meaningful.

TABLE XX: RADIAL DISTRIBUTION DATA

ANNULUS NO.	MAX. POS. RADIUS (INCHES)	MID-POS. RADIUS (INCHES)	SLICE 1 3.0 - 3.5 DROP-LET NO.	VOL. FRAC.	CUM. VOL. FRAC.	SLICE 2 3.5 - 4.0 DROP-LET NO.	VOL. FRAC.	CUM. VOL. FRAC.
1	.053	.027	6	0	0	0	0	0
2	.107	.080	0	0	0	1	.0009	.0009
3	.160	.133	5	.0062	.0062	17	.0534	.0543
4	.213	.187	19	.0646	.0708	32	.1430	.2073
5	.266	.240	37	.1839	.2547	46	.1512	.3585
6	.320	.293	60	.2715	.5262	71	.1726	.5311
7	.373	.346	62	.2697	.7959	63	.1872	.7183
8	.426	.400	43	.1150	.9109	53	.1248	.8431
9	.480	.453	19	.0488	.9597	50	.1028	.9459
10	.533	.506	15	.0244	.9841	42	.0278	.9737
11	.586	.560	11	.0154	.9995	17	.0161	.9898
12	.640	.613	1	.0005	1.0000	7	.0086	.9984
13	.693	.666				1	.0016	1.0000
			Σ 272			Σ 400		

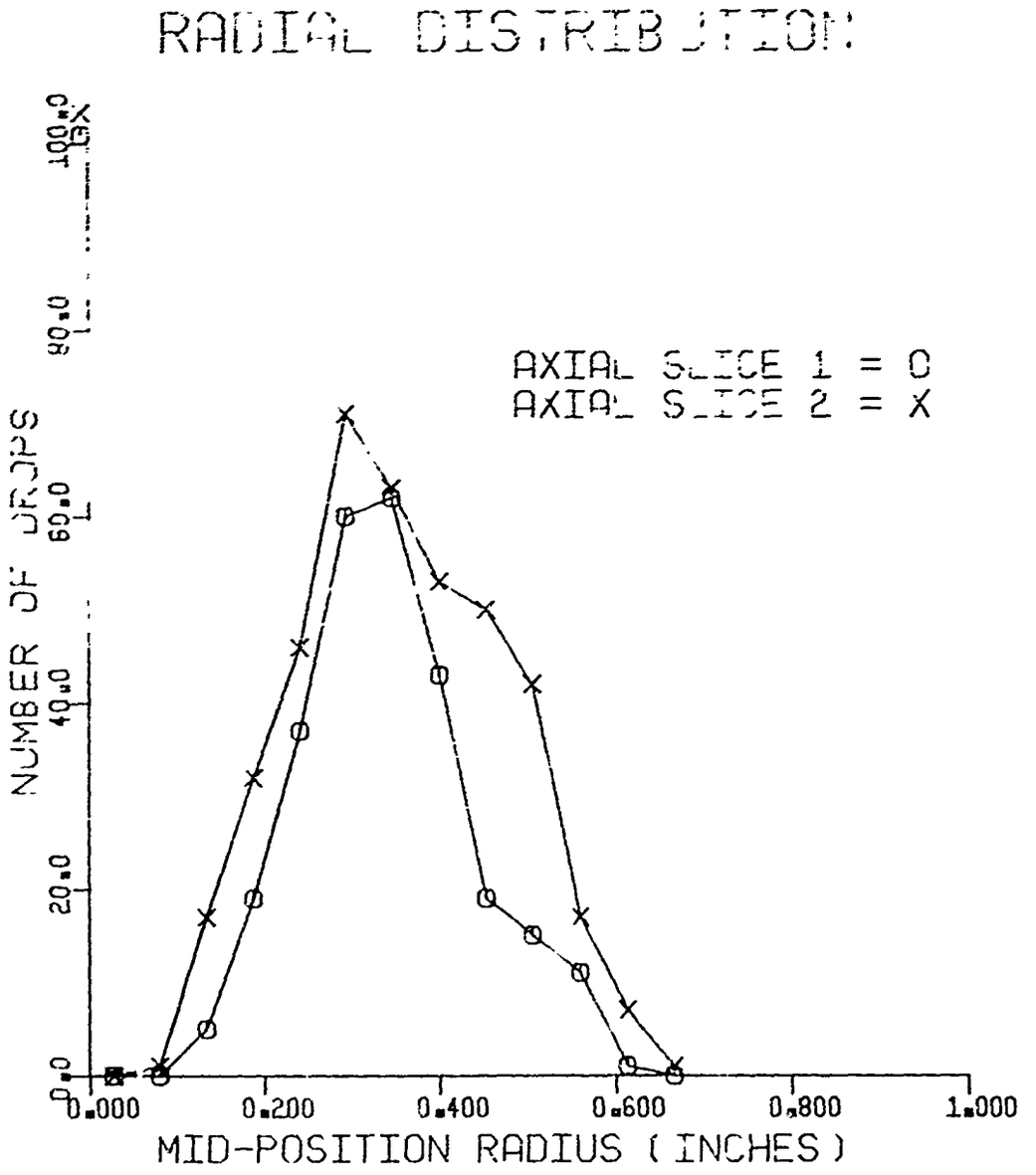

Figure 49. Radial Distribution, Number of Drops

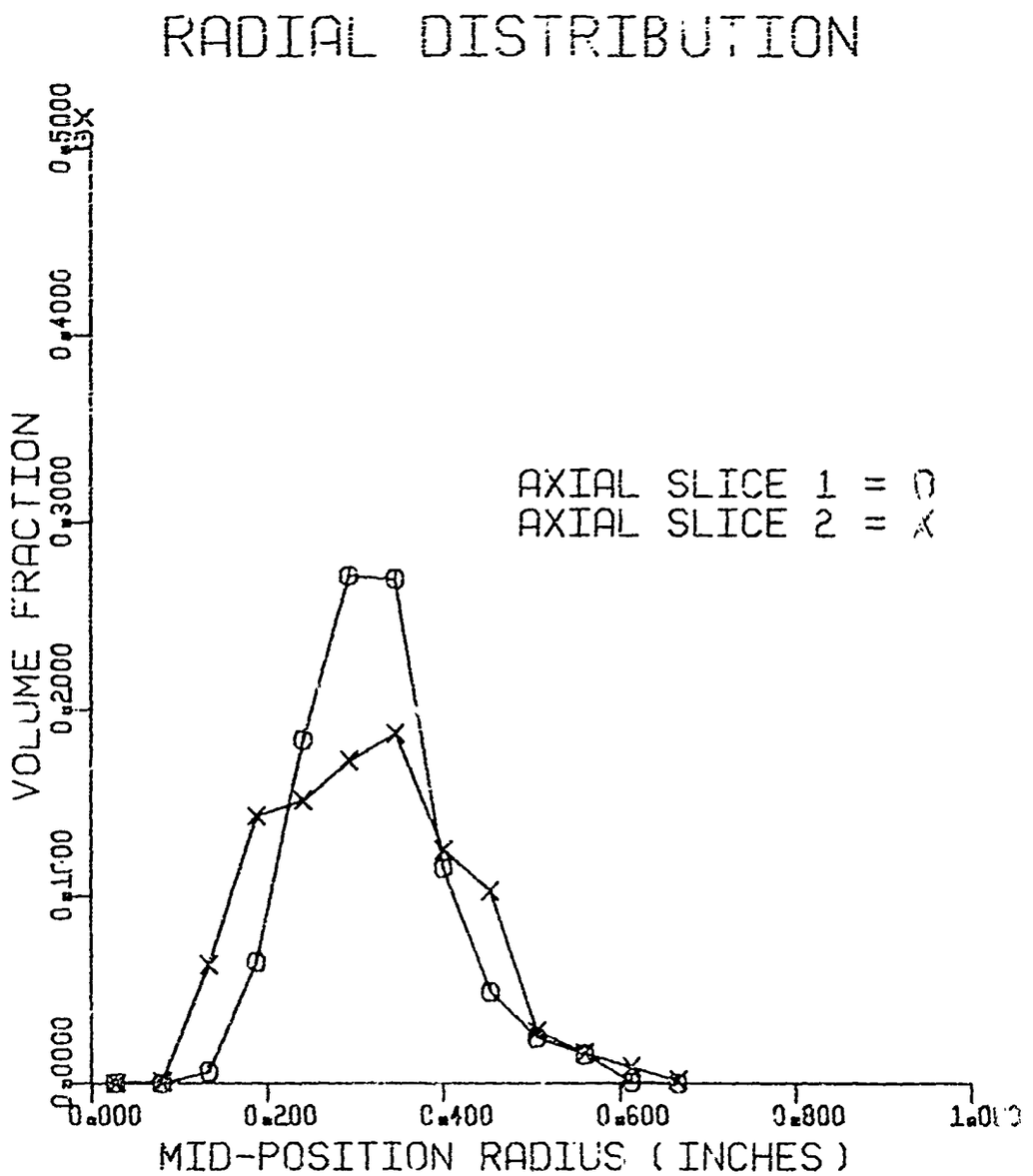

Figure 50. Radial Distribution, Volume Fraction

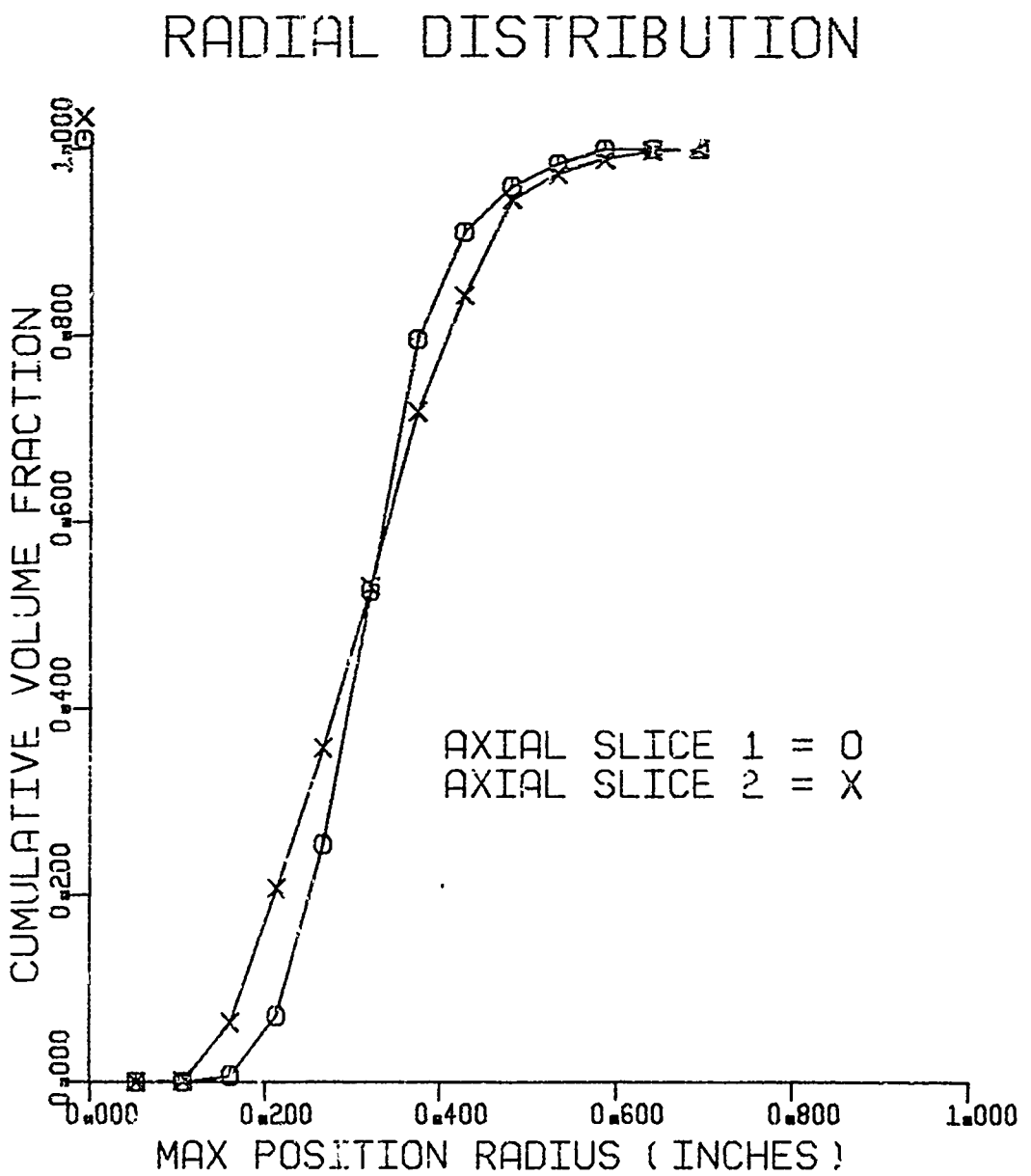

Figure 51. Radial Distribution, Cumulative Volume Fraction

Since there is a droplet size distribution within each annulus, one can calculate the various mean diameters for each annulus. A variation in these mean diameters will occur among the annuli, but is this variation statistically significant? In other words, is there a meaningful variation in mean droplet diameter from annulus to annulus? Here the situation is different from the radial number and mass distribution, since the number of class sizes in which the droplets occur and span must be considered instead of the annuli. Table XXI presents the number of class sizes spanned by the droplets, droplet number count and the calculated D_{30} in each annulus. Application of the Chi-square criteria revealed an insufficient number of droplets existed, for the class size range in each annulus, for 95% confidence that the variation in D_{30} with radial position was significant. Even by regrouping the droplet data and decreasing the confidence level to 90%, application of the Chi-square test indicated, again, there was an insufficient number of droplets to state positively that a radial variation in mean diameter occurs.

As noted above, some of the droplets were blocked by the solid core of the liquid jet. An analysis was conducted to determine if the droplet mass contained in the portion of each annulus blocked by the jet core was significant. It was not. Maximum change in droplet volume (mass) in any annulus, due to spatial area correction, was 3%, which is within the accuracy of the data. The correction method is explained in Appendix IV.

b. Droplet Size Distribution: After investigating the radial distribution of the droplets, their corresponding spatial coordinates were deleted from the data sets. Size distribution of the droplets in

TABLE XXI: DROP SIZE RADIAL VARIATION

ANNULUS NO.	POSITION RADIUS (INCHES)	AXIAL SLICE 3.0-3.5 CLASSES k	DROP NO. N	D_{30}	AXIAL SLICE 3.5-4.0 CLASSES k	DROP NO. N	D_{30}
1	.053	0	0	0	0	0	0
2	.107	0	0	0	1	1	190
3	.160	14	5	217	26	17	320
4	.213	21	19	317	41	32	360
5	.266	42	38	362	29	46	329
6	.320	40	59	363	30	7.	302
7	.373	29	62	360	38	63	328
8	.426	25	43	308	31	53	305
9	.480	18	19	304	28	49	295
10	.533	17	15	263	13	43	199
11	.586	14	11	250	15	17	228
12	.640	1	1	170	13	7	248
13	.693	0	0	0	1	1	270
			$\Sigma 272$			$\Sigma 400$	

each axial slice was then investigated, and this is the topic of discussion in this subsection. The number distribution (frequency diagram) for the droplets in slices 1 and 2 are shown in Figures 52, 53 and 54. A look at Figures 52 and 54 will reveal the following:

1) The number of droplets in each diameter class size increases monotonically to the mode; after that there is scatter in the data. This appears to be a typical behavior of droplet data, since other investigators have experienced similar results.

2) The mode for slice 2 is 95 microns as compared to 216 microns for slice 1. Since slice 2 is farther from the injection point than axial slice 1, the inference is that the droplet sizes decrease with increase in distance from the injection point. This would lead one to believe that jet core size has an effect on the resulting droplet sizes. As the droplets are shed, the core size becomes smaller until finally the jet is completely broken up into droplets. Figure 53 shows the resulting droplet frequency when the last 5 droplets are regrouped into one class size interval. The purpose for doing this is to reduce the scatter of the data. The effect will be discussed below.

As previously mentioned in this treatise, four known distribution functions (Log-Probability (L-P), Upper-Limit (U-L), Nukiyama-Tanasawa (N-T) and General Exponential (GE))were selected to model the data to determine if any of them could be used to characterize the spray. Initially, these models were written in terms of volume fraction derivative and cumulative volume fraction. The data was normalized by the droplet total volume which was the standard procedure followed by previous investigators. However, this caused problems in curve fitting

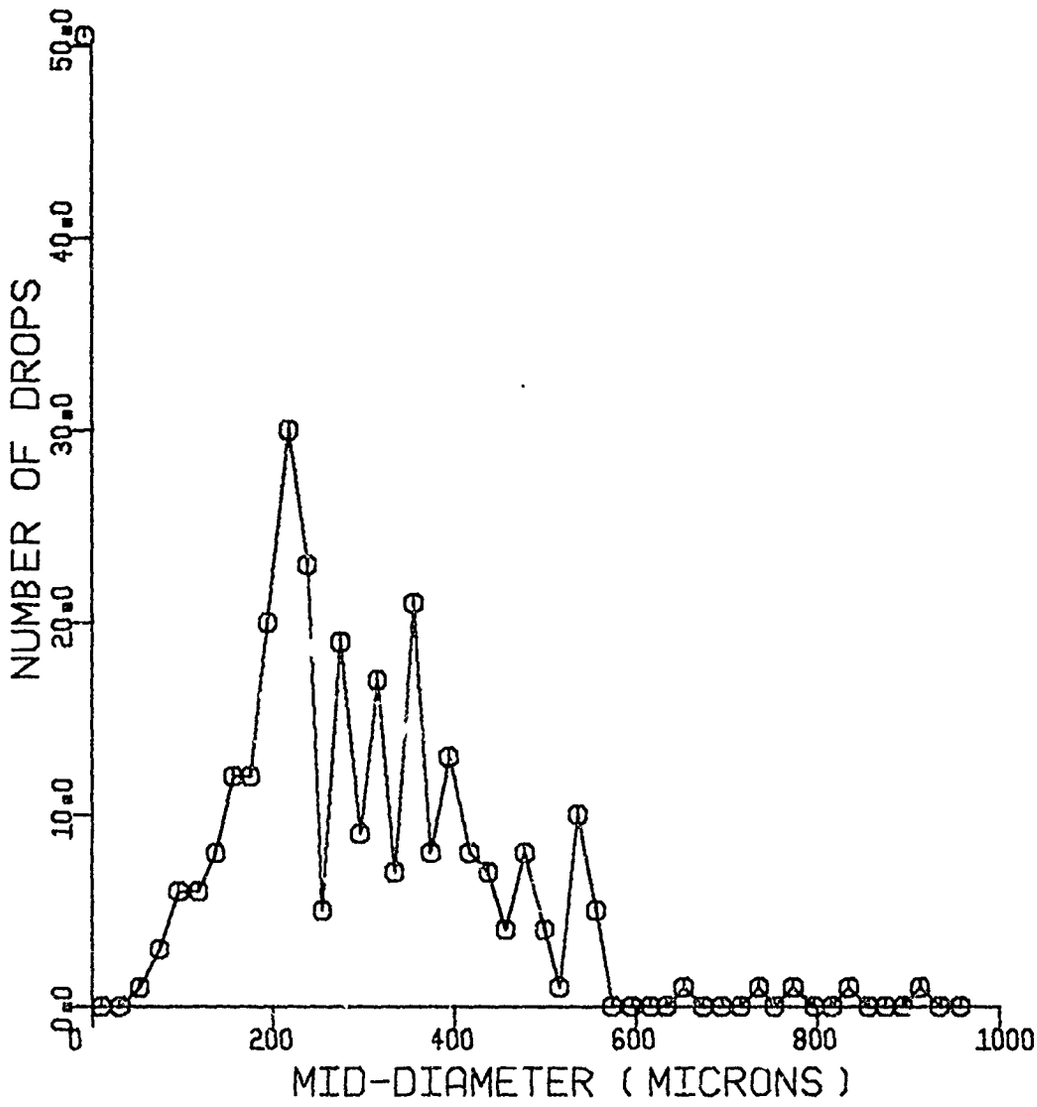

Figure 52. Frequency Diagram, Slice 1, Actual Data

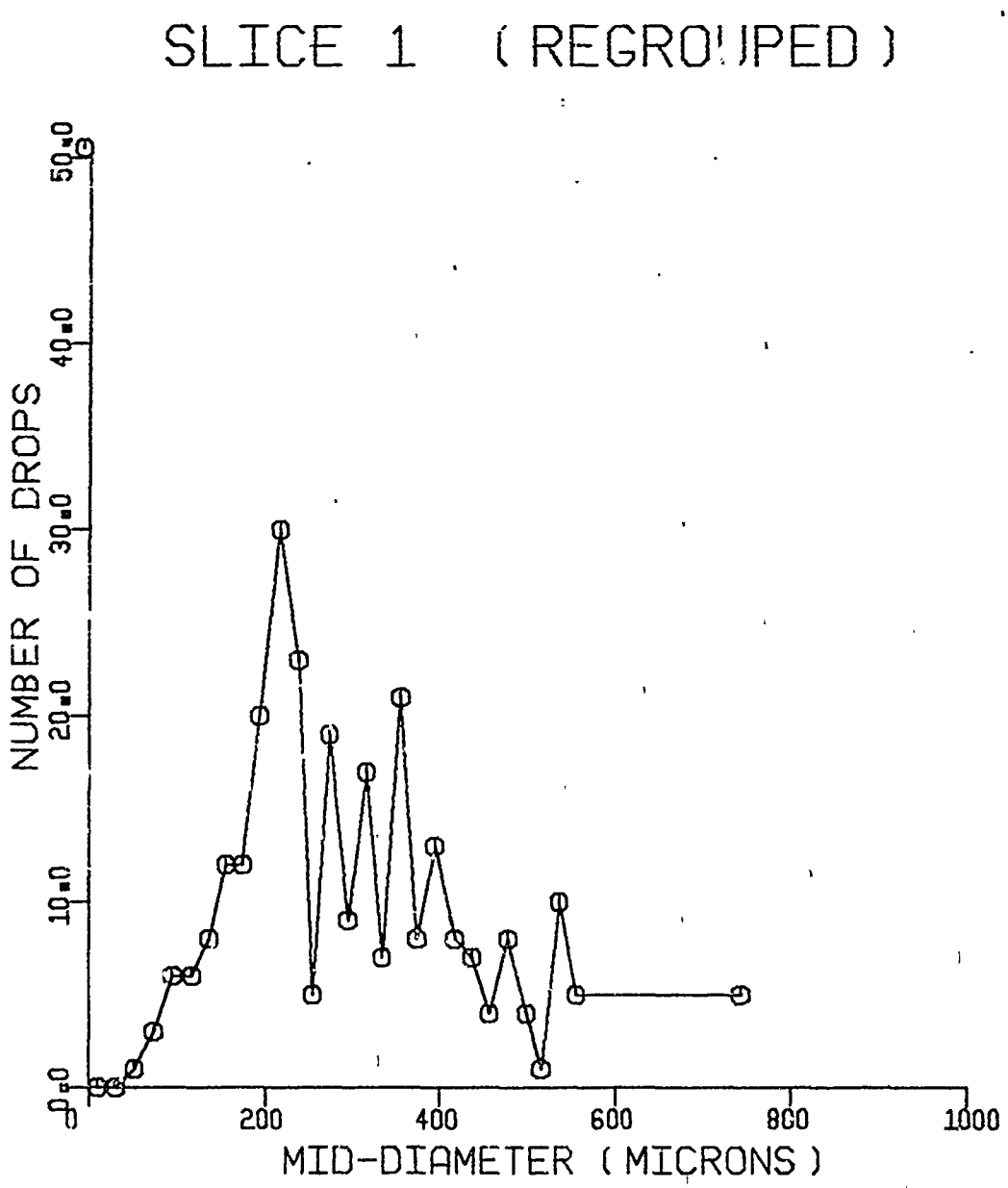

Figure 53. Frequency Diagram, Slice 1, Regrouped Data

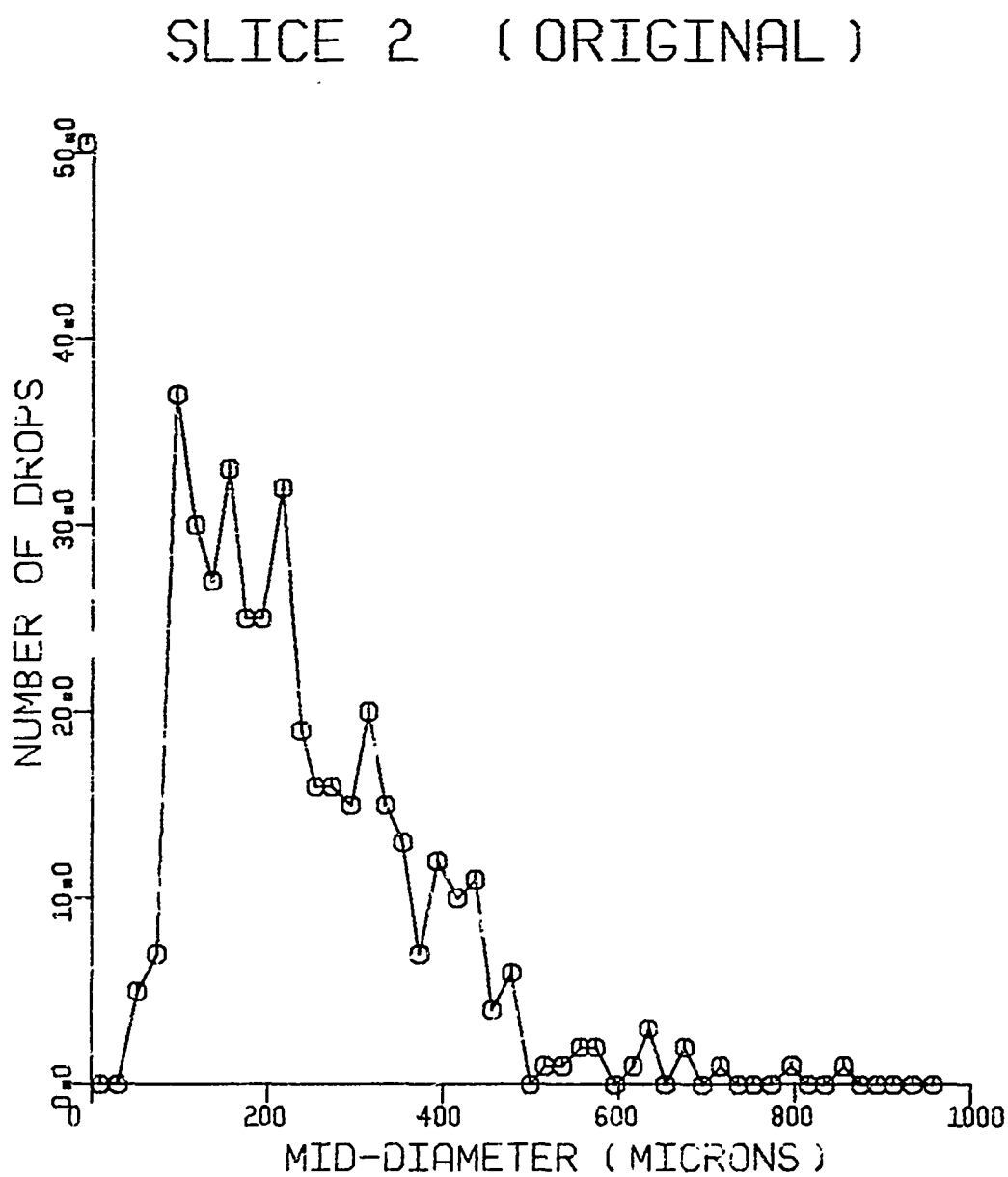

Figure 54. Frequency Diagram, Slice 2, Actual Data

the models to the data. The droplet volumes predicted by the models were much greater than those of the data since the distribution functions were integrated from 0 to ∞ whereas the data was summed to a given maximum diameter. This problem was observed when the coefficients obtained from the cumulative volume fraction (CFV) models were not the same as or equal to those obtained from the volume fraction derivative (VFD) models. The coefficients from these models should be the same, since the VFD models are the derivatives of the CFV models and conversely, the CFV models are the integrals of the VFD models. The problem was eliminated by writing the models in terms of volume for curve fitting to the data. See Appendix II. After the coefficients were obtained, the equations were converted to volume fraction and cumulative volume fraction by normalizing them with the total volume predicted by the models. The data was also normalized by the model predicted volume. The procedure described above is a more accurate way of curve fitting the data than had been done previously. Conversion to the volume fraction derivative and cumulative volume fraction was done to present the information in a familiar manner.

The best results were obtained with the Log-Probability and modified General Exponential functions, as determined from the MM-203 Nonlinear Regression Analysis computer program. For the data in this investigation, the U-L function collapsed to the L-P function, of which it is a modified version. The U-L function has 3 coefficients while the L-P function has 2 coefficients. The program indicated, through the t-statistics for the coefficients, that a 3-coefficient function was overparameterized for the data. Another finding was that the N-T and GE functions were very sensitive to the data set. Many

iterations were required for convergence regardless of the initial estimates of the coefficients. By setting the "b" coefficient of the GE function equal to one, thus modifying the function and reducing the number of coefficients to two, this function converged more rapidly than before and yielded the best characterization of the spray. The resulting equation was

$$\frac{dVol}{dD} = \frac{V_{total}\, q\, D^{p}\, e^{-D^{q}}}{\Gamma\left[(p+1)/q\right]} \qquad (36)$$

The values of the coefficients for the L-P and modified GE functions are presented in Table XXII. The differences in the values for the cumulative volume and volume derivative models for a given distribution function are attributed to round off errors and errors in the approximation procedure. Also, the cumulative volume model accumulates error in each class size interval. Also presented in the Table is pertinent statistical information. One can observe the following:

1) The per cent variation of the data explained by the volume derivative is poor. This is attributed to the scatter in the data.

2) There is less data scatter in axial slice 2 than in slice 1. Regrouping of the data reduces the scatter and improves the per cent variation explained by the volume derivative models. The coefficients for the original (actual) and regrouped data are quite similar.

3) There is excellent agreement between the cumulative volume models and the data.

The statements made relative to slice 1 and 2 data, the effect of regrouping the data and characterization of the data by the volume fraction derivative and cumulative volume fraction, are substantiated in

TABLE XXII: MODEL COEFFICIENT VALUES AND STATISTICAL INFORMATION

		Log-Probability				Modified General Exponential (b = 1)			
		Cumulative Volume		Volume Derivative		Cumulative Volume		Volume Derivative	
		Slice 1		Slice 1		Slice 1		Slice 1	
		Original	Regrouped	Original	Regrouped	Original	Regrouped	Original	Regrouped
Final Values of Coefficients	δ*	1.930	1.959	1.978	1.583	q* .5377	.5425	.5441	.4995
	D	454.4	461.6	463.4	587.4	p13.586	14.275	14.43	10.972
	V	6.37E+09	6.61E+09	6.19E+09	10.48E+09	V 6.28E+09	6.52E+09	6.08E+09	9.71E+09
T-stats. for Coefficients	δ	23.10	22.55	5.81	4.27	q 62.12	65.33	15.56	11.04
	D	84.24	62.01	15.51	5.53	p 15.19	16.40	3.75	3.20
	V	65.56	34.638	6.52	2.88	V 72.80	39.89	6.70	3.34
F-Ratio**		2629.25	1402.1	8.59	14.75	2571.9	1631.26	8.58	15.12
% Explained		99.43	99.39	36.70	62.99	99.42	99.47	36.38	63.58
D_{30}		371	379	383	435	363	373	372	418
D_{32}		425	433	435	532	419	427	425	507
		Slice 2		Slice 2		Slice 2		Slice 2	
Final Values of Coefficients	δ	1.516	1.534	1.689	1.616	q .4916	.4972	.5109	.5077
	D	455.1	452.9	451.2	463.1	p 9.083	9.485	10.701	10.47
	V	6.54E+09	6.51E+09	6.48E+09	6.82E+09	V 6.40E+09	6.30E+09	6.41E+09	6.55E+09
T-stats. for Coefficients	δ	32.62	20.58	7.70	6.162	q 80.07	50.34	19.81	15.77
	D	81.98	38.22	17.30	11.67	p 21.77	14.29	5.09	4.29
	V	69.14	26.65	8.52	6.22	V 76.48	29.04	8.84	6.85
F-Ratio		5588.6	1945.07	14.57	12.62	5067.9	1791.76	14.51	12.56
% Explained		99.74	99.52	50.40	57.48	99.72	99.48	50.35	57.38
D_{30}		328	329	347	347	313	316	332	332
D_{32}		403	407	413	421	398	396	403	406

δ * δ, D̄ and V and q, p and V are coefficients in the Log-Probability and General Exponential equations, respectively, presented in Appendix II.

F-Ratio ** Confidence level for all F-Ratios is 99.9%.

Figures 55 through 61. Tabulated output corresponding to Figures 59 and 61 are presented in Tables XXIII and XXIV, respectively.

c. Droplet Velocity and Stability: Droplet velocity was calculated from the momentum equation

$$F = m\frac{dV}{dt} \tag{37}$$

Constant droplet mass was assumed. $\left(m = \frac{\pi D^3 \rho_l}{6}\right)$

Drag on a droplet

$$F = C_D A \tfrac{1}{2} \rho_g V^2 \tag{38}$$

Neglect gravity effect.

Substitute into equation (37)

$$C_D \left(\frac{\pi}{4} D^2\right) \tfrac{1}{2} \rho_g V^2 = \frac{\pi D^3}{6} \rho_l \left|\frac{-dV}{dt}\right| \tag{39}$$

Integrate equation (39). Use the initial condition that at $t = 0$, $V = V_{injection}$, then eliminate t by $t = x/v$. The resulting equation is

$$V_l = \left(1 - 3/4 \frac{\rho_g}{\rho_l} \frac{C_D}{D} x\right) V_{injection}, \tag{40}$$

where C_D was assumed constant. Actually $C_D = f(Re)$. An analysis was conducted with C_D as a variable.

$$C_D = C_o \left(1 + \frac{\delta_o}{Re^{\frac{1}{2}}}\right)^2 \tag{41}$$

where $C_o \delta_o^2 = 24$

$\delta_o = 9.06$

This expression for drag coefficient was obtained from Abraham[74] and gives excellent correlation with data for $0 \leq Re \leq 5000$. A closed form

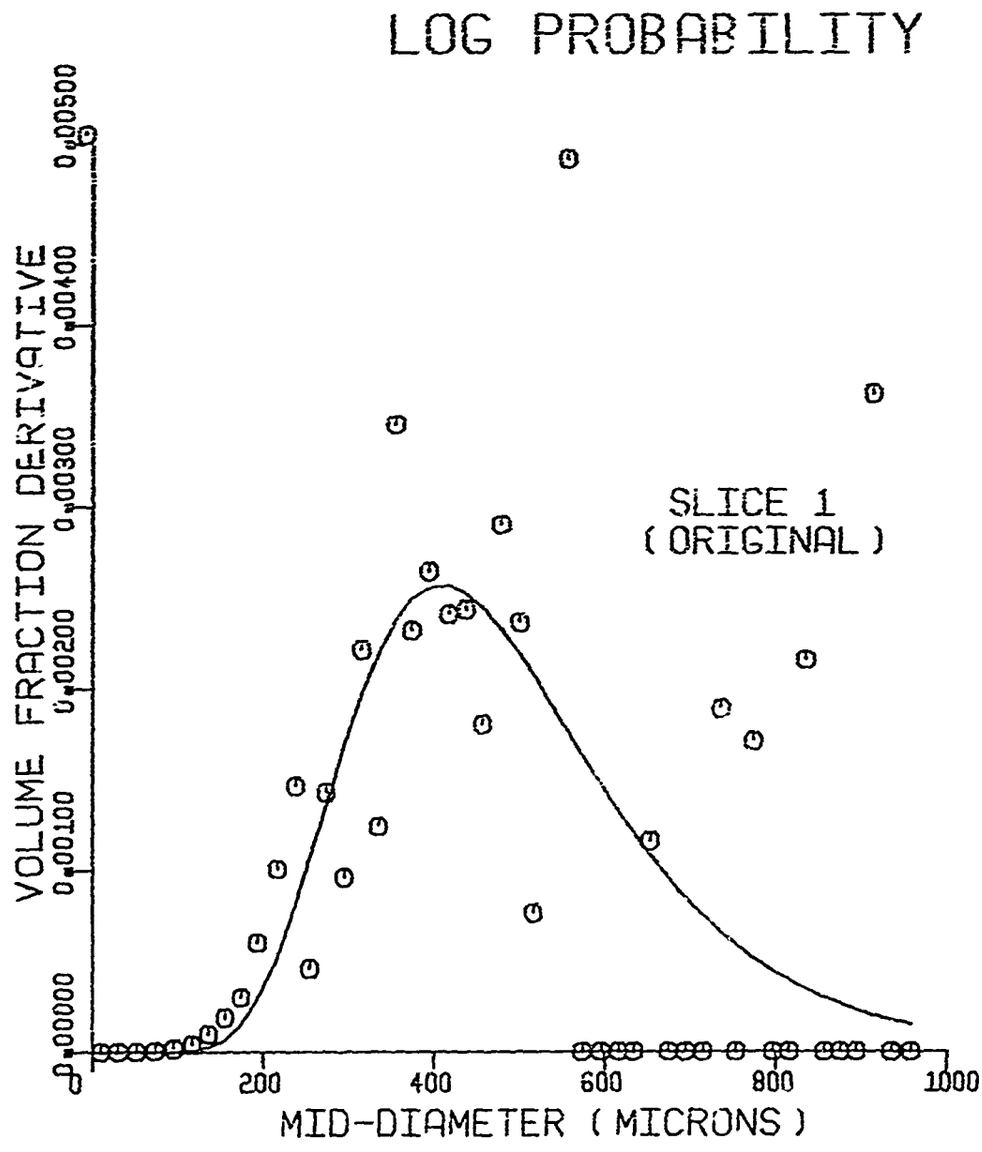

Figure 55. Droplet Data Distribution and Model Prediction Curve

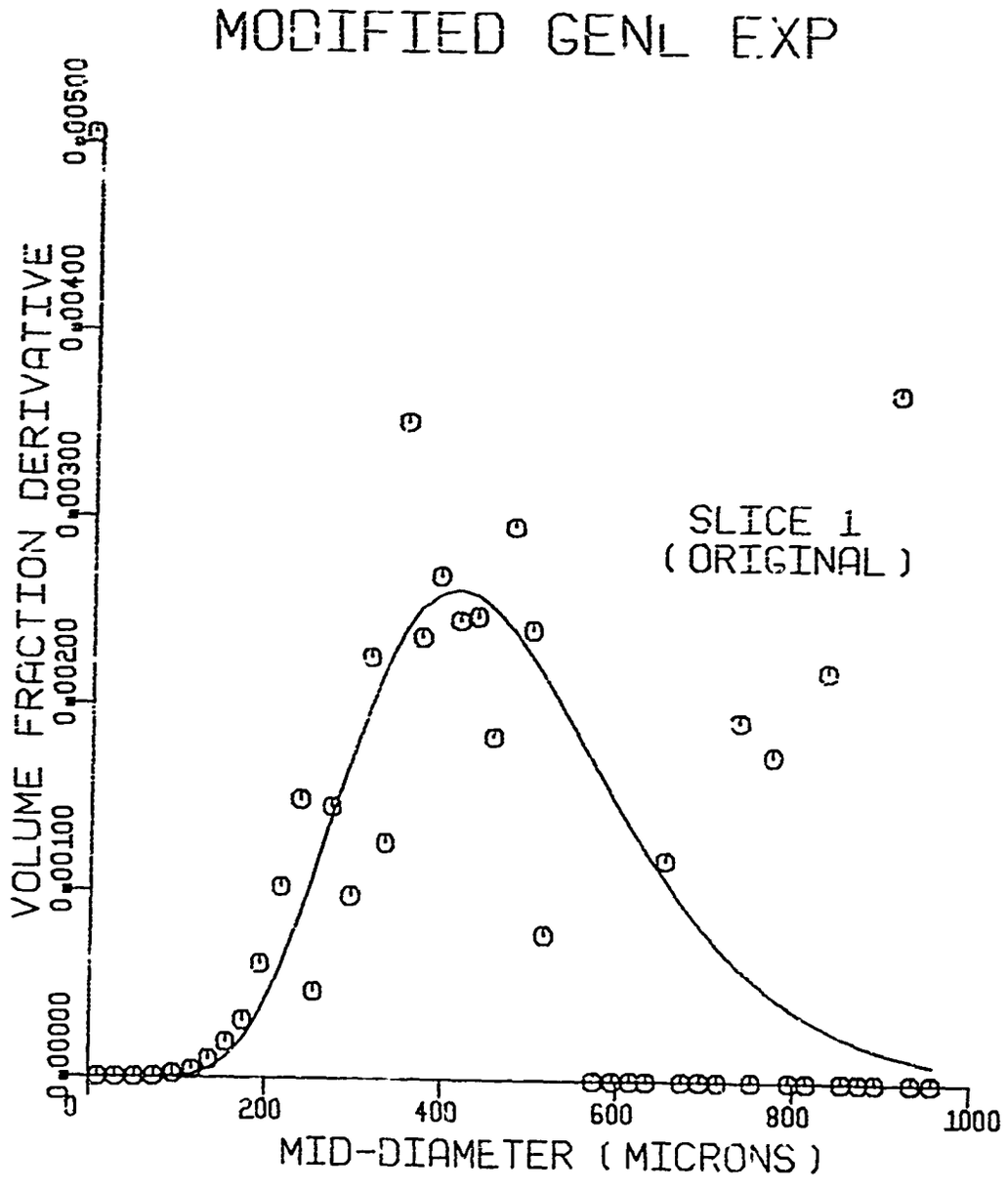

Figure 56. Droplet Data Distribution and Model Prediction Curve

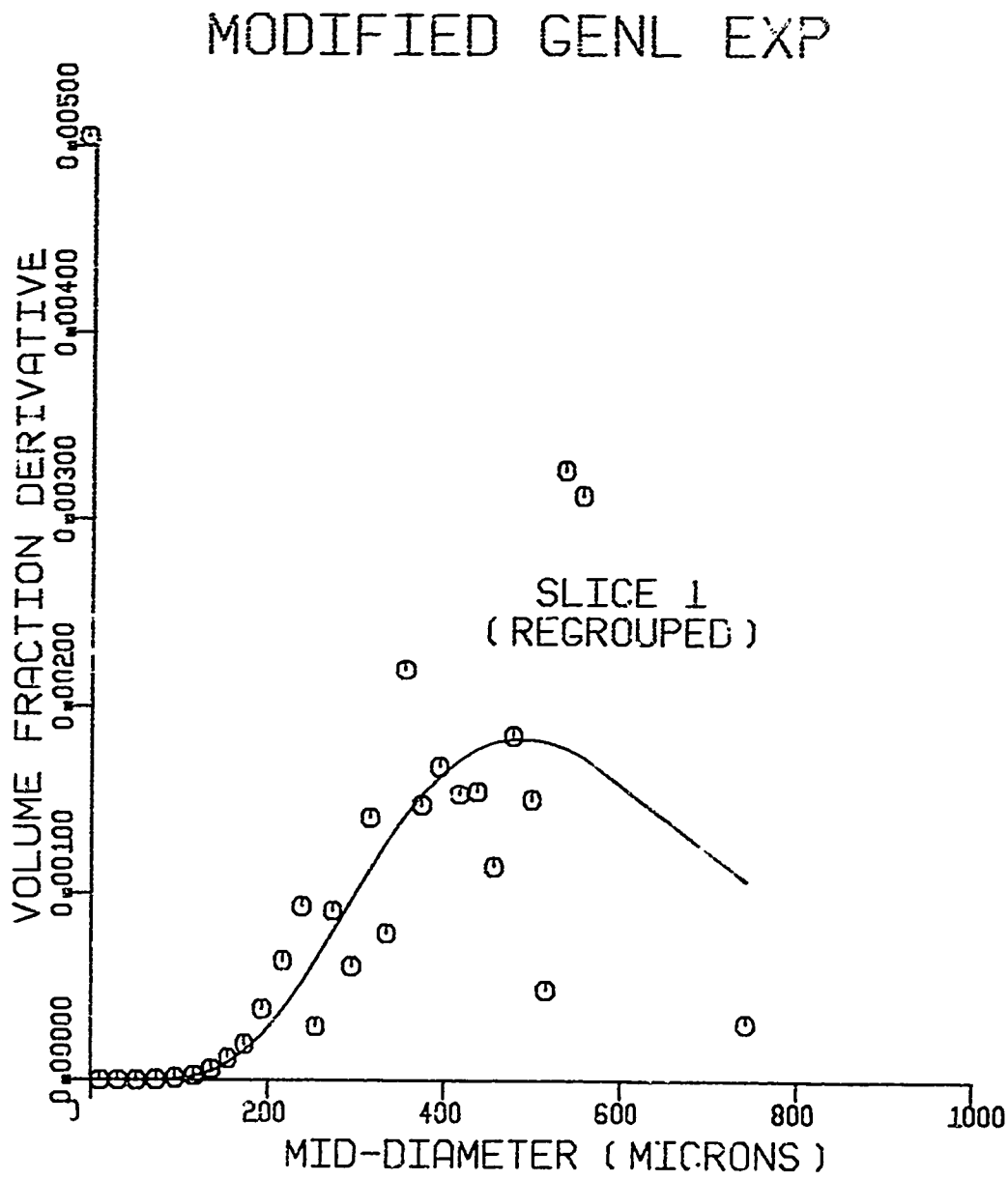

Figure 57. Droplet Data Distribution and Model Prediction Curve

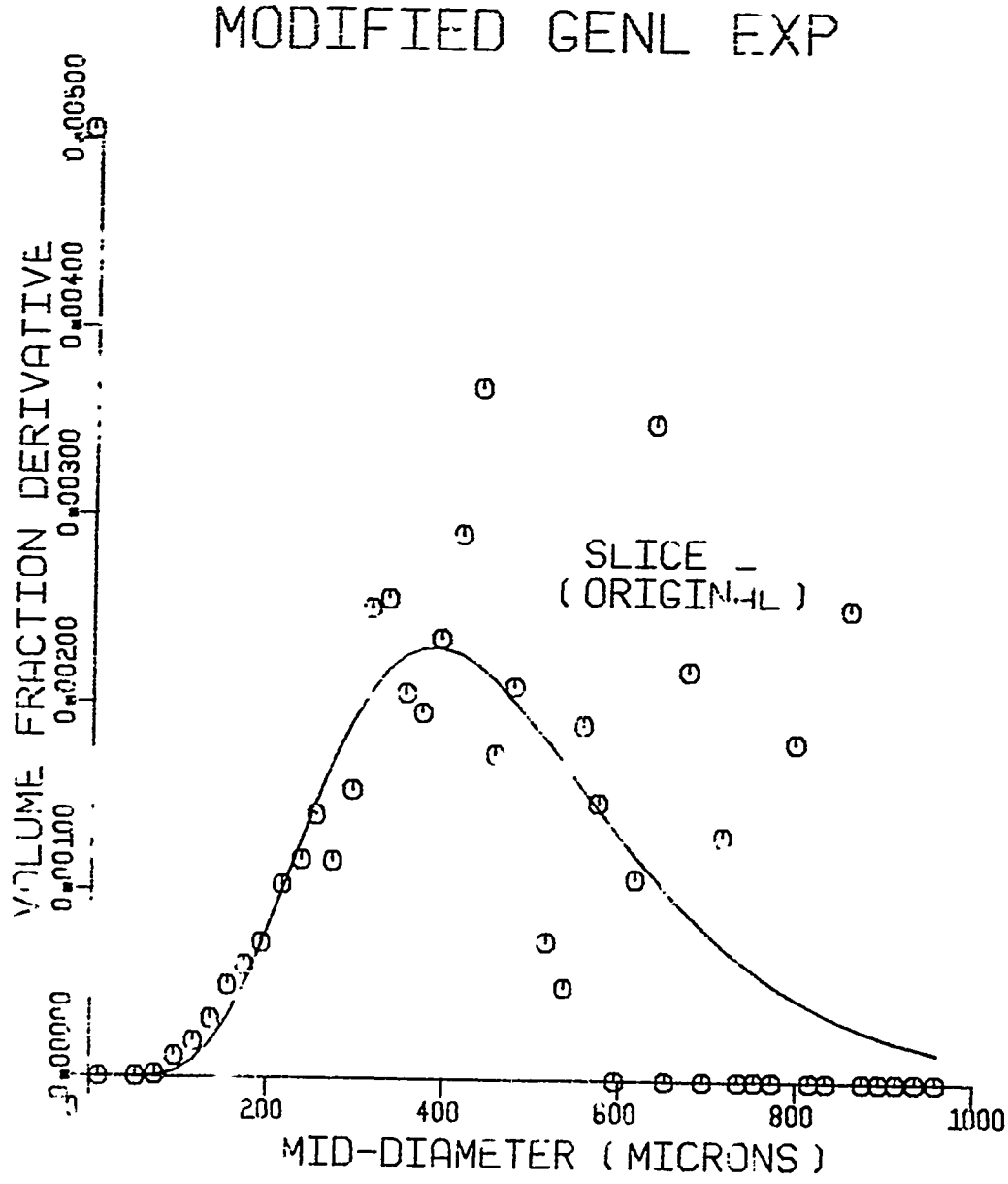

Figure 58. Droplet Data Distribution and Model Prediction Curve

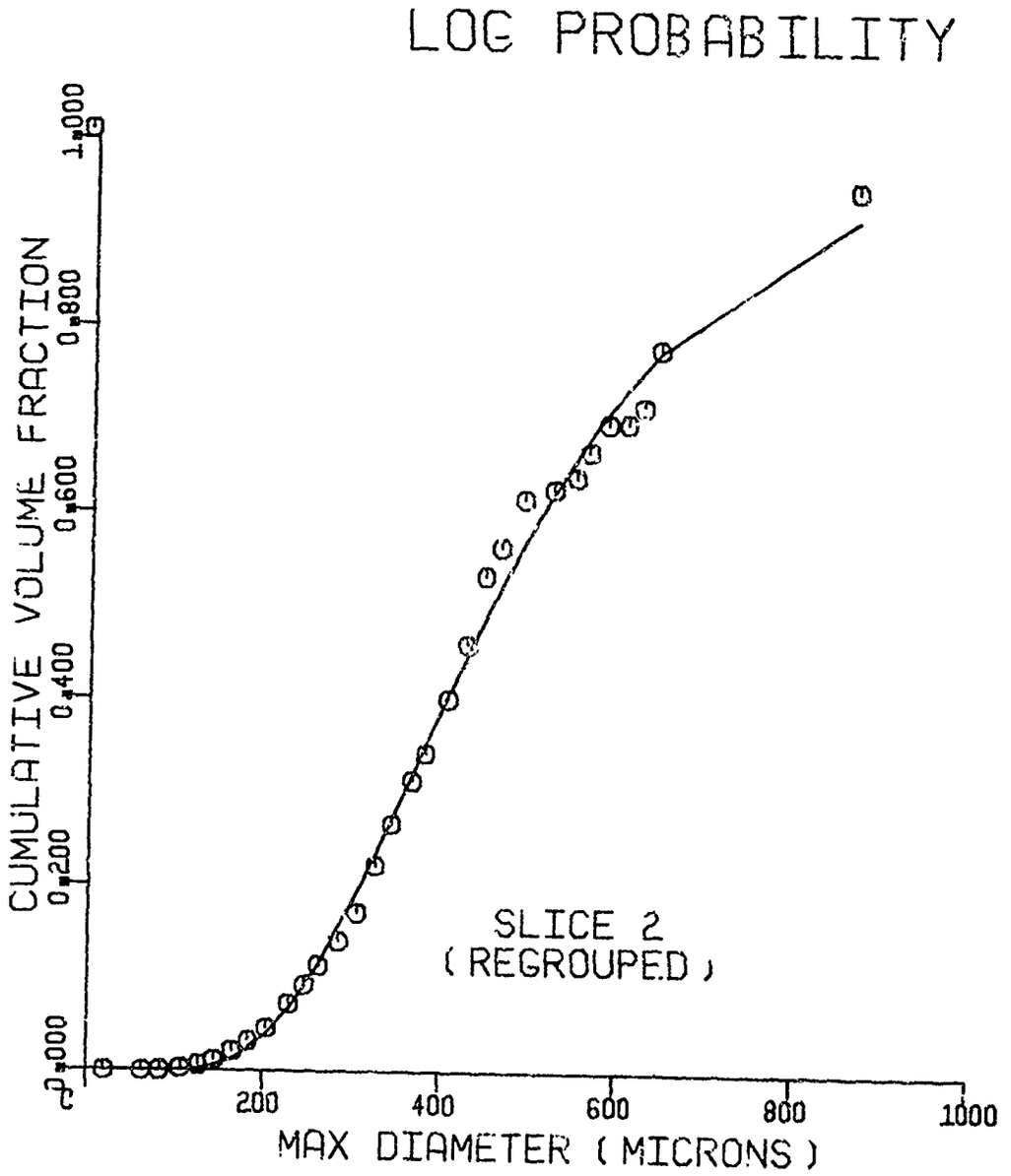

Figure 59. Droplet Data Distribution and Model Prediction Curve

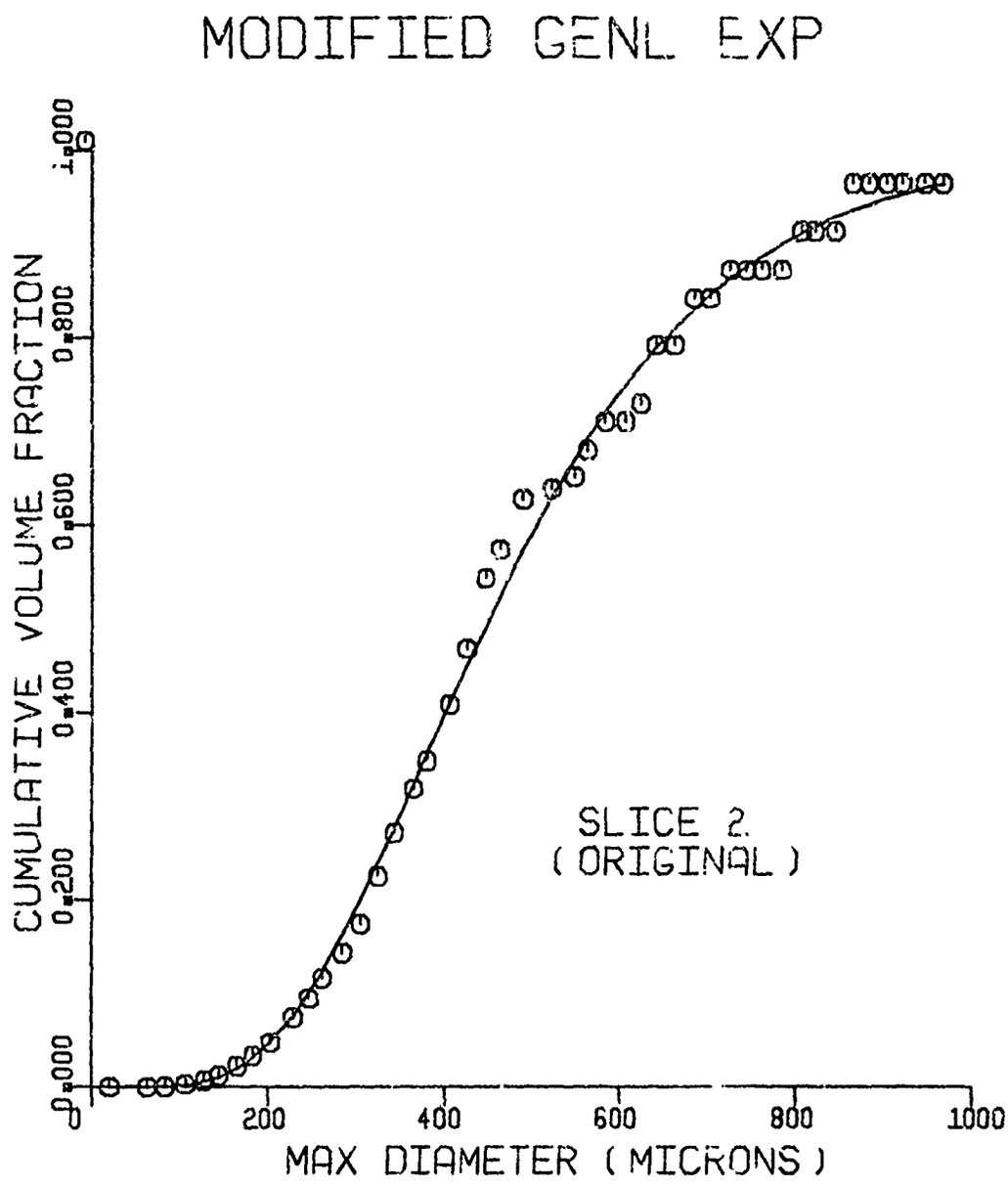

Figure 60. Droplet Data Distribution and Model Prediction Curve

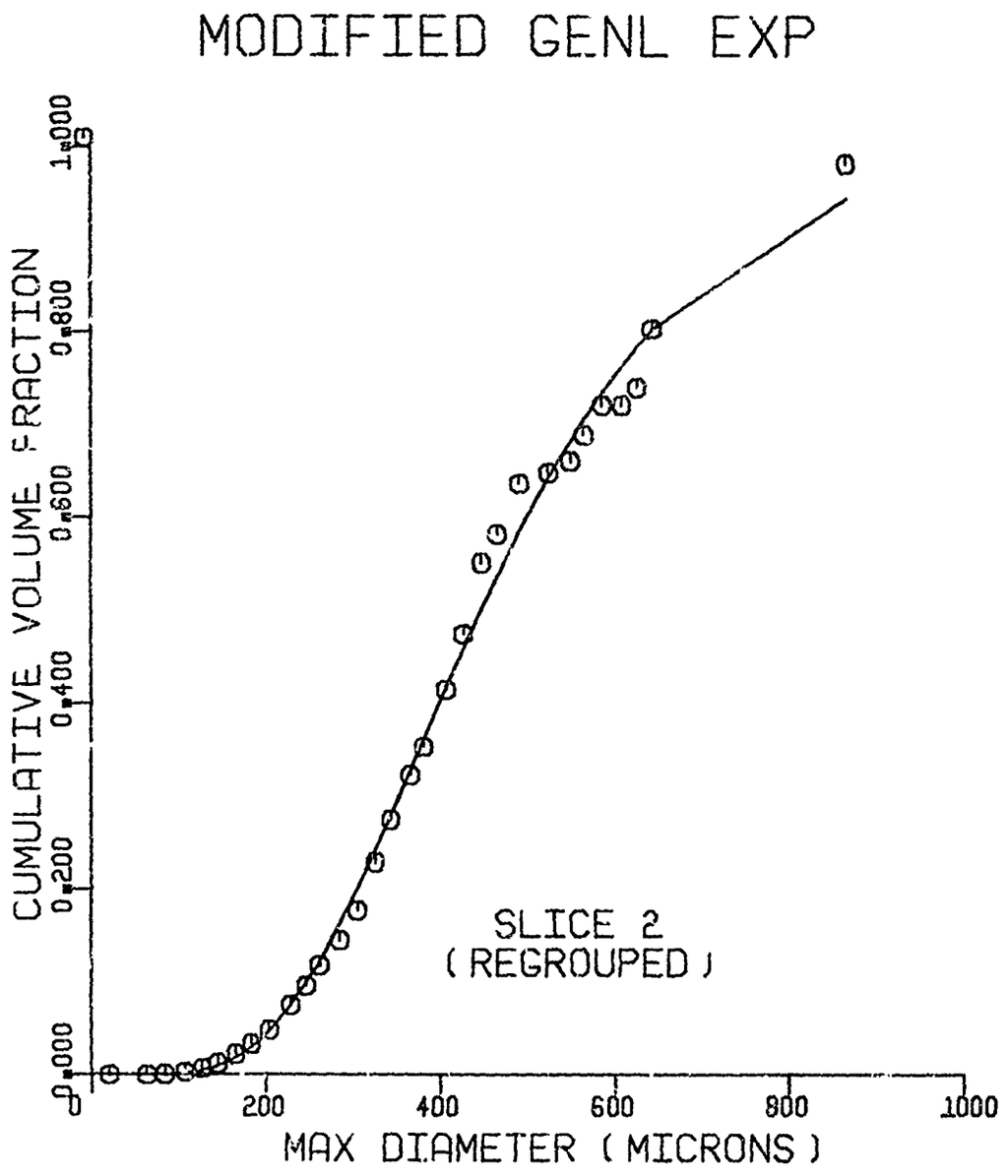

Figure 61. Droplet Data Distribution and Model Prediction Curve

TABLE XXIII: LOG-PROBABILITY DISTRIBUTION, OBSERVED AND PREDICTED VALUES

HOLOGRAPHIC INFORMATION PROCESSOR DATA — PROG ID HM-203 PAGE NO. 2

TEST ID 3.5-4.0 INJECTOR ID SINGLE JET PROJECT NO. 573010CV HSPRAY — COMPUTER RUN DATE 24 APR 1972

PROPELLANT FLOWED WATER — TEST DATE OCT. 1, 1971

HEADER GEORGE/VENEZIANO

DROPLET SIZE MEASUREMENTS FOR SPRAY CHARACTERIZATION

*** LOG-PROBABILITY DISTRIBUTION *** (DEPENDENT VARIABLE = CUM. VOLUME)

DELTA = 1.534010 DBAR = 452.9489 D30 = 329.3308 D32 = 407.2961

CLASS NO.	MED DIAM (MICRONS)	VOLUME FRACTION DERIVATIVE (DV/DD) OBSERVED	PREDICTED	RESIDUAL (O-P)	MAX DIAM (MICRONS)	CUMULATIVE VOLUME FRACTION DISTRIBUTION OBSERVED	PREDICTED	RESIDUAL (O-P)	(O-P)/O
1	10.1	0.	1.536753E-16	-1.53675E-16	20.3	0.	0.	0.	0.
2	30.5	. . .	. . .	. . .	. . .	. . .	. . .	. . .	. . .
3	52.0	2.477814E-06	2.734670E-07	2.20435E-06	83.5	.0000567	.0000101	.000046627	82.175
4	73.7	1.108644E-05	4.989531E-06	6.09691E-06	83.8	.0002818	.0001258	.000155965	55.347
5	95.2	1.123655E-04	2.975911E-05	8.26064E-05	106.7	.0028550	.0008550	.001999947	70.051
6	116.8	1.897506E-04	9.852805E-05	9.12226E-05	127.0	.0067069	.0029023	.003804565	56.726
7	135.9	3.063896E-04	2.103319E-04	9.60577E-05	144.8	.0121606	.0066794	.005481288	45.074
8	154.9	4.367036E-04	3.725113E-04	1.14192E-04	165.1	.0220407	.0142825	.007756194	35.199
9	174.0	5.954422E-04	5.771223E-04	1.83200E-05	182.9	.0326396	.0245735	.008066120	24.713
10	193.1	7.130587E-04	8.096188E-04	-9.65601E-05	203.2	.0471147	.0410191	.006095618	12.938
11	215.9	1.020343E-03	1.101305E-03	-8.09620E-05	228.6	.0730314	.0689761	.004055293	5.553
12	237.5	1.150791E-03	1.366518E-03	-2.15727E-04	246.4	.0935155	.0932854	.000230064	.246
13	254.0	1.388192E-03	1.550486E-03	-1.62294E-04	261.6	.1146160	.1168406	-.002224642	1.941
14	273.0	1.144677E-03	1.734682E-03	-5.90005E-04	284.5	.1408291	.1565163	-.015687189	11.139
15	294.6	1.521200E-03	1.901040E-03	-3.79840E-04	304.8	.1717095	.1950717	-.023362239	13.606
16	315.0	2.477027E-03	2.014075E-03	4.62951E-04	325.1	.2219931	.2359227	-.013929585	6.275
17	334.0	2.526868E-03	2.082874E-03	4.43994E-04	342.9	.2669713	.2729761	-.006004767	2.249
18	354.4	2.032718E-03	2.119479E-03	-8.67612E-05	365.8	.3135206	.3214713	-.007950752	2.536
19	373.4	1.929526E-03	2.123052E-03	-1.93532E-04	381.0	.3428493	.3537315	-.010882168	3.174
20	393.7	2.320148E-03	2.098953E-03	2.21195E-04	406.4	.4017810	.4070056	-.005224522	1.300
21	416.5	2.865347E-03	2.043686E-03	8.21662E-04	426.7	.4599476	.4484771	.011470539	2.494
22	436.9	3.635512E-03	1.975070E-03	1.66044E-03	447.0	.5337485	.4885595	.045189007	8.466
23	455.9	1.713644E-03	1.898194E-03	-1.84550E-04	464.8	.5642514	.5223417	.041909627	7.427
24	477.5	2.069710E-03	1.806665E-03	2.69047E-04	490.2	.6168220	.5680683	.048753681	7.904
25	499.1	. . .	. . .	. . .	. . .	. . .	. . .	. . .	. . .
26	515.6	7.257166E-04	1.613570E-03	-8.87854E-04	523.2	.6278529	.6227824	.005070457	.808
27	535.9	4.875289E-04	1.511011E-03	-1.02338E-03	548.6	.6402387	.6611651	-.020926482	3.268
28	556.0	1.869238E-03	1.410050E-03	4.59188E-04	563.4	.6679034	.6820326	-.014129195	2.115
29	573.8	1.461908E-03	1.322302E-03	1.39607E-04	584.2	.6983111	.7095393	-.011228190	1.608
30	595.7	0.	1.217887E-03	-1.21789E-03	607.1	.6983111	.7374337	-.039122635	5.602
31	616.0	1.062515E-03	1.124980E-03	-6.24654E-05	624.8	.7171176	.7573484	-.040230825	5.610
32	633.7	3.451630E-03	1.047448E-03	2.40418E-03	642.6	.7795566	.7759958	.002560847	.329
33	652.7	. . .	. . .	. . .	. . .	. . .	. . .	. . .	. . .
34	754.3	7.728284E-04	6.219906E-04	1.50838E-04	866.1	.9512837	.9201770	.031106788	3.270

TABLE XXIV: MODIFIED GENERAL EXPONENTIAL DISTRIBUTION, OBSERVED AND PREDICTED VALUES

HOLOGRAPHIC INFORMATION PROCESSOR DATA

PROG ID HH-203 PAGE NO. 7
COMPUTER RUN DATE 28 APR 1972
TEST DATE OCT. 1, 1971
READER GEORGE/VERZIAN)

TEST ID 3.5-4.0 INJECTOR ID SINGLE JET PROJECT NO. 573010CV MSPRAY
PROPELLANT FLOWED WATER

DROPLET SIZE MEASUREMENTS FOR SPRAY CHARACTERIZATION

** MODIFIED GENERAL EXPONENTIAL DIST. ** (DEPENDENT VARIABLE = CUM. VOLUME)

Q = .4972077 B = 1.000000 P = 9.485036 D30 = 315.7661 D32 = 396.2260

CLASS NO.	MED DIAM (MICRONS)	VOLUME FRACTION DERIVATIVE (DV/DD) OBSERVED	PREDICTED	RESIDUAL (O-P)	MAX DIAM (MICRONS)	CUMULATIVE VOLUME FRACTION DISTRIBUTION OBSERVED	PREDICTED	RESIDUAL (O-P)	(O-P)/O
1	10.1	0.	2.326878E-11	-2.32688E-11	20.3	0.	.0000000	-.000000011	0.
2	30.5								
3	52.0	2.558934E-06	2.379849E-06	1.79046E-07	83.5	.0000586	.0000695	-.000010927	18.648
4	73.7	1.144940E-05	1.669875E-05	-5.24936E-06	83.8	.0002910	.0004304	-.000139366	47.888
5	95.2	1.160443E-04	6.022135E-05	5.58229E-05	106.7	.0029484	.0018594	.001089446	36.950
6	116.8	1.959629E-04	1.492905E-04	4.66724E-05	127.0	.0069265	.0049301	.001996345	28.822
7	135.9	3.164205E-04	2.722042E-04	4.42163E-05	144.8	.0125588	.0098016	.002757164	21.954
8	154.9	5.026377E-04	4.352043E-04	6.74334E-05	165.1	.0227623	.0186679	.004094371	17.987
9	174.0	6.149364E-04	6.309445E-04	-1.60081E-05	182.9	.0337082	.0299129	.003795297	11.259
10	193.1	7.364035E-04	8.483982E-04	-1.11995E-04	203.2	.0486572	.0471482	.001513018	3.110
11	215.9	1.053748E-03	1.120235E-03	-6.64877E-05	228.6	.0754224	.0755879	-.000165491	.219
12	237.5	1.185466E-03	1.370519E-03	-1.85052E-04	246.4	.0965771	.0999721	-.003395006	3.515
13	254.0	1.433640E-03	1.547819E-03	-1.14179E-04	261.6	.1183684	.1234843	-.005120950	4.326
14	273.0	1.182152E-03	1.730228E-03	-5.48075E-04	284.5	.1454397	.1630713	-.017631672	12.123
15	294.6	1.571003E-03	1.901778E-03	-3.30775E-04	304.8	.1773310	.2016463	-.024315243	13.712
16	315.0	2.558122E-03	2.025235E-03	5.32887E-04	325.1	.2292609	.2427267	-.013465799	5.871
17	334.0	2.609595E-03	2.106976E-03	5.02619E-04	342.9	.2757117	.2802101	-.004498355	1.632
18	354.4	2.099267E-03	2.158914E-03	-5.96474E-05	365.8	.3237849	.3296081	-.005823189	1.798
19	373.4	1.992690E-03	2.176710E-03	-1.84019E-04	381.0	.3540738	.3628833	-.008809470	2.488
20	393.7	2.396107E-03	2.166286E-03	2.29821E-04	406.4	.4149349	.4176634	-.002728517	.658
21	416.5	2.959156E-03	2.123378E-03	8.35778E-04	426.7	.4750058	.4607500	.014255795	3.001
22	436.9	3.754535E-03	2.062411E-03	1.69212E-03	447.0	.5512228	.5026026	.048620257	8.820
23	455.9	1.769747E-03	1.989641E-03	-2.19914E-04	464.8	.5827243	.5380110	.044713281	7.673
24	477.5	2.137470E-03	1.893308E-03	2.44163E-04	490.2	.6370141	.5860858	.050930279	7.995
25	499.1								
26	515.6	7.494757E-04	1.700285E-03	-9.50810E-04	523.2	.6484081	.6037251	.004682975	.722
27	535.9	5.035934E-04	1.591206E-03	-1.08761E-03	548.6	.6611994	.6841400	-.022940602	34.670
28	556.0	1.930435E-03	1.482105E-03	4.48329E-04	563.4	.6897698	.7060754	-.016305616	2.364
29	573.8	1.509770E-03	1.386127E-03	1.23643E-04	584.2	.7211730	.7349089	-.013735902	1.905
30	595.7	0.	1.270763E-03	-1.27076E-03	607.1	.7211730	.7640158	-.042840749	5.940
31	616.0	1.097300E-03	1.167263E-03	-6.99623E-05	624.8	.7905952	.7846768	.005918608	5.952
32	633.7	3.564633E-03	1.080414E-03	2.48422E-03	642.6	.8040457	.8039111	.000134597	.017
33	652.7								
34	754.3	7.981299E-04	6.019474E-04	1.96183E-04	866.1	.9824277	.9245666	.037861152	3.854

solution was obtained. However, the increased complexity by introducing C_D as a variable was not warranted by the intent of this analysis, which was to determine the velocities for the range of droplet sizes found in the data. The minimum, mode and maximum diameter droplets for axial slices 1 and 2 were used in the analysis. The results are presented in Table XXV. It shows the distance different size droplets travel before their velocities are zero. Actually, the droplets would not travel as far as is shown because, as they decelerate, the Reynolds number decreases and C_D increases, bringing the droplet velocity to zero much quicker. Recall constant C_D was assumed. The droplet velocities at different axial positions from their formation point is also shown.

Droplet velocities are seen to vary significantly over the range of droplet sizes. Hence, mass loss rate from the jet at given axial positions or slices cannot be determined unless the origin (formation position) of the various droplets was known.

The Weber number criteria for droplet stability ($We \approx 10$) was applied to the flow conditions of the liquid jet. The result was a droplet whose diameter was 1060 microns or less was stable. The largest droplet observed in this investigation was 913 microns. Hence, all droplets were stable. This implies no secondary breakup. The droplet distribution is a direct result of jet breakup. As cited earlier, one can infer that jet core size has an effect on droplet size. As the core becomes smaller the droplet size shed becomes smaller based on the observation of mode shift between axial slices 1 and 2. The droplet size distributions observed at various distances from the injection point are also affected by the variation in velocity of the different

TABLE XIV: DROPLET AXIAL VELOCITY

D (microns)	$X_{V=0}$ (inches)	$V_x = 3.25"$ (fps)	$V_x = 3.75"$ (fps)	$Re_{V=282fps}$	C_D Eqn. (41)
52	1.99	---	---	83.9	1.153
95	4.72	24.2	15.9	152.2	.878
216	14.3	60.2	57.5	340	.649
856	81.2	74.8	74.3	1349	.453
913	87.7	75.1	74.1	1440	.448

size droplets. The larger droplets travel farther and maintain their velocities longer than do the smaller droplets. In summary, it appears two conflicting phenomena are interacting to produce droplet size distribution at various distances from the injection point.

d. Comparison of Data: The data obtained from this investigation was compared with that of Popov[37]. Predicted mean diameter, D_{32}, was obtained from the Harmon correlation equation (21). Popov was the only source found which had droplet data for a jet into still air at the flow conditions similar to those of this investigation. In fact, Popov is the only known source of recent times with single liquid jet, atmospheric air droplet data. Harmon's equation is the only known droplet diameter correlation equation for a liquid jet into still air. Comparison of data with that of Popov is presented in Table XXVI. One can observe the following:

1) The number fraction of droplets within the various size ranges were quite similar. Comparison was made with slice 2 data which was obtained at approximately 35 orifice diameters from the injection point. Popov data was taken 130 diameters from the injection point. In addition to the location at which the data was taken, the only other significant difference in test conditions between this investigation and that of Popov was the orifice diameter. The fact that drop size distribution does not appear to be proportional to orifice diameter substantiates the hypothesis that size distribution is affected simultaneously by jet core size and velocity variation of the droplets at different locations from their formation point, due to differences in drag on various sized droplets.

2) The Sauter mean diameters, D_{32}, compare closely. It is not

TABLE XXVI: POPOV DATA COMPARISON

	George	Popov
D/D_o	number fraction	
.05	.47	.42
.10	.30	.23
.15	.17	.16
.20	.04	.08
D_o, in.	.107	.039
Re_{jet}	65.4×10^3	59.1×10^3
ρ_g/ρ_l	1.2×10^{-3}	1.2×10^{-3}
μ_g/μ_l	1.7×10^{-2}	1.7×10^{-2}
Z	$.24 \times 10^{-2}$	$.39 \times 10^{-2}$
Fluids	air/H_2O	air/H_2O
D_{32}, microns	390	375

known for certain that Popov's mean diameter is D_{32}. However, this is the commonly used mean diameter in Russian literature. The predicted D_{32} from the Harmon equation for the flow conditions of this investigation was 81 microns and that for the Popov conditions at the same Re (65×10^3) was 35 microns. An explanation for this is that Harmon correlated to data that was mostly obtained from jets injected at high pressures (velocities) into chambers whose air densities were an order of magnitude or more than atmospheric air. It has been shown by many investigators that as velocity and gas density increase droplet diameter decreases. See Table II in Chapter II, Section 3. Popov also shows that air density increase has an effect of decreasing droplet size. Some data to which Harmon correlated was obtained from swirler type atomizers. Since the range of conditions to which Harmon correlated was different from those of this investigation and of Popov, and in some cases the injector geometry was not that of a simple solid jet, a true comparison with the Harmon equation cannot be made.

CHAPTER VIII

SUMMARY AND CONCLUSIONS

1. Amplitude growth of a liquid jet injected perpendicularly into a supersonic gas stream is a function of distance from the injection point and inertial forces acting on the jet. Fluid physical properties such as surface tension and viscosity had a negligible effect on jet breakup under the test conditions of this investigation. Amplitude variation can be modeled by an equation whose form is

$$A = CS^{\frac{N}{q}}H$$

More than one mode of amplitude was observed to occur along the jet trajectory.

2. Wavelength growth is also a function of distance from the injection point and inertial forces, and can be modeled by an equation similar in form to that which models amplitude variation. It appears that wavelength is more sensitive to the whipping action of the liquid jet than is amplitude.

3. A relationship between jet amplitude and wavelength can be obtained. Each of these phenomena may have a bearing on droplet size distribution resulting from jet breakup.

4. Holography can be applied to supersonic fields to obtain liquid jet amplitude and wavelength data. Acquisition of droplet data is limited by droplet size and speed. That is, droplet size in a supersonic gas stream may be below the resolution capability of the holographic recording system (in this case approximately 15 microns) and droplet motion may be sufficient to smear the image, although laser pulse width is extremely small (50 nanoseconds for the laser used in

this investigation).

5. Two methods have been devised for retrieval of holographic data. One retrieves the data directly from the hologram and inputs it on magnetic tape for reduction and analysis. The alternate method, which is less sophisticated but workable, has an intermediate step of photographing planes within the holographic scene volume and processing the resulting film on a reading machine to prepare the data for reduction and analysis.

6. An analytical method for reducing three-dimensional droplet data has been developed. The method consists of a system of computer programs which analyze spatial, size and mass distribution of the droplets.

7. Off-axis, transmission holography can be used to determine, quantitatively, spatial distribution of droplet number, size and mass under certain flow conditions. This has been demonstrated by injecting a turbulent liquid jet into quiescent, atmospheric air. Acquisition of holographic droplet data in gas streams is possible with limitations.

8. Radial distribution of droplet number and mass is well behaved, and monotonically increases to a maximum, then decreases as radial position increases. No radial variation in mean droplet diameter was detected, bearing in mind that the number of droplets in each annulus was small for the class size range which they spanned. Jet spreading increases with increase in distance from the injection point.

9. A variation in droplet size distribution exists with axial position from the injection point. The mode (the size interval in which the maximum number of droplets occur) becomes smaller with increase in axial distance. This may be due to the reduced size of the jet core with distance. The droplet size distribution for the data from this investigation is best characterized by a modified general exponential or log-probability function. Mass loss rate from the jet at various longitudinal positions could not be determined because droplet velocity varied widely, depending on droplet diameter.

10. The literature search revealed that dimensionless parameters in the form of Reynolds and Weber numbers, but not necessarily according to the conventional definition of these numbers, were most prevalent in droplet mean diameter correlation equations. Over the gas environments from still air to supersonic streams, the variables of jet orifice diameter, gas and liquid densities, gas velocity and surface tension appeared most frequently in the correlation equations. Regardless of environment, each had the same effect, stabilizing or destabilizing, on jet breakup, but the degree of influence of these parameters varied in the different flow regimes. Gas velocity or relative velocity has the greatest affect on jet breakup regardless of flow regime.

BIBLIOGRAPHY

BIBLIOGRAPHY

1. Rayleigh, Lord. "On the instability of jets." Proceedings of the London Mathematical Society, 10:4, 1878.

2. Harmon, D.B., Jr. Prediction of the mean drop size in a spray from a cylindrical nozzle with flow at high Reynolds moduli. Ph.D. in Engineering. University of California, Los Angeles, July 1953.

3. Ingebo, R.D. and H.P. Foster. "Drop-size distribution for cross-current breakup of liquid jets in airstreams." NACA TN-4087, October 1957.

4. Nukiyama, S. and Y. Tanasawa. "Experiments on the atomization of liquids in an air stream." Reports 1-6. Translated from the Transac. Soc. of Mech. Engr. (Japan) Vols. 4, 5 and 6, 1938-40, by E. Hope (AD 456252), March 1950.

5. Volynskiy, M.S. "Atomization of a liquid in a supersonic flow." Wright-Patterson Air Force Base, Foreign Technical Division, Ohio, Translation Report FTD-MT-63-186 (AD 602597), 1963.

6. Weiss, M.A. and C.H. Worsham. "Atomization in high velocity airstreams." ARS Journal, 29:252-59, April 1959.

7. Luna, R.E. and W.A. Klikoff, Jr. "On aerodynamic breakup of liquid drops." Sandia Laboratories Research Report SC-RR-66-2716, June 1967.

8. Hinze, J.O. "Critical speeds and sizes of liquid globules." Appl. Sci. Res., 1:273-288, 1949.

9. Morrell, G. "Critical conditions for drop and jet shattering." NASA TN D-677, February 1961.

10. Wolfe, H.E. and W.H. Andersen. "Kinetics, mechanism and resultant droplet sizes of the aerodynamic breakup of liquid drops." Aerojet General Corporation, Report No. 0395-04(18)SP on U.S. Army Chemical Center Contract No. DA-18-108-405CML829 (AD 437340), April 1964.

11. Dowdy, M.W. and J.F. Newton, Jr. "Investigation of liquid and gaseous secondary injection phenomena on a flat plate with M = 2.01 to M = 4.54." Jet Propulsion Laboratory, Pasadena, California, TR 32-542, December 1963.

12. McRae, R.P. "Experimental investigations of a liquid jet injected into a Mach 4 stream." Douglas Aircraft Company, Inc. Report SM-47879, Santa Monica, California, May 1966.

13. Harvey, D.W. "Longitudinal waves on a liquid jet in a high velocity gas stream." Douglas Aircraft Company, Inc. Report SM-49287, Santa Monica, California, November 1965.

14. Harvey, D.W. "Drop size distribution resulting from liquid jet injection across a supersonic stream." McDonnell Douglas Astronautics Company, Huntington Beach, California, May 1971 (paper to be published AIAA Journal).

15. Mayer, E. "Theory of liquid atomization in high velocity gas streams." ARS Journal, 31:1783-85, December 1961.

16. Adelberg, M. "Mean drop size resulting from the injection of a liquid jet into a high-speed gas stream." AIAA Journal, 6:1143-47, June 1968.

17. Bitron, M.D. "Atomization of liquids by supersonic air jets." Indust. Engr. Chem., 47:23-28, January 1955.

18. Gooderum, P., D. Bushnell and J. Huffman. "Mean droplet size for cross-stream water injection into a Mach 8 air flow." J. Spacecraft, 4:534-35, April 1967.

19. Sherman, A. and J. Schetz. "Breakup of liquid sheets and jets in a supersonic gas stream." Paper presented at AIAA 8th Aerospace Sciences Meeting, January 19-21, 1970, New York, paper no. 70-89, New York, American Institute of Aeronautics and Astronautics, 1970.

20. Yates, C.L. "Liquid injection into supersonic airstreams." Paper presented at AIAA/SAE 7th Propulsion Joint Specialist Conference, June 14-18, Salt Lake City, Utah, paper no. 71-724, New York, American Institute of Aeronautics and Astronautics, 1971.

21. Catton, I., D.E. Hill and R.P. McRae. "Study of a liquid jet penetration in a hypersonic stream." AIAA Journal, 6:2084-89, November 1968.

22. Forde, J.M., S. Molder and E.J. Szpiro. "Secondary liquid injection into a supersonic airstream." J. Spacecraft, 3:1172-76, August 1966.

23. Horn, K.P. and R.E. Reichenbach. "Further experiments on spreading of liquids injected into a supersonic flow." AIAA Journal, 7:358-59, February 1969.

24. Gooderum, P.B. and D.M. Bushnell. "Incipient cross-stream liquid atomization at high altitude and velocity." J. Spacecraft, 7:1014-17, August 1970.

25. Gooderum, P., D. Bushnell and J. Huffman. "Mean droplet size for cross-stream water injection into a Mach 8 air flow." J. Spacecraft, 4:534-35, April 1967.

26. Williams, F. "Atomization processes and ignition criteria for supersonic combustion with liquid fuel injection." International Colloquim on Gasdynamics of Explosions. Proceedings, reat Britain, Pergamon Press, 1970, pp. 547-554.

27. Catton, I. and D.W. Harvey. "Deformation of a liquid jet injected across a high velocity gas stream." Douglas Aircraft Company, Inc. Report SM-59036, Santa Monica, California, June 1966.

28. Morrell, G. "Breakup of liquid jets by transverse shocks." Eighth Symposium (international) on Combustion. Proceedings. Baltimore, The Williams & Wilkins Company, 1962, pp. 1059-1068.

29. Morrell, G. "Rate of liquid jet breakup by a transverse shock wave." NASA TN D-1728, May 1963.

30. Kurzius, S.C. and F.H. Raab. "Measurement of droplet sizes in liquid jets atomized in low-density supersonic streams." AeroChem. Res. Labs., Report TP152, March 1967.

31. Nugele, R.A. and H.D. Evans. "Droplet size distribution in sprays." Ind. and Engr. Chem., 43:1317-24, June 1951.

32. Hrubecky, H.F. "Experiments in liquid atomization by air streams." J. Appl. Phy., 29:572-78, March 1958.

33. Clark, B.J. "Breakup of a liquid jet in a transverse flow of gas." NASA TN D-2424, August 1964.

34. Limper, A.F. Atomization of liquids by injection into high velocity gas streams. M.S. in Chemical Engineering. University of Illinois, Urbana, May 1947.

35. Mayer, E. "Capillary mechanisms of liquid atomization in high velocity gas streams." 12th International Astronautical Congress. Proceedings. New York, Academic Press, 1963, p. 731.

36. Adelberg, M. "Breakup rate and penetration of a liquid jet in a gas stream." AIAA Journal, 5:1408-15, August 1967.

37. Popov, M. "Model experiments on atomization of liquids." NASA TT F-65, July 1961.

38. Eisenklam, P. and P.C. Hooper. "The flow characteristics of laminar and turbulent jets of liquid." Interim Report. Imperial College Report J.R.L. No. 42 (AD 207284), September 1958.

39. Putnam, A.A., et al. "Injection and combustion of liquid fuels." Wright Air Development Center Technical Report 56-344 (AD 118142), March 1957.

40. Harmon, D.B. "An equation for predicting a mean drop size in a high speed spray." University of California Publications and Engineering, 5:145-158, 1955.

41. Chen, Tsu-Fang and J.R. Davis. "Disintegration of a turbulent water jet." J. of the Hydraulics Division Proceedings of the A.S.C.E.,

Hy 1:175-206, January 1964.

42. Borodin, V.A. and Yu. F. Dityakin, et al, "Atomization of liquids." Wright-Patterson Air Force Base, Foreign Technical Division, Ohio, Translation FTD-MT-24-97-68 (AD 685151), July 1968.

43. Sitkei, G. "Contribution to the theory of jet atomization." NASA TT F-129, October 1963.

44. Lewis, J.D. "Liquid atomization from rocket engine injectors." Rocket Propulsion Establishment, Westcott, England, TM RPE 341, January 1965.

45. Matthews, B.J., R.F. Wuerker and D.T. Harrje. "Small droplet measuring technique." TRW Systems, Redondo Beach, California, Phase I Technical Report, Technical Report AFRPL-TR-6[illegible]295, February 1968.

46. Rice, E.J. The effect of selected fluid parameters on spatial drop size distribution. Ph.D. in Mechanical Engineering. University of Wisconsin, January 1966.

47. "Agfa-Gevaert technical information bulletin on scientific photography." Operational Manual for Transmission Holocamera. R.F. Wuerker (author). Air Force Rocket Propulsion Laboratory, Edwards Air Force Base, California, TRW Report No. 11709-6002-RO-00 under Contract F04611-69-C-0015, February 1970.

48. Leith, E.N. and J. Upatnieks. "Modern holography." SPIE Seminar Proceedings on Holography, Vol. 15, Society of Photo-Optical Instrumentation Engineers, 1968.

49. Leith, E.N. and J. Upatnieks. "Reconstructed wavefronts and communication theory." J. Opt. Soc. Am., 52:1123, 1962.

50. Leith, E.N. and J. Upatnieks. "Wavefront reconstruction with diffused illumination and three-dimensional objects." J. Opt. Soc. Am., 54:1295-1301, 1964.

51. Wuerker, R.F. "Instruction manual for ruby laser holographic illuminator." Air Force Rocket Propulsion Laboratory, Edwards Air Force Base, California, TRW Report No. 11709-6003-RO-00, under Contract F04611-69-C0015, February 1970.

52. Wuerker, R.F. and L.O. Heflinger. "Ruby laser holography." SPIE Journal, 9:122-30, April-May 1971.

53. Champagne, E.B. and N.G. Massey. "Resolution in holography." Applied Optics, 8:1879-85, September 1969.

54. Latta, J.N. "Computer-based analysis of hologram imagery and aberrations. I. Hologram types and their nonchromatic aberrations." Appl. Optics, 10:599-608, March 1971.

55. Latta, J.N. "Computer-based analysis of hologram imagery and aberrations. II. Aberrations induced by a wavelength shift." Appl. Optics, 10:609-18, March 1971.

56. Meier, R.W. "Magnification and third-order aberrations in holography." J. Opt. Soc. Am., 55:987-992, August 1965.

57. Smith, H.M. Principles of holography. New York, Wiley-Interscience, 1969.

58. DeVelis, J.B. and G.O. Reynolds. The theory and applications of holography. Reading, Addison-Wesley Publishing Co., 1967.

59. Dobbins, R.A., L. Crocco and I. Glassman. "Measurement of mean particle sizes of sprays from diffractively scattered light." AIAA Journal, 1:1883-86, August 1963.

60. Herdan, G. Small particle statistics. 2nd ed, London, Butterworths, 1960.

61. Hiroyasu, H, "Mathematical expression for drop size distribution in sprays." NASA CR-72272, November 1967.

62. Brown, R.E. and K.L. Leonard. "Methods of describing droplet-size distributions from atomized solutions." Aerojet General Corporation, Report No. 0395-04(15)SP on U.S. Army Chemical Center Contract DA-18-108-405-CML-829 (AD 434106), March 1964.

63. Sauter, J. "Determining the efficiency of atomization by its fineness and uniformity." NACA TM-396, January 1927.

64. Cary, D.A., L. Crocco and D.T. Harrje. "A study of injector spray characteristics in a simulated rocket combustion chamber including longitudinal mode pressure oscillations." National Aeronautics and Space Administration Technical Report No. 730 on NASA Contract NASr-217, June 1966.

65. Pope, A. and K.L. Goin. High speed wind tunnel testing. New York, Wiley, 1965.

66. Liepmann, H.W. and A. Roshko. Elements of gas dynamics. New York, Wiley, 1957.

67. Spaid, F.W. "Fabrication of nozzle blocks for the UCLA supersonic wind tunnel by computer," High-Speed Aerodynamics and Propulsion Laboratory, University of California, Los Angeles, California Report No. 69-14, March 1969.

68. Wuerker, R.F. "Operational manual for transmission holocamera." Air Force Rocket Propulsion Laboratory, Edwards Air Force Base, California, TRW Report No. 11709-6002-RO-00, under Contract F04611-69-C-0015, February 1970.

69. Marquardt, D.W. "An algorithm for least-squares estimation of non-linear parameters." J. Soc. Indust. Appl. Math., 11:431-441, June 1963.

70. Strobridge, T.R. "The thermodynamic properties of H_2 from 64 to 300°K between .1 and 200 atmospheres." National Bureau of Standards Technical Note TN 129 (PB 161630), January 1962.

71. International Critical Tables of Numerical Data, Physics, Chemistry and Technology. Vols. III and IV. New York, McGraw-Hill, 1928.

72. "Transport properties of freon." E.I. duPont de Nemours and Co., Technical Bulletins C-30 and D-27, 1967.

73. Matthews, B.J. "Holography of JP-4 droplets and combusting boron particles." TRW Report No. 18077-6001-RO-00, on Contract No. F 33615-71-C-1821, October 1971.

74. Abraham, F.F. "Functional dependence of drag coefficient of a sphere on Reynolds number." The Physics of Fluids, 13:2194-95, August 1970.

75. Pearson, Karl. Tables of the incomplete Gamma function. London, Cambridge University Press, 1922.

76. Abramowitz, M. and I. Stegun (editors). Handbook of mathematical functions with formulas, graphs and mathematical tables. Washington, D.C., U.S. Government Printing Office, 1970.

APPENDICES

APPENDIX I

Nozzle Block Contour Boundary Layer Correction

The basic nozzle block design which was used was the same as that for the UCLA supersonic wind tunnel. However, due to the difference in operating pressure level (the UCLA tunnel operates at atmospheric pressure in the plenum chamber, whereas the tunnel used in this investigation is a blowdown type which operates at a total pressure from 100 to 300 psia) between the two wind tunnels, a correction to the boundary layer had to be made to maintain the flow at Mach 3 in the test section.

The procedure which Sandberg-Serrell, designers of the UCLA tunnel, used in establishing the proper nozzle contour is described below. Boundary layer development along the two-dimensional nozzle wall was assumed to be turbulent.

Use the well-known Crocco temperature profile

$$\frac{\rho_\infty}{\rho} = \frac{T}{T_\infty} = \frac{T_w}{T_\infty} + \left(\frac{T_{aw} - T_w}{T_\infty}\right)\frac{u}{U_\infty} + \left(\frac{T_\infty - T_{aw}}{T_\infty}\right)\left(\frac{u}{U_\infty}\right)^2 \qquad (1)$$

and the velocity profile law

$$\frac{u}{U_\infty} = \left(\frac{y}{\delta}\right)^{1/n} \qquad (2)$$

in calculating the displacement thickness

$$\frac{\delta^*}{\delta} = \int_0^1 \left[1 - \frac{\rho}{\rho_\infty}\left(\frac{u}{U_\infty}\right)\right] d\left(\frac{y}{\delta}\right) \qquad (3)$$

and momentum thickness

$$\frac{\Theta}{\delta} = \int_0^1 \left(\frac{\rho}{\rho_\infty}\right)\left(\frac{u}{U_\infty}\right)\left(1 - \frac{u}{U_\infty}\right) d\left(\frac{y}{\delta}\right) \qquad (4)$$

by numerical integration.

From equations (3) and (4), calculate the shape factor

$$H = \frac{\delta^*}{\Theta} \qquad (5)$$

The von Karman momentum integral for steady two-dimensional flow can be derived in terms of δ^* and Θ

$$\frac{d\Theta}{dz} + \frac{1}{U}\frac{dU}{dz}\left(2\Theta + \delta^*\right) + \frac{\Theta}{\rho_\infty}\frac{d\rho_\infty}{dz} = \frac{\tau_w}{\rho_\infty U^2} \qquad (6)$$

The mainstream is isentropic and isenergic in the absence of heat sources. Equation (6) can be put in a more usable form in the following manner:

Use the Bernoulli equation

$$\frac{P}{\rho} + \frac{u^2}{2} = \text{constant}$$

and differentiate it

$$\frac{1}{\rho}\frac{dP}{dz} = -U\frac{dU}{dz}$$

Use the following relationships

$$\frac{dP}{d\rho} = a^2 \qquad \text{(isentropic flow)}$$

$$\delta^* = H\Theta$$

$$\frac{C_f}{2} = \frac{\tau_w}{\rho U^2}$$

$$M = \frac{U}{a}$$

Now substitute these into equation (6) to obtain

$$\frac{d\theta}{dz} + \left(2 + H - M_\infty^2\right)\frac{1}{\bar{U}}\frac{d\bar{U}}{dz}\theta = \frac{C_f}{2} \qquad (7)$$

Now concentrate on the expression $\frac{1}{\bar{U}}\frac{d\bar{U}}{dz}$ to put in terms of Mach number.

From the definition of Mach number for a perfect gas

$$M = \frac{\bar{U}}{a} = \frac{\bar{U}}{\sqrt{kR\bar{T}}}$$

take the logarithm and differentiate to obtain

$$\frac{d\bar{U}}{\bar{U}} = \frac{dM}{M} + \frac{d\bar{T}}{\bar{T}} = \frac{dM}{M} + \frac{d\left(\bar{T}/T_0\right)}{\bar{T}/T_0} \qquad (8)$$

Substitute the isentropic relationship

$$\frac{T_0}{\bar{T}} = 1 + \frac{k-1}{2}M^2$$

into equation (8) and perform the differentiation on that term to obtain

$$\frac{1}{\bar{U}}\frac{d\bar{U}}{dz} = \frac{1}{M}\,\frac{1}{1+\frac{k-1}{2}M^2}\,\frac{dM}{dz}$$

Equation (7) now becomes

$$\frac{d\theta}{dz} + \left(\frac{2 + H - M_\infty^2}{1+\frac{k-1}{2}M_\infty^2}\right)\left(\frac{1}{M_\infty}\right)\frac{dM_\infty}{dz}\theta = \frac{C_f}{2} \qquad (9)$$

Bartz proposed the following expression for skin friction

$$\frac{C_f}{2} = \left(K\eta\right)^{\frac{1-n}{1+n}}\left[\frac{1}{Re_\theta\left(\frac{\delta}{\theta}\right)}\right]^{\frac{2}{n+1}}\left(\frac{2T_\infty}{T_w + T_\infty}\right)^{\frac{n-2\omega-1}{n+1}} \qquad (10)$$

where $Re_\theta = \frac{\rho\theta\bar{U}_\infty}{\mu}$

Substitute equation (10) into (9) and bring out θ from Re_θ so (9) can now be written in the form

$$\frac{d\theta}{dz} + P_1(z)\theta = Q_1(z)\theta^{-\frac{2}{n+1}} \qquad (11)$$

where

$$P_1(z) = \left(\frac{2+H-M_\infty^2}{1+\frac{k-1}{2}M_\infty^2}\right)\left(\frac{1}{M_\infty}\right)\frac{dM_\infty}{dz}$$

and

$$Q_1(z) = \left(K\eta\right)^{\frac{1-n}{1+n}}\left[\frac{1}{\frac{\rho U_\infty}{\mu}\left(\frac{\delta}{\theta}\right)}\right]^{2/n+1}\left(\frac{2T_\infty}{T_w+T_\infty}\right)^{\frac{n-2\omega-1}{n+1}}$$

Divide equation (11) through by $\theta^{-\frac{2}{n+1}}$, note that

$$\theta^{2/n+1}\frac{d\theta}{dz} = \frac{n+1}{n+3}\frac{d\theta^{\frac{n+3}{n+1}}}{dz}$$

and make the transformation

$$\bar{\theta} = \theta^{\frac{n+3}{n+1}}$$

one will obtain

$$\frac{d\bar{\theta}}{dz} + P(z)\bar{\theta} = \frac{n+3}{n+1}Q_1(z) = Q(z) \qquad (12)$$

where

$$P(z) = \frac{n+3}{n+1}P_1(z)$$

Equation (12) is a linear first order equation whose solution is

$$\bar{\theta}(z) = e^{-\int_0^z P\,dz}\left[\int_0^z e^{\int_0^z P\,dz}Q\,dz + \bar{\theta}_i\right] \qquad (13)$$

where $\bar{\theta}_i$ is the initial momentum thickness.

After solving for $\bar{\theta}$, θ can be obtained. Finally, δ^* can be obtained from equation (5). The variation in δ^* along the longitudinal axis of the nozzle is applied to the ideal nozzle contour to correct for boundary layer growth.

To correct δ^* from atmospheric to some other total pressure one need only correct for the change in mass flux, ρU_∞, in the expression for Q assuming the shape factor remains constant. $H_{p_o} = H_{atmos}$. In equation (13)

$$\bar{\theta} \propto Q \propto \left(\frac{1}{\rho U}\right)^{2/n+1}$$

So

$$\frac{\bar{\theta}_{P_c}}{\bar{\theta}_{atmos}} = \left(\frac{\rho U_{atmos}}{\rho U_{P_c}}\right)^{2/n+1}$$

$$\frac{\theta_{P_0}}{\theta_{atmos}} = \left(\frac{\bar{\theta}_{P_c}}{\bar{\theta}_{atmos}}\right)^{\frac{n+1}{n+3}} = \left(\frac{\rho U_{atmos}}{\rho U_{P_c}}\right)^{2/n+3}$$

$$\frac{\delta^*_{P_0}}{\delta^*_{atmos}} = \frac{\theta_{P_c}}{\theta_{atmos}} = \left(\frac{\rho U_{atmos}}{\rho U_{P_c}}\right)^{2/n+3} \qquad (14)$$

Using Fliegner's equation holding throat area and total temperature constant, the flow rate becomes a function of total pressure only

$$\frac{\dot{w}}{A^*} = \sqrt{\frac{k}{R}\left(\frac{2}{k+1}\right)^{\frac{k-1}{k+1}}} \frac{P_c}{\sqrt{T_c}} = \rho U \qquad (15)$$

Normally n = 7 according to the 1/7 power law for velocity distribution. Using this with equations (14) and (15) the ratio of $\delta^*_{P_0} / \delta^*_{atmos}$ can be determined. Knowing δ^*_{atmos}, then $\delta^*_{P_0}$ can be determined and the correction to the nozzle contour made.

Distribution Function Equations

Log-Probability Distribution (volume models)

$$\frac{d\,VOL}{d\chi} = \frac{V_{total}\,\xi}{\chi\sqrt{\pi}}\, e^{-\delta^2 \ln^2(\chi/\bar{\chi})}$$

$$VOL(\chi) = V_t\left(\tfrac{1}{2} + \tfrac{1}{2}\,erf(t)\right) \qquad t = \delta \ln(\chi/\bar{\chi})$$

$$\bar{\chi}_{32} = \bar{\chi}\, e^{-1/4\delta^2}$$

$$\bar{\chi}_{30} = \bar{\chi}\, e^{-3/4\delta^2}$$

$$\frac{\partial\left(\frac{d\,VOL}{d\chi}\right)}{\partial\,\delta} = \left(\frac{d\,VOL}{d\chi}\right)\frac{(1-2t^2)}{\delta}$$

$$\frac{\partial\left(\frac{d\,VOL}{d\chi}\right)}{\partial\,\bar{\chi}} = \left(\frac{d\,VOL}{d\chi}\right)\frac{(2\delta^2 \ln \chi/\bar{\chi})}{\bar{\chi}}$$

$$\frac{\partial\left(\frac{d\,VOL}{d\chi}\right)}{\partial\,V_t} = \left(\frac{d\,VOL}{d\chi}\right)\Big/ V_t$$

$$\frac{\partial\,VOL(\chi)}{\partial\,\delta} = \frac{V_t\, t\, e^{-t^2}}{\delta\sqrt{\pi}}$$

$$\frac{\partial\,VOL(\chi)}{\partial\,\bar{\chi}} = -\frac{V_t\,\delta\, e^{-t^2}}{\bar{\chi}\sqrt{\pi}}$$

$$\frac{\partial\,VOL(\chi)}{\partial\,V_t} = VOL(\chi)\Big/ V_t$$

Upper-Limit Distribution (volume models)

$$\frac{dVOL}{dx} = V_t\left[\frac{1}{x} + \frac{1}{D-x}\right]\frac{\delta}{\sqrt{\pi}} e^{-\delta^2 \ln^2\left(\frac{Ax}{D-x}\right)}$$

$$VOL(x) = V_t\left(\tfrac{1}{2} + \tfrac{1}{2}\,\mathrm{erf}(t)\right) \qquad t = \delta \ln\frac{Ax}{D-x}$$

$$\bar{x}_{32} = D/\left(1+Ae^{1/4\delta^2}\right)$$

$$\bar{x}_{30} = D/\left(1+3Ae^{1/4\delta^2}+3A^2e^{1/\delta^2}+A^3e^{9/4\delta^2}\right)^{1/3}$$

$$\frac{\partial\left(dVOL/dx\right)}{\partial\delta} = \left(\frac{dVOL}{dx}\right)\left(\frac{1-2t^2}{\delta}\right)$$

$$\frac{\partial\left(dVOL/dx\right)}{\partial D} = \left(\frac{dVOL}{dx}\right)\left(\frac{2\delta t \cdot x/D}{(D-x)}\right)$$

$$\frac{\partial\left(dVOL/dx\right)}{\partial A} = \left(\frac{dVOL}{dx}\right)\left(\frac{-2\delta t}{A}\right)$$

$$\frac{\partial\left(dVOL/dx\right)}{\partial V_t} = \left(\frac{dVOL}{dx}\right)/V_t$$

$$\frac{\partial VOL(x)}{\partial\delta} = V_t\, t\, e^{-t^2}/\delta\sqrt{\pi}$$

$$\frac{\partial VOL(x)}{\partial D} = -V_t\,\delta\, e^{-t^2}/\sqrt{\pi}\,(D-x)$$

$$\frac{\partial VOL(x)}{\partial A} = V_t\,\delta\, e^{-t^2}/A\sqrt{\pi}$$

$$\frac{\partial VOL(x)}{\partial V_t} = VOL(x)/V_t$$

Nukiyama-Tanasawa Distribution (volume models)

$$\frac{dVOL}{d\chi} = V_t \frac{\delta z^c e^{-z}}{\chi \Gamma(c)} = V_t \frac{\delta b^{6/\delta} \chi^5 e^{-b\chi^\delta}}{\Gamma(6/\delta)}$$

$$VOL(\chi) = V_t \frac{\gamma(c,z)}{\Gamma(c)} \qquad c = 6/\delta \;,\; z = b\chi^\delta$$

$$\bar{\chi}_{32} = b^{-1/\delta} \Gamma(6/\delta) \Big/ \Gamma(5/\delta)$$

$$\bar{\chi}_{30} = b^{-1/\delta} \left[\Gamma(6/\delta) \Big/ \Gamma(3/\delta)\right]^{1/3}$$

$$\frac{\partial(dVOL/d\chi)}{\partial b} = \left(\frac{dVOL}{d\chi}\right) \frac{(c-z)}{b}$$

$$\frac{\partial(dVOL/d\chi)}{\partial \delta} = \left(\frac{dVOL}{d\chi}\right) \left[\frac{1 + c\,\Psi(c) - c \ln b}{\delta} - z \ln \chi\right]$$

$$\frac{\partial(dVOL/d\chi)}{\partial V_t} = \left(\frac{dVOL}{d\chi}\right) \Big/ V_t$$

$$\frac{\partial VOL(\chi)}{\partial b} = V_t z^c e^{-z} \Big/ b\Gamma(c)$$

$$\frac{\partial VOL(\chi)}{\partial \delta} = b \ln \chi \left[\frac{\partial VOL(\chi)}{\partial b}\right] - \frac{cV_t}{\delta}\left[\frac{\partial VOL(\chi)}{\partial c}\right]$$

$$\frac{\partial VOL(\chi)}{\partial V_t} = VOL(\chi) \Big/ V_t$$

$$\frac{\partial VOL(\chi)}{\partial c} = \frac{\gamma(c+\epsilon,z)/\Gamma(c+\epsilon) - \gamma(c-\epsilon,z)/\Gamma(c-\epsilon)}{2\epsilon}$$

Set b = 1 for the modified distribution

General Exponential Distribution (volume models)

$$\frac{d\,VOL}{d\chi} = \frac{V_t\, q\, z^c e^{-z}}{\chi\,\Gamma(c)} = V_t \frac{q\, b^{(p+1)/q}\, \chi^p e^{-b\chi^q}}{\Gamma\left((p+1)/q\right)}$$

$$VOL(\chi) = V_t \frac{\gamma(c,z)}{\Gamma(c)} \qquad c = \frac{p+1}{q} \qquad z = b\chi^q$$

$$\bar{\chi}_{32} = b^{-1/q}\,\Gamma\left((p+1)/q\right) \Big/ \Gamma\left(p/q\right)$$

$$\bar{\chi}_{30} = b^{-1/q}\left[\Gamma\left((p+1)/q\right) \Big/ \Gamma\left((p-2)/q\right)\right]^{1/3}$$

$$\frac{\partial\left(dVOL/d\chi\right)}{\partial b} = \left(\frac{dVOL}{d\chi}\right)\frac{(c-z)}{b}$$

$$\frac{\partial\left(dVOL/d\chi\right)}{\partial p} = \left(\frac{dVOL}{d\chi}\right)\frac{\ln z - \psi(c)}{q}$$

$$\frac{\partial\left(dVOL/d\chi\right)}{\partial q} = \left(\frac{dVOL}{d\chi}\right)\left[\frac{1 + c\,\psi'(c) - c\ln b}{q} - z\ln\chi\right]$$

$$\frac{\partial\left(dVOL/d\chi\right)}{\partial V_t} = \left(\frac{dVOL}{d\chi}\right) \Big/ V_t$$

$$\frac{\partial\, VOL(\chi)}{\partial b} = V_t \frac{z^c e^{-z}}{b\,\Gamma(c)}$$

$$\frac{\partial\, VOL(\chi)}{\partial p} = \frac{V_t}{q}\left(\frac{\partial\, VOL(\chi)}{\partial c}\right) \quad \text{(see Nukiyama-Tanasawa for } \frac{\partial\, VOL(\chi)}{\partial c}\text{)}$$

$$\frac{\partial\, VOL(\chi)}{\partial q} = b\ln\chi\left(\frac{\partial\, VOL(\chi)}{\partial b}\right) - c\left(\frac{\partial\, VOL}{\partial p}\right)$$

$$\frac{\partial\, VOL(\chi)}{\partial V_t} = VOL(\chi) \Big/ V_t$$

Set b = 1 for the modified distribution

APPENDIX III

Liquid Injection into a Supersonic Stream Data Reduction Equations

1. Mach No.

$$M = \left\{ \frac{2}{k-1} \left[\left(\frac{P_o}{P} \right)^{k-1/k} - 1 \right] \right\}^{1/2}$$

2. Static Temperature

$$T = T_o / \left(1 + \frac{k-1}{2} M^2 \right)$$

or from isentropic relations

$$T = T_o \left(P/P_o \right)^{k-1/k}$$

3. Sonic Velocity

$$a = (kRT)^{1/2}$$

4. Local Gas Velocity

$$V_g = M a$$

5. Gas Flow Rate

$$W_g = A_t \sqrt{\frac{kg}{R} \left(\frac{2}{k+1} \right)^{\frac{k+1}{k-1}}} \quad \frac{P_o}{\sqrt{T_o}}$$

6. Liquid Flow Rate

W_l - Obtain from flowmeter and check with

$$W_l = C_d A_o \sqrt{2g \rho_l \Delta P}$$

7. Injectant Velocity

$$V_l = W_l / \rho_l A_o$$ and check with

$$V_l = C_d \sqrt{\frac{2g \Delta P}{\rho_l}}$$

8. Velocity Ratio

$$VR = V_g / V_l$$

9. Momentum Ratio

$$MR = W_g V_g / W_l V_l$$

10. Dynamic Pressure Ratio

$$\bar{q} = \rho_l V_l^2 / 144 g_k P M^2$$

APPENDIX IV

Droplet Spatial Volume Correction

By geometry and reference to the Spatial Volume Correction figure, one can show that the area blocked by the solid jet is

$$\Delta A_N = \left[\frac{N^2-1}{2}\pi + \sqrt{N^2+1} - N^2 \cos^{-1}\left(\frac{1}{N}\right)\right] R_1^2 \qquad (1)$$

where N is the annulus number $1, 2, \ldots N$.

The general equation for the circle segment area is

$$A_{seg_N} = \left[N^2 \cos^{-1}\left(\frac{1}{N}\right) - \sqrt{N^2-1}\right] R_1^2 \qquad (2)$$

Total Area

$$A_{tot} = \Delta A + A_{seg}$$

Assuming symmetrical distribution of the droplets

$$\frac{V_{tot}}{A_{tot}} = \frac{V_{seg}}{A_{seg}}$$

where

V_{tot} = Volume of droplets in the total annular area

$$V_{tot} = V_{seg}\frac{A_{tot}}{A_{seg}} = V_{seg}\frac{(\Delta A + A_{seg})}{A_{seg}} \qquad (3)$$

Substituting from equations (1) and (2)

$$V_{tot_N} = V_{seg_N}\left[\frac{\frac{N^2-1}{2}\pi}{N^2\cos^{-1}\left(\frac{1}{N}\right) - \sqrt{N^2-1}}\right] \qquad (4)$$

The expression in the brackets is the area correction term for adjusting the droplet volume observed to the true volume.

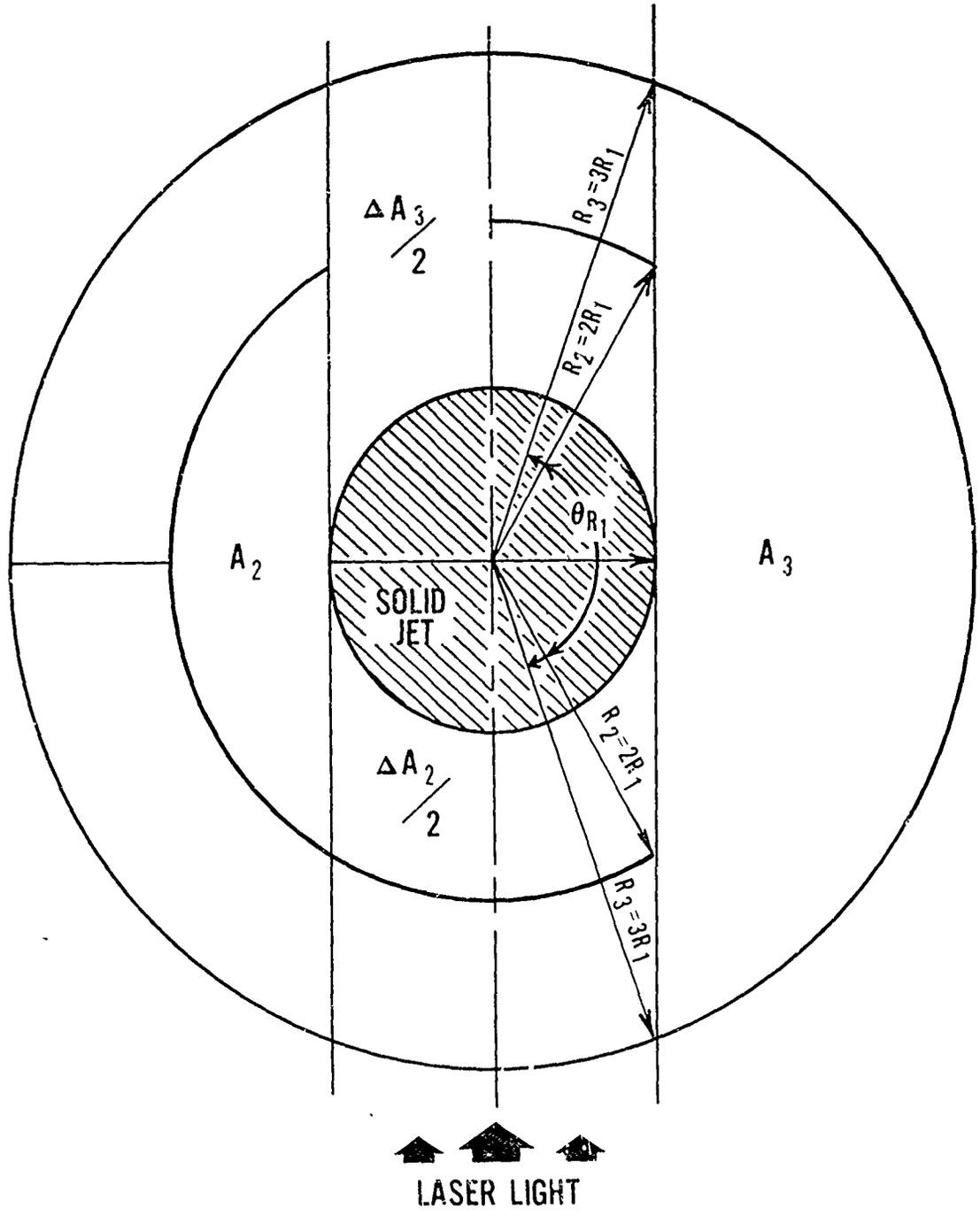

DROPLET SPATIAL VOLUME CORRECTION

APPENDIX V

Jet Amplitude and Wavelength Growth vs. Trajectory Distance

Liquid Jet Amplitude

The following discussion and figures are presented to give the reader a better physical picture of the liquid jet amplitude behavior. The data plotted in Figures V-1 through V-6 is that tabulated in Table X of Chapter VI. Each Figure contains data from the various tests grouped in ascending value of $\bar{q}$. The purpose for this grouping is to observe the dynamic pressure ratio variation effect on amplitude. If one would overlay the Figures or place them side by side, he would observe that the mean line drawn through the data points shifts from the upper left side for Figure V-1 to the lower right side for Figure V-6. This indicates that there is a trend with $\bar{q}$ and amplitude growth decreases with increasing $\bar{q}$. This confirms that equation (32) in Chapter VII predicts the correct behavior of amplitude with dynamic pressure ratio. Also, the Figures reveal that amplitude increases with increase in distance from the injection point. This too is predicted by equation (32). A closer study of the Figures will reveal that the $\bar{q}$ trend is not monotonic in the mid-range ($\bar{q}$ = 20's and 30's, Figures V-3 and V-4) and the slopes of the lines vary somewhat from figure to figure. This perhaps is due to the fluctuating nature of the jet breakup and the fact that an instantaneous record was made of a time varying phenomena. If the holograms of each of the flow fields were taken when the jet penetration was a maximum, for example, one would expect amplitude variation with $\bar{q}$ to be monotonic.

Another observation which can be made is that segregation of the data by liquid type does not occur; the only exception is of the methanol test,

⊡ $\bar{q}$ = 6.7, H_2O, DR-22
⊙ $\bar{q}$ = 11.0, H_2O, DR-4
◑ $\bar{q}$ = 11.4, H_2O, DR-15

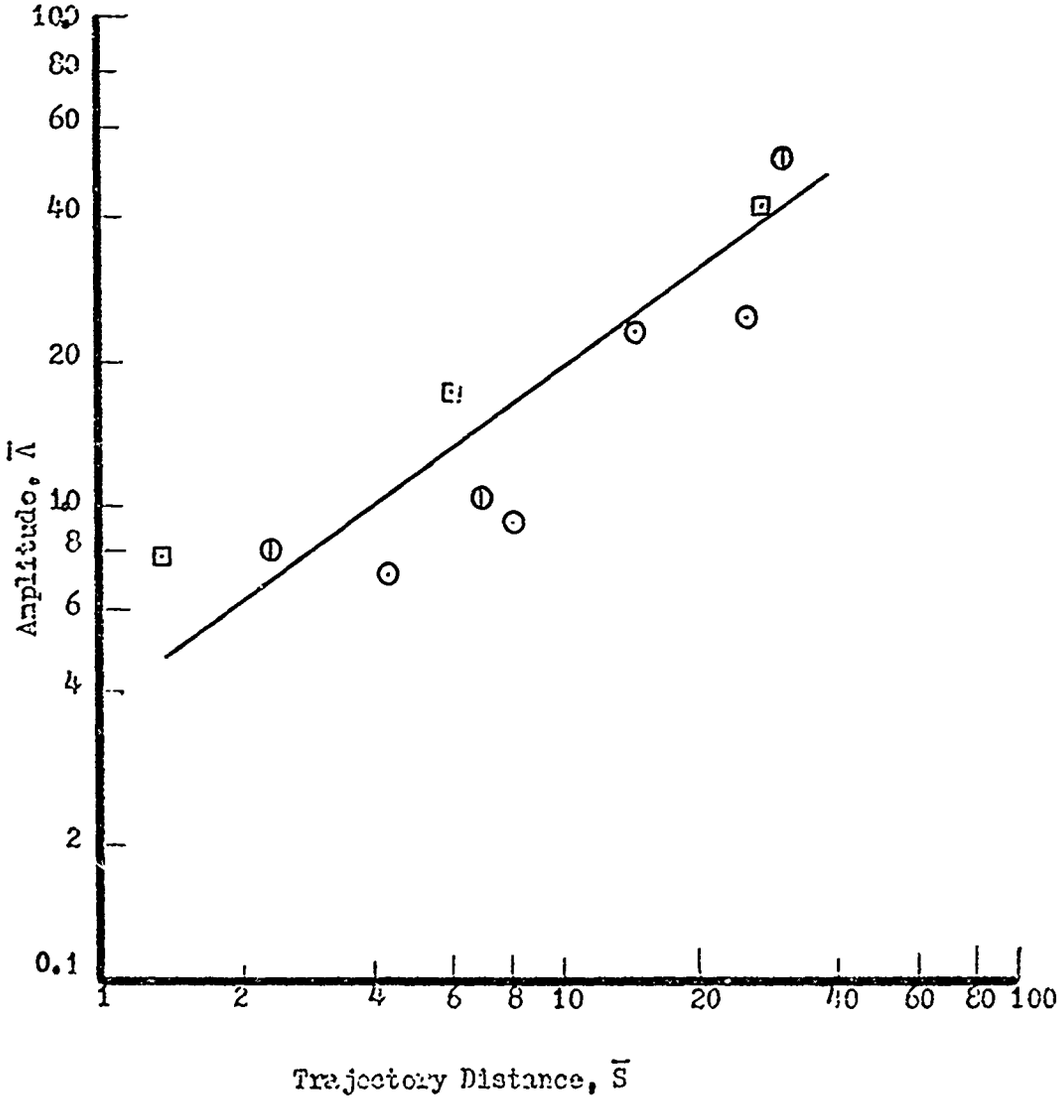

Figure V-1. Amplitude vs. Trajectory Distance

⊙ $\bar{q}$ = 14.0, H_2O, DR-17
⊡ $\bar{q}$ = 14.5, H_2O, DR-12
⊕ $\bar{q}$ = 15.7, H_2O, DR-2
⊞ $\bar{q}$ = 15.7, H_2O, DR-14
⊙ $\bar{q}$ = 16.4, H_2O, DR-5
⊕ $\bar{q}$ = 16.4, H_2O, DR-20
◇ $\bar{q}$ = 16.6, H_2O, DR-11
△ $\bar{q}$ = 17.4, Trich, DR-23

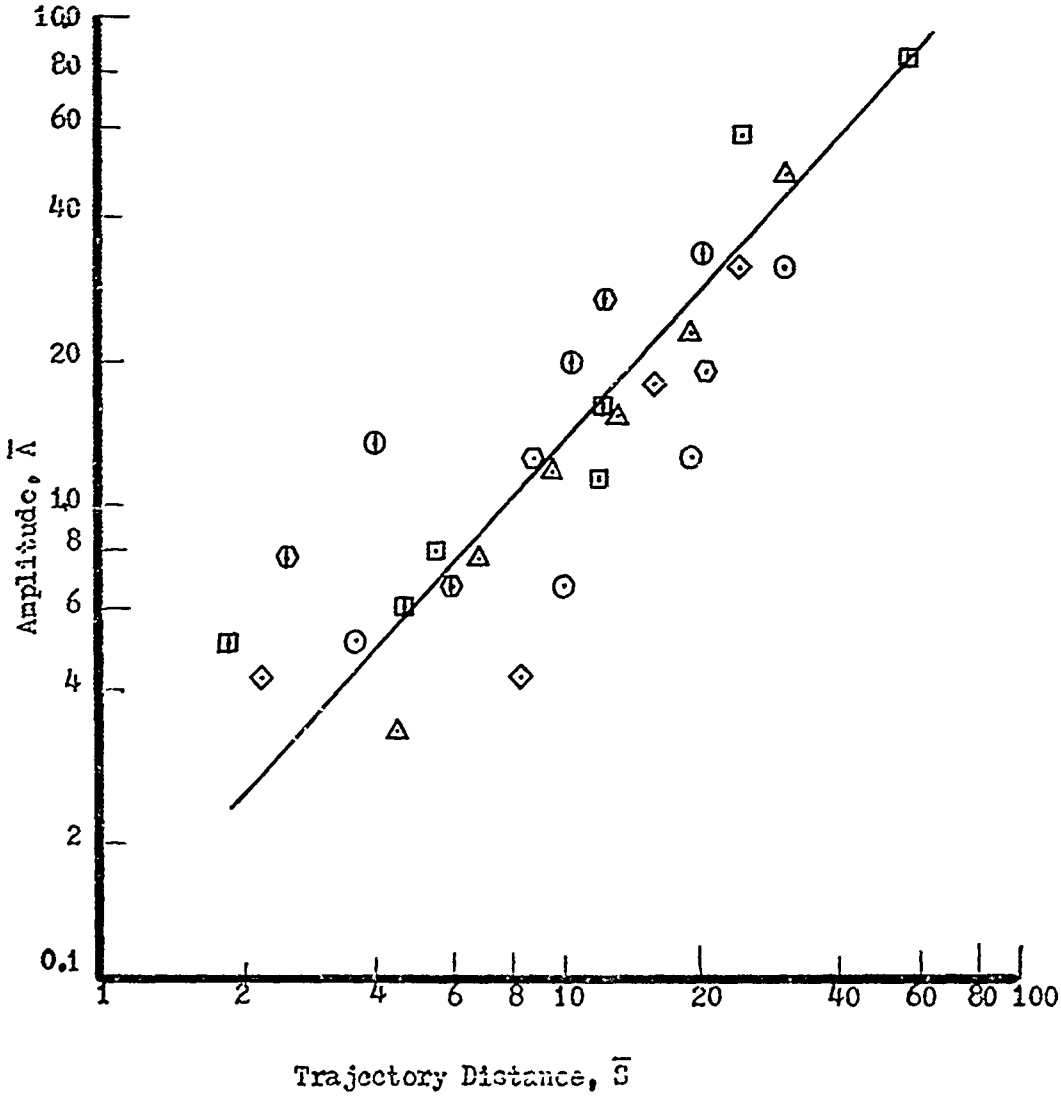

Figure V-2. Amplitude vs. Trajectory Distance

⊙ $\bar{q}$ = 23.9, Trich, DR-24
⊙ $\bar{q}$ = 25.0, Trich, DR-26
⊡ $\bar{q}$ = 27.2, H_2O, DR-
△ $\bar{q}$ = 28.6, H_2O, DR-13

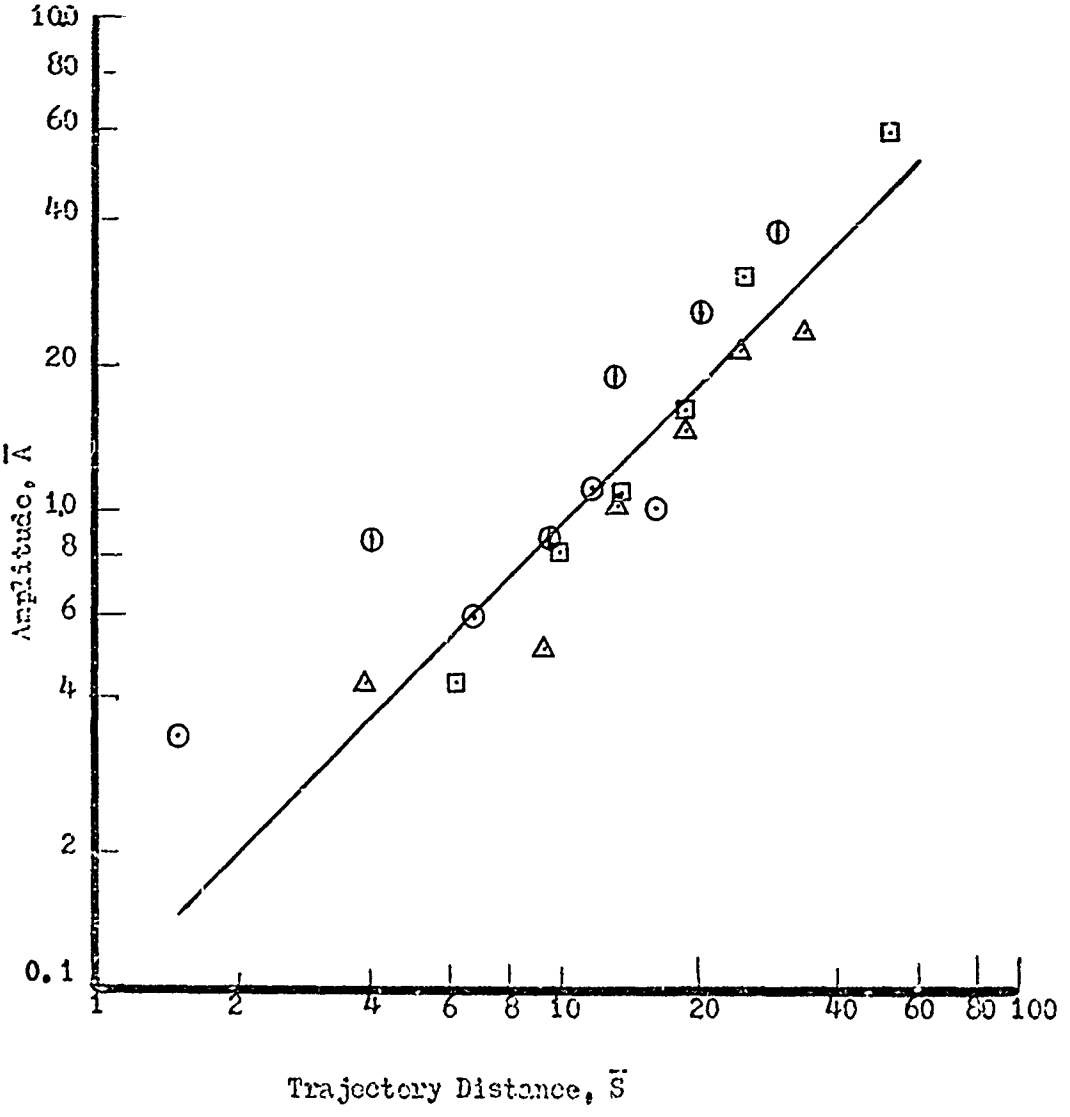

Figure V-3. Amplitude vs. Trajectory Distance

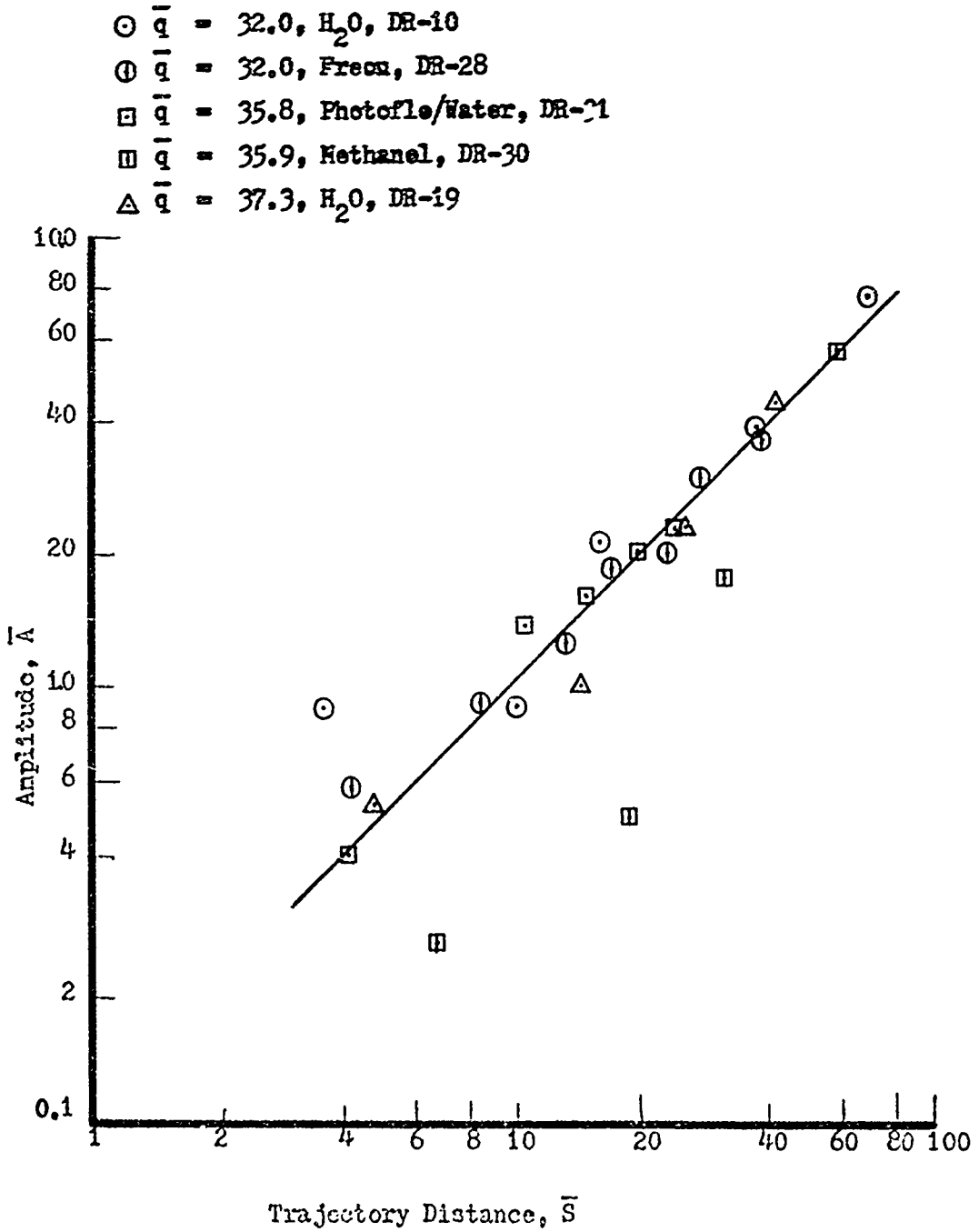

Figure V-4. Amplitude vs. Trajectory Distance

⊙ $\bar{q}$ = 39.6, H_2O, DR-8
⊡ $\bar{q}$ = 45.5, Freon, DR-27
△ $\bar{q}$ = 47.9, Methanol, DR-29

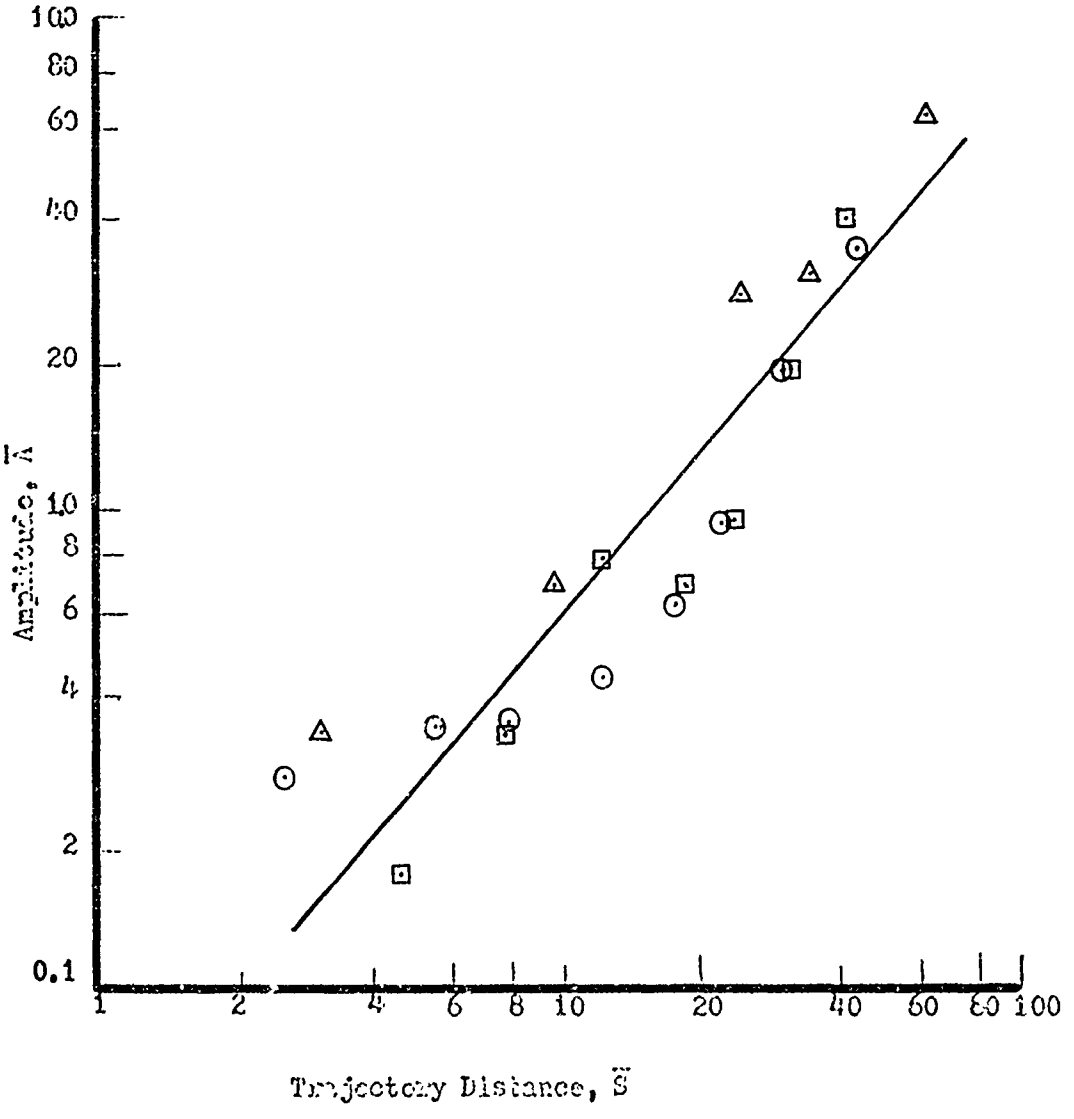

Figure V-5. Amplitude vs. Trajectory Distance

⊙ $\bar{q}$ = 52.5, Trich, DR-25

⊡ $\bar{q}$ = 53.2, Photoflo/Water, DR-32

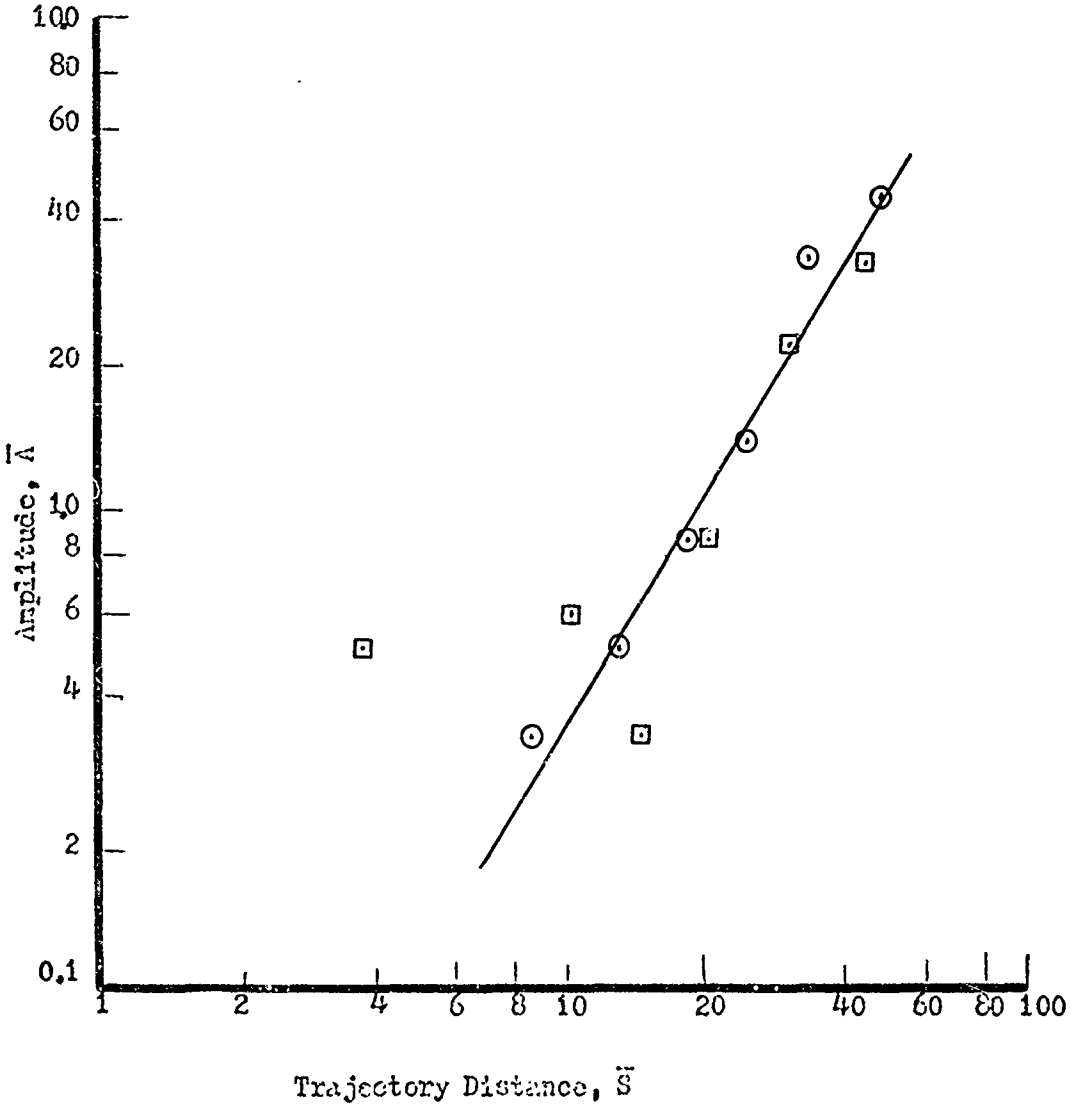

Figure V-6. Amplitude vs. Trajectory Distance

DR-30, in Figure V-4. An explanation for this in terms of fluid physical properties cannot be given.

Liquid Jet Wavelength

The wavelength data presented in Figures V-7 through V-12 is that tabulated in Table XI of Chapter VI. The statements made above about the amplitude data apply equally well to the wavelength data. The wavelength data for test DR-30 in Figure V-10, however, is very much in line with the other test data on the same figure. The data of the trichloroethylene test, DR-23, of Figure V-8 and the methanol test, DR-29, of Figure V-11 tend to separate from the rest of the data in their respective figures. The explanation offered for this behavior is perhaps the jet penetration trajectories for these tests were in a different position than those of the other tests on the respective curves at the time the holograms were taken.

⊙ $\bar{q}$ = 6.7, H_2O, DR-22
⊡ $\bar{q}$ = 11.0, H_2O, DR-4
△ $\bar{q}$ = 11.4, H_2O, DR-15

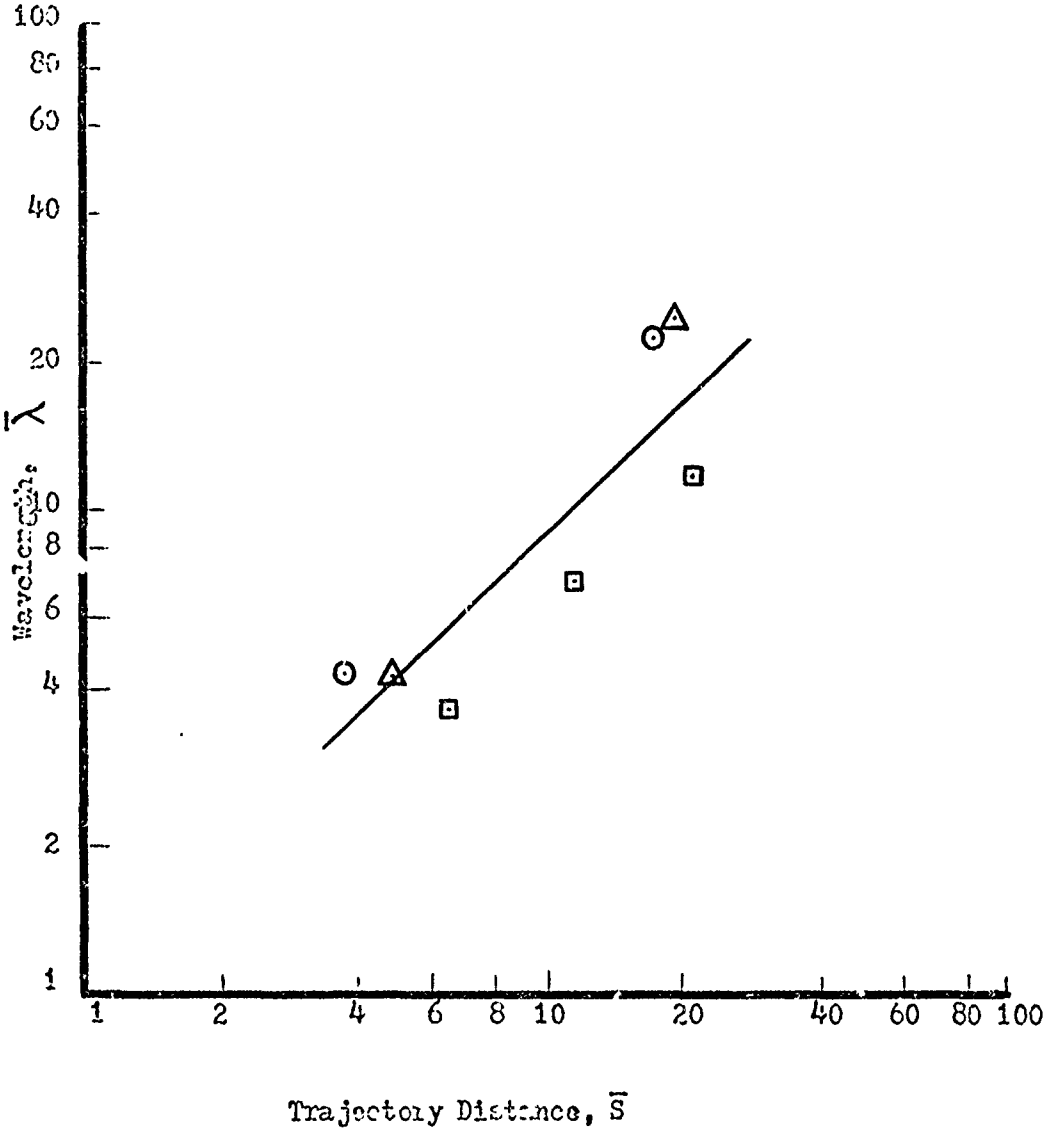

Figure V-7. Wavelength vs. Trajectory Distance

⊙ $\bar{q}$ = 14.0, H_2O, DR-17
⊡ $\bar{q}$ = 14.5, H_2O, DR-12
◐ $\bar{q}$ = 15.7, H_2O, DR-2
▣ $\bar{q}$ = 15.7, H_2O, DR-14
⊙ $\bar{q}$ = 16.4, H_2O, DR-5
◐ $\bar{q}$ = 16.4, H_2O, DR-20
◇ $\bar{q}$ = 16.6, H_2O, DR-11
△ $\bar{q}$ = 17.4, Trich, DR-23

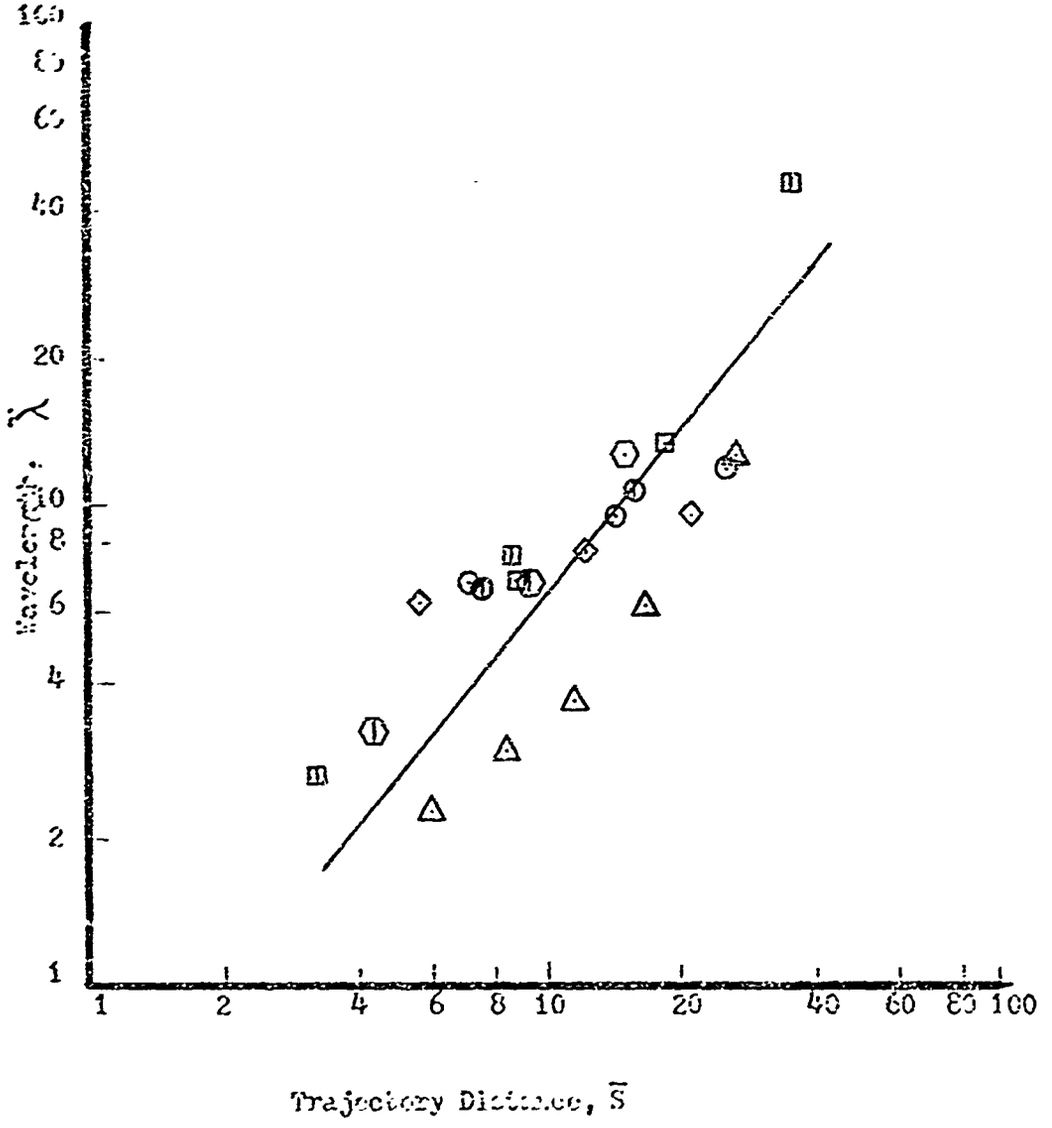

Figure V-8. Wavelength vs. Trajectory Distance

⊙ $\bar{q}$ = 23.9, Trich, DR-24
⊕ $\bar{q}$ = 25.0, Trich, DR-26
⊡ $\bar{q}$ = 27.2, H_2O, DR-3
△ $\bar{q}$ = 28.6, H_2O, DR-13

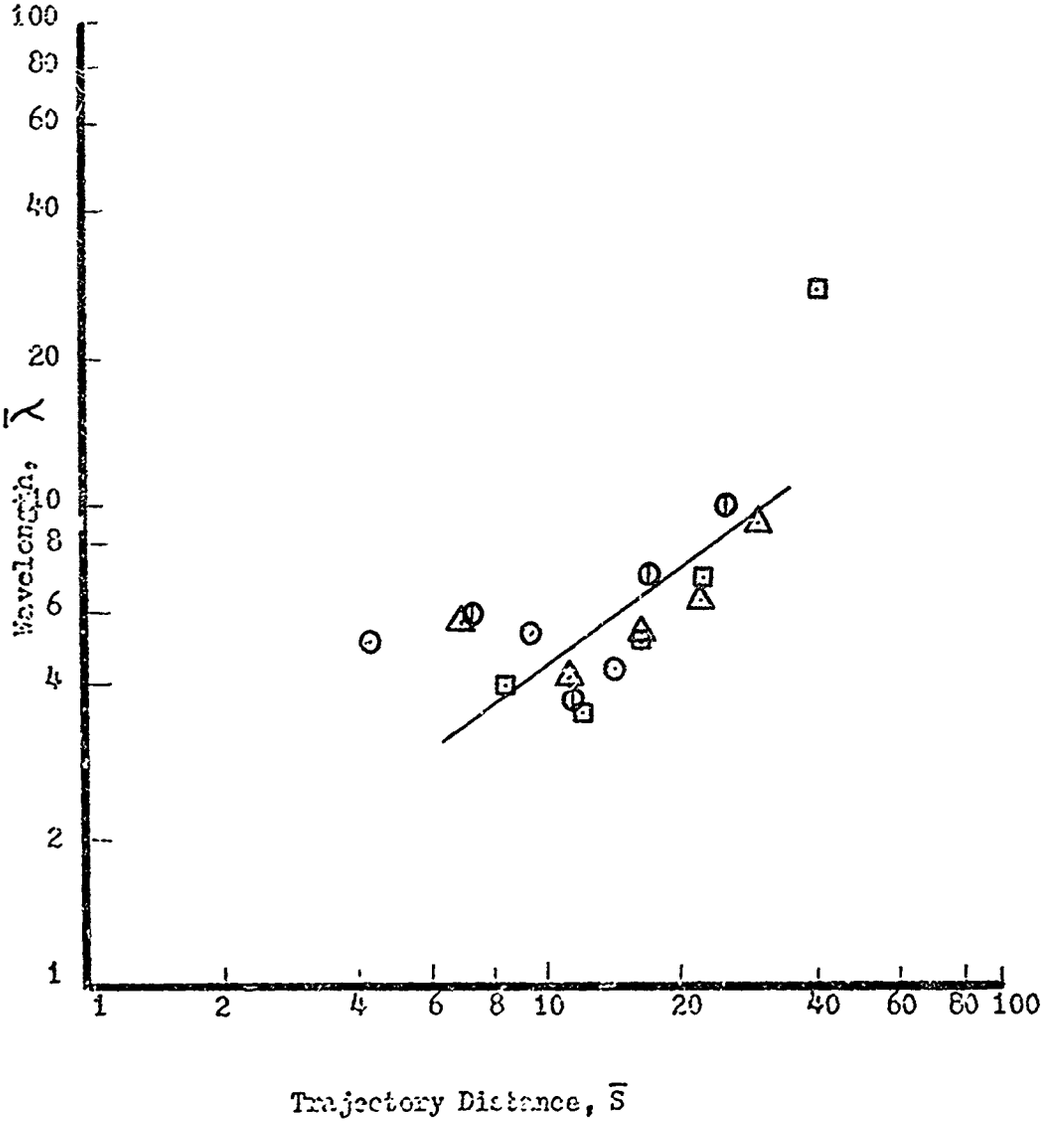

Figure V-9. Wavelength vs. Trajectory Distance

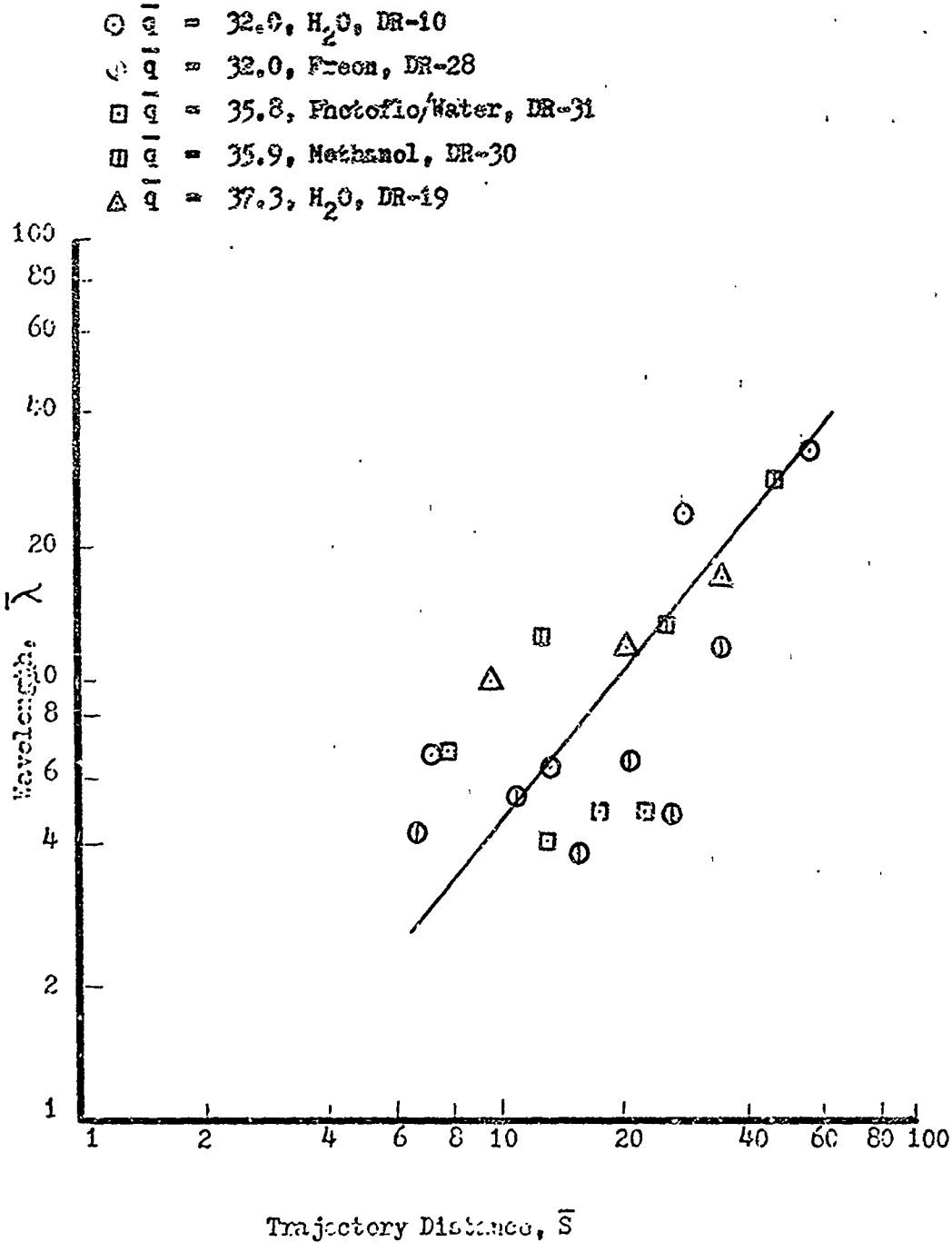

Figure V-10. Wavelength vs. Trajectory Distance

○ $\bar{q}$ = 39.6, H_2O, DR-8

□ $\bar{q}$ = 45.5, Freon, DR-27

△ $\bar{q}$ = 47.9, Methanol, DR-29

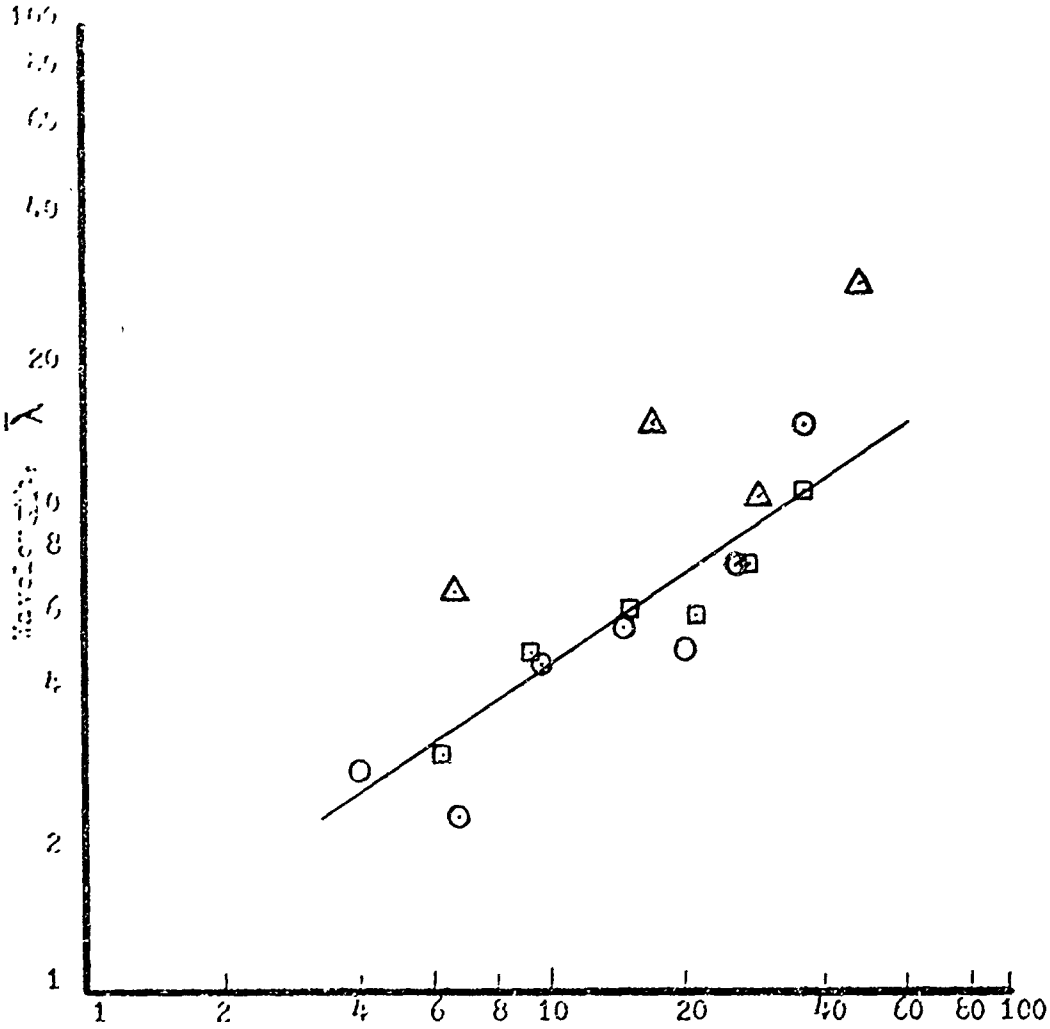

Figure V-11. Wavelength vs. Trajectory Distance

⊙ $\bar{q}$ = 52.5, Tribh, DR-25

⊡ $\bar{q}$ = 53.2, Photoflo/Water, DR-32

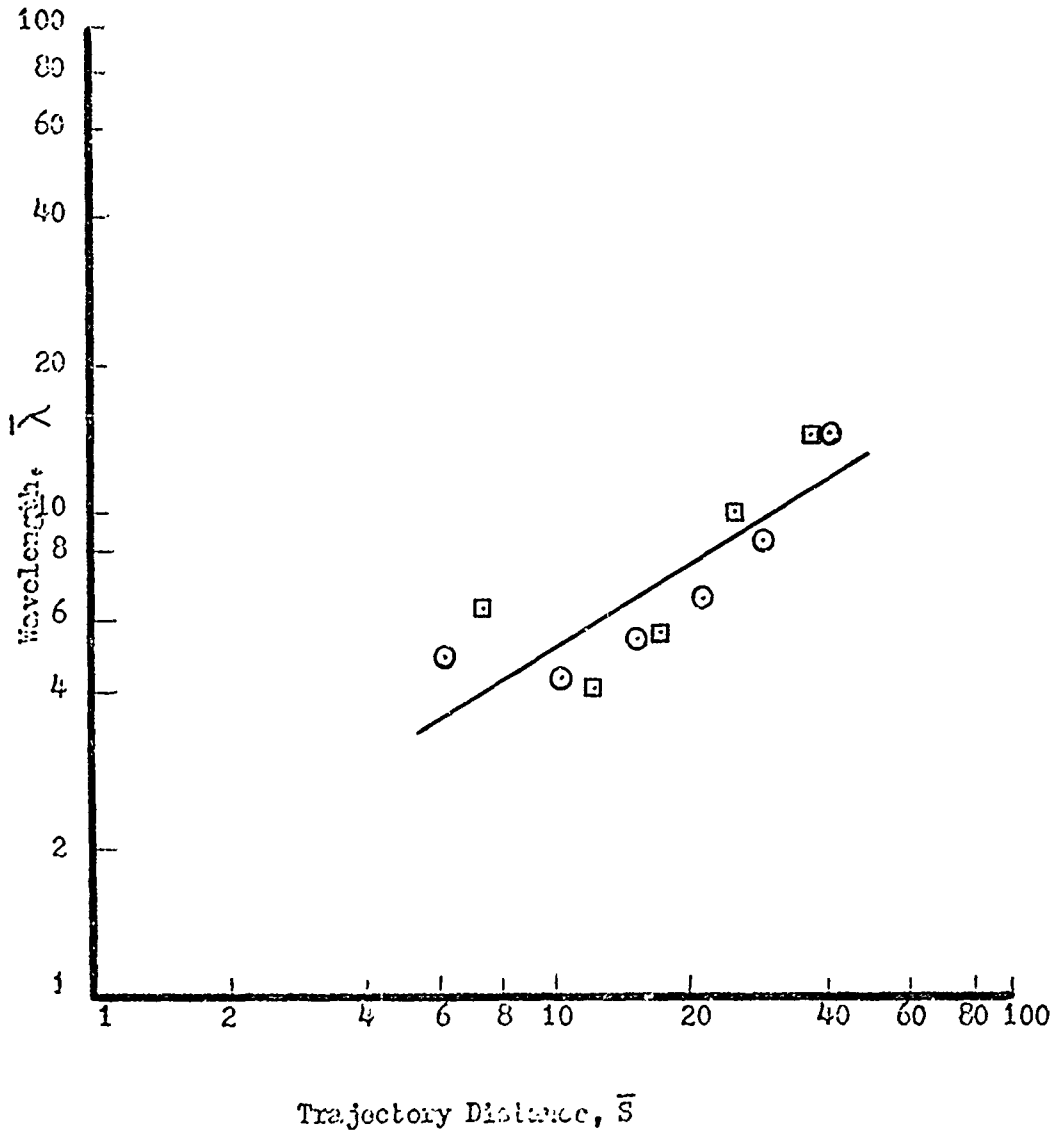

Figure V-12. Wavelength vs. Trajectory Distance